Charge carrier and exciton dynamics within hybrid lead halide perovskites of mixed composition and dimensionality

Thèse N° 9668

Présentée le 23 août 2019

à la Faculté des sciences de base
Groupe Moser
Programme doctoral en chimie et génie chimique

pour l'obtention du grade de Docteur ès Sciences

par

Marine Eva Fedora BOUDUBAN

Acceptée sur proposition du jury

Prof. M. Chergui, président du jury
Prof. J.-E. Moser, directeur de thèse
Prof. T. Feurer, rapporteur
Prof. C. Silva, rapporteur
Prof. N. Grandjean, rapporteur

2019

ÉCOLE POLYTECHNIQUE
FÉDÉRALE DE LAUSANNE

Résumé

Par les temps qui courent, la recherche est principalement dirigée par son potentiel à générer des applications technologiques applicables à notre contexte environnemento-socio-économique, ce qui peut être considéré légitime. Pour nous scientifiques, ceci peut toutefois être frustrant et incarner un obstacle à notre curiosité et notre liberté scientifique. Il en découle que les sujets de recherches qui présentent à la fois un grand impact et un fort intérêt scientifique (au niveau de la stimulation d'idées nouvelles et de la remise en question des modèles établis) constituent une sorte de Graal au sein de la communauté. Les perovskites hybrides organique-inorganique d'halogénures de plomb (PHOIs) rentrent parfaitement dans cette description. Elles présentent en effet un potentiel extraordinaire pour des applications dans le domaine de l'optoélectronique, et sont caractérisées par une grande versatilité en termes de compositions et de dimensions qui donne l'opportunité d'explorer un grand nombre de phénomènes physiques fascinants. Ce travail de thèse reflète cette double nature : chacun des projets scientifiques discutés décrit un type de perovskite de composition ou de dimension différentes, ou traite de questions liées à leur utilisation dans des dispositifs technologiques.

Le chapitre 1 est destiné à fournir au lecteur les concepts scientifiques nécessaires à la compréhension de ce travail, depuis les notions fondamentales décrivant l'interaction lumière-matière, aux spécificités des PHOIs et de leurs applications, en passant par la photo-physique des semi-conducteurs. Le deuxième chapitre présente les idées principales qui sous-tendent les méthodes expérimentales utilisées dans ce travail. Plus spécifiquement, l'interprétation de résultats obtenus par des mesures d'absorption transitoire résolue en temps et leur analyse est discutée, de même que la nature du signal d'électro-absorption et les informations qu'il est possible d'en tirer.

Dans les chapitres 3 et 4, nous considérons des PHOIs tridimensionnelles de composition mixte ($MA_yFA_{1-y}PbI_{3-x}Br_{x.}$), et discutons la photo-physique au sein de leur couche mince de même qu'à leur interface avec des transporteurs d'électrons et de trous (respectivement SnO_2 and spiro-OMeTAD) utilisées dans le cadre de dispositifs photovoltaïques. Il est montré que des excitons à transfert de charge (ETC) se forment entre des domaines de perovskite caractérisés par des proportions d'iodure et de bromure différentes, ce qui génère une séparation de charges de longue durée et des performances photovoltaïques améliorées. En complément, par le biais d'une nouvelle stratégie expérimentale, nous suggérons que l'injection de charges à l'interface SnO_2 | perovskite se fait par l'intermédiaire d'ETC interfaciaux, ce qui ralentit le processus. De plus, notre méthode nous permet de mettre en évidence l'accumulation des charges injectées au sein du matériau spiro-OMeTAD non dopé, ce qui confirme l'importance de l'usage d'additifs dans la fabrication de couches transporteuses de trous utilisées dans des cellules solaires photovoltaïques.
Le chapitre 5 constitue une transition vers des perovskites de plus basses dimensions, en cela qu'il présente une étude fondamentale d'agrégats de nanoparticules de $MAPbBr_3$ (MA = CH_3NH_3), dans des solutions incluant une distrtibution de nanoparticules 3D et de

nanoplaquettes de dimensions quasi-2D de différentes épaisseurs. Nous mettons en lumière des interactions inter-structures sous la forme de transferts d'énergie et de de charges en cascade, ces derniers encore une fois promus par la formation d'excitons TC inter-particules.

Dans le chapitre 6, nous continuons notre exploration de la multi-dimensionalité des PHOIs et considérons des couches doubles du type perovskite 3D/2D impliquant deux différents cations pour la couche 2D, le phenethylammonium (PEA) et le 4-fluorophenethylammonium (FPEA), selon la perspective de leurs performances photovoltaïques. Nous démontrons notamment la relation entre la photophysique de ces interfaces 3D/2D et l'orientation cristalline de la couche 2D, déterminée directement par la structure du cation organique. Plus spécifiquement, nous suggérons qu'une orientation des plans inorganiques de la perovskite 2D parallèle au substrat est la plus efficace pour passiver l'interface et éviter la recombinaison inverse, ce qui se traduit par des voltages à circuit ouvert (V_{CO}) plus élevés.

Enfin, le chapitre 7 spécule à propos de la nature des espèces photoinduites dans les PHOIs 2D et de leur relation avec la structure du cation organique. Nous effectuons des mesures d'absorbance transitoire dépendantes de la densité de porteurs de charges, ainsi que des mesures d'électroabsorption, sur une série de perovskites 2D constituées des cations butylammonium (BUA), FPEA et d'un cation développé récemment, A43. Sur cette base, nous proposons que la photo-physique des PHOIs 2D est dominée par des polarons, dont la taille (et donc l'amplitude du couplage charges-vibration) est déterminée par le désordre du cation.

Mots-clés : perovskites hybrides, photophysique, excitons de transfert de charge, dynamique des porteurs de charges, interfaces, absorbance transitoire femtoseconde, électroabsorption.

Abstract

Research is nowadays usually directed by its potentiality to birth technological applications of relevance in the present environmental-socio-economical context, which can be seen as fair. This can, however, appear frustrating to us scientists, as it sometimes embodies an obstacle to our curiosity and creative freedom. As a consequence, research topics exhibiting both high impact potential and strong scientific interest, in terms of novel ideas and self-questioning driving force, can be seen as some kind of Holy Grail. Hybrid lead halide perovskites (HOIPs) seem to fit this profile; demonstrating an extraordinary potential for optoelectronic applications, their high versatility in terms of composition and dimensionality allows for the exploration of a large number of fascinating solid-state physics phenomena. This thesis faithfully reflects this double nature: each of the projects described is dedicated to a different type of perovskite, at the compositional or dimensional level, or to questions pertaining their embodiment in application-intended devices.

Chapters 1 provides the scientific background necessary for the understanding of this work, from the fundamental concepts underlying light-matter interaction and semiconductor photophysics to the specificities of HOIPs and their optoelectronic devices. The second chapter presents the main concepts related to the experimental methods used in this work. In particular, we discuss the interpretation of femtosecond time-resolved transient absorbance measurements and their analysis, as well as the nature of the electroabsorption signal and the information it holds about the systems being studied.

In chapters 3 and 4, we discuss 3D HOIPs of mixed composition ($MA_yFA_{1-y}PbI_{3-x}Br_x$.), and address both the photophysics in their bulk and at their interfaces with electron-transporting and hole-transporting materials used in photovoltaic devices (SnO_2 and spiro-OMeTAD). We show the formation of bulk charge transfer (CT) excitons between domains of different iodide/bromide proportions, and suggest this to be the origin of a sustained charge separation, yielding better photovoltaic performance. Similarly, using a novel experimental strategy, we propose that charge injection at the SnO_2/perovskite interface is mediated by interfacial CT excitons, and thus, slowed down. Furthermore, our experimental strategy also confirms the importance of additives in photovoltaic-intended spiro-OMeTAD layers, by demonstrating that injected charges accumulate in undoped spiro-OMeTAD.
Chapter 5 constitutes the transition towards perovskite systems of lower dimensionality: it presents a fundamental study of $MAPbBr_3$ (MA = CH_3NH_3) nanoparticle aggregates, solutions involving a distribution of 3D nanoparticles, and quasi-2D nanoplatelets of different thicknesses. We highlight inter-structure interactions in the form of a cascade of energy and charge transfer, the latter being mediated by the formation of interparticle CT excitons.
In chapter 6, we continue our exploration of the multi-dimensionality of HOIPs by focusing on 3D/2D perovskite bilayers, where the 2D layer involves the cations phenethylammonium (PEA) and 4-fluorophenethylammonium (FPEA), in the context of their photovoltaic performance. In particular, we demonstrate a strong relationship between the photophysics at 3D/2D interfaces

and the crystal growth and orientation of the 2D layer, directly determined by the structure of its organic cation. We then go one step further by stating that an orientation of the 2D inorganic planes parallel to the substrate yields the most efficient interfacial passivation and protection against back recombination, which translates into larger open-circuit voltages (V_{OC}).
Finally, chapter 7 speculates the nature of the photoinduced species in 2D HOIPs and how they relate to the structure of their organic cation. We carry out carrier density-dependent transient absorbance and electroabsorption measurements, on a series of 2D systems based on butylammonium (BUA), FPEA, and the newly developed A43 cation. On this basis, we propose that the photophysics of 2D HOIPs is largely dominated by polarons, whose size (and thus the charge-coupling strength) is determined by the disorder of the organic cation.

Keywords : hybrid perovskites, photophysics, charge transfer excitons, charge carriers dynamics, interfaces, femtosecond transient absorbance, electroabsorption.

Foreword

My driving force always has been what I would call “The wonder”. Grasping what the World represents, and trying to grasp what it is, without ever actually succeeding. Patiently creating my own “World model”, and perpetually confronting it with observations and thoughts, mine or ones coming from others, human or not. This brings a real thrill. And I am fairly certain that most scientists, or more globally, most thinkers are driven by the same thrill. But, for some reason, we are not allowed to claim rights to do research just because it is thrilling. We need to motivate it through its alleged impact on the World we are trying to understand. We need to state what it will bring or destroy, whether or not it can bring cures, money or mind-breaking solutions to fashionable problems. We then study, research and solve. Then we sell, and we pretend. Don’t get me wrong: Knowing the broad context and possible impact of my research is exciting, but it does not reduce to this and is should not be justified by it. What is fascinating is the science, the stretch of the model or the world that lives in my mind; not that it allegedly can have any predictable impact on the World.

Table of contents

1 Introduction

As scientists, we always wonder, with varying degrees of awareness, what is science, and how to do science in a satisfying manner. There are, of course, numerous answers to this question, and it has been at the center of philosophical debates for centuries. In this respect, I am particularly fond of Karl Popper (1902-1994), who proposes a view that completely refutes inductive logic, so far ubiquitous in the perception of scientific theories and processes. [1-5] While inductivism allows to map a particular observation ("this swan is white") to general scientific statements ("all swans are white), Popper's deductivism is grounded on the falsifiability of scientific theories: "*These considerations suggest that not the verifiability but the falsifiability of a system is to be taken as a criterion of demarcation*[1]." [6]. As such, Popper describes a scientist as follows: *"Scientists do not confirm hypotheses, they may only corroborate or decisively refute them."*[6]

Based on this, the scientific method can be seen as a stepwise process, similar to "natural selection, as is clearly depicted in Popper's Objective Knowldege (1979): "*The growth of our knowledge is the result of a process closely resembling what Darwin called "natural selection"; that is, the natural selection of hypotheses: our knowledge consists, at every moment, of those hypotheses which have shown their (comparative) fitness by surviving so far in their struggle for existence, a competitive struggle which eliminates those hypotheses which are unfit."* [7,8]

My favourite example of such a process is how the advent of quantum mechanics marginalized the so far undisputed Newtonian mechanics. Since the second half of the 19th century, a sum of seemingly unrelated, fundamental observations and hypotheses were reported. Among them, we can evoke the study of blackbody radiation by Kirchoff, Hertz's report of the photoelectric effect, Planck's law, Bohr's magneton and Einstein's energy quantas. All of those reports (and many others) ultimately falsified Newtonian mechanics, and, together, formed the quantum description of physics. [9] The birth, and subsequent development, of quantum mechanics indubitably led to a broad range of high impact technological applications, such as improvements in the fields of telecommunications, MRI, quantum computing and, my personal favourite of course, lasers.

As a consequence, research in fundamental sciences constitutes the context in which science can be tried, falsified, recreated and pushed further. Then, along this process, various applications can branch out. But they do not constitute a justification for fundamental research, as they are just incidental bonuses from the natural selection within science. And this is what I am getting at with this (only) marginally pedantic introduction; although harbored within the context of renewable energy and solar cell technologies, the work presented is really of fundamental nature and it will not pretend to be otherwise. It indeed might be completely and

[1] NDA : between science and pseudoscience.

utterly useless, or it might one day be part of a multitude of observations constituting a new evolution of science, who knows.

1.1 Light-matter interactions

1.1.1 Useful quantities

Although the following statement is admittedly subjective, one of the greatest achievements of quantum mechanics is a better understanding of light and its interaction with matter. As this thesis does not involve any innovative optical development or technical constructions, we will not enter into the genesis of the electromagnetic wave equation and its various mono- or multidimensional solutions. Instead, let us consider how to model the interaction of light with matter. In this respect, one quantity is of particular importance: the linear dielectric susceptibility χ, as it represents the (linear) response of a material to an applied field $\boldsymbol{E}$. In the present context, $\boldsymbol{E}$ is a light field, that is, an oscillatory function with a time dependence following $e^{(i\omega t-\phi)}$, where ω is the angular frequency and ϕ the possible phase shift. As a consequence, we define the complex, frequency-dependent susceptibility as (in the MKSA system):

$$\chi(\omega) = \frac{\boldsymbol{P}(\omega)}{\varepsilon_0 \boldsymbol{E}(\omega)}, \tag{1.1}$$

where $\boldsymbol{P}$ is the polarization density of the system, ε_0 is the free space permittivity and $\boldsymbol{E}$ is the electric field. As the susceptibility essentially contains all the information needed to describe the linear response of a particular material to a light field, χ is a useful starting point to grasp the physical pictures of other quantities it relates to, which are used more frequently in an experimental context. We start by defining the frequency-dependent dielectric constant $\varepsilon_r(\omega)$, as:

$$\varepsilon_r(\omega) = 1 - \chi(\omega), \tag{1.2}$$

with $\varepsilon_r$complex, yielding:

$$\varepsilon_r = \varepsilon' + i\varepsilon''. \tag{1.3}$$

Note that the frequency dependence will be dropped from now on, as it is implied in the context of complex numbers.

The next quantity of importance is the complex refractive index n^*, which can be seen as a high frequency dielectric constant, relevant for interactions occurring on a fast timescale:

$$n^* = n + i\kappa, \tag{1.4}$$

where n is the ordinary refractive index, while κ is usually denoted as the damping constant, or the extinction coefficient (*vide infra*). Note that the use of n and κ, instead of n' and n'' simply pertains to tradition.

n^* relates to $\varepsilon_r$and χ via:

$$n^* = \sqrt{\varepsilon_r} = \sqrt{1-\chi}. \tag{1.5}$$

In other words, ε_r and $(n^*)^2$carry essentially the same physical meaning, that can be inferred from their relation to χ. Geometrically, their real parts ($\varepsilon'$and n) represent the response of the material that is in phase with the incoming light field, while their imaginary part ($\varepsilon''$and κ) describe the response occurring with a phase shift of 90°. It follows that $\varepsilon'$and $n\,'$ represent the strength of the interaction between the light field and the materials it is moving across, and thus, how much the light is slowed down by this interaction. In turn, $\varepsilon''$and κ can be described as damping factors and reflect the loss of light upon this same interaction.

Importantly, the damping factor (represented by κ from now on) relates to the absorption coefficient, α, via:

$$\alpha = \frac{4\pi\nu\kappa}{c}, \tag{1.6}$$

where ν is the frequency of the incoming light wave and c is the speed of light.

1.1.2 How to describe absorption: Lambert-Bouguer law, transition dipole moment and oscillator strength

As stated above, when a ray of light interacts with a medium with a given refractive index n*, it will be both slowed down and attenuated, according to n and κ in equation (1.4). The attenuation arises from either light absorption or reflection. Reflection is a process through which the direction of an incoming light beam is modified when reaching an interface between two media. The nature (specular or diffuse) and amplitude of the reflection is then determined by the structure and composition of the interface. Alternatively, absorption is a process intrinsic to the material under study: It constitutes a unique access to its structure at the molecular level and its behavior under photoexcitation.

In this context, the absorption coefficient α, defined above, is of great importance as it provides a phenomenological description of light attenuation when crossing a material of thickness dx:

$$\frac{dI(x)}{dx} = -\alpha I(x), \tag{1.7}$$

where α is the absorption coefficient of the material, and I the intensity of the light.

Integrating the above equation yields Lambert's law, and the well-known exponential attenuation of light absorption across a material:

$$I(x) = I_0 e^{-\alpha x}, \tag{1.8}$$

where x, α, and I are defined similarly as in equation (1.7), and I_0 is the intensity of the incident light beam.

Lambert's law provides the fate of an incoming light beam once it is absorbed by a material, but does not provide information regarding the nature of this absorption. Indeed, in the context of the present work, we are mainly interested in electronic absorption processes. We define two conditions for light absorption yielding electronic excited states:

1. The incoming photon must match the energy separation between the two electronic states of interest (energy conservation).
2. The transition dipole moment $\boldsymbol{m}$ must be nonzero.

The transition dipole moment, $\boldsymbol{m}$, is defined as:

$$\boldsymbol{m}_{l \leftarrow k} = \langle \psi_l | \boldsymbol{\mu} | \psi_k \rangle, \tag{1.9}$$

where ψ_l and ψ_k are the total wavefunctions of states l and k respectively, and $\boldsymbol{\mu}$ is the electric dipole moment. In light of equation (1.9), it appears clearly that $\boldsymbol{m}$ defines the interaction between the electronic states of interest and the electric component of the light field. The second of the above-mentioned two conditions for light absorption thus emerges naturally. For practical reasons, it is convenient to explicate equation (1.9):

$$\langle \psi_l | \boldsymbol{m} | \psi_k \rangle = \langle \varphi_l | \boldsymbol{\mu} | \varphi_k \rangle \langle \sigma_l | \sigma_k \rangle \langle \chi_l | \chi_k \rangle, \tag{1.10}$$

where σ_l and σ_k are the spin wavefunctions for states k and l, while χ_l and χ_k denote their nuclear wavefunctions. In turn, $\langle \sigma_l | \sigma_k \rangle$ and $\langle \chi_l | \chi_k \rangle$ represent the spin and nuclear overlap integrals between states l and k. This yields the well-known selection rules for electronic excitation that essentially relate to the symmetry of the wavefunctions of states k and l (total angular momentum conservation), the conservation of the total spin quantum number upon this transition, and finally, to the parity of the nuclear wavefunctions of interest.[10]

The transition dipole moment is, furthermore, directly related to another quantity more widely used in an experimental context: the oscillator strength $f_{l,k}$, given by:

$$f_{l,k} = \frac{8\pi^2 m_e c}{3he^2} \, \bar{v}_{max} \, \boldsymbol{m}_{l \leftarrow k}^2, \tag{1.11}$$

where m_e is the mass of an electron, h is Planck's constant, e is the elementary charge of an electron, $\bar{\nu}_{max}$ is the frequency corresponding to the maximum of an absorption peak (cm^{-1}) and $\boldsymbol{m}$ is the transition dipole moment.

1.2 About semiconductors

1.2.1 Definition and fundamental properties

The quantization of energy states arises from the enforcing of boundary conditions when solving the molecular Schrödinger equation.[11] It thus relates to the components of the potential term in the Hamiltonian, determined by the density and distribution of positive and negative charges in the system. As such, when the number of atoms becomes larger, the number of solutions of the Schrödinger equation fulfilling the boundary conditions increases, yielding a larger density of eigenstates. Aside from quantization, another notion of importance in the context of quantum theory is the Pauli exclusion principle: Two electrons cannot coexist with the exact same set of quantum numbers.

Semiconductors are solids, and solids are essentially a repetition of a single molecular unit in the three-dimensional space, with a correspondingly high atom density. In light of the previous paragraph, the nature of their eigenstates can be understood as follows: First, as stated above, the large number of atoms yields a high density of eigenstates. Second, the overlap of the individual atomic wavefunctions induces a lifting of the degeneracies present, due to the Pauli exclusion principle. This creates a series of almost degenerate electronic states, forming continuums called bands, as illustrated in Figure 1-1.

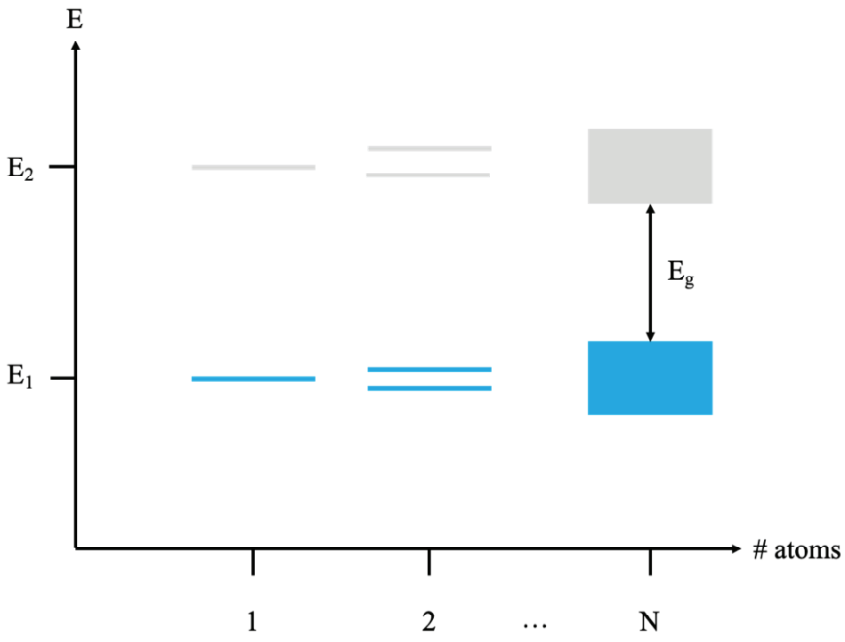

Figure 1-1 From discrete states to bands.

In solids, energy bands where electrons are allowed to exist (in accordance with the above-mentioned parameters) are separated by bands that are forbidden. The lowest lying allowed band is called the valence band, while the other allowed bands are called conduction bands. The energy difference between two allowed bands is called the band gap (E_g), and is the determinant in assessing numerous material properties, for example their ability to transport charges or the way they absorb light.

The ability of a solid to transport charges is called electric conductivity, and directly depends upon the availability of accessible empty states for valence band electrons. Importantly, conductivity (at room temperature) constitutes a classification criterion to distribute solids into the following three categories: metals, semiconductors and insulators.

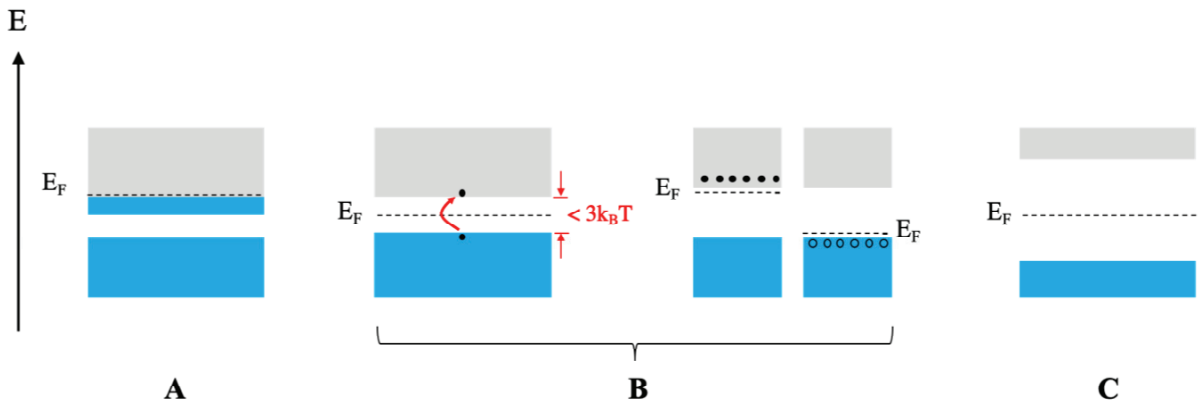

Figure 1-2 The conductive properties of solids. Full bands are indicated in blue, while empty bands are in grey. Dotted lines represent the Fermi level, filled and empty black circles respectively denote electrons and holes. **A**. Metal. **B.** Semiconductor, via thermal promotion of electrons across the bandgap (left) or chemical doping (right). **C**. Insulator.

Metals are characterized by overlapping conduction and valence bands, or by a partially filled conduction band, and, thus, by an efficient electric conductivity at room temperature (Figure 1-2A). On the contrary, as shown in Figure 1-2C, insulators exhibit large band gaps, preventing any thermal promotion of electrons from the valence to the conduction band (i.e. no empty states are available to allow charge carrier motion). Finally, semiconductors (Figure 1-2B) are insulators that can possibly be conductors through thermal promotion of electrons across the bandgap ($E_g < 3k_BT$), doping or intrinsic light absorption.

1.2.2 Light absorption by semiconductors

Because of the large density of states of solids (the bands), it is useful to describe the selection rules governing their electronic transitions within the reciprocal space (k-space) instead of using the explicit treatment described in section 1.1.2 . The critical parameters described there can indeed be fitted into the following two simple conditions:

1. The incoming photon must match the energy separation between the two electronic bands of interest (energy conservation).

2. Because optical photons only carry a negligible momentum, any allowed transition must preserve the initial momentum (momentum conservation).

In the k-space, transitions can be deemed vertical (direct) or non-vertical (indirect). Direct transitions fulfill the momentum conservation condition, while indirect transitions can only occur via coupling with a phonon (Figure 1-3).

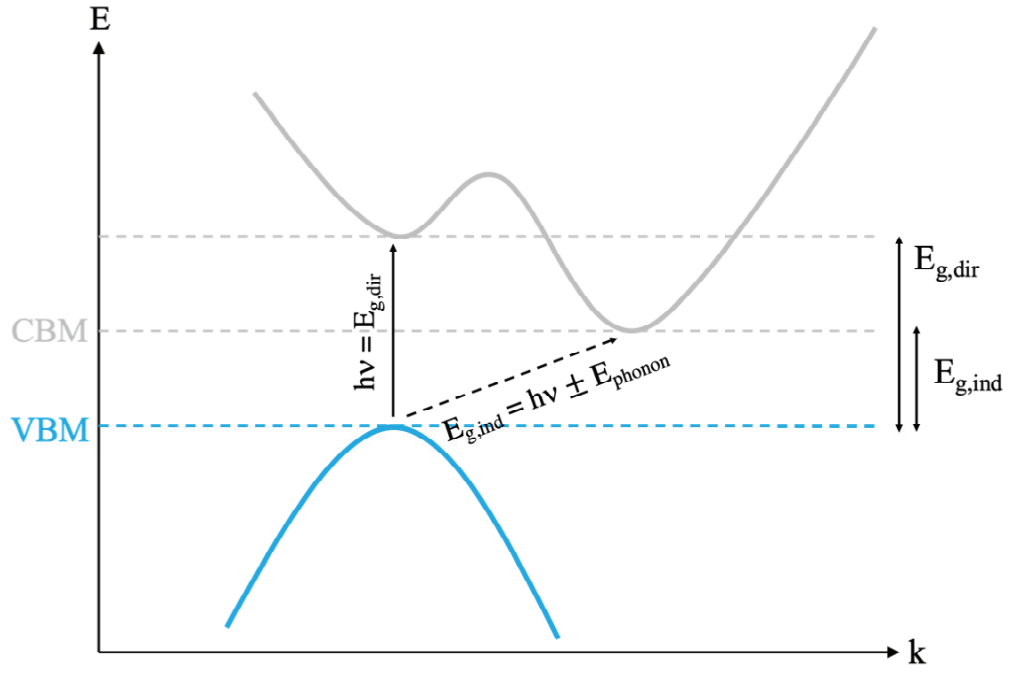

Figure 1-3 Direct and indirect transitions in k-space with corresponding contributions.

Note that, as expected, direct transitions feature large oscillator strengths, with α values typically larger by 3 orders of magnitude compared to indirect transitions.

1.2.3 Band structure of solids

For any quantum system, energy states are obtained by solving the time-dependent Schrödinger equation, whose solutions (both eigenvalues and eigenfunctions) strongly depend on the Hamiltonian involved, in particular, on the potential energy term V(r). As stated previously, bulk semiconductors are repetitions of a single molecular unit in the three-dimensional space, and it follows that the potential of such a system must be periodic. In this respect, Bloch's theorem provides us with a straightforward solution for the wavefunction (in 3D):

$$\psi_k(r) = e^{ikr} u_k(r), \tag{1.12}$$

where $u_k(r)$ is a periodic function with the same periodicity as V(r), and k is the wavevector (or quasi wavevector, as the potential is not constant). A consequence of Bloch's theorem is the possibility to completely describe the electronic structure of a semiconductor by focusing solely on the first Brillouin zone, a uniquely defined primitive cell in the reciprocal space.

To provide a physical picture of the electronic structure arising from a system described by Bloch functions, we consider two limiting cases in the resolution of the Schrödinger equation. First, we take the limit for $V(r) \longrightarrow 0$: this is the free electron model, where the Schrödinger equation is solved perturbatively (as $V(r) \ll E_{kin}$). The following expression is obtained for the energy eigenstates:

$$E(k) = \frac{\hbar^2 k^2}{2m^*} , \tag{1.13}$$

where $\hbar$ is the reduced Planck's constant and m^* the carriers' effective mass. This yields parabolic dispersion curves, which constitute an accurate approximation for most systems around the maximum (minimum) of the valence band (conduction band). Intuitively, this model thus describes electrons trapped in individual parabolic potential boxes, periodically repeated as follows from the Bloch states.

Alternatively, we can consider the limit of large $V(r)$, and the corresponding model: the tight-binding approximation. In particular, the electron-nucleus interaction potential is assumed large and the electrons remain localized around the nuclei. The Bloch states are thus well-approximated by the linear combination of atomic orbitals (LCAO). However, even for a single one-dimensional band, this results in energy dispersion relations with parameters often obtained from experimental data. In this work, we will thus focus on the physical picture drawn by the free electron model, assuming we consider mostly the dynamics of relaxed systems.

1.2.4 Types of photocarriers and characteristic quantities.

Performing experiments involving the absorption of a photon by a system of interest brings direct insight on two parameters of importance: its ground-state electronic structures (allowed vibronic transitions), and its excited-state properties (excited-state electronic structure and the nature of the photoinduced species).

1.2.4.1 Typology of charge carriers

In the case of semiconductors, the nature of the photoinduced species covers a broad range of possibilities, and is of particular importance. When a photon is absorbed, an electron is promoted from the valence to the conduction band. The promoted electron might then remain correlated to the electronic lacuna, the hole, it left behind. It is the degree of this correlation that determines the type of photocarriers involved, and thus, the fundamental properties of the material.

Which photocarrier can be found in which system has a lot to do with the dielectric constant of the material. A high dielectric constant, and thus, a large susceptibility, means that the material can easily accommodate a displaced charge, and screen it efficiently. Alternatively, systems with a low dielectric constant have a diminished ability to stabilize the displaced charges, which will remain strongly correlated.

In light of this, and neglecting any type of coupling to the lattice, photogenerated electrons and holes in semiconductors essentially belong to two categories: free carriers and excitons. In the former case, the electron and the hole are uncorrelated and simply coexist in the system (Figure 1-4A). Alternatively, within an exciton, the photocarriers are Coulomb-correlated: they form a bound electron-hole pair, with a characteristic size and binding energy E_b, directly reflecting the strength of the electron-hole correlation. Because of the broad range of values that E_b can adopt, various types of excitons exist that exhibit very different properties.

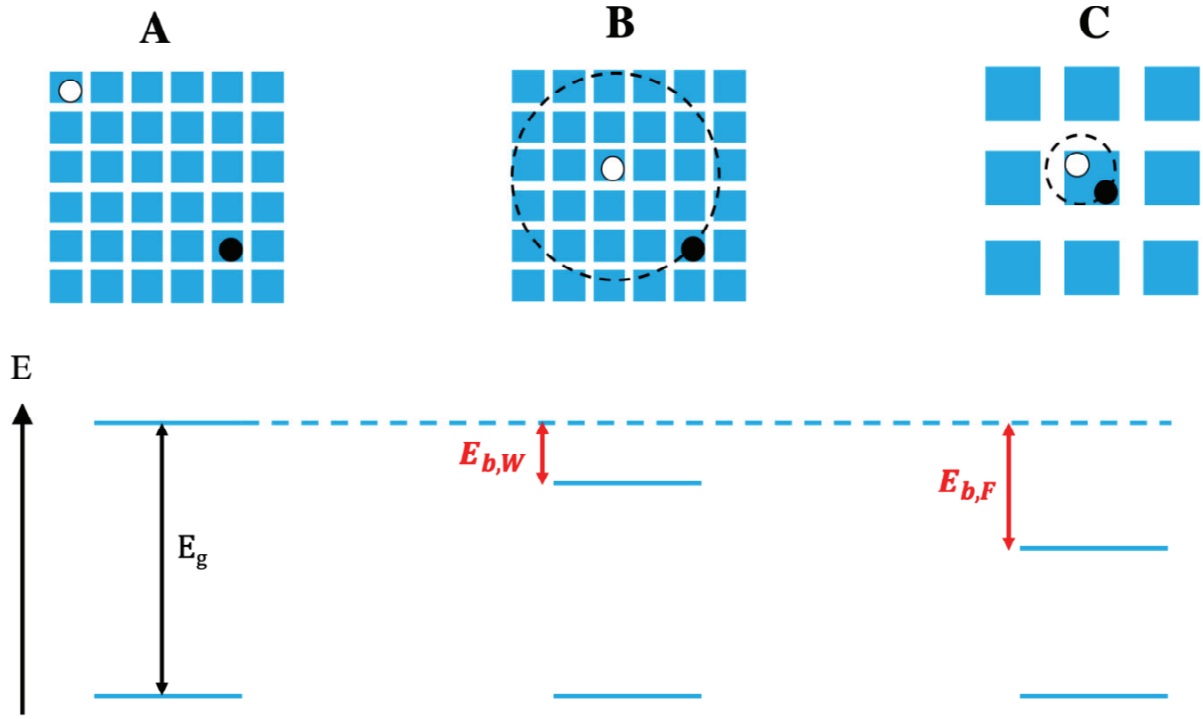

Figure 1-4 Photocarriers in semiconductors with various degrees of correlation. **A.** Free carriers: The electron and its valence band lacuna are uncorrelated. **B.** Wannier-Mott exciton, characterized by a large Bohr radius, a smaller effective mass/larger band curvature and a small binding energy relative to Frekhel excitons. **C.** Frenkel exciton. This species is characterized by a small Bohr radius, a large effective mass/small band curvature and a larger band energy than Wannier excitons. $E_{b,W}$ and $E_{b,F}$ describe the binding energy of the Wannier and the Frenkel exciton, respectively.

Frenkel excitons are characteristic of systems with a low dielectric constant: they feature large binding energies, are localized within one unit cell, and are typically found in organic or highly polar semiconductors (Figure 1-4C). In turn, Wannier-Mott excitons are usually delocalized over several unit cells, and are customarily associated to inorganic semiconductors (Figure 1-4B). In organic systems, or equivalent, we can define a third type of exciton, intermediate between the Frenkel and Wannier-Mott types: the charge-transfer (CT) exciton. This species is usually defined as an electron and hole interacting across an interface, a junction, or domain boundaries, and, as such, carries a significant dipole moment.

1.2.4.2 The Wannier-Mott exciton and the Bohr planetary model

We mentioned that excitons can be differentiated according to their size and binding energy. The definition of those quantities becomes simple in the context of the Bohr planetary model for the hydrogen atom, with the hole in place of the H nucleus (Figure 1-5). This hydrogenic

modelling of an exciton, however, only works for excitons of the Wannier-Mott type, or similar; Frenkel excitons, for instance, are too small and too strongly correlated to be accurately described in this way.

Because the electron is viewed as orbiting around the hole, the size of an exciton within an hydrogenic model is assimilated to a radius, called the Bohr radius, defined as follows:

$$r_{B,x} = \varepsilon \cdot \frac{m_e^*}{m^*} \cdot r_{B,H}, \tag{1.14}$$

where m^* is the electron and the hole's reduced mass, m_e^* is the electron effective mass and ε is the dielectric constant of the material. $r_{B,H}$ is the Bohr radius for the hydrogen atom, given by:

$$r_{B,H} = n^2 \cdot \frac{\hbar^2 \varepsilon_0}{\mu e^2}, \tag{1.15}$$

where μ is the reduced mass for the proton and the electron, $\hbar$ the reduced Planck's constant, ε_0 the vacuum permittivity and e the elementary charge. n is nothing but the principal quantum number assessing the transition under focus: excitons are thus often labelled according to hydrogenic transitions: 1s, 2s, etc.

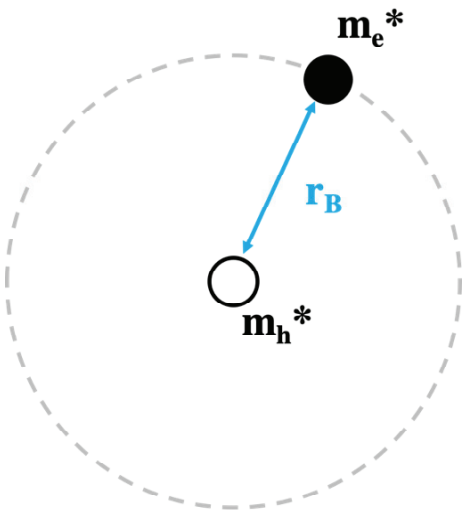

Figure 1-5 Bohr planetary model adapted to the case of Wannier-Mott excitons.

In turn, the binding energy of a Wannier-Mott-like exciton is given by:

$$E_b = \frac{m^*}{m_e \varepsilon^2} \cdot \frac{e^2}{2 r_{B,H}}, \tag{1.16}$$

which, for the 1s exciton, comes down to:

$$E_b = \frac{m^*}{m_e \varepsilon^2} \cdot 13.6[eV] \tag{1.17}$$

Importantly, the binding energy is thus directly proportional to the electron and the hole effective masses and, as such, reflects the local topology of the band structure (as illustrated in Figure 1-4).

1.2.4.3 Optical properties of excitons

Excitons are easily identifiable optically; they indeed have their own absorption peak, located below the band edge, at a wavelength dependent on their binding energy. The total absorbance spectra of semiconductors with excitonic interaction thus includes contributions both from the continuum (free carrier absorption) and from the exciton, as illustrated in Figure 1-6.

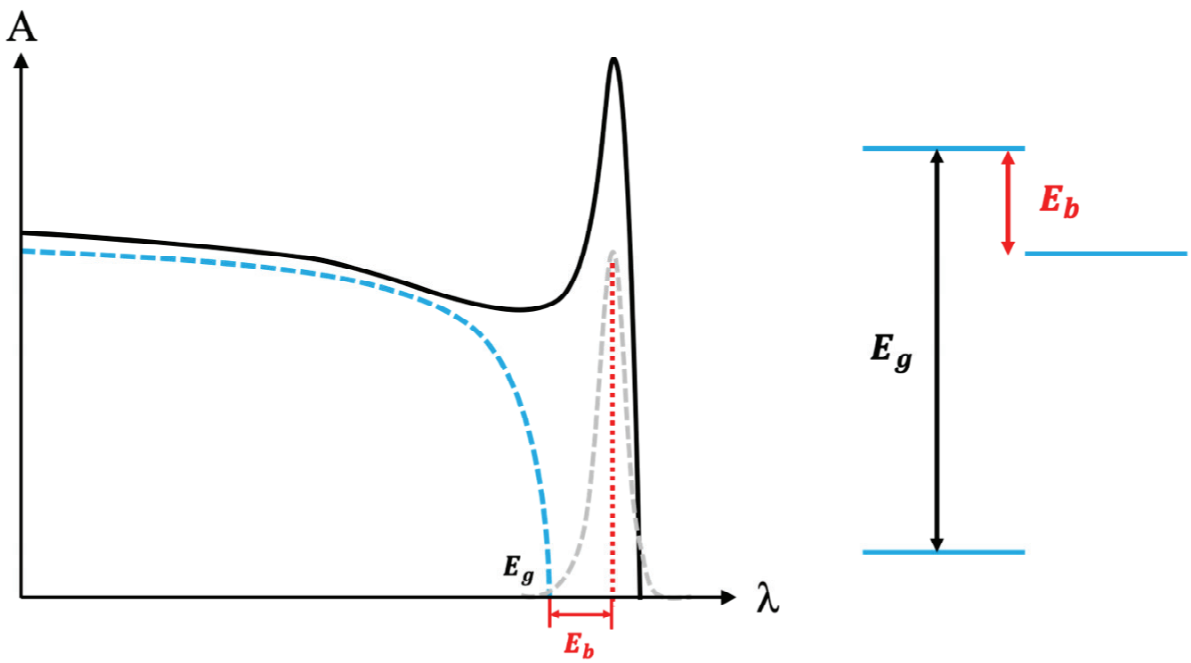

Figure 1-6 Contributions within the absorbance spectrum of a semiconductor with excitonic interactions.

In addition, referring to equation (1.11) presented in section 1.1.2, and because the electron and the hole wavefunctions within an electron exhibit a strong overlap, the oscillator strength of an exciton is usually large ($\propto E_b$).

1.2.5 Recombination mechanisms

If no external forces intervene, a photoexcited electron-hole pair will eventually collapse back into a valence band electron via recombination. In the context of semiconductors, the evolution of the number of carriers N over time is given by:

$$\frac{dN(t)}{dt} = -k_3N^3 - k_2N^2 - k_1N, \tag{1.18}$$

where k_3, k_2 and k_1 are the rate constants associated to the following three recombination mechanisms, respectively: Auger recombination, band-to-band bimolecular recombination and Shockley-Read-Hall (trap-assisted) recombination. The mechanisms associated to those processes are illustrated in Figure 1-7 below (for electrons; holes undergo mirror processes): In Auger recombination (Figure 1-7A), the energy of the photoexcited electron is transferred to a third carrier (electron or hole), which is in turn promoted to higher energy levels (within the same band). Band-to-band recombination occurs when the conduction band electron recombines back with its hole, yielding an N^2 dependence (Figure 1-7B). Finally, trap-assisted recombination is rate-limited by the concentration of electrons (holes) in traps, that subsequently recombine with a hole (electron) in the valence (conduction) band. As a consequence, this mechanism evolves linearly with the number of photocarriers (Figure 1-7C).

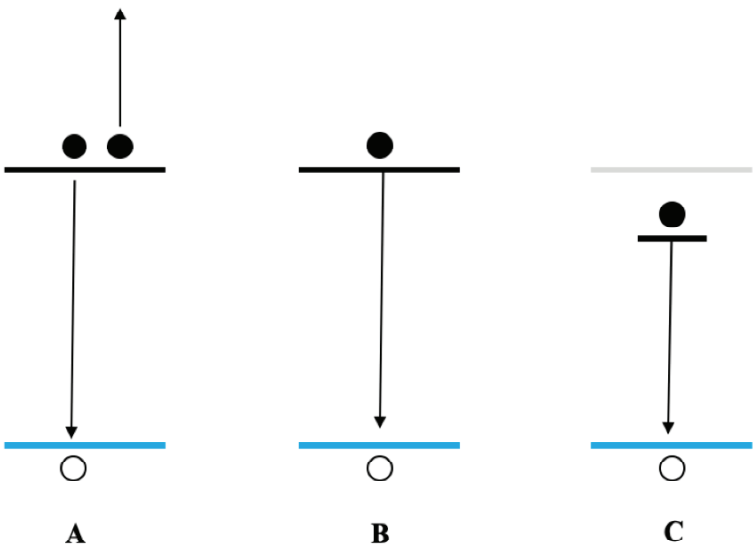

Figure 1-7 Recombination mechanisms within photoexcited semiconductors. **A.** Auger recombination ($\propto \boldsymbol{N^3}$). **B.** Band-to-band recombination ($\propto \boldsymbol{N^2}$). **C.** Trap-assisted recombination ($\propto \boldsymbol{N}$).

Among those processes, some can be accompanied by the emission of a photon: they are then called radiative recombination. Auger recombination is never radiative, as the excess energy is used to excite another carrier. Band-to-band recombination is radiative, provided the transition is direct (otherwise, instead of a photon, a phonon is emitted). Within the SHR mechanism, the trapping process in itself is non-radiative, but the subsequent recombination itself can be radiative (although with very low oscillator strength).

1.2.6 Confinements : Definition and consequences

So far, we have considered semiconductors in their three-dimensional versions, where charges are free to evolve in any direction. Alternatively, lower dimensional systems exist: two-dimensional (2D) sheets, one-dimensional (1D) wires and zero-dimensional (0D) quantum dots,

also called 2D, 1D and 0D potential wells. In these systems, photocarriers experience a restricted range of motion, called quantum confinement. Depending on the dimensionality of the system, a particle can experience quantum confinement in one dimension (2D sheets), two dimensions (1D wires) or three dimensions (0D quantum dots).
To understand quantum confinement, we introduce the concept of de Broglie wavelength λ_B. Due to the wave-particle duality, charge carriers are indeed associated with a wavelength, related to their momentum p via the Planck's constant h:

$$\lambda_B = \frac{h}{p}. \tag{1.19}$$

The motion of a particle is hence described as restricted when the size of the potential well it lies in is smaller than its de Broglie wavelength. This is also true for excitons, which undergo confinement when the size of the well is smaller than their Bohr radius.

The consequences of quantum confinement on the electronic structure of a solid are significant; it causes a size-dependent discretization of the energy levels that triggers a splitting of the bands back into discrete states. Intuitively, this can once more be understood as the effect of the boundary conditions: as the particles motions are restricted, the number of available states that satisfy the boundary conditions of the Schrödinger equation becomes smaller, yielding discretization. A more quantitative explanation can be proposed, referring to the simple model of the particle-in-the-box. In this case, eigenvalues are given by

$$E_n = \frac{h^2 n^2}{8mL^2}, \tag{1.20}$$

with L the length of the box (the potential well), and n the principal quantum number. Clearly, for the limit of small L, the right-hand side of the above expression becomes large, and so does the energy difference between states with consecutive n numbers. It follows that the band gap will also be modified in the presence of quantum confinement, increasing as the size of the system decreases, as illustrated in Figure 1-8 below.

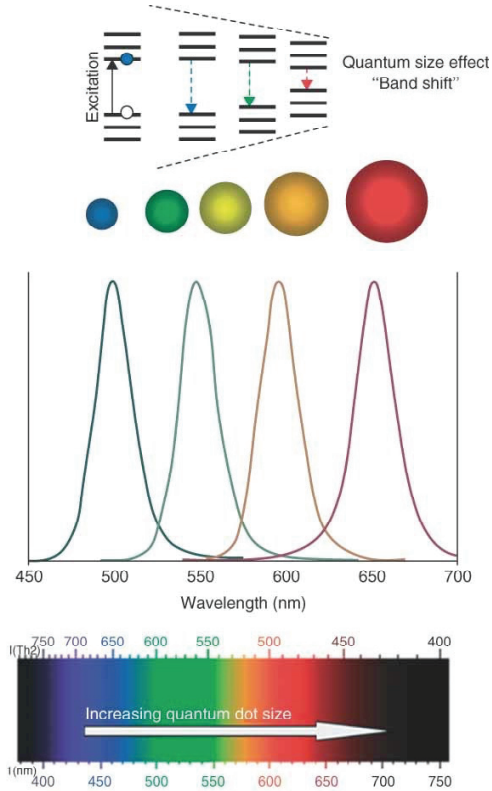

Figure 1-8 Size dependence of the band gap on the size of a quantum confined system (quantum dots in the present case). Adapted from ref. [12].

Note that the presence of quantum confinement not only affects the electronic structure, but also the degree of correlation of the photogenerated carriers: the stronger the confinement, the larger their binding energy.

Aside from quantum confinement, we define a second type of confinement, of large importance in 2D systems (quantum wells): the dielectric confinement. Dielectric confinement arises when the photoactive layer is sandwiched between two layers exhibiting a much lower dielectric constant. To understand this effect, recall that an exciton can be described as a Coulomb-correlated electron-hole pair, with the corresponding electric field. The situation for a 3D semiconductor with dielectric constant ε_{3D} is illustrated in Figure 1-9A: All electric field lines experience a dielectrically isotropic environment. In turn, when focusing on a 2D monolayer with dielectric constant ε_{2D}, as shown in Figure 1-9B, the electric field lines experience mostly the dielectric constant ε_0 of the neighboring material (for instance, air or organic molecules). As $\varepsilon_0 < \varepsilon_{2D}$, the screening of the electric field felt by both charges is significantly decreased, which enhances the strength of their interaction.

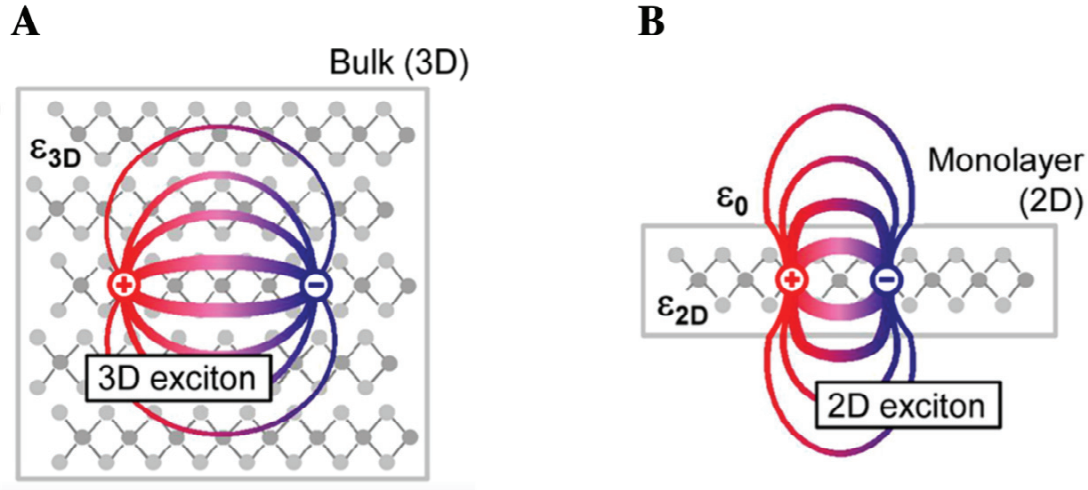

Figure 1-9 Electric field lines for an exciton in the bulk (**A**), and confined in a 2D monolayer (**B**). Adapted with permission from ref. [13].

1.3 Hybrid lead halide perovskites: hottest of the hot topics

1.3.1 3D perovskites

1.3.1.1 Structure

Originally designating a particular mineral, $CaTiO_3$, the term "perovskite" has quickly been generalized to any compounds exhibiting a similar ABX_3 structure (Figure 1-10A): A central, divalent, metal ion (B) and its six coordinating anions (X) form a 3D network of corner-sharing octahedra. In addition, a second cation (A) fills cavities inbetween each octahedron.

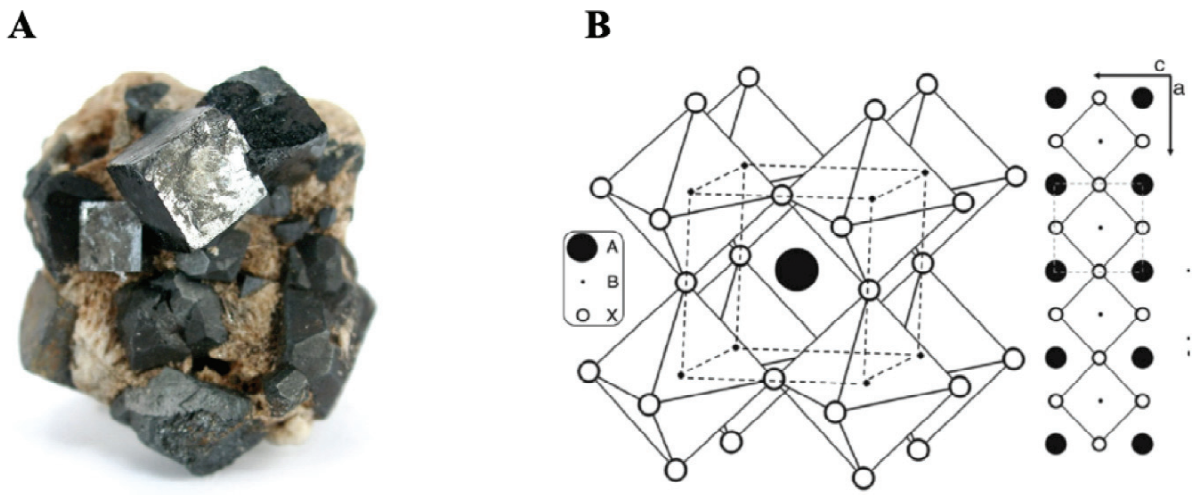

Figure 1-10 A. Specimen of calcite perovskite (Hot Spring county, Arkansas). Taken from iRocks.com (Rob Lavinsky). **B.** ABX_3 structure with cubic symmetry, reproduced from ref.[14]

The perovskites of interest in this work, which caused a breakthrough in the field of optoelectronics, are the so-called hybrid organic-inorganic lead halide perovskites (HOIP). In this case, the divalent metal ion B is lead (Pb^{2+}); the coordinating anions X are halides (chloride, bromide and/or iodide depending on the field of application); and the compounds used at the A cation site are aliphatic organic cations (methylammonium MA^+, formamidinium FA^+) or inorganic cations (Cs^+, Rb^+).

1.3.1.2 Electronic structure

The electronic structure landscape of 3D HOIPs was extensively studied, both experimentally and theoretically. Relevant computational methods include spin-orbit coupling (SOC) and many-body corrections.[15-17]

In $MAPbI_3$, the conduction band has been shown to mainly involve contributions from the Pb 6p orbitals. In turn, the valence band is dominated by the 5s orbitals of the iodide atoms, which can be extended to other X atoms as well (with an appropriate modification of the principal quantum number).[16] Furthermore, several studies have demonstrated the multiplicity of both the valence and conduction bands.[16,18-21] On the one hand, the "double" valence band arises from symmetry considerations (symmetry-breaking). On the other hand, the strong SOC present in HOIPs significantly affects the band structure (heavy-atom effect): The conduction band is subjected to an important spin-orbit split-off, yielding a "double" conduction band. More specifically, symmetry analyses in the double group result in the splitting of the triply degenerate T_{1u} state into the respectively two- and four-fold degenerate $E_{1/2u}$ and $F_{3/2u}$ states.

The organic cation at the A site also affects the electronic structure of HOIPs, both directly (via H-bonding to the lattice) and indirectly (steric effect yielding a distortion of the octahedral lattice). Cation modifications have been reported to affect the size of the band gap, as well as to impact charge carrier correlation and dynamics. The importance of the cation in the overall electronic structure of 3D HOIPs is of particular interest in the perspective of material tuning towards various applications. [21-27]

3D HOIPs exhibit large oscillator strengths, as expected for direct band gap semiconductors. However, they also feature long charge carrier lifetimes, which indicates an indirect character. This apparent contradiction can be unraveled by the reports of a strong Rashba spin-splitting at the CBM of 3D HOIPs. They indeed feature the two necessary conditions for the occurrence of Rashba-type effects: A sizeable SOC and a noncentrosymmetry, which is believed to arise from the (static or dynamic) disorder induced by the A cation.[28,29] Rashba-type effects yield a lifting of the spin degeneracy in the k-space, which results in two local conduction band minima, separated by 50 meV.[30] The first of those minima lies vertically above the VBM in the k-space. This leads to a vertical VBM-CBM electronic transition, responsible for the strong absorption of 3D perovskites. In turn, the second minimum is shifted with respect to the VBM. Because it is believed to lie at lower energies, it controls the charge recombination of cooled charge carriers, which is thus considerably slowed down.[23,30-35]

1.3.1.3 Exciton binding energy, carrier diffusion length and mobility

Some properties are of great importance to assess the underlying physics of a material (and thus its possible applications). In particular, the quantities relating to the nature and dynamics of photocarriers are essential in optoelectronics, namely the exciton binding energy E_b (*vide supra*), and the carrier diffusion length L and mobility μ.[36]

A constant in the research efforts addressing 3D HOIPs is the large spread of the values for some well-defined observables, for instance the exciton binding energy. This stems from the following two factors: the use of different methodologies to access the same quantities, each with their own experimental errors, and the large variety of fabrication and processing methods, yielding thin-films with very different microstructures. This is illustrated in Table 1-1 displaying E_b values for $MAPbI_3$, $MAPbBr_3$ and $MAPbCl_3$.

Compound	E_b (meV)	Method
$MAPbI_3$	50	Magneto-absorption[37]
	37	Magneto-absorption[38]
	32	MW photoconductance[39]
	25	Elliott fitting[40]
	19	Temperature-dependent PL[41]
	17	THz spectroscopy[42]
	16	Magneto-absorption[43]
	12	Permittivity measurements[44]
	12	Magneto-absorption[45]
	9	Transient absorption[46]
	2	Electro-optical measurements[47]
$MAPbBr_3$	150	Optical absorption[48]
	76	Magneto-absorption[37]
	64	Elliott Fitting[40]
	60	F-sum /absorption[49]
	40	Optical absorption[46]
	35	Permittivity measurements[44]
$MAPbCl_3$	69	Elliott Fitting[40]
	50	UPS[50]

Table 1-1 Exciton binding energies in HOIPs. Note that the present table is an updated version of the one presented in ref. [51].

As for the binding energy, despite the large spread of values, two trends emerge: First, all the calculated values for $MAPbI_3$ are similar to, or smaller than, the thermal energy at room temperature (k_BT); second, iodide substitution by smaller halogens yields larger binding energies.

Similarly differing values can be found for the charge carrier mobility μ, mostly obtained via THz spectroscopy and Hall effect measurements. $MAPbBr_3$ perovskites exhibit mobilities ranging from 0.5 to 30 $cm^2 V^{-1} s^{-1}$, while the values reported for $MAPbI_3$ are larger (around 60 $cm^2 V^{-1} s^{-1}$).[52-54] Interestingly, such mobility values constitute an intermediate case: They are higher than for conventional organic semiconductors, but significantly lower than in their inorganic equivalent.[55-59].

The mobility is the main ingredient in the determination of the charge carrier diffusion length.[36] However, diffusion lengths experimentally measured within HOIPs yield values greater than what should be expected from the typical mobilities described above, up to 5 μm.[60,61]

1.3.1.4 Photoinduced species

The question of the type of carriers or quasiparticles generated upon photoexcitation of bulk lead-halide perovskites appears tricky. Indeed, they are hybrid organic-inorganic systems: it is thus not clear whether they would behave like inorganic semiconductors (like GaAs) or closer to organic semiconductors. In the former case, free carriers are expected (electronic behavior), while bound electron-hole pairs are a characteristic of the latter (excitonic behavior). As described earlier, the nature of the photoinduced carriers within a system is directly reflected by the binding energy of the electron-hole pairs. From Table 1-1, we know that E_b values for 3D HOIPs span a broad range of values, and might not sit completely on the electronic nor the excitonic side.

The origin of this variability of E_b was briefly discussed in the preceding section. On the one hand, the chemical tunability of the X and A ion sites yields compounds with different bandgaps and dielectric constants. On the other hand, several papers have shown the dependence of the carrier correlation on the material fabrication and processing (for all HOIPs): both $MAPbI_3$ and $MAPbBr_3$ thin-films with larger grain sizes feature a larger binding energy than small grain equivalents, as shown by Grancini et al.[62] Similarly, a study on single crystals of $MAPbI_3$ demonstrated larger binding energies for large crystals compared to small ones.[63] In this respect, the so-called Saha equation is of great interest, as it provides the statistical ratio between free carriers and excitons as a function of the binding energy of the system, at a given temperature (provided the system is at equilibrium).[64] Figure 1-11, reproduced from the work by Saba *et al.,* represents this ratio as a function of both the density of excited states and the binding energy.[40]

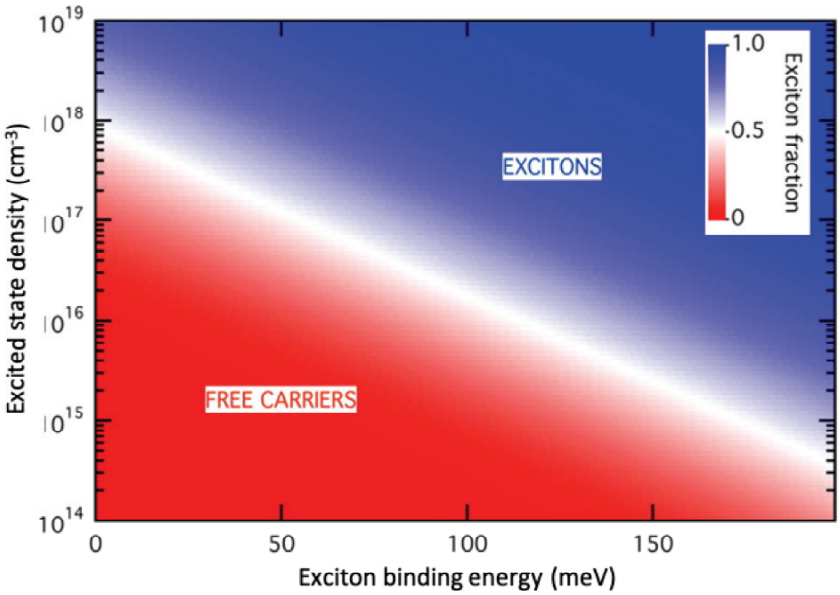

Figure 1-11 Exciton fraction calculated according to the Saha equilibrium condition as a function of exciton binding energy and excited state density (T=300 K). Reproduced from [40].

If we believe Table 1-1, we know that the binding energy of $MAPbI_3$ does not exceed 50 meV: Under solar irradiation (10^{15}-10^{16} carriers/cm^3), free carriers constitute by far the major type of photoexcited species in this system. Alternatively, under fs or ns laser excitation (10^{17}-10^{19} carriers/cm^3), the proportion of excitons is bound to increase significantly. Moving to smaller X anions yields an enhancement of E_b, with a largest reported value of 150 meV, and an average around 60 meV. Under 1 sun, although the photophysics appears to still be dominated by free carriers, the proportion of excitons increases and is expected to impact the overall charge dynamics. In turn, when subjected to fs or ns laser excitation, excitons constitute the primary photoinduced species.

1.3.2 2D perovskites

1.3.2.1 Structure and electronic properties

To understand the genesis of 2D perovskites, it is useful to start with the Goldschmidt tolerance factor, which describes the stability of perovskites as a function of the ionic radii of the ions involved in their structure:

$$t_G = \frac{r_A + r_X}{\sqrt{2}(r_B + r_X)}, \tag{1.21}$$

where r_A, r_B and r_X are the ionic radii of the A, B and X ions respectively.[65]

The values calculated for the current stable 3D HOIPs range between 0.8 and 1. As such, deviation from those numbers yields a destabilization of the pristine perovskite structure, which translates into a tilt of the octahedra for moderately larger ions and eventually leads to a complete dimensional reduction of the 3D perovskite structure. 2D perovskites can exist in

different phases, but here we will focus on the so-called Ruddlesden-Popper (RP) structure, with general formula $R_2A_{n-1}B_nX_{3n+1}$. Here, A, B and X have the same meaning as mentioned previously, and the additional component, R, is a divalent (ammonium) cation that intercalates between the inorganic 2D sheets ($A_{n-1}B_nX_{3n+1}$). Finally, n describes the number of adjacent inorganic layers: Indeed, RP perovskites not only exist as pure two-dimensional systems with n = 1, but can take the form of quasi-2D (q-2D) perovskite with n > 1 (Figure 1-12A).

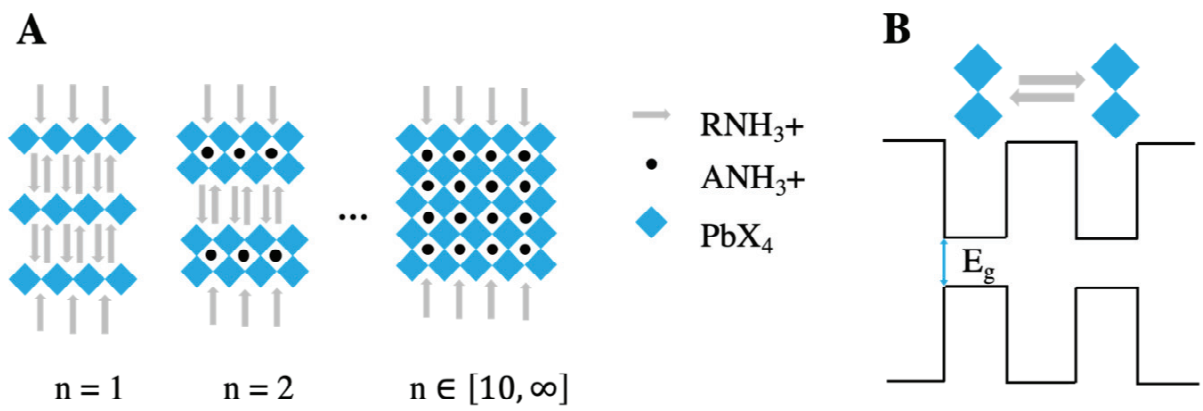

Figure 1-12 Structural insights for $R_2A_{n-1}B_nX_{3n+1}$. **A**. Structure for q-2D RP, for different n values. **B**. Self-assembled quantum well structure arising from the stacking of two moieties having very different energetics (long-chain organic cation versus inorganic PbX_4 layer).

The alternation between organic and inorganic moieties with very different energetics is of great interest. Indeed, it results in spontaneous multiple quantum well structures, as illustrated in Figure 1-12B. This type of structure usually exhibits quantum confinement properties, which strongly impacts the charge carrier correlation (*vide supra*). Furthermore, the dielectric constants of both moieties differ: The dielectric constant of the barrier (the long-chain organic cation) $\varepsilon_B = 2.1$, while the one of the well (the PbX_4 layer) $\varepsilon_W = 6.1$.[66,67] As was explained in section 1.2.6 , this calls for the presence of dielectric confinement, on top of the quantum confinement.

1.3.2.2 Exciton binding energies and photoinduced species

Depending on the size of the well (that is, on the value of n as defined above), photogenerated electrons and holes in RP 2D perovskites will experience a sizeable quantum confinement. This, together with the dielectric confinement discussed above expectedly yields strongly-correlated carriers, which translates into high exciton binding energies.

Compound	Dimension	E_b (meV)	Band gap (eV)
$(C_4H_9NH_3)_2PbI_4$	2D	360	2.38[68]
$(C_6H_5C_2H_4NH_3)_2PbI_4$	2D	230	2.30[69]
$(F\text{-}C_6H_4C_2H_4NH_3)_2PbI_4$	2D	540	2.35[70]
$(C_6H_{13}NH_3)_2PbI_4$	2D	361	2.34[72]

$(C_6H_{13}NH_3)_2(MA)Pb_2I_7$	q-2D (n = 2)	260	2.14[71]
$(C_6H_{13}NH_3)_2(MA)Pb_3I_{10}$	q-2D (n = 3)	150	2.02[71]
$(C_6H_{13}NH_3)_2(MA)Pb_4I_{13}$	q-2D (n = 4)	100	1.92[71]

Table 1-2 Exciton binding energy and band gap for some examples of 2D and q-2D RP perovskites with n= 2, 3 or 4 (number of adjacent inorganic layers). Adapted from ref. [72].

Table 1-2 shows the binding energy and band gap for some examples of 2D and q-2D RP perovskites. First, the presence of quantum confinement is clear: For a homologous series of compounds that solely differ by their thickness (n), both the band gap and the binding energy decrease with increasing n. Second, 2D compounds with different R cations exhibit different binding energies while featuring similar band gaps: This is evidence of the involvement of dielectric confinement in the charge carrier correlation.

The type of photoinduced carriers that can be found in those compounds is thus clear: excitons will strongly dominate the photoexcited dynamics in 2D RP perovskites. Alternatively, q-2D RP can be shifted towards an excitonic or electronic behavior simply by tuning the thickness n.

1.3.2.3 Role of the organic cation

R-site cations in 2D RP perovskites do not have to follow the Goldschmidt tolerance factor, as they are not required to fit within the octahedral cages of the 3D lattice. As a consequence, the number of possible candidates is almost unlimited, and understanding how the R cation impacts upon the physical properties of layered perovskite compounds is necessary.
Recall that 2D RP perovskites are essentially self-assembled quantum wells, with strongly correlated charge carriers due to the quantum and dielectric confinements. If the former is solely determined by the size of the well, the latter is directly R cation-dependent: a careful cation selection is therefore a direct path towards charge correlation tuning for different applications. [73-77]

In addition, the R cation has also been reported to induce structural distortions in the inorganic lattice, for instance octahedral distortion (*vide supra*) and modifications of the Pb-I-Pb angle between adjacent octahedra, which reduces the wavefunction overlap within the inorganic layers. Those lattice distortions thus have a strong impact on the size of the band gap and the exciton photophysics.[78,79]

1.3.3 Perovskite solar cells (PSCs)

1.3.3.1 3D PSCs: Active layer and architecture

The nature of the perovskite used in the fabrication of perovskite solar cells (PSCs) has significantly varied throughout the last years: the seminal 2012 paper by Lee et al. was focusing on methylammonium lead iodide chloride perovskite ($MAPbI_2Cl$) with a calculated efficiency of 10.9%.[14] Contemporary efforts from other groups alternatively considered pure methylammonium lead iodide perovskite ($MAPbI_3$), reporting efficiencies exceeding 9%.[80] In

2014, the larger formamidinium (FA^+) A-site cation started to emerge as an interesting replacement for MA^+, in an effort to shift the optical absorption onset of PSCs more towards the red. [81] Efficiencies, however, remained limited due to the inherent moisture-induced instability of the black phase of $FAPbI_3$ (transition towards the yellow δ-phase). It quickly became apparent that fabricating iodide perovskite layers involving a mixture of FA^+ and other cations (MA^+, Cs^+, Rb^+) was an efficient solution to stabilize the black phase, yielding devices with efficiencies above 20%.[82-85] Band gap tuning attempts were also carried out by exploiting the versatility of the X anion site, resulting in various bromide-iodide ratios. [86-88] Interestingly, the presence of a carefully controlled stoichiometric excess of iodide in such mixed anion perovskites turned out to decrease the amount of charge recombination, leading to a larger V_{OC}. [89-91] Recent record-breaking solar cells were based on mixed-halide (I, Br) and mixed-cation (FA^+, MA^+) perovskite layers, with certified efficiencies of 22.1%.[89]

The performance of a solar cell does not only depend upon the composition and fabrication of the active layer, but also on the global device architecture. 3D HOIPs were primarily considered as a bare light absorber: The perovskite was thus first inserted into typical dye-sensitized solar cells (DSCs) structures. Designed to minimize the distance traveled by photogenerated carriers (optimization of the charge-separation step), they typically consisted of a porous layer of TiO_2 infiltrated with an absorbing medium (the dye). This heterojunction is then either immersed in a liquid electrolyte (liquid DSCs) or infiltrated with a molecular hole acceptor, such as Spiro-MeOTAD (solid-state DSCs).[92] Both liquid- and solid-state-based DSCs architectures were proposed for the first PSCs, with a clear better performance in the latter case.[14,93] Then, because lead-halide perovskites not only revealed to be good absorbers, but also ambipolar conductors, several studies focused on the importance and nature of the selective extracting layers. For instance, it was demonstrated that perovskite solar cells performed significantly better with a much thinner layer of mesoporous TiO_2 (350 nm compared to 3µm for solid-state DSCs). Similarly, adding a perovskite capping layer on top of the mesoporous scaffold further improved the efficiency.[94] Branching out from the traditional DSC-inspired structure, architectures involving planar heterojunctions were also explored, featuring SnO_2 instead of TiO_2. The resulting mixed halide, mixed cation solar cells showed efficiencies of 18.1%.[95] The role of the molecular hole acceptor was also thoroughly investigated; although PSCs without any sort of hole transporting material (HTM) were demonstrated (8% efficiencies), state-of-the-art PSCs still include Spiro-MeOTAD or other type of amine-based compounds (larger V_{OC}). [89,96,97]

1.3.3.2 Mixed 2D/3D PSCs

Current PSCs have reached efficiencies that make them competitive on the photovoltaic market[83,84], but their stability to heat and moisture is still a large issue. In this respect, 2D RP perovskites were seen as a promising alternative. Indeed, although pure 2D perovskite solar cells feature expectedly low performance, they exhibit a high resistance to moisture and an overall good stability (conventionally assigned to the hydrophobic properties of the R cation).[98,99] Active layers consisting of blends of 2D (phenetylammonium PEA^+, butylammonium BUA^+) and 3D (MA^+, FA^+, Cs^+) perovskites were thus inserted into

conventional PSCs architectures and appeared promising with efficiencies of up to 18% and improved stability to ambient conditions.[100,101,102,103] As an alternative to 2D/3D blends, 2D/3D heterojunctions or graded interfaces were also designed: The 2D layer there plays the role of a selective extracting layer and/or a protecting layer, and the resulting devices display the expected enhanced stability and satisfying efficiencies. [104-106]

References

(1) Bacon, F. *Novum Organum*; Clarendon Press, 1878.

(2) Anderson, F. H. *The Philosophy of Francis Bacon*; Chicago Illinois, 1948.

(3) Smith, N. K. *The Philosophy of David Hume: a Critical Study of Its Origins and Central Doctrines*; Palgrave-Macmillan, 1941.

(4) Buchdahl, G. *Metaphysics and the Philosophy of Science: the Classical Origins: Descartes to Kant*; MA-MIT Press: Cambridge, 1969; Vol. 69.

(5) Esfeld, M. *Philosophie Des Sciences: Une Introduction.*; PPUR presses polytechniques, 2006.

(6) Popper, K. R. *The Logic of Scientific Discovery*; Hutchinson & Co., London, 1959.

(7) Popper, K. R. *Objective Knowledge: an Evolutionary Approach*; Oxford University Press Inc., New York, 1979.

(8) Simonton, D. K. *Origins of Genius: Darwinian Perspectives on Creativity*; Oxford University Press Inc., New York, 1999.

(9) Guillemin, V. *The Story of Quantum Mechanics*; Charles Scribner's Sons: New York, 1968.

(10) Aruldhas, G. *Molecular Structure and Spectroscopy*, 2nd ed.; PHI Learning Private Limited: New Delhi, 2008.

(11) Berezin, F. A.; Shublin, M. *The Schrödinger Equation*; Springer Science + Business Media: Dordrecht, 1991.

(12) Mansur, H. S. Quantum Dots and Nanocomposites. *WIREs Nanomed Nanobiotechnol* **2010**, *2* (2), 113–129.

(13) Chernikov, A.; Berkelbach, T. C.; Hill, H. M.; Rigosi, A.; Li, Y.; Aslan, O. B.; Reichman, D. R.; Hybertsen, M. S.; Heinz, T. F. Exciton Binding Energy and Nonhydrogenic Rydberg Series in Monolayer WS2. *Phys. Rev. Lett.* **2014**, *113* (7), 658–5.

(14) Lee, M. M.; Teuscher, J.; Miyasaka, T.; Murakami, T. N.; Snaith, H. J. Efficient Hybrid Solar Cells Based on Meso-Superstructured Organometal Halide Perovskites. *Science* **2012**, *338* (6107), 643–647.

(15) Even, J.; Pedesseau, L.; Jancu, J.-M.; Katan, C. Importance of Spin–Orbit Coupling in Hybrid Organic/Inorganic Perovskites for Photovoltaic Applications. *J. Phys. Chem. Lett.* **2013**, *4* (17), 2999–3005.

(16) Brivio, F.; Butler, K. T.; Walsh, A.; van Schilfgaarde, M. Relativistic Quasiparticle Self-Consistent Electronic Structure of Hybrid Halide Perovskite Photovoltaic Absorbers. *Phys. Rev. B* **2014**, *89* (15), 155204–155206.

(17) Menéndez-Proupin, E.; Palacios, P.; Wahnón, P.; Conesa, J. C. Self-Consistent Relativistic Band Structure of the CH3NH3PbI3perovskite. *Phys. Rev. B* **2014**, *90* (4), 3586–3587.

(18) Pedesseau, L.; Jancu, J.-M.; Rolland, A.; Deleporte, E.; Katan, C.; Even, J. Electronic Properties of 2D and 3D Hybrid Organic/Inorganic Perovskites for Optoelectronic and Photovoltaic Applications. *Opt Quant Electron* **2013**, *46* (10), 1225–1232.

(19) Even, J.; Pedesseau, L.; Jancu, J.-M.; Katan, C. DFT and K· Pmodelling of the Phase Transitions of Lead and Tin Halide Perovskites for Photovoltaic Cells. *Phys. Status Solidi RRL* **2013**, *8* (1), 31–35.

(20) Even, J.; Pedesseau, L.; Katan, C.; Kepenekian, M.; Lauret, J.-S.; Sapori, D.; Deleporte, E. Solid-State Physics Perspective on Hybrid Perovskite Semiconductors. *J. Phys. Chem. C* **2015**, *119* (19), 10161–10177.

(21) Leguy, A. M. A.; Azarhoosh, P.; Alonso M. I.; Campoy-Quiles M.; Weber, O. J.; Yao, J.; Bryant, D; Weller, M. T.; Nelson, J.; Walsh, A.; van Schilfgaarde, M.; Barnes, P. R. F. Experimental and Theoretical Optical Properties of Methylammonium Lead Halide Perovskites. *Nanoscale* **2016**, *8*, 6317–6327.

(22) Kais, S.; Tabet, N.; Alharbi, F.; Sanvito, S.; Motta, C.; El-Mellouhi, F. Revealing the Role of Organic Cations in Hybrid Halide Perovskite CH3NH3PbI3. *Nat. Commun.* **2015**, *6*, 1–7.

(23) Xiao, Z.; Yan, Y. Progress in Theoretical Study of Metal Halide Perovskite Solar Cell Materials. *Adv. Energy Mater.* **2017**, *7* (22), 1701136–20.

(24) Amat, A.; Mosconi, E.; Ronca, E.; Quarti, C.; Umari, P.; Nazeeruddin, M. K.; Grätzel, M.; De Angelis, F. Cation-Induced Band-Gap Tuning in Organohalide Perovskites: Interplay of Spin–Orbit Coupling and Octahedra Tilting. *Nano Lett.* **2014**, *14* (6), 3608–3616.

(25) Lee, J.-H.; Bristowe, N. C.; Lee, J. H.; Lee, S.-H.; Bristowe, P. D.; Cheetham, A. K.; Jang, H. M. Resolving the Physical Origin of Octahedral Tilting in Halide Perovskites. *Chem. Mater.* **2016**, *28* (12), 4259–4266.

(26) Yaffe, O.; Guo, Y.; Tan, L. Z.; Egger, D. A.; Hull, T.; Stoumpos, C. C.; Zheng, F.; Heinz, T. F.; Kronik, L.; Kanatzidis, M. G.; et al. Local Polar Fluctuations in Lead Halide Perovskite Crystals. *Phys. Rev. Lett.* **2017**, *118* (13), 136001–136006.

(27) Stoumpos, C. C.; Malliakas, C. D.; Kanatzidis, M. G. Semiconducting Tin and Lead Iodide Perovskites with Organic Cations: Phase Transitions, High Mobilities, and Near-Infrared Photoluminescent Properties. *Inorg. Chem.* **2013**, *52* (15), 9019–9038.

(28) Rashba, E. I. Properties of Semiconductors with an Extremum Loop. I. Cyclotron and Combinational Resonance in a Magnetic Field Perpendicular to the Plane of the Loop. *Sov. Phys., Solid State* **1960**, *2*, 1109–1122.

(29) Kepenekian, M.; Robles, R.; Katan, C.; Sapori, D.; Pedesseau, L.; Even, J. Rashba and Dresselhaus Effects in Hybrid Organic–Inorganic Perovskites: From Basics to Devices. *ACS Nano* **2015**, *9* (12), 11557–11567.

(30) Stranks, S. D.; Plochocka, P. The Influence of the Rashba Effect. *Nature Materials* **2018**, *17* (5), 381–382.

(31) Etienne, T.; Mosconi, E.; De Angelis, F. Dynamical Origin of the Rashba Effect in Organohalide Lead Perovskites: a Key to Suppressed Carrier Recombination in Perovskite Solar Cells? *J. Phys. Chem. Lett.* **2016**, *7* (9), 1638–1645.

(32) Wang, T.; Daiber, B.; Frost, J. M.; Mann, S. A.; Garnett, E. C.; Walsh, A.; Ehrler, B. Indirect to Direct Bandgap Transition in Methylammonium Lead Halide Perovskite. *Energy Environ. Sci.* **2017**, *10*, 509–515.

(33) Hutter, E. M.; Gélvez-Rueda, M. C.; Osherov, A.; Bulović, V.; Grozema, F. C.; Stranks, S. D.; Savenije, T. J. Direct–Indirect Character of the Bandgap in Methylammonium Lead Iodide Perovskite. *Nature Materials* **2016**, *16* (1), 115–120.

(34) Kirchartz, T.; Rau, U. Decreasing Radiative Recombination Coefficients via an Indirect Band Gap in Lead Halide Perovskites. *J. Phys. Chem. Lett.* **2017**, *8* (6), 1265–1271.

(35) Zheng, F.; Tan, L. Z.; Liu, S.; Rappe, A. M. Rashba Spin–Orbit Coupling Enhanced Carrier Lifetime in CH 3NH 3PbI 3. *Nano Lett.* **2015**, *15* (12), 7794–7800.

(36) Lundstrom, M. *Fundamentals of Carrier Transport*, Second edition. Cambridge University Press, 2000.

(37) Tanaka, K.; Takahashi, T.; Ban, T.; Kondo, T.; Uchida, K.; Miura, N. Comparative Study on the Excitons in Lead-Halide-Based Perovskite-Type Crystals $CH_3Nh_3PbBr_3$ $Ch_3Nh_3PbI_3$. *Solid State Commun.* **2003**, *127* (9-10), 619–623.
(38) Hirasawa, M.; Ishihara, T.; Goto, T.; Uchida, K.; Miura, N. Magnetoabsorption of the Lowest Exciton in Perovskite-Type Compound $(CH_3NH_3)PbI_3$. *Physica* **1994**, 427–430.
(39) Savenije, T. J.; Ponseca, C. S., Jr.; Kunneman, L.; Abdellah, M.; Zheng, K.; Tian, Y.; Zhu, Q.; Canton, S. E.; Scheblykin, I. G.; Pullerits, T.; et al. Thermally Activated Exciton Dissociation and Recombination Control the Carrier Dynamics in Organometal Halide Perovskite. *J. Phys. Chem. Lett.* **2014**, *5* (13), 2189–2194.
(40) Saba, M.; Quochi, F.; Mura, A.; Bongiovanni, G. Excited State Properties of Hybrid Perovskites. *Acc. Chem. Res.* **2015**, 166–173.
(41) Sun, S.; Salim, T.; Mathews, N.; Duchamp, M.; Boothroyd, C.; Xing, G.; Sum, T. C.; Lam, Y. M. The Origin of High Efficiency in Low-Temperature Solution-Processable Bilayer Organometal Halide Hybrid Solar Cells. *Energy Environ. Sci.* **2014**, *7* (1), 399–407.
(42) Valverde-Chàvez, D. A.; Ponseca, C. S.; Stoumpos, C. C.; Yartsev, A.; Kanatzidis, M. G.; Cooke, D. G.; Sundström, V. Intrinsic Femtosecond Charge Generation Dynamics in Single Crystal CH3NH3PbI3. *Energy Environ. Sci.* **2015**, *8* (12), 3700–3707.
(43) Miyata, A.; Mitioglu, A.; Plochocka, P.; Portugall, O.; Wang, J. T.-W.; Stranks, S. D.; Snaith, H. J.; Nicholas, R. J. Direct Measurement of the Exciton Binding Energy and Effective Masses for Charge Carriers in Organic–Inorganic Tri-Halide Perovskites. *Nat. Phys.* **2015**, *11* (7), 582–587.
(44) Soufiani, A. M.; Huang, F.; Reece, P.; Sheng, R.; Ho-Baillie, A.; Green, M. A. Polaronic Exciton Binding Energy in Iodide and Bromide Organic-Inorganic Lead Halide Perovskites. *Appl. Phys. Lett.* **2015**, *107* (23), 231902–231906.
(45) Galkowski, K.; Mitioglu, A.; Miyata, A.; Plochocka, P.; Portugall, O.; Eperon, G. E.; Wang, J. T.-W.; Stergiopoulos, T.; Stranks, S. D.; Snaith, H. J.; et al. Determination of the Exciton Binding Energy and Effective Masses for Methylammonium and Formamidinium Lead Tri-Halide Perovskite Semiconductors. *Energy Environ. Sci.* **2016**, 1–9.
(46) Yang, Y.; Yang, M.; Li, Z.; Crisp, R.; Zhu, K.; Beard, M. C. Comparison of Recombination Dynamics in $CH_3Nh_3PbBr_3$ And $CH_3Nh_3PbI_3$ Perovskite Films: Influence of Exciton Binding Energy. *J. Phys. Chem. Lett.* **2015**, 4688–4692.
(47) Lin, Q.; Armin, A.; Nagiri, C. R.; Burn, P. L.; Meredith, P. Electro-Optics of Perovskite Solar Cells. *Nat. Photon.* **2014**, *9* (2), 106–112.
(48) Koutselas, I. B.; Ducasse, L.; Papavassiliou, G. C. Electronic Properties of Three- and Low-Dimensional Semiconducting Materials with Pb Halide and Sn Halide Units. *J. Phys.: Condens. Matter* **1999**, *8* (9), 1217–1227.
(49) Sestu, N.; Cadelano, M.; Sarritzu, V.; Chen, F.; Marongiu, D.; Piras, R.; Mainas, M.; Quochi, F.; Saba, M.; Mura, A.; et al. Absorption F-Sum Rule for the Exciton Binding Energy in Methylammonium Lead Halide Perovskites. *J. Phys. Chem. Lett.* **2015**, *6* (22), 4566–4572.
(50) Comin, R.; Walters, G.; Thibau, E. S.; Voznyy, O.; Lu, Z.-H.; Sargent, E. H. Structural, Optical, and Electronic Studies of Wide-Bandgap Lead Halide Perovskites. *J. Mater. Chem. C* **2015**, *3* (34), 8839–8843.
(51) Sum, T. C.; Mathews, N. Advancements in Perovskite Solar Cells: Photophysics Behind the Photovoltaics. *Energy Environ. Sci.* **2014**, *7* (8), 2518–2534.

(52) Saidaminov, M. I.; Abdelhady, A. L.; Murali, B.; Alarousu, E.; Burlakov, V. M.; Peng, W.; Dursun, I.; Wang, L.; He, Y.; Maculan, G.; et al. High-Quality Bulk Hybrid Perovskite Single Crystals Within Minutes by Inverse Temperature Crystallization. *Nat. Commun.* **2015**, *6*, 1–6.

(53) Wehrenfennig, C.; Eperon, G. E.; Johnston, M. B.; Snaith, H. J.; Herz, L. M. High Charge Carrier Mobilities and Lifetimes in Organolead Trihalide Perovskites. *Adv. Mater.* **2013**, *26* (10), 1584–1589.

(54) Chen, Y.; Yi, H. T.; Wu, X.; Haroldson, R.; Gartstein, Y. N.; Rodionov, Y. I.; Tikhonov, K. S.; Zakhidov, A.; Zhu, X. Y.; Podzorov, V. Extended Carrier Lifetimes and Diffusion in Hybrid Perovskites Revealed by Hall Effect and Photoconductivity Measurements. *Nat. Commun.* **2016**, *7*, 1–9.

(55) Brenner, T. M.; Egger, D. A.; Rappe, A. M.; Kronik, L.; Hodes, G.; Cahen, D. Are Mobilities in Hybrid Organic–Inorganic Halide Perovskites Actually "High?" *J. Phys. Chem. Lett.* **2015**, *6* (23), 4754–4757.

(56) Ma, J.; Nissimagoudar, A. S.; Li, W. First-Principles Study of Electron and Hole Mobilities of Si and GaAs. **2018**, 1–9.

(57) Bashir, A.; Heck, A.; Narita, A.; Feng, X.; Nefedov, A.; Rohwerder, M.; Müllen, K.; Elstner, M.; Wöll, C. Charge Carrier Mobilities in Organic Semiconductors: Crystal Engineering and the Importance of Molecular Contacts. *Phys. Chem. Chem. Phys.* **2015**, *17* (34), 21988–21996.

(58) Kang, E.; Lee, J.-H.; Borghs, G.; Heremans, P.; Genoe, J.; Rolin, C. Charge Carrier Mobility in Thin Films of Organic Semiconductors by the Gated Van Der Pauw Method. *Nat. Commun.* **2017**, *8*, 1–9.

(59) Nathan, M. I.; Dumke, W. P.; Wrenner, K.; Tiwari, S.; Wright, S. L.; Jenkins, K. A. Electron Mobility in P-Type GaAs. *Appl. Phys. Lett.* **1988**, *52* (8), 654–656.

(60) Shi, D.; Adinolfi, V.; Comin, R.; Yuan, M.; Alarousu, E.; Buin, A.; Chen, Y.; Hoogland, S.; Rothenberger, A.; Katsiev, K.; et al. Low Trap-State Density and Long Carrier Diffusion in Organolead Trihalide Perovskite Single Crystals. *Science* **2015**, *347* (6221), 519–522.

(61) Nie, W.; Tsai, H.; Asadpour, R.; Blancon, J.-C.; Neukirch, A. J.; Gupta, G.; Crochet, J. J.; Chhowalla, M.; Tretiak, S.; Alam, M. A.; et al. High-Efficiency Solution-Processed Perovskite Solar Cells with Millimeter-Scale Grains. *Science* **2015**, *347* (6221), 519–522.

(62) Grancini, G.; Kandada, A. R. S.; Frost, J. M.; Barker, A. J.; De Bastiani, M.; Gandini, M.; Marras, S.; Lanzani, G.; Walsh, A.; Petrozza, A. Role of Microstructure in the Electron-Hole Interaction of Hybrid Lead Halide Perovskites. *Nat. Photon.* **2015**, *9* (10), 695–701.

(63) Dong, Q.; Fang, Y.; Shao, Y.; Mulligan, P.; Qiu, J.; Cao, L.; Huang, J. Electron-Hole Diffusion Lengths > 175 Mm in Solution-Grown $CH_3Nh_3PbI_3$ Single Crystals. *Science* **2015**, *347* (6225), 967–970.

(64) Innocenzo, V. D. R.; Grancini, G.; Alcocer, M. J. P.; Kandada, A. R. S.; Stranks, S. D.; Lee, M. M.; Lanzani, G.; Snaith, H. J.; Petrozza, A. Excitons Versus Free Charges in Organo-Lead Tri-Halide Perovskites. *Nat. Commun.* **1AD**, *5*, 1–6.

(65) Goldschmidt, V. M. Die Gesetze Der Krystallochemie. *Die Naturwissenschaften* **1926**, *14* (21), 477–485.

(66) Ishihara, T.; Takahashi, J.; Goto, T. Optical Properties Due to Electronic Transitions in Two-Dimensional Semiconductors $(C_NH_{2n+1}Nh_3)_2PbI_4$. **1990**, *42* (17), 11099–11107.

(67) Tanaka, K.; Sano, F.; Takahashi, T.; Kondo, T.; Ito, R.; Ema, K. Two-Dimensional Wannier Excitons in a Layered-Perovskite-Type Crystal □$(C_6H_{13}Nh_3)_2PbI_4$. *Solid State Commun.* **2002**, *122*, 249–252.
(68) Wu, X.; Trinh, M. T.; Zhu, X. Y. Excitonic Many-Body Interactions in Two-Dimensional Lead Iodide Perovskite Quantum Wells. *J. Phys. Chem. C* **2015**, *119* (26), 14714–14721.
(69) A V Nurmikko, X. H. T. I. Dielectric Confinement Effect on PbI_4-Based Layered Semiconductors. *Phys. Rev. B* **1992**, *45* (12), 6961–6964.
(70) Dammak, T.; Koubaa, M.; Boukheddaden, K.; Bougzhala, H.; Mlayah, A.; Abid, Y. Two-Dimensional Excitons and Photoluminescence Properties of the Organic/Inorganic (4-FC 6H 4C 2H 4NH 3) 2[PbI 4] Nanomaterial. *J. Phys. Chem. C* **2009**, *113* (44), 19305–19309.
(71) Tanaka, K.; Kondo, T. Bandgap and Exciton Binding Energies in Lead-Iodide-Based Natural Quantum-Well Crystals. *Science and Technology of Advanced Materials* **2003**, *4* (6), 599–604.
(72) Chen, P.; Bai, Y.; Lyu, M.; Yun, J.-H.; Hao, M.; Wang, L. Progress and Perspective in Low-Dimensional Metal Halide Perovskites for Optoelectronic Applications. *Sol. RRL* **2018**, *2* (3), 1700186–28.
(73) García-Benito, I.; Quarti, C.; Queloz, V. I. E.; Orlandi, S.; Zimmermann, I.; Cavazzini, M.; Lesch, A.; Marras, S.; Beljonne, D.; Pozzi, G.; et al. Fashioning Fluorous Organic Spacers for Tunable and Stable Layered Hybrid Perovskites. *Chem. Mater.* **2018**, *30* (22), 8211–8220.
(74) Du, K.-Z.; Tu, Q.; Zhang, X.; Han, Q.; Liu, J.; Zauscher, S.; Mitzi, D. B. Two-Dimensional Lead(II) Halide-Based Hybrid Perovskites Templated by Acene Alkylamines: Crystal Structures, Optical Properties, and Piezoelectricity. *Inorg. Chem.* **2017**, *56* (15), 9291–9302.
(75) Traore, B.; Pedesseau, L.; Assam, L.; Che, X.; Blancon, J.-C.; Tsai, H.; Nie, W.; Stoumpos, C. C.; Kanatzidis, M. G.; Tretiak, S.; et al. Composite Nature of Layered Hybrid Perovskites: Assessment on Quantum and Dielectric Confinements and Band Alignment. *ACS Nano* **2018**, *12* (4), 3321–3332.
(76) Misra, R. K.; Cohen, B.-E.; Iagher, L.; Etgar, L. Low-Dimensional Organic-Inorganic Halide Perovskite: Structure, Properties, and Applications. *ChemSusChem* **2017**, *10* (19), 3712–3721.
(77) Quarti, C.; Marchal, N.; Beljonne, D. Tuning the Optoelectronic Properties of Two-Dimensional Hybrid Perovskite Semiconductors with Alkyl Chain Spacers. *J. Phys. Chem. Lett.* **2018**, *9* (12), 3416–3424.
(78) Saparov, B.; Mitzi, D. B. Organic–Inorganic Perovskites: Structural Versatility for Functional Materials Design. *Chem. Rev.* **2016**, *116* (7), 4558–4596.
(79) Liu, C.; Huhn, W.; Du, K.-Z.; Vazquez-Mayagoitia, A.; Dirkes, D.; You, W.; Kanai, Y.; Mitzi, D. B.; Blum, V. Tunable Semiconductors: Control Over Carrier States and Excitations in Layered Hybrid Organic-Inorganic Perovskites. *Phys. Rev. Lett.* **2018**, *121* (14), 146401.
(80) Kim, H.-S.; Lee, C.-R.; Im, J.-H.; Lee, K.-B.; Moehl, T.; Marchioro, A.; Moon, S.-J.; Humphry-Baker, R.; Yum, J.-H.; Moser, J. E.; et al. Lead Iodide Perovskite Sensitized All-Solid-State Submicron Thin Film Mesoscopic Solar Cell with Efficiency Exceeding 9%. *Sci. Rep.* **2012**, *2*, 1–7.
(81) Pellet, N.; Gao, P.; Gregori, G.; Yang, T.-Y.; Nazeeruddin, M. K.; Maier, J.; Grätzel, M. Mixed-Organic-Cation Perovskite Photovoltaics for Enhanced Solar-Light Harvesting. *Angew. Chem. Int. Ed.* **2014**, *53* (12), 3151–3157.

(82) Lee, J.-W.; Kim, D.-H.; Kim, H.-S.; Seo, S.-W.; Cho, S. M.; Park, N.-G. Formamidinium and Cesium Hybridization for Photo- and Moisture-Stable Perovskite Solar Cell. *Adv. Energy Mater.* **2015**, *5* (20), 1501310–1501319.
(83) Saliba, M.; Matsui, T.; Seo, J.-Y.; Domanski, K.; Correa-Baena, J.-P.; Nazeeruddin, M. K.; Zakeeruddin, S. M.; Tress, W.; Abate, A.; Hagfeldt, A.; et al. Cesium-Containing Triple Cation Perovskite Solar Cells: Improved Stability, Reproducibility and High Efficiency. *Energy Environ. Sci.* **2016**, *9* (6), 1989–1997.
(84) Saliba, M.; Matsui, T.; Domanski, K.; Seo, J.-Y.; Ummadisingu, A.; Zakeeruddin, S. M.; Baena, J. P. C.; Tress, W.; Abate, A.; Hagfeldt, A.; et al. Incorporation of Rubidium Cations Into Perovskite Solar Cells Improves Photovoltaic Performance. *Science* **2016**, *354* (6309), 206–209.
(85) Yi, C.; Luo, J.; Meloni, S.; Boziki, A.; Ashari-Astani, N.; Grätzel, C.; Zakeeruddin, S. M.; Rothlisberger, U.; Grätzel, M. Entropic Stabilization of Mixed a-Cation ABX_3 Metal Halide Perovskites for High Performance Perovskite Solar Cells. *Energy Environ. Sci.* **2016**, *9* (2), 656–662.
(86) Hoke, E. T.; Slotcavage, D. J.; Dohner, E. R.; Bowring, A. R.; Karunadasa, H. I.; McGehee, M. D. Reversible Photo-Induced Trap Formation in Mixed-Halide Hybrid Perovskites for Photovoltaics. *Chem. Sci.* **2015**, *6* (1), 613–617.
(87) Noh, J. H.; Im, S. H.; Heo, J. H.; Mandal, T. N.; Seok, S. I. Chemical Management for Colorful, Efficient, and Stable Inorganic–Organic Hybrid Nanostructured Solar Cells. *Nano Lett.* **2013**, *13* (4), 1764–1769.
(88) Stranks, S. D.; Snaith, H. J. Metal-Halide Perovskites for Photovoltaic and Light-Emitting Devices. *Nature,* **2015**, *10* (5), 391–402.
(89) Yang, W. S.; Park, B.-W.; Jung, E. H.; Jeon, N. J.; Kim, Y. C.; Lee, D. U.; Shin, S. S.; Seo, J.; Kim, E. K.; Noh, J. H.; et al. Iodide Management in Formamidinium-Lead-Halide–Based Perovskite Layers for Efficient Solar Cells. *Science* **2017**, *356* (6345), 1376–1379.
(90) Jacobsson, T. J.; Correa-Baena, J.-P.; Pazoki, M.; Saliba, M.; Schenk, K.; Grätzel, M.; Hagfeldt, A. Exploration of the Compositional Space for Mixed Lead Halogen Perovskites for High Efficiency Solar Cells. *Energy Environ. Sci.* **2016**, *9* (5), 1706–1724.
(91) Jacobsson, T. J.; Correa-Baena, J.-P.; Halvani Anaraki, E.; Philippe, B.; Stranks, S. D.; Bouduban, M. E. F.; Tress, W.; Schenk, K.; Teuscher, J. L.; Moser, J. E.; et al. Unreacted PbI 2as a Double-Edged Sword for Enhancing the Performance of Perovskite Solar Cells. *J. Am. Chem. Soc.* **2016**, *138* (32), 10331–10343.
(92) Hagfeldt, A.; Boschloo, G.; Sun, L.; Kloo, L.; Pettersson, H. Dye-Sensitized Solar Cells. *Chem. Rev.* **2010**, *110* (11), 6595–6663.
(93) Kojima, A.; Teshima, K.; Shirai, Y.; Miyasaka, T. Organometal Halide Perovskites as Visible-Light Sensitizers for Photovoltaic Cells. *J. Am. Chem. Soc.* **2009**, *131* (17), 6050–6051.
(94) Heo, J. H.; Im, S. H.; Noh, J. H.; Mandal, T. N.; Lim, C.-S.; Chang, J. A.; Lee, Y. H.; Kim, H.-J.; Sarkar, A.; Nazeeruddin, M. K.; et al. Efficient Inorganic-Organic Hybrid Heterojunction Solar Cells Containing Perovskite Compound and Polymeric Hole Conductors. *Nat. Photon.* **2013**, *7* (6), 1–6.
(95) Baena, J. P. C.; Steier, L.; Tress, W.; Saliba, M.; Neutzner, S.; Matsui, T.; Giordano, F.; Jacobsson, T. J.; Kandada, A. R. S.; Zakeeruddin, S. M.; et al. Highly Efficient Planar Perovskite Solar Cells Through Band Alignment Engineering. *Energy Environ. Sci.* **2015**, *8* (10), 2928–2934.

(96) Etgar, L.; Gao, P.; Xue, Z.; Peng, Q.; Chandiran, A. K.; Liu, B.; Nazeeruddin, M. K.; Grätzel, M. Mesoscopic $CH_3Nh_3PbI_3/TiO_2$ Heterojunction Solar Cells. *J. Am. Chem. Soc.* **2012**, *134* (42), 17396–17399.

(97) Sum, T. C.; Mathews, N. Advancements in Perovskite Solar Cells: Photophysics Behind the Photovoltaics. *Energy Environ. Sci.* **2014**, *7* (8), 2518–2534.

(98) Tsai, H.; Nie, W.; Blancon, J.-C.; Stoumpos, C. C.; Asadpour, R.; Harutyunyan, B.; Neukirch, A. J.; Verduzco, R.; Crochet, J. J.; Tretiak, S.; et al. High-Efficiency Two-Dimensional Ruddlesden– Popper Perovskite Solar Cells. *Nature* **2016**, *536* (7616), 312–316.

(99) Koh, T. M.; Shanmugam, V.; Schlipf, J.; Oesinghaus, L.; Müller-Buschbaum, P.; Ramakrishnan, N.; Swamy, V.; Mathews, N.; Boix, P. P.; Mhaisalkar, S. G. Nanostructuring Mixed-Dimensional Perovskites: a Route Toward Tunable, Efficient Photovoltaics. *Adv. Mater.* **2016**, *28* (19), 3653–3661.

(100) Li, N.; Zhu, Z.; Chueh, C.-C.; Liu, H.; Peng, B.; Petrone, A.; Li, X.; Wang, L.; Jen, A. K. Y. Mixed Cation $FA_XPea_{1-X}PbI_3$ With Enhanced Phase and Ambient Stability Toward High-Performance Perovskite Solar Cells. *Adv. Energy Mater.* **2016**, *7* (1), 1601307–1601309.

(101) Chen, Y.; Sun, Y.; Peng, J.; Zhang, W.; Su, X.; Zheng, K.; Pullerits, T.; Liang, Z. Tailoring Organic Cation of 2D Air-Stable Organometal Halide Perovskites for Highly Efficient Planar Solar Cells. *Adv. Energy Mater.* **2017**, *7* (18), 1700162–1700167.

(102) Wang, Z.; Lin, Q.; Chmiel, F. P.; Sakai, N.; Herz, L. M.; Snaith, H. J. Efficient Ambient-Air-Stable Solar Cells with 2D–3D Heterostructured Butylammonium-Caesium-Formamidinium Lead Halide Perovskites. *Nat. Energy* **2017**, *2* (9), 1004–1010.

(103) Iagher, L.; Etgar, L. Effect of Cs on the Stability and Photovoltaic Performance of 2D/3D Perovskite-Based Solar Cells. *ACS Energy Lett.* **2018**, *3* (2), 366–372.

(104) Bai, Y.; Xiao, S.; Hu, C.; Zhang, T.; Meng, X.; Lin, H.; Yang, Y.; Yang, S. Dimensional Engineering of a Graded 3D-2D Halide Perovskite Interface Enables Ultrahigh VocEnhanced Stability in the P-I-N Photovoltaics. *Adv. Energy Mater.* **2017**, *7* (20), 1701038–1701038.

(105) Grancini, G.; Roldan-Carmona, C.; Zimmermann, I.; Mosconi, E.; Lee, X.; Martineau, D.; Narbey, S.; Oswald, F.; De Angelis, F.; Graetzel, M.; et al. One-Year Stable Perovskite Solar Cells by 2D/3D Interface Engineering. *Nat. Commun.* **2017**, *8*, 1–8.

(106) Yan, J.; Qiu, W.; Wu, G.; Heremans, P.; Chen, H. Recent Progress in 2D/Quasi-2D Layered Metal Halide Perovskites for Solar Cells. *J. Mater. Chem. A* **2018**, *6* (24), 11063–11077.

2 Methods

This chapter aims at presenting the methods that have been used throughout this work. This thesis is not about method development and set-up implementation: We will therefore focus on the kind of observables that can be measured with these techniques, and how to translate those observations into usable information towards the understanding of the photophysics of complex materials.

2.1 Femtosecond transient absorption spectroscopy

Femtosecond transient absorption spectroscopy (TAS or sometimes TA) is a time-resolved optical method that allows to probe the dynamical processes at the time scale of the molecular vibrations and typical electron transfer processes (fs-ps). Because the targeted time-resolution is so short, it is impossible to use typical electronic detection methods (for instance, by transforming the optical signal into an electrical one and detecting it on an oscilloscope). As a consequence, one has to resort to what is called optical gating: a first beam (the pump) is sent onto the sample and induces changes. A second beam (the probe) is then focused on the same sample area, and probes the perturbations induced by the pump. The dynamics of those pump-induced changes is determined by modifying the time-delay between the two beams: the time-resolution is thus only restricted by their pulse lengths and their cross-correlation (instrument response function, IRF).

Because of this detection pattern, the TAS signal is defined as:

$$\Delta A(\lambda, t) = A(\lambda, t)_{pump} - A(\lambda, t)_{no\ pump}. \tag{2.1}$$

Two different signals are measured, due to chopping of the pump at half the frequency of the laser repetition rate: the absorbance of the probe in the presence of the modifications caused by the pump, and the absorbance of the same sample area unperturbed. As a consequence, pump-induced signals that yield an enhanced amount of probe light to the detector appear as negative, while those that decrease this amount will appear positive.
In this respect, three types of signals are usually defined in TAS: ground-state bleaching (GSB), stimulated emission (SE) and excited-state absorption (ESA). A GSB signal arises when the pump depletes the valence band and fills the conduction band for a given transition: the probe cannot be absorbed by this particular transition, thus resulting in a negative signal. Because this is nothing but an “absorption competition” between the pump and the probe, a GSB usually reflects the steady-state absorbance spectra. Emission is a fundamental process in which light is emitted upon recombination of an electron with a hole (for semiconductors). It can be spontaneous (said to arise from vacuum fluctuations), or stimulated. In this case, conduction band electrons interact with an incoming radiation field (here: the pump) that causes them to collapse back to the valence band. Additional photons thus reach the detector, again resulting in a negative signal. Finally, ESA describes the absorption of the probe by new states, created

by the pump. In presence of the pump, the probe can thus induce new electronic transitions, decreasing the amount of light to the detector: An ESA signal is therefore positive.

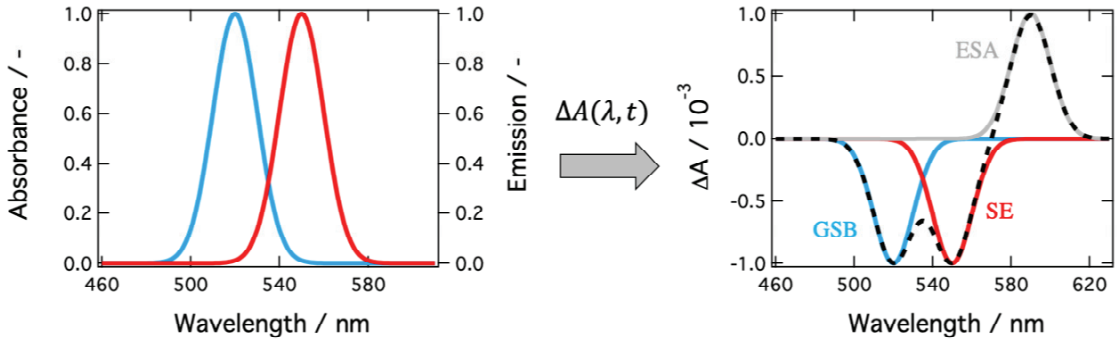

Figure 2-1 Typology of transient absorbance spectroscopy signals and their meaning. Left: Examples of absorbance (blue) and emission (red) signals. Right: Corresponding signals as seen in a transient absorbance spectroscopy measurement, on top of an ESA signal (grey). The dotted black line indicates the sum of the individual signals that constitutes the actual output of the measurement.

Figure 2-1 illustrates those various processes, and maps them to corresponding steady-state features if relevant. As also shown, the transient absorption (TA) signal is the sum of all those features; because they often overlap and exhibit different dynamics, peak assignment and analysis often proves tricky. For such tangled signals, one tool is of great help: Global analysis.

2.1.1 Treating complex TA signals: Global analysis

Global analysis refers to the simultaneous analysis of all relevant datasets; in particular, by taking advantage of the presence of connected parameters across those datasets, global analysis allows to extract a single parameter set containing all the needed information in relation to the chosen connected parameters.[1]

Transient absorbance spectroscopy data are two-way: The measurement outputs take the shape of a two-dimensional matrix $\boldsymbol{S}(\lambda, t)$ involving two independent experimental variables, namely the spectral variable (λ, the wavelength) and the variable measuring the time-evolution of the spectral changes (t, the time delay between the pump and the probe). As is clear from the definition provided above, at the core of global analysis is the assumption that those two variables are independent, and thus separable, leading to:

$$\boldsymbol{S}(\lambda, t) = \sum_{i=1}^{n} \varepsilon_i(\lambda) \cdot \chi_i(t) \tag{2.2}$$

where i designates the individual components of the total TA signal and n the total number of components. The goal is to then determine $\varepsilon_i(\lambda)$ and $\chi_i(t)$, which constitute the "relevant datasets" mentioned above. Usually neither $\varepsilon_i(\lambda)$ or $\chi_i(t)$ are known, and resorting to kinetic or spectral models is required. Herein, we will focus on kinetic models involving first-order decays: We assume that the n components evolve independently from each other. In this

context, the problem simply reduces to a system of linear differential equations, whose solutions are sums of monoexponentials, convoluted with the IRF if needed (usually approximated by a gaussian).[2,3] In addition, the parameter connecting those differential equations is usually chosen to be the time constant(s) of the multiexponential functions representing each kinetic trace.

In practice, the procedure reads as:

1. Extraction of some kinetic traces from $S(\lambda, t)$. The number and wavelength spacing of the extracted traces depends upon the complexity of the spectral signal.
2. Determination of the proper kinetic model to use: Individual fitting of a few sampled traces. This aims at getting to the best possible model as well as to provide a good initial guess for the global fitting procedure itself (faster convergence).
3. Performing of the global fit: fitting the kinetic traces selected in step 1 with the model determined in step 2, with the same time constant(s) τ throughout.
4. Extraction of the amplitude coefficient of each exponential for every kinetic trace into new sets of data: These constitute the so-called decay associated spectra (DAS). One DAS thus represents the spectral dependence of a given time constant throughout the spectral window of the measurement.

The fitting functions used in a system accurately represented by a system of linear differential equations are as follows:

$$\Delta A(\lambda, t) = \frac{1}{2} \cdot \sum_{i=1}^{n} A_i(\lambda) \cdot e^{\left[\frac{\mu - t}{\tau_i} + \frac{1}{2}\left(\frac{\sigma}{\tau_i}\right)^2\right]} \cdot \left[1 + erf\left(\frac{t - \left(\mu + \frac{\sigma^2}{\tau_i}\right)}{\sqrt{2}\sigma}\right)\right], \tag{2.3}$$

when convolution with a gaussian IRF is needed (for processes occurring on a timescale close to the time-resolution of the experiment). And:

$$\Delta A(\lambda, t) = y_0 + \sum_{i=1}^{n} A_i(\lambda) \cdot e^{\frac{t - t_0}{\tau_i}}, \tag{2.4}$$

when early-time processes are neglected.

As stated in the procedure above, the output of a global fit involving a kinetic model is a series of n DASs, n being the number of individual components involved in the fitting (usually determined from step 2, or through previous knowledge of the system). Plotting those DAS versus the wavelength brings to light the spectral dependence of processes occurring on different timescales: The assignment of TA peaks and the meaning of their dynamics therefore becomes clearer, and complex photodynamical features can be explicated.

2.1.2 Exploiting the polarization of the light field: Anisotropic versus classical transient absorbance measurements.

The light out of a chirped pulse amplifier (CPA) laser, as used in this work, is linearly polarized along one given direction (horizontal or vertical polarization, depending on the set-up). [4] Because of their interaction with numerous optics along the way to the sample, the polarization of the pump and the probe, although still linear, are more randomly oriented. This induces both an uncontrolled photoselection preventing a proper analysis of the results of the measurement, and yields mixed contributions to the time-evolution of the spectral features: They do not solely reflect the excited-state population dynamics, but also include the contribution from orientational relaxation. [5]
As a consequence, a thorough control of the relative polarizations of the pump and the probe at the sample is necessary, and can easily be achieved with appropriate optics. In the framework of what will be called here "classical transient absorbance spectroscopy", those polarizations are oriented as to be at about 54.7° from each other. This corresponds to the so-called magic angle, which can be shown to be the only configuration for which the orientational dynamics contribution to the global dynamics cancel out. [6] However, samples are not always isotropic, in particular when measuring thin-films (solid state): linearly polarized light thus becomes an efficient tool for probing structural anisotropy and reorganization within such samples, bringing the focus on "anisotropic transient absorbance spectroscopy".

In the context of transient absorbance spectroscopy, anisotropy is defined as follows:

$$r(t) = \frac{\Delta A_{\parallel}(t) - \Delta A_{\perp}(t)}{(\Delta A_{\parallel}(t) + 2\Delta A_{\perp}(t))}, \tag{2.5}$$

where $\Delta A_{\parallel}(t)$ and $\Delta A_{\perp}(t)$ describe the transient absorbance signals of the sample when the polarization of the pump and the probes are set parallel and perpendicular to each other, respectively. This can be obtained either via two separate measurements or simultaneously with the proper set-up.[7]
In practice, depending on the nature of the sample, results of anisotropic relative to classical TAS involve modifications in the spectra and/or the dynamics. Spectral modifications inform on the structural dependence and the localization of the photogenerated species, while changes in the dynamics shed light on the reorganization processes involving those species.

2.2 Electromodulated differential absorption spectroscopy

This section is adapted from ref. [8].

Similarly to TAS, electromodulated differential absorption (EDA) spectroscopy belongs to the family of "differential" techniques, where the signal is defined as the difference between the optical properties of a sample in the presence and in the absence of a perturbation. In the present

context, the perturbation is an externally applied or photoinduced (local) electric field, and the signal monitored at a wavelength λ is given as an absorbance change $\Delta A(\lambda)$:

$$\Delta A(\lambda) = A(\lambda)_{field} - A(\lambda)_{nofield} \tag{2.6}$$

It emerges that the spectral shape and amplitude of the electroabsorption signal is directly related to the response of the sample upon application of a field. When an electric field is applied on a quantum system, it induces a reorganization of its electronic density and hence a modification of the nuclear configuration, ultimately modifying the electronic structure.[9] As a consequence, the electroabsorption response could be obtained theoretically by solving the delicate problem of a quantum hydrogenic system in a field, for which no analytical solution exists. The functional form of the solution is thus highly dependent on the type of approximation employed, and hence this response will differ tremendously when considering a solid or a molecular system.

2.2.1 Electroabsorption of molecules or confined excitonic states

In the context of molecules or confined excitonic states, the Coulomb interaction within the hydrogenic model is large, and the applied electric field can be considered negligible. As a consequence, one can resort to a perturbative solution, that is, the response of the system of interest in the field can be modelled in the framework of Stark theory. The absorbance change is then given by a perturbative expansion: [10]

$$\Delta\mathrm{A}(\lambda) = -\frac{d\mathrm{A}(\lambda)}{d\lambda} \cdot \boldsymbol{m}_{0k} \cdot \boldsymbol{E} - \frac{1}{2}\frac{d\mathrm{A}(\lambda)}{d\lambda} \cdot \boldsymbol{p}_{0k} \cdot \boldsymbol{E}^2 + \frac{1}{2}\frac{d^2A(\lambda)}{d\lambda^2} \cdot (\boldsymbol{m}_{0k} \cdot \boldsymbol{E})^2 \tag{2.7}$$

where $\boldsymbol{E}$ denotes the externally applied vectorial field, while $\boldsymbol{m}_{0k}$ and $\boldsymbol{p}_{0k}$ correspond to the permanent dipole moment and polarizability changes upon the optical transition of interest (0 → k), respectively.

As the first term is linear in the field, it cancels out for isotropic samples. The result is that the response of a molecular or confined excitonic system subjected to an electric field is quadratic in the field intensity $|\boldsymbol{E}|$ (quadratic Stark effect). In addition, it can be decomposed into a linear combination of first and second derivatives of the linear absorption spectrum, whose relative weight provides direct insight into the type of photogenerated carriers. Light absorption by charge-transfer (CT) excitons, occurring from the Coulomb interactions of an electron and a hole separated by an interface, for instance, is characterized by a change in the permanent dipole moment. The contribution of these CT states to the electroabsorption response can, thus, be directly inferred from the weight of the second-derivative term.

2.2.2 Electroabsorption of solids

In the case of solids, the assumption of a small perturbative applied field cannot be made generally, as the electrostatic interactions are significantly smaller overall than for the confined case, rendering the use of a perturbative solution highly inappropriate. In addition, a general

solution for solid-state systems is a tricky problem, as the level of classical correlation of the electron-hole pairs, *ie.* the amplitude of the Coulomb interaction, varies significantly from one system to another. This variation indeed depends on the intrinsic properties of the solid-state system of interest, such as the nature of its chemical bonds and, hence, its electric susceptibility (related to the dielectric constant), which directly determines to what extent electron-hole pairs are correlated. For example, ionic solids exhibit a weaker wavefunction overlap, and are characterized by a wider bandgap and a lower susceptibility than their covalent analogs.[11]

From the above paragraph, a broad spectrum of interactions emerges, starting with the simplest model to describe a solid-state system: a continuum of single-particle states where electrons and holes are by definition uncorrelated. Then, if, from this point, we adiabatically switch on the correlation, we progressively move towards the other extreme of this spectrum where the exciton, the bound-pair state solution to the Wannier equation, lies.
The problem of a continuum in an electric field has been tackled by Franz and Keldysh in the 1950's.[12] They showed that the resulting eigenfunctions were not plane waves but Airy functions, accounting for the observed electroabsorption signals, scaling as $|\boldsymbol{E}|^{-2/3}$ and involving both a red-shift (photon-assisted tunnelling between bands) and oscillations above the band edge. Interestingly, experiments originally carried out on GaAs revealed a different field-dependence in the limit of low field intensities. [13-15] In this case, the electroabsorption signal scales as $|\boldsymbol{E}]^2$, similarly to the Stark effect and is modeled by the so-called low-field Franz-Keldysh-Aspnes (FKA) effect. Importantly, while the Stark effect is determined by a combination of first and second derivatives of the absorption spectrum, the low-field FKA effect appears to depend upon its third derivative.

The continuum model breaks down when the electron-hole interaction becomes significant, ultimately leading to the formation of so-called Wannier-Mott excitons. This calls for other theoretical treatments, namely the excitonic electroabsorption theories. As stated before, no analytical solution exists for the Schrödinger equation of a Wannier exciton in an electric field, and excitonic electroabsorption theories rely on two different approaches: they either resort to approximations (for example to model the external potential) to go back to an analytically solvable problem[16,17] or focus on the development of numerical resolution routines.[11,18-22]

2.2.3 Obtaining EA signals

The understanding of electroabsorption signals is essential as they do not only appear in the results of classical EDA measurements, but also in TAS, for instance. In an EDA experiment, instead of modulating the pump, voltage pulses from a function generator are applied to the sample at half the frequency of the laser repetition rate. A broad-spectrum (white light) laser beam is then sent onto the sample to probe its absorption with and without the perturbation (the electric field): This allows to calculate the signal defined in equation (2.6). The shape, duration, period and amplitude of the voltage pulses are thoroughly controlled parameters: they are optimized so that (i) the probe light reaches the sample at equilibrium and (ii) the perturbation is over by the time the next probe pulse reaches the sample.

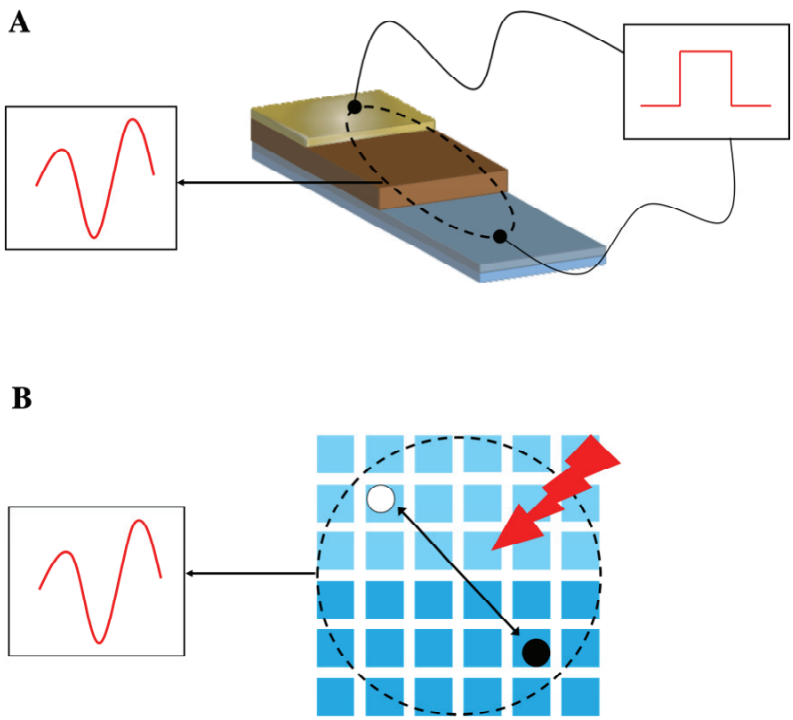

Figure 2-2 Two ways to obtain an EA signal**. A.** Electromodulated differential absorption (EDA) spectroscopy: the active layer (brown) is sandwiched between a conductive glass (FTO) and a metal (Au) electrode. The sample is then subjected to an externally applied electric field by the means of a voltage pulse generator. A white light probe then provides the resulting EA spectrum**. B.** Transient absorbance spectroscopy: the pump pulse creates photocarriers inducing an electric field. This field affects the surroundings, causing an EA response recorded by the probe beam.

EDA experiments require samples with a well-defined architecture. First, the active layer must be sandwiched between two electrodes: at least one electrode must be transparent so that the probing laser beam can reach its target (conductive glass); the other electrode is usually metallic, and must constitute an ohmic contact (typically Au, Al). Second, charges must not be able to leak from the active layer to one of the two electrodes, as it would screen the applied field. EDA measurements on organic samples are usually not problematic in this respect because of their low charge mobilities. On the contrary measuring semiconductors with better conductive properties requires the intercalation of proper insulating layers inbetween the electrodes and the active layer.[19-21] Figure 2-2A schematizes a typical EDA measurement with a proper sample architecture (here: without insulating layers).

However, the electric field does not have to be externally applied and explicitly modulated to yield an EA signal. Indeed, photoexciting a sample can create species that carry a sizeable electrical dipole, generating an internal electric field that affects their surroundings. In a TAS measurement, the creation of those internal electric fields coincides with the presence of the pump, causing the resulting TA difference spectrum to include EA contributions on top of the typical GSB, SE and ESA. These types of EA signals are called “photoinduced” and their measurement does not require specific sample architectures (Figure 2-2B).

2.2.4 Unravelling the properties of photocarriers using electroabsorption spectroscopy

The various types of electroabsorption responses described earlier exhibit well defined field-dependence. Their spectral lineshapes also differ: For instance, the Stark effect is characterized by an EA spectrum, which displays a mixture of first- and second-derivatives of the absorption spectrum, while the low-field FKA effect corresponds to the third derivative. As a consequence, a spectral lineshape analysis of the electroabsorption signal constitutes a probe of the degree of correlation between photocarriers, and hence, of the type of charged particle or quasiparticle involved.

In practice, the analysis of the electroabsorption signals can be described as follows:

1. Assessing the relevant theoretical model: Field dependence.
   The most straightforward way to achieve this is by evaluating the field dependence of the EA signal, if accessible: Franz-Keldysh signals have an $\boldsymbol{E}|^{-2/3}$ dependence while other models will evolve according to $|\boldsymbol{E}|^2$ or $|\boldsymbol{E}|$.
2. Assessing the relevant theoretical models: Lineshape analysis
   On the one hand, lineshape analysis allows you to discriminate between the low-field FKA and the Stark effects; on the other hand, it provides an unambiguous assessment of the dominant contributions towards the latter. In this context, functions involving a linear combination of the three first derivatives must then be constructed and fitted to the experimental data:

$$\Delta A(\lambda) = \sum_{i=1}^{3} A_i \cdot \frac{d^i A(\lambda)}{d\lambda^i}. \tag{2.8}$$

   The relative amplitudes A_i impart the necessary information.

As is often the case in modelling, short cuts can be done when prior knowledge of the sample is available, from literature or complementary experimental data. This is, for example, useful when a reliable field dependence cannot be acquired, as is frequent for photoinduced EA signals or EDA samples with unoptimized architecture (e.g. leakage current due to improper insulation).

References

(1) Holzwarth, A. R. Data Analysis of Time-Resolved Measurements. In *Biophysical Techniques in Photosynthesis*; J, A., J, H. A., Eds.; Dordrecht, 1996; Vol. 3.

(2) van Stokkum, I. H. M.; Larsen, D. S.; van Grondelle, R. Global and Target Analysis of Time-Resolved Spectra. *Biochim. Biophys. Acta, Bioenerg.* **2004**, *1657* (2-3), 82–104.

(3) Bonneau, R.; Wirz, J.; Zuberbühler, A. D. Methods for the Analysis of Transient Absorbance Data. *Pure & Appl. Chem* **1997**, *69* (5), 979–992.

(4) Svelto, O. *Principles of Lasers*, Fifth Edition. Hanna, D. C., Translator; Springer: New York, 2010.

(5) Tan, H.-S.; Piletic, I. R.; Fayer, M. D. Polarization Selective Spectroscopy Experiments: Methodology and Pitfalls. *J. Opt. Soc. Am. B* **2005**, *22* (9), 2009–2017.

(6) Berera, R.; van Grondelle, R.; Kennis, J. T. M. Ultrafast Transient Absorption Spectroscopy: Principles and Application to Photosynthetic Systems. *Photosynth Res* **2009**, *101* (2-3), 105–118.

(7) Fleming, G. R. *Chemical Applications of Ultrafast Spectroscopy*; Oxford University Press: New York.

(8) Bouduban, M. F.; Burgos-Caminal, A.; Teuscher, J.; Moser, J. E. Unveiling the Nature of Charge Carrier Interactions by Electroabsorption Spectroscopy: an Illustration with Lead-Halide Perovskites. *chimia (aarau)* **2017**, *71* (4), 231–235.

(9) Nakatsuji, H.; Hayakawa, T.; Yonezawa, T. Molecules in an Electric Field. Model for Molecular Geometry. *J. Am. Chem. Soc.* **1981**, *103*, 7426–7432.

(10) Lanzani, G. The Photophysics Behind Photovoltaics and Photonics. **2012**, 1–4.

(11) Blossey, D. F. Wannier Exciton in an Electric Field. I. Optical Absorption by Bound and Continuum States. *Physical Review B*, **1970,** *2*, 3976–3990.

(12) Franz, W. Einfluß Eines Elektrischen Feldes Auf Eine Optische Absorptionskante. *Zeitschrift für Naturforschung A* **1958**, *13* (6), 484–489.

(13) Aspnes, D. E.; Rowe, J. E. Resonant Nonlinear Optical Susceptibility: Electroreflectance in the Low-Field Limit. *Phys. Rev. B* **1971**, *5*, 4022–4030.

(14) Aspnes, D. E.; Frova, A. Influence on Spatially Dependent Perturbation on Modulated Reflectance and Absorption of Solids. *Solid State Commun.* **1969**, *7*, 155–159.

(15) Frova, A.; Handler, P.; Germano, F. A.; Aspnes, D. E. Electro-Absorption Effects at the Band Edges of Silicon and Germanium. *Phys. Rev. B* **1966**, *145*, 575–583.

(16) Duke, C. B.; Alferieff, M. E. Solvable Model of a Hydrogenic System in a Strong Electric Field: Application to Optical Absorption in Semiconductors. *Phys. Rev* **1966**, *145*, 583–592.

(17) Penchina, C. M.; PRIBRAM, J. K.; Sak, J. Electric Field Effects on Excitonic Absorption in Semiconductors. *Phys. Rev* **1969**, *188*, 1240–1245.

(18) Cardona, M. Modulation Spectroscopy of Semiconductors. In *Festkörperprobleme 10*; Advances in Solid State Physics; Springer Berlin Heidelberg: Berlin, Heidelberg, 1970; Vol. 10, pp 125–173.

(19) Ralph, H. I. On the Theory of the Franz-Keldysh Effect. *J. Phys. C: Solid State Phys.* **1968**, *1*, 378–386.

(20) Dow, J. D.; Redfield, D. Electroabsorption in Semiconductors: the Excitonic Absorption Edge. *Physical Review B*, **1970**, *1*, 3358–3371.

(21) Blossey, D. F. Wannier Exciton in an Electric Field. II. Electroabsorption in Direct-Band-Gap Solids. *Physical Review B*, **2016**, 1382–1391.

(22) Blossey, D. F. Wannier Exciton in an Electric Field. II. Electroabsorption in Direct-Band-Gap Solids. *Physical Review B*, 1971, 1382–1391.

3 Inter-Domain Charge Transfer as a Rationale for Superior Photovoltaic Performances of Mixed Halide Lead Perovskites

3.1 Introduction

Since their inception as very promising photovoltaic materials, lead halide perovskites have attracted an enormous scientific interest across the fields of chemistry, solid-state physics, photonics, and material sciences. Power conversion efficiencies achieved with simple, solution-processed donor-acceptor heterojunction devices based on this type of semiconductor now exceed 22%,[1,2] while their stability appears to be continuously improving.[3,4]

The constituents of the perovskite materials have significantly evolved since the first devices made out of the standard methylammonium lead triiodide perovskite ($MAPbI_3$, MA = $CH_3NH_3^+$) to the latest developments relying on mixed cation, mixed anion perovskite systems. Currently, optimal perovskite compositions are based on formamidinium (FA^+) as the majority cation. The cubic perovskite α-$FAPbI_3$ black phase has a bandgap of 1.40 eV, which is smaller than that of $MAPbI_3$ (1.57 eV) and, thus, closer to the optimum Shockley-Queisser value of 1.34 eV.[5] The α-$FAPbI_3$ phase, however, is unstable in ambient conditions and undergoes a transition to a non-perovskite, inactive yellow δ-phase. Recent progresses have been made in stabilizing the black α-$FAPbI_3$ phase through the use of 2-D intercalates and molecular additives.[6] Incorporation of methylammonium (MA^+) cations has been shown to hinder the phase transition and allow for the preparation of more efficient and stable photovoltaic cells.[7]

It has clearly emerged, from the past two years, that perovskites formulated with mixed cations (MA^+, FA^+) and mixed halides (I^-, Br^-) consistently perform better in solar cells than standard systems, via both a better short-circuit current, and a larger open-circuit voltage .[1,8-10] Mixed-halide materials could appear problematic, as halide segregation tends to occur gradually in the dark [11] and under irradiation.[12-14] This phase separation effect, though, is attenuated in mixed-cation materials.[12] The addition of ca. 5% molar percentage Cs^+ to the perovskite precursors was also found to enhance phase stabilization by tuning the tolerance factor and suppressing the inactive $FAPbI_3$ yellow phase.[8,15,16] Finally, Rb^+ addition has been recently reported to further improve the performance and stability of mixed cation, mixed halide lead perovskite cells, exhibiting a power conversion efficiency of 21.6%.[1]

The preparation of lead halide perovskites containing a mixture of organic (MA^+, FA^+) and inorganic (Cs^+, Rb^+) cations yield large monolithic grains, the dimensions of which can reach 1 μm, far exceeding the typical 200 nm film thickness used in photovoltaic devices. The absence of grain boundaries along the transport path of the charge carriers improves significantly their diffusion length and is beneficial to the photovoltaic conversion efficiency.[8,10,17,18] Mixed halide materials containing both Br^- and I^- anions are quite attractive for LED applications, due to the continuous tunability of their bandgap obtained by adjusting the Br^-/I^- content ratio and to the larger excitonic character of bromide-containing materials. Though, it remains to be understood which mechanism could make mixed halide perovskites exhibit enhanced

photovoltaic conversion efficiencies compared to mixed cation lead triiodide, in spite of potential heterogeneities and an increased bandgap of the material that aggravates the absorption mismatch with the solar spectrum.
Here, we used a combination of ultrafast transient absorption (TAS) and fluorescence up-conversion spectroscopy (FLUPS) techniques to study charge- and energy transfer processes taking place in transparent thin-films of lead halide perovskites of the composition $MA_{1-y}FA_yPbI_{3-x}Br_x$, containing a mixture of methylammonium (MA^+) and formamidinium (FA^+) cations, as well as mixed iodide (I^-) and bromide (Br^-) anions. The exploitation of the dynamics of transient photoinduced electroabsorption signals observed in TAS spectra provided evidence of charge transfer between domains of various chemical compositions taking place in competition with energy transfer. These findings suggest that the separation of photogenerated carriers in regions characterized by a gradient of the valence band edge energy is at the origin of the improved efficiency of solar cells based on mixed halide perovskites.

3.2 Methods

3.2.1 Samples

The samples under consideration here are, on the one hand, thin-films of mixed cations (MA^+, FA^+), mixed anions (Br^-, I^-) lead halide perovskites. The initial stoichiometry of the solution reactant was $MA_{0.15}FA_{0.85}PbI_{2.55}Br_{0.45}$. However, as the final composition of the material after crystallization is not precisely determined, the material under study here will be denoted $MA_yFA_{1-y}PbI_{3-x}Br_x$. or "mixed perovskite". Thin-films of the standard $MAPbI_3$ perovskite composition will also be examined for a comparison.
On top of different materials, two different sample architectures were used, which were adapted to the spectroscopic techniques employed: Perovskite/glass and insulating layer/perovskite/insulating layer/gold samples were studied with ultrafast transient absorption spectroscopy (TAS) in transmission mode and broadband fluorescence up-conversion spectroscopy (FLUPS), respectively.
The samples were prepared according to previously reported protocols with the exception of the concentration of the perovskite precursor solution which was kept at 0.7 M in order to obtain a thinner layer of the absorber material to facilitate the optical and spectroscopic measurements.[19,20] The same precursor concentration was used to prepare complete solar cell devices, to ensure a direct correlation between the spectroscopic characterization and the photovoltaic results.
Nippon Sheet Glass 10 Ω/sq substrates (for the fluorescence up-conversion spectroscopy measurements) and microscope glass (transient absorbance spectroscopy experiments) were cleaned by ultra-sonication in a bath of 2% Hellmanex aqueous solution for 30 minutes. After rinsing with deionised water and ethanol, the substrates were further cleaned with UV ozone treatment for 15 min.
The perovskite films were deposited on the substrate from a precursor solution containing either $MA_{0.15}FA_{0.85}PbI_{2.55}Br_{0.45}$, or standard $MAPbI_3$ in anhydrous DMF:DMSO 4:1 (v:v) at a concentration of 0.7 M. The perovskite solution was spin-coated in a two step program at 1000

and 6000 rpm for 10 and 30 s, respectively. During the second step, 120 μL of chlorobenzene was poured onto the spinning substrate 10 s prior to the end of the program. The substrates were then annealed at 100°C for 1 hour in a dry-air filled glove box.
The insulating layers for the FLUPS samples comprised of a first coating of pure PMMA and a second layer of PMMA and alumina nanoparticles. This insulating double layer was applied on bare FTO and on top of the perovskite. The PMMA layer was deposited by spin-coating for 20 s at 4000 rpm with a ramp of 2000 rpm, using a solution of 20 mg/mL of PMMA solution in toluene. The PMMA/alumina mixed layer was deposited by spin-coating for 20 s at 4000 rpm with a ramp of 2000 rpm. The dispersion of alumina nanoparticles (Aldrich) was diluted 10:1 in volume with a PMMA/toluene solution (3 mg/mL). Finally, to make sure the samples intended to be studied with FLUPS were properly working devices, a small gold electrode (120 mm-thick) was thermally evaporated under high vacuum onto each of them, allowing for PV characterization. The subsequent FLUPS measurements were carried out on the electrode-free area of the samples, in transmittance mode.

3.2.2 Photovoltaic devices fabrication and testing

Complete solar cell devices were prepared by depositing the perovskite solution precursor onto a FTO substrate (Nippon Sheet Glass 10 Ω/sq) comprising a 15 nm thin coating of SnO_2 deposited by ALD as the electron transporting layer. After annealing the perovskite layer, 100 nm of *spiro*-MeOTAD was spincast to form the hole transporting material (HTM) layer. The HTM was doped at a molar ratio of 0.5, 0.03 and 3.3 with bis(trifluoromethylsulfonyl)-imide lithium salt (Li-TFSI, Sigma Aldrich), tris(2-(1H-pyrazol-1-yl)-4-tert-butylpyridine)–cobalt(III) (FK209, Dyenamo), and 4-tert-butylpyridine (TBP, Sigma Aldrich), respectively. Finally, a 70-80 nm-thick gold electrode was thermally evaporated on top of the HTM layer. Test solar cell elements had a 5 × 5 mm square geometry.
Solar cell merit parameters were measured using a 300 W xenon light source (Ushio). The spectral mismatch between AM1.5G and the simulated illumination was reduced by the use of an AM1.5G filter (Newport). The light intensity was calibrated with a Si photodiode equipped with an IR-cutoff filter (KG3, Schott) and it was recorded prior to each measurement. Current-voltage characteristics of the cells were obtained by applying an external voltage bias while measuring the current response with a digital source meter (Keithley 2400). The voltage scan rate was 10 mV s^{-1}. The cell area was defined by a 4 × 4 mm (0.16 cm^2) black metal mask.

3.2.3 Spectroscopic methods

Ultrafast transient absorbance (TA) spectra of standard and mixed perovskites thin-films were acquired using femtosecond pump-probe spectroscopy with a pump wavelength λ_{ex} = 390 nm. The pump beam was obtained by frequency doubling the output of a chirped pulse amplified Ti:Sapphire laser (CPA-2001, Clark-MXR, 778 nm fundamental central wavelength, 120 fs pulse duration, 1 kHz repetition rate) in a BBO crystal, yielding 200 fs pulses. The probe beam was generated by directing a portion of the 778 nm fundamental output of the laser into a CaF_2 crystal, yielding a white light continuum measured over a 400-780 nm spectral domain. The probe fluence at the sample was much lower than that of the pump (7-35 μJ cm^{-2}). Similarly,

the diameter of the probe beam was smaller to ensure homogeneous excitation of the probed area. The dynamics of the photo-induced signals were obtained with a computer-controlled delay-line on the pump path. The probe beam was split, before the sample, into a beam going through the sample (signal beam) and a reference beam. Both signal and reference beams were directed to respective spectrographs (Princeton Instruments, Spectra Pro 2150i) and detected pulse-to-pulse with 512x58 pixel back-thinned CCD cameras (Hamamatsu S07030-0906). The pump beam was chopped at half of the laser frequency (500 Hz) and a satisfying signal-to-noise ratio was obtained by typically averaging 3,000 spectra. The time resolution of the experiment was 250 fs.

Femtosecond time-resolved broadband fluorescence up-conversion spectra (FLUPS) were measured with a previously described instrument. [21] The setup had a time-resolution of 170 fs (FWHM of the instrument response function). The experimental spectra were corrected for the wavelength-dependent detection sensitivity, using a set of secondary emissive standards (covering the spectral range 415-850 nm), and for the temporal chirp, using the wavelength-independent instantaneous response of 2,5-bis(5-*tert*-butyl-benzoxazol-2-yl)thiophene (BBOT) in acetonitrile. The samples were not moved during the measurement. Integration times per time-delay were in the range of 2-4 s, with each time-scan being averaged 10 times.

3.3 Results and Discussion

Ultrafast transient absorption spectroscopy was applied to solution-processed mixed $MA_yFA_{1-y}PbI_{3-x}Br_x$ and standard $MAPbI_3$ perovskite thin films spin-coated on glass. The mixed-cation, mixed-halide perovskite material was prepared from solution reactants with an initial stoichiometry corresponding to the fractions $x = 0.45$ and $y = 0.15$. Although the composition of the final solid material is not expected to be significantly different, its exact stoichiometry has not been determined.

The ultrafast transient absorption (TA) spectrum of the standard perovskite layer observed upon pulsed excitation of the sample at a pump wavelength $\lambda_{ex} = 390$ nm (Figure 3-1A) exhibits a large negative feature at a probe wavelength $\lambda = 760$ nm, assigned to a combination of ground-state bleaching and stimulated emission, a broad positive band at shorter wavelengths and, finally, a second negative band at 480 nm, the assignment of which remains under discussion.[22-28] The transient spectrum of the mixed perovskite recorded in identical conditions reveals a similar negative feature centred at 750 nm (Figure 3-1B), on top of strong oscillations in the $\lambda = 500$-630 nm region. These peculiar features are only observed in the mixed perovskite samples, where they are not modified by the film thickness, nor by the light angle of incidence. The occurrence of spectral artefacts due to interferences can, therefore, be excluded. In the following, we focus on explaining the complexity of the obtained spectra that hints at the presence of more dynamical processes or photo-excited populations than in the standard material case.

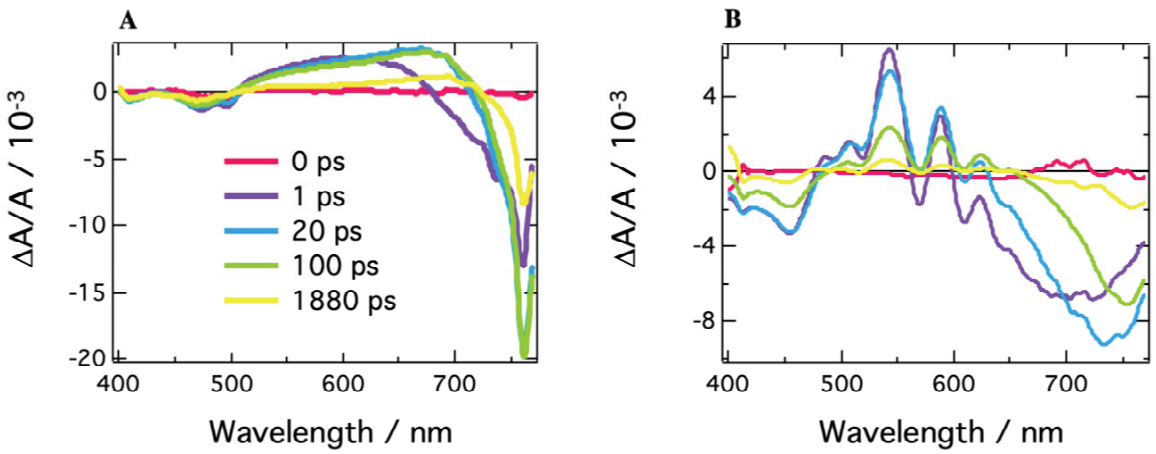

Figure 3-1 Ultrafast TA spectra recorded upon pulsed photoexcitation of perovskite thin-films at a pump wavelength λ_{ex} = 390 nm and various probe time delays: red: 0 ps, purple: 1 ps, blue: 5 ps, green: 100 ps and yellow: 1880 ps. **A**. MAPbI3, pump energy fluence 7 μJ cm^{-2}. **B**. $MA_yFA_{1-y}PbI_{3-x}Br_x$, pump energy fluence 35 μJ cm^{-2}.

As a first step, we consider the oscillations observed at λ = 500-630 nm in Figure 3-1B, which we assign to a photoinduced electroabsorption signal.[29,30] This feature arises from the photogeneration of electron-hole pairs that induce local electric fields, affecting the surrounding material and yielding changes in its absorption properties. Depending on the type of sample under study and, more specifically, on the level of correlation of the charge carriers, the electroabsorption can be modelled in different ways: Stark effect, Franz-Keldysh effect, or excitonic electroabsorption theories.[31]

Methylammonium lead triiodide perovskite exhibits low exciton binding energy and, hence, low correlation between charge carriers.[31-38] As such, its electroabsorption signal has been shown to correspond to the low-field Franz-Keldysh-Aspnes effect.[39] On the other hand, the exciton binding energy of hybrid lead halide perovskite increases as one moves up the halogen column of the periodic table.[31,34,37,40] As a consequence, we assume that the electroabsorption of perovskite layers involving mixed Br^-/I^- anions can be modelled reasonably well within the Stark theory. In such a framework, the electroabsorption signal can be shown to correspond to a linear combination of the first and second derivatives of the linear absorbance spectrum (see Supplementary Information). For isotropic samples, the related amplitudes of these two components are given by the change in the polarizability of the material and by the change in the dipole moment upon the electronic transition of interest, respectively.

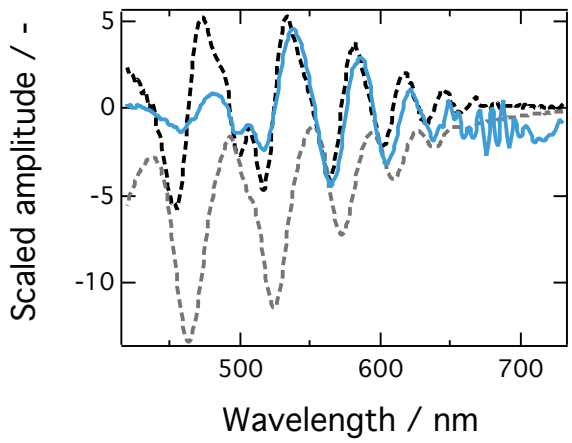

Figure 3-2 Superposition of the TA spectrum of the mixed perovskite sample measured at a probe time delay of 0.2 ps (blue line), with the first and second derivatives of the linear absorbance spectrum (grey and black dotted lines, respectively). The transient spectrum was obtained upon photoexcitation at λ_{ex} = 390 nm and at a pump energy fluence of 20 μJ cm^{-2}.

Figure 3-2 displays the transient absorbance spectrum of a thin film of $MA_yFA_{1-y}PbI_{3-x}Br_x$ mixed perovskite measured at a probe time delay of 0.2 ps, together with the first and second derivatives of the linear absorbance spectrum of the same sample. Both derivatives exhibit broadband oscillations, and the TA signal appears to be clearly dominated by a second-derivative contribution. This implies the occurrence of a dipole moment change upon photoexcitation. Such a dipole moment change can only arise from charge-transfer excitons (CTEs), namely electrostatically-bound electron-hole pairs, where both photogenerated carriers are separated by a junction or a domain boundary.[41] As a consequence, the second derivative-dominated line-shape of the observed photoinduced electroabsorption signal, in the framework of Stark theory, constitutes evidence for the generation of CTEs at boundaries between grains of homogeneous composition, or at junctions between hetero-domains. From Figure 3-2, it appears clearly that the latter is the most likely conclusion, as the CTE signature spans a broad spectral region, from 500 nm to 630 nm, where several shoulders are observed in the absorption spectrum that are likely to correspond to excitonic bands of domains characterized by various degrees of halide mixing. We dismiss here the possibility of light-induced phase segregation to stand at the origin of this observation as no sample modification, nor aging, occurred during the measurements. We therefore conclude that the mixed halide perovskite film is intrinsically constituted of heterogeneous domains, at the boundaries of which photogenerated electron-hole pairs get trapped in the form of charge transfer excitons.

The valence band maximum of lead halide perovskites is determined by the nature of the halide, due to the change from 4p (for Br^-) to 5p (for I^-) valence orbitals. As a result, the bandgap of the material is directly affected by the Br^-/I^- content ratio, while the effect of the cation proportion is limited. We can, therefore, go one step further by explaining the compositional range suggested by the oscillations of the electroabsorption signal: The first clear oscillation peaks at 530 nm correspond to the absorption maximum of $MA_yFA_{1-y}PbBr_3$ for a large span of y fraction values. The last observable peak on Figure 3-1B is centred at 670 nm, and has previously been assigned to a $Br_{1.5}I_{1.5}$ halide mixture.[42] Note that the amplitude of the oscillations decreases as one moves towards a smaller Br/I ratio, in the lower energy part of the

spectrum. This is expected to be due to the decreased exciton binding energy of iodide rich materials, translating into a smaller dipole moment change and a smaller CTE-dominated Stark signal.

The presence of heterogeneous domains within mixed halide perovskite films raises questions about the way charge carriers travel through the material. In other words, it questions the nature of the interaction between those domains and their impact on charge separation and transport, a key process for device efficiencies, potentially accounting for the better performance of mixed perovskite-based solar cells. In such a context, we wish to decompose our time-series of transient absorbance spectra into a linear combination of the important processes underlying it. Those processes can then be identified, and one can assess their role in the fate of charge carriers within the material. A straightforward way to achieve this is to resort to a global analysis of our time-resolved spectral data, which consists of considering our system as being comprised of independent species, each evolving mono-exponentially. The outcomes of such a global analysis procedure are the decay associated spectra (DAS) of each of the identified processes. By design, each DAS is associated with a time-constant that represents the decay time of the process underlying the spectral signature under consideration.[43]

The results of the global fitting procedure of the data presented in Figure 3-1 are displayed in Figure 3-3. Figure A-1 (Appendix) assesses the fitting quality by displaying it on top of experimental points. For consistence and comparison purposes, both sets of data have been fitted with three exponentials starting 2 ps after pulsed photoexcitation.

When looking at Figure 3-3A, it is clear that the resulting three DAS correspond well to the data from Figure 3-1B, revealing a good fit quality. It also emerges that all three DAS exhibit the oscillatory contribution discussed above, assigned to the presence of CTEs. In addition, the DAS feature a large negative component that describes the photoexcited population itself (decay of the bleaching signal). This feature shifts from 670 nm at 11 ps to 720 nm at 97 ps, to settle at 750 nm at longer time-delays, i.e. 1500 ps. The three DAS can thus be assigned as follows: The 6 ps component involves contributions from the short-time phenomena (bandgap renormalisation and carrier thermalisation), together with the population decay arising from CTE-mediated transfer from a large bandgap (Br-rich) domain to an intermediate bandgap domain. The second DAS (378 ps) represents CTE-mediated transfer from the latter intermediate bandgap domain to the lowest bandgap one. In turn, the last component features the decay of the equilibrium population from the latter composition. We can here be even more specific by assigning those various bandgaps to a given Br/I ratio, within the assumption of a fixed MA, FA proportion or a negligible effect of the cation: In this context, the species at 670 nm, 720 nm and 750 nm correspond to the halide compositions $x = 1.5$, $x = 1$, and $x = 0.5$, respectively.[42] Other intermediate compositions, such as the ones highlighted in Figure 3-2, might exist as well, but are not resolved in this study.

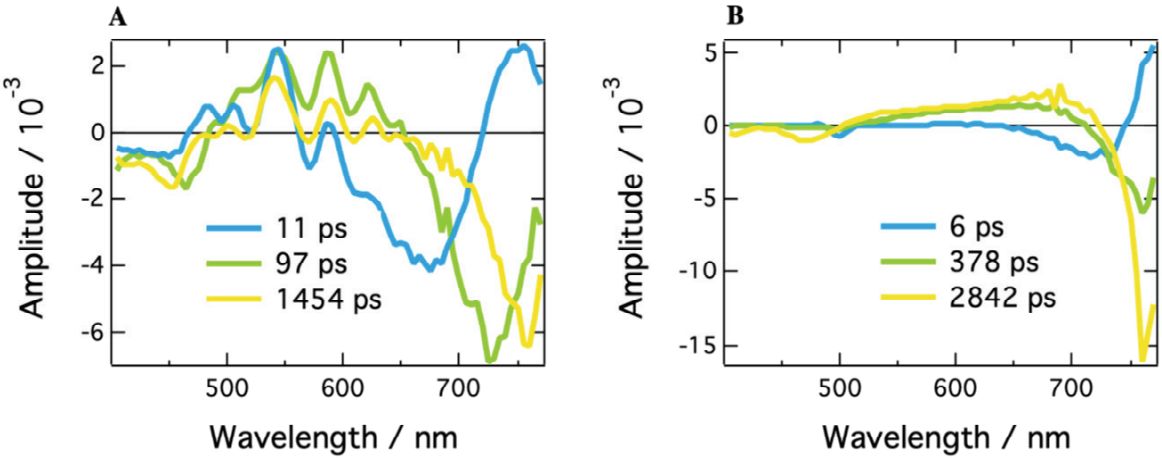

Figure 3-3 Results of the global fitting procedure (tri-exponential): decay associated spectra (DAS). **A.** $MA_yFA_{1-y}PbI_{3-x}Br_x$. Blue: 11 ps, green: 97 ps and yellow: 1454 ps. **B.** $MAPbI_3$. Blue: 6 ps, green: 378 ps and yellow: 2842 ps

Moving to Figure 3-3B, featuring the global analysis result for the standard $MAPbI_3$ perovskite, we see that the three obtained DAS differ significantly from the mixed halide case. Again, the first DAS involves the aforementioned short-time phenomena, while the second and third DAS represent the decay of the photoexcited population via different mechanisms, such as radiative and non-radiative recombination, that cannot be distinguished with our technique.[44] No sign of population transfer is visible, in this case, which is compatible with a homogeneous material.

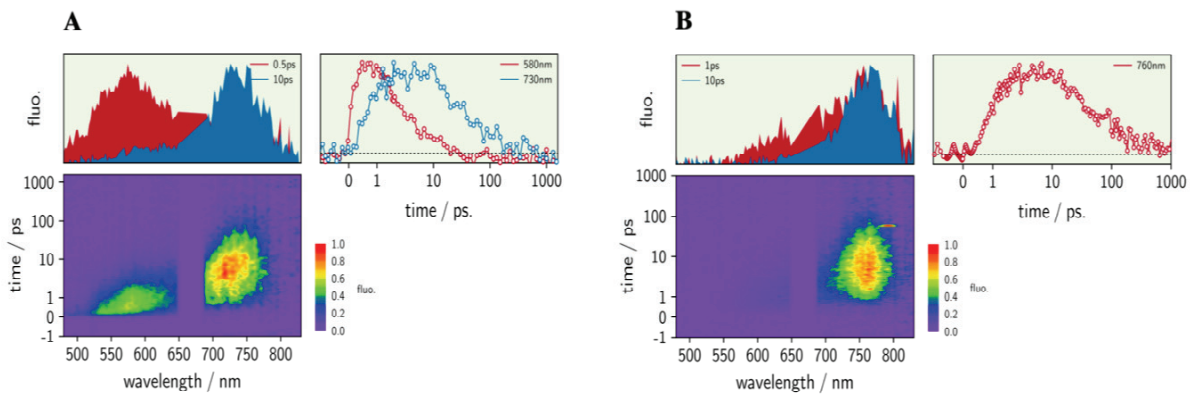

Figure 3-4 Fluorescence up-conversion measurements of insulated thin-films of $MA_yFA_{1-y}PbI_{3-x}Br_x$ upon pulsed photoexcitation at a pump wavelength $\lambda_{ex} = 400$ nm. **A**. Pulse excitation energy: 200 nJ. **B.** Pulse excitation energy: 50 nJ. For both A and B, bottom left panels feature the 3D data, with (normalized) luminescence intensities indicated as a color scale. Top left panels represent spectra at selected times, and top right panels display the dynamics extracted at the maxima of the emission peaks.

To support the conclusion of inter-domain charge transfer in mixed perovskite materials, fluorescence up-conversion measurements at two different excitation energies have been performed on $MA_yFA_{1-y}PbI_{3-x}Br_x$ perovskite films and are displayed in Figure 3-4. Figure 3-4A, featuring the data obtained at the highest excitation energy (200 nJ), shows that the mixed halide perovskite layer exhibits multisite emission, with two peaks centred at 570 and 780 nm, respectively, and generally evolving towards the red. In addition, the dynamics of those peaks

differ but are linked: The 570 nm signal rises quickly (within the instrument response function), and its decay takes place on a timescale that corresponds to the rise of the 780 nm peak. Coexistence of different perovskite compositions, which are interacting within our mixed perovskite layer is evidenced by this shift in emission energy over time.

Figure 3-4B shows the same sample at a lower excitation energy and it emerges that most of the emitted light is here centred at 770 nm, with a greatly reduced contribution from the blue side of the spectrum at early times. This observation is, in turn, compatible with a kinetic competition of the 570 nm emission with another deactivation channel, favoured at lower carrier densities. This particular process is assigned to charge transfer towards smaller bandgap neighbouring domains, in agreement both with the related dynamics in Figure 3-4A and with the global fitting results.

In addition, knowing that the nature of the halide mostly affects the valence band, we state that the carrier under observation in those charge transfers is the hole, and not the electron.[12,45,46] The occurrence of selective hole transfer in mixed perovskite systems, therefore, is likely to play a key role in the enhanced performance of $MA_yFA_{1-y}PbI_{3-x}Br_x$ and other mixed composition PSCs.[1,8,10] Indeed, the ability to selectively transfer a charge carrier across a boundary ensures an efficient charge separation within the perovskite layer, and fewer losses due to trap-assisted recombination that are vertical in the k-space. We know that charge separation indeed occurs, as our samples exhibit good photovoltaic performance. However, the process over which it occurs remains under debate, and has been the topic of numerous studies in the field of bulk heterojunction organic solar cells (BHJ OSC).[47,48,49] Decisive criteria include the electron-hole separation distance (localized or delocalized CTE), as well as the difference between the energy of the hole/electron in the donor moiety and the acceptor moiety (LUMO offset). Indeed, it is suggested that the energy released through the formation of the CTE itself allows for its dissociation later on, through the formation of hot phonons and subsequent transfer to the CTE. This transfer reportedly only occurs if the electron and the hole are delocalized, to an extent depending on the material itself. As a consequence, we suggest that the process of CTE dissociation is favorable in our samples: first, the binding energy of the CTE in PSCs is lower, due to the larger dielectric constant of perovskites compared to molecular systems; the energy offset between the donor and acceptor moieties thus does not need to be large. Second, the larger density of states in semiconductor systems typically allows significant delocalization of the electron-hole pair, rendering the excess energy transfer favorable and allowing the CTE dissociation to occur. Finally, we propose that the subsequent transport of the separated hole occurs through percolation across domains with progressively lower Br^- content.[50,51] This sets the focus on the importance of the optimization of the relative proportion of iodide and bromide domains, as the percolation threshold must be reached for the extraction of charge carriers towards their selective extracting layers to occur. The model proposed here is illustrated by Figure 3-5. Similar transfer processes and their beneficial effects have already been reported for different types of perovskite systems, for example as a cascade transfer between nanoparticles or in the form of photon recycling in thin films.[50-52] In addition, fast hole transfer towards iodide-rich regions in $CsPbI_{3-x}Br_x$ has already been reported and suggested as an aid towards charge separation in $CsPbI_{3-x}Br_x$ PSCs.[53]

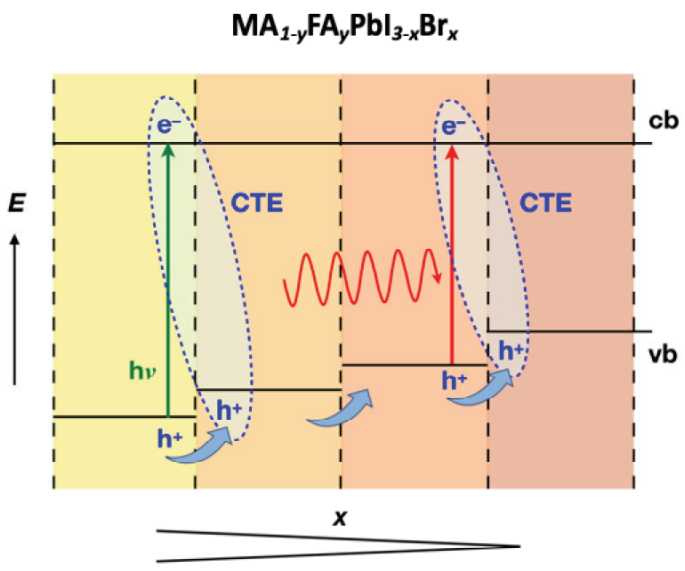

Figure 3-5 Cartoon illustrating domains in the $MA_yFA_{1-y}PbI_{3-x}Br_x$ perovskite, whose bromide content is decreasing from left to right. Charge transfer excitons (CTE) formed at domain boundaries (dashed ellipses) mediate the transport of photogenerated holes in the same direction. CTE formation competes kinetically with energy transfer to narrower bandgap domains (wavy red arrow).

To show that TAS and FLUPS measurements and the conclusions drawn from them are indeed relevant to real functional solar cells, mixed perovskite films prepared exactly in the same conditions were incorporated in devices and their photovoltaic performances compared to those of the standard $MAPbI_3$. JV-curve measurements are presented in the appendix (Figure A-2 and A-3) and the results are summarized in Table 3-1. As expected, mixed perovskite films exhibit a better power conversion efficiency, as well as reduced hysteresis

Perovskite	Scan Direction	J_{sc} (mA cm^{-2})	V_{oc} (V)	*FF*	*PCE* (%)	Light Intensity (mW cm^{-2})
Standard	Backward	-18.24	1.074	0,72	14.42	97.9
	Forward	-18.24	1.072	0,62	12.42	
Mixed	Backward	-18.13	1.088	0,76	15.30	97.9
	Forward	-18.13	1.075	0,73	14.59	

Table 3-1 JV-curve electrochemical characterization of perovskite solar cells. The films were prepared in the same ways as for the spectroscopic measurements. J_{SC} is the short-circuit current density, V_{OC} the open-circuit voltage, *FF* the fill-factor, and *PCE* the incident solar-to-electrical power conversion efficiency.

3.4 Conclusion

Ultrafast transient absorption spectra of thin-films of $MA_yFA_{1-y}PbI_{3-x}Br_x$ appear quite different to those obtained from $MAPbI_3$. Large oscillations are observed for the mixed halide perovskite samples in the visible range. These oscillations are characteristic of a photoinduced transient Stark effect and are fitted by the second derivative of the ground state absorbance spectrum of the material, which features several excitonic bands of domains of various mixed halide composition. The transient Stark signal asserts the formation of permanent dipoles upon photoexcitation, corresponding to charge transfer excitons (CTE) generated astride the boundaries of domains in the bulk of the semiconductor.

A global analysis of transient absorbance data confirms that the mixed halide perovskite films contain heterogeneous domains characterized by different degrees of halide mixing. These exhibit different bandgap energies and excitonic peak positions, assigned to different mixed perovskite stoichiometries. The photogenerated carrier population in each of those domains furthermore undergoes CTE- mediated hole transfer from the largest (Br-rich) to the smallest (I-rich) bandgap domains. This scenario is supported by fluorescence up-conversion measurements of $MA_yFA_{1-y}PbI_{3-x}Br_x$ samples: Multisite emission is observed, assessing the presence of various radiative recombination energies, which confirms the occurrence of hetero-domains with different energetics. Alternatively, at lower excitation density, the main portion of the radiative relaxation occurs at 770 nm, corresponding to the steady-state emission wavelength. This demonstrates the presence of competing deactivation pathways, namely radiative recombination, statistically favoured at high fluence, and charge transfer towards neighbouring domains, dominating at low fluence.

We furthermore suggest that, following their transfer, holes percolate along channels of decreasing bromide content until they reach their selective extracting layer. A random distribution of hetero-domains within the film implies that only a minority of photogenerated carriers are actually concerned by this effect. Still, such a mechanism for selective hole transfer across the active layer enhances the efficiency of charge separation and accounts for the superior performances of mixed halide perovskite systems.

Our observations open the door to specific active layer engineering to achieve an optimum charge separation process. They suggest in particular that a gradient of the halide composition

could be used to selectively drive the holes towards the iodide-rich side placed at the contact of the hole transporting material.

References

(1) Bi, D.; Tress, W.; Dar, M. I.; Gao, P.; Luo, J.; Renevier, C.; Schenk, K.; Abate, A.; Giordano, F.; Correa Baena, J. P.; et al. Efficient Luminescent Solar Cells Based on Tailored Mixed-Cation Perovskites. *Sci. Adv.* **2016**, *2* (1), e1501170–e1501170.

(2) Yang, W. S.; Park, B.-W.; Jung, E. H.; Jeon, N. J.; Kim, Y. C.; Lee, D. U.; Shin, S. S.; Seo, J.; Kim, E. K.; Noh, J. H.; et al. Iodide Management in Formamidinium-Lead-Halide–Based Perovskite Layers for Efficient Solar Cells. *Science* **2017**, *356* (6345), 1376–1379.

(3) Arora, N.; Dar, M. I.; Hinderhofer, A.; Pellet, N.; Schreiber, F.; Zakeeruddin, S. M.; Grätzel, M. Perovskite Solar Cells with CuSCN Hole Extraction Layers Yield Stabilized Efficiencies Greater Than 20%. *Science* **2017**, *358* (6364), 768–771.

(4) Grancini, G.; n-Carmona, C. R. A.; Zimmermann, I.; Mosconi, E.; Lee, X.; Martineau, D.; Narbey, S.; Oswald, F.; De Angelis, F.; Graetzel, M.; et al. One-Year Stable Perovskite Solar Cells by 2D/3D Interface Engineering. *Nat. Commun.* **2017**, *8*, 1–8.

(5) Weller, M. T.; Weber, O. J.; Frost, J. M.; Walsh, A. Cubic Perovskite Structure of Black Formamidinium Lead Iodide, A-[HC(NH 2) 2]PbI 3, at 298 K. *J. Phys. Chem. Lett.* **2015**, *6* (16), 3209–3212.

(6) Niu, T.; Lu, J.; Tang, M.-C.; Barrit, D.; Smilgies, D.-M.; Yang, Z.; Li, J.; Fan, Y.; Luo, T.; McCulloch, I.; et al. High Performance Ambient-Air-Stable FAPbI 3perovskite Solar Cells with Molecule-Passivated Ruddlesden–Popper/3D Heterostructured Film. *Energy Environ. Sci.* **2018**, *11* (12), 3358–3366.

(7) Pellet, N.; Gao, P.; Gregori, G.; Yang, T.-Y.; Nazeeruddin, M. K.; Maier, J.; Grätzel, M. Mixed-Organic-Cation Perovskite Photovoltaics for Enhanced Solar-Light Harvesting. *Angew. Chem. Int. Ed.* **2014**, *53* (12), 3151–3157.

(8) Saliba, M.; Matsui, T.; Seo, J.-Y.; Domanski, K.; Correa-Baena, J.-P.; Nazeeruddin, M. K.; Zakeeruddin, S. M.; Tress, W.; Abate, A.; Hagfeldt, A.; et al. Cesium-Containing Triple Cation Perovskite Solar Cells: Improved Stability, Reproducibility and High Efficiency. *Energy Environ. Sci.* **2016**, *9* (6), 1989–1997.

(9) Park, N.-G.; Grätzel, M.; Miyasaka, T. *Organic- Inorganic Halide Perovskite Photovoltaics*; Grätzel, M., Park, N.-G., Miyasaka, T., Eds.; 2016; pp 1–366.

(10) Saliba, M.; Matsui, T.; Domanski, K.; Seo, J.-Y.; Ummadisingu, A.; Zakeeruddin, S. M.; Baena, J. P. C.; Tress, W.; Abate, A.; Hagfeldt, A.; et al. Incorporation of Rubidium Cations Into Perovskite Solar Cells Improves Photovoltaic Performance. *Science* **2016**, *354* (6309), 206–209.

(11) Sadhanala, A.; Deschler, F.; Thomas, T. H.; Dutton, S. E.; Goedel, K. C.; Hanusch, F. C.; Lai, M. L.; Steiner, U.; Bein, T.; Docampo, P.; et al. Preparation of Single-Phase Films of CH 3NH 3Pb(I 1– xBr X) 3with Sharp Optical Band Edges. *J. Phys. Chem. Lett.* **2014**, *5* (15), 2501–2505.

(12) Yoon, S. J.; Draguta, S.; Manser, J. S.; Sharia, O.; Schneider, W. F.; Kuno, M.; Kamat, P. V. Tracking Iodide and Bromide Ion Segregation in Mixed Halide Lead Perovskites During Photoirradiation. *ACS Energy Lett.* **2016**, *1* (1), 290–296.

(13) Slotcavage, D. J.; Karunadasa, H. I.; McGehee, M. D. Light-Induced Phase Segregation in Halide-Perovskite Absorbers. *ACS Energy Lett.* **2016**, *1* (6), 1199–1205.

(14) Barker, A. J.; Sadhanala, A.; Deschler, F.; Gandini, M.; Senanayak, S. P.; Pearce, P. M.; Mosconi, E.; Pearson, A. J.; Wu, Y.; Srimath Kandada, A. R.; et al. Defect-Assisted Photoinduced Halide Segregation in Mixed-Halide Perovskite Thin Films. *ACS Energy Lett.* **2017**, *2* (6), 1416–1424.

(15) Li, Z.; Yang, M.; Park, J.-S.; Wei, S.-H.; Berry, J. J.; Zhu, K. Stabilizing Perovskite Structures by Tuning Tolerance Factor: Formation of Formamidinium and Cesium Lead Iodide Solid-State Alloys. *Chem. Mater.* **2016**, *28* (1), 284–292.
(16) Amat, A.; Mosconi, E.; Ronca, E.; Quarti, C.; Umari, P.; Nazeeruddin, M. K.; Grätzel, M.; De Angelis, F. Cation-Induced Band-Gap Tuning in Organohalide Perovskites: Interplay of Spin–Orbit Coupling and Octahedra Tilting. *Nano Lett.* **2014**, *14* (6), 3608–3616.
(17) Paraecattil, A. A.; De Jonghe-Risse, J.; Pranculis, V.; Teuscher, J.; Moser, J. E. Dynamics of Photocarrier Separation in MAPbI 3Perovskite Multigrain Films Under a Quasistatic Electric Field. *J. Phys. Chem. C* **2016**, *120* (35), 19595–19602.
(18) Teuscher, J.; Brauer, J. C.; Stepanov, A.; Solano, A.; Boziki, A.; Chergui, M.; Wolf, J.-P.; Rothlisberger, U.; Banerji, N.; Moser, J. E. Charge Separation and Carrier Dynamics in Donor-Acceptor Heterojunction Photovoltaic Systems. *Structural Dynamics* **2017**, *4* (6), 061503–061528.
(19) Baena, J. P. C.; Steier, L.; Tress, W.; Saliba, M.; Neutzner, S.; Matsui, T.; Giordano, F.; Jacobsson, T. J.; Kandada, A. R. S.; Zakeeruddin, S. M.; et al. Highly Efficient Planar Perovskite Solar Cells Through Band Alignment Engineering. *Energy Environ. Sci.* **2015**, *8* (10), 2928–2934.
(20) Giordano, F.; Abate, A.; Baena, J. P. C.; Saliba, M.; Matsui, T.; Im, S. H.; Zakeeruddin, S. M.; Nazeeruddin, M. K.; Hagfeldt, A.; Graetzel, M. Enhanced Electronic Properties in Mesoporous TiO2 via Lithium Doping for High-Efficiency Perovskite Solar Cells. *Nat. Commun.* **1AD**, *7*, 1–6.
(21) Gerecke, M.; Bierhance, G.; Gutmann, M.; Ernsting, N. P.; Rosspeintner, A. Femtosecond Broadband Fluorescence Upconversion Spectroscopy: Spectral Coverage Versus Efficiency. *Review of Scientific Instruments* **2016**, *87* (5), 053115–053116.
(22) Stamplecoskie, K. G.; Manser, J. S.; Kamat, P. V. Dual Nature of the Excited State in Organic–Inorganic Lead Halide Perovskites. *Energy Environ. Sci.* **2014**, *8* (1), 208–215.
(23) deQuilettes, D. W.; Vorpahl, S. M.; Stranks, S. D.; Nagaoka, H.; Eperon, G. E.; Ziffer, M. E.; Snaith, H. J.; Ginger, D. S. Impact of Microstructure on Local Carrier Lifetime in Perovskite Solar Cells. *Science* **2015**, *348* (6235), 683–686.
(24) Manser, J. S.; Reid, B.; Kamat, P. V. Evolution of Organic–Inorganic Lead Halide Perovskite From Solid-State Iodoplumbate Complexes. *J. Phys. Chem. C* **2015**, *119* (30), 17065–17073.
(25) Long-Range Balanced Electron- and Hole-Transport Lengths in Organic-Inorganic CH NH PbI. **2015**, 1–5.
(26) Piatkowski, P.; Cohen, B.; Javier Ramos, F.; Di Nunzio, M.; Nazeeruddin, M. K.; Grätzel, M.; Ahmad, S.; Douhal, A. Direct Monitoring of Ultrafast Electron and Hole Dynamics in Perovskite Solar Cells. *Phys. Chem. Chem. Phys.* **2015**, *17* (22), 14674–14684.
(27) Price, M. B.; Butkus, J.; Jellicoe, T. C.; Sadhanala, A.; Briane, A.; Halpert, J. E.; Broch, K.; Hodgkiss, J. M.; Friend, R. H.; Deschler, F. Hot-Carrier Cooling and Photoinduced Refractive Index Changes in Organic&Ndash;Inorganic Lead Halide Perovskites. *Nat. Commun.* **2015**, *6*, 1–8.
(28) Xing, G.; Mathews, N.; Sun, S.; Lim, S. S.; Lam, Y. M.; Yeng; Grätzel, M.; Mhaisalkar, S.; Sum, T. C. Long-Range Balanced Electron- and Hole-Transport Lengths in Organic-Inorganic $CH_3Nh_3PbI_3$. *Science* **2013**, *342*, 344–347.
(29) Trinh, M. T.; Wu, X.; Niesner, D.; Zhu, X. Y. Many-Body Interactions in Photo-Excited Lead Iodide Perovskite. *J. Mater. Chem. A* **2015**, *3* (17), 9285–9290.

(30) Roiati, V.; Mosconi, E.; Listorti, A.; Colella, S.; Gigli, G.; De Angelis, F. Stark Effect in Perovskite/TiO 2Solar Cells: Evidence of Local Interfacial Order. *Nano Lett.* **2014**, *14* (4), 2168–2174.
(31) Koutselas, I. B.; Ducasse, L.; Papavassiliou, G. C. Electronic Properties of Three- and Low-Dimensional Semiconducting Materials with Pb Halide and Sn Halide Units. *J. Phys.: Condens. Matter* **1996**, *8*, 1217–1227.
(32) Tanaka, K.; Takahashi, T.; Ban, T.; Kondo, T.; Uchida, K.; Miura, N. Comparative Study on the Excitons in Lead-Halide-Based Perovskite-Type Crystals $CH_3Nh_3PbBr_3$ $Ch_3Nh_3PbI_3$. *Solid State Commun.* **2003**, *127* (9-10), 619–623.
(33) Savenije, T. J.; Ponseca, C. S., Jr.; Kunneman, L.; Abdellah, M.; Zheng, K.; Tian, Y.; Zhu, Q.; Canton, S. E.; Scheblykin, I. G.; Pullerits, T.; et al. Thermally Activated Exciton Dissociation and Recombination Control the Carrier Dynamics in Organometal Halide Perovskite. *J. Phys. Chem. Lett.* **2014**, *5* (13), 2189–2194.
(34) Saba, M.; Quochi, F.; Mura, A.; Bongiovanni, G. Excited State Properties of Hybrid Perovskites. *Acc. Chem. Res.* **2015**, 166–173.
(35) Miyata, A.; Mitioglu, A.; Plochocka, P.; Portugall, O.; Wang, J. T.-W.; Stranks, S. D.; Snaith, H. J.; Nicholas, R. J. Direct Measurement of the Exciton Binding Energy and Effective Masses for Charge Carriers in Organic–Inorganic Tri-Halide Perovskites. *Nat. Phys.* **2015**, *11* (7), 582–587.
(36) Soufiani, A. M.; Huang, F.; Reece, P.; Sheng, R.; Ho-Baillie, A.; Green, M. A. Polaronic Exciton Binding Energy in Iodide and Bromide Organic-Inorganic Lead Halide Perovskites. *Appl. Phys. Lett.* **2015**, *107* (23), 231902–231906.
(37) Yang, Y.; Yang, M.; Li, Z.; Crisp, R.; Zhu, K.; Beard, M. C. Comparison of Recombination Dynamics in $CH_3Nh_3PbBr_3$ And $CH_3Nh_3PbI_3$ Perovskite Films: Influence of Exciton Binding Energy. *J. Phys. Chem. Lett.* **2015**, 4688–4692.
(38) Galkowski, K.; Mitioglu, A.; Miyata, A.; Plochocka, P.; Portugall, O.; Eperon, G. E.; Wang, J. T.-W.; Stergiopoulos, T.; Stranks, S. D.; Snaith, H. J.; et al. Determination of the Exciton Binding Energy and Effective Masses for Methylammonium and Formamidinium Lead Tri-Halide Perovskite Semiconductors. *Energy Environ. Sci.* **2016**, 1–9.
(39) Ziffer, M. E.; Mohammed, J. C.; Ginger, D. S. Electroabsorption Spectroscopy Measurements of the Exciton Binding Energy, Electron–Hole Reduced Effective Mass, and Band Gap in the Perovskite CH 3NH 3PbI 3. *ACS Photonics* **2016**, *3* (6), 1060–1068.
(40) Sestu, N.; Cadelano, M.; Sarritzu, V.; Chen, F.; Marongiu, D.; Piras, R.; Mainas, M.; Quochi, F.; Saba, M.; Mura, A.; et al. Absorption F-Sum Rule for the Exciton Binding Energy in Methylammonium Lead Halide Perovskites. *J. Phys. Chem. Lett.* **2015**, *6* (22), 4566–4572.
(41) Lanzani, G. The Photophysics Behind Photovoltaics and Photonics. **2012**, 1–4.
(42) Jacobsson, T. J.; Correa-Baena, J.-P.; Pazoki, M.; Saliba, M.; Schenk, K.; Grätzel, M.; Hagfeldt, A. Exploration of the Compositional Space for Mixed Lead Halogen Perovskites for High Efficiency Solar Cells. *Energy Environ. Sci.* **2016**, *9* (5), 1706–1724.
(43) van Stokkum, I. H. M.; Larsen, D. S.; van Grondelle, R. Global and Target Analysis of Time-Resolved Spectra. *Biochim. Biophys. Acta, Bioenerg.* **2004**, *1657* (2-3), 82–104.
(44) Grancini, G.; Kandada, A. R. S.; Frost, J. M.; Barker, A. J.; De Bastiani, M.; Gandini, M.; Marras, S.; Lanzani, G.; Walsh, A.; Petrozza, A. Role of Microstructure in the Electron-Hole Interaction of Hybrid Lead Halide Perovskites. *Nat. Photon.* **2015**, *9* (10), 695–701.

(45) Brivio, F.; Butler, K. T.; Walsh, A.; van Schilfgaarde, M. Relativistic Quasiparticle Self-Consistent Electronic Structure of Hybrid Halide Perovskite Photovoltaic Absorbers. *Phys. Rev. B* **2014**, *89* (15), 155204–155206.
(46) Even, J.; Pedesseau, L.; Katan, C.; Kepenekian, M.; Lauret, J.-S.; Sapori, D.; Deleporte, E. Solid-State Physics Perspective on Hybrid Perovskite Semiconductors. *J. Phys. Chem. C* **2015**, *119* (19), 10161–10177.
(47) Devižis, A.; De Jonghe-Risse, J.; Hany, R.; Nüesch, F.; Jenatsch, S.; Gulbinas, V.; Moser, J. E. Dissociation of Charge Transfer States and Carrier Separation in Bilayer Organic Solar Cells: a Time-Resolved Electroabsorption Spectroscopy Study. *J. Am. Chem. Soc.* **2015**, *137* (25), 8192–8198.
(48) Ono, S.; Ohno, K. Origin of Charge Transfer Exciton Dissociation in Organic Solar Cells. In *Excitons*; InTech, 2018; pp 1–14.
(49) Singh, J. Dissociation of Charge Transfer Excitons at the Donor–Acceptor Interface in Bulk Heterojunction Organic Solar Cells. *Journal of Materials Science: Materials in Electronics* **2017**, *28* (10), 7095–7099.
(50) Gratia, P.; Grancini, G.; Audinot, J.-N.; Jeanbourquin, X.; Mosconi, E.; Zimmermann, I.; Dowsett, D.; Lee, Y.; Grätzel, M.; De Angelis, F.; et al. Intrinsic Halide Segregation at Nanometer Scale Determines the High Efficiency of Mixed Cation/Mixed Halide Perovskite Solar Cells. *J. Am. Chem. Soc.* **2016**, *138* (49), 15821–15824.
(51) Bouduban, M. E. F.; Burgos-Caminal, A.; Ossola, R.; Teuscher, J.; Moser, J. E. Energy and Charge Transfer Cascade in Methylammonium Lead Bromide Perovskite Nanoparticle Aggregates. *Chem. Sci.* **2017**, *00* (6), 1–10.
(52) Pazos-Outòn, L. M.; Szumilo, M.; Lamboll, R.; Richter, J. M.; Crespo-Quesada, M.; Abdi-Jalebi, M.; Beeson, H. J.; Vrućinić, M.; Alsari, M.; Snaith, H. J.; et al. Photon Recycling in Lead Iodide Perovskite Solar Cells. *Science* **2016**, *351* (6280), 1430–1433.
(53) Hoffman, J. B.; Schleper, A. L.; Kamat, P. V. Transformation of Sintered CsPbBr 3Nanocrystals to Cubic CsPbI 3and Gradient CsPbBr xI 3– Xthrough Halide Exchange. *J. Am. Chem. Soc.* **2016**, *138* (27), 8603–8611.

4 Unravelling Interfacial processes in mixed anion, mixed cation perovskite solar cells

4.1 Introduction

As mentioned numerous times before, and as will be mentioned numerous times after, hybrid lead halide perovskites (HOIPs) hold great promise in the context of efficient and potentially cheap solar cells. In the past years, efforts have been directed both towards the improvement of the perovskite active layer itself (the emergence of mixed halide, mixed cation perovskites) and towards an optimization of the device architectures (*vide supra*). Indeed, the main limiting factor towards high efficiencies in PSCs is charge recombination via defect states.[1,2] Because 3D HOIPs exhibit charge carrier lifetimes and diffusion lengths exceeding the typical thickness of a perovskite layer within a device, it is reasonable to assume that most photovoltaic losses occur at the interfaces with electron-transporting and hole-transporting layers (ETL and HTL respectively). Interfaces are indeed never perfect, due to unwanted chemical interactions and/or physical inhomogeneities arising from the deposition method.[3] Within a device, interfaces are thus considered as the determining factor for the open-circuit voltage (V_{OC}), and sometimes deemed responsible for the well-known I-V hysteresis in PSCs, when interfacial charge accumulation occurs.[4-7] For instance, several reports have demonstrated the tendency of electrons to accumulate at the perovskite/ETL interface, contrarily to the perovskite/HTL interface, for various metal oxides.[4,8-10]

Because of their significant consequences on solar cell efficiencies, understanding the physics at interfaces within PSCs is a key towards smart device design, both in terms of efficiency and stability. Although numerous methods exist that characterize the structure of interfaces, addressing the behavior and dynamics of photocarriers is a tricky endeavor. A method of choice in this context is impedance spectroscopy, which characterizes the frequency dependent impedance of a system via the application of a sinusoidal AC voltage. Subsequent analysis by means of equivalent circuit modelling sheds light on both bulk (conductivity) and interfacial properties (capacitance).[11,12] This method however exhibits a limited time-resolution, and rarely yields unambiguous interpretations and assignments.[13]
Herein, we present a novel way to assess the nature of the photocarriers at solid interfaces and their dynamics following injection using femtosecond transient absorbance (TA) spectroscopy. In particular, we describe an experimental scheme that elucidates the main factor limiting charge collection at the electrodes (injection versus transport across the ETL/HTL), and demonstrate it for well-known interfaces: perovskite/spiro-OMeTAD and SnO_2/perovskite. In more detail, we exploit the exponential attenuation of light when it crosses a material to disentangle bulk from interfacial phenomena in the TA signal. The illumination-face dependence of the TA signal coupled with a thorough analysis of the photoinduced electroabsorption signal, which is very clear in mixed halide, mixed cation systems, sheds light on the injection process.[14] Subsequent anisotropic transient absorbance measurements determine the amplitude of the interfacial built-in field, and thus, the tendency of charges to

accumulate at or close to the interface. We show that, due to the amorphous nature of ALD-deposited SnO_2, electron transfer is mediated by the formation of charge-transfer excitons, limiting the rate of charge transfer and yielding interfacial charge accumulation, in accordance with literature.[15,16] We then confirm the ultrafast hole injection in doped state-of-the-art spiro-OMeTAD and exploit the effect of additives in limiting charge accumulation to prove the ability of our experimental scheme to fully characterize the interface dynamics in PSCs.

4.2 Methods

4.2.1 Samples

The samples under consideration here are thin-films of mixed cation (MA^+, FA^+), mixed anion (Br^-, I^-) lead halide perovskites, with the following initial stoichiometry of the solution reactant: $MA_{0.15}FA_{0.85}PbI_{2.55}Br_{0.45}$. However, as the final composition of the material after crystallization is not precisely determined and yields domains with varying bromide concentration, the material under study here will be called $MA_yFA_{1-y}PbI_{3-x}Br_x$. or "mixed perovskite".

The samples were prepared according to previously reported protocols with the exception of the concentration of the perovskite precursor solution, which was kept at 0.7 M in order to obtain a thinner layer of the absorber material to facilitate the optical measurements.[17,18]

4.2.2 TA measurements

Ultrafast transient absorption data for $MA_xFA_{1-x}PbI_yBr_{3-y}$ were acquired using femtosecond pump-probe spectroscopy with the same laser source as described in chapter 3 (sect. 3.2.3). The 475 nm pump beam was obtained by directing the CPA output into a non-collinear parametric amplifier (NOPA), with subsequent compression to ~43 fs FWHM with a pair of SF10 prisms. The pump fluences at the sample were 120 $\mu J \cdot cm^{-2}$ and 200 $\mu J \cdot cm^{-2}$. The white light continuum (WLC) probe beam (400-780 nm) was obtained in a manner similar to that described in sect. 3.2.3 . The polarization of the pump compared to the probe beam was set with a $\lambda/2$ waveplate: for the anisotropy measurements, the pump polarization was alternatively set parallel (0°) or perpendicular (90°) with respect to the probe polarization. A satisfying signal-to-noise ratio was obtained by averaging 6000 spectra, with a time-resolution of 110 fs.

4.3 Results and discussion

As stated in chapter 1 (sect. 1.1.2), when light crosses a material, it undergoes an exponential attenuation (Beer-Bouguer law). As a consequence, when two materials exhibiting different optical properties are interfaced, charges can be selectively photogenerated close or away from this interface by controlling which layer first interacts with the excitation light (illumination-side dependence), as illustrated in Figure 4-1A. This is useful to disentangle interfacial from bulk processes, and is applied here to study the perovskite/spiro-OMeTAD and the

SnO_2/perovskite interfaces via two half-cells (H-spiro and H-SnO_2 respectively). We obtain four different samples (Figure 4-1B): front-face (1) and back-face (2) illumination for H-SnO_2, and front-face (3) and back-face illumination (4) for H-spiro.

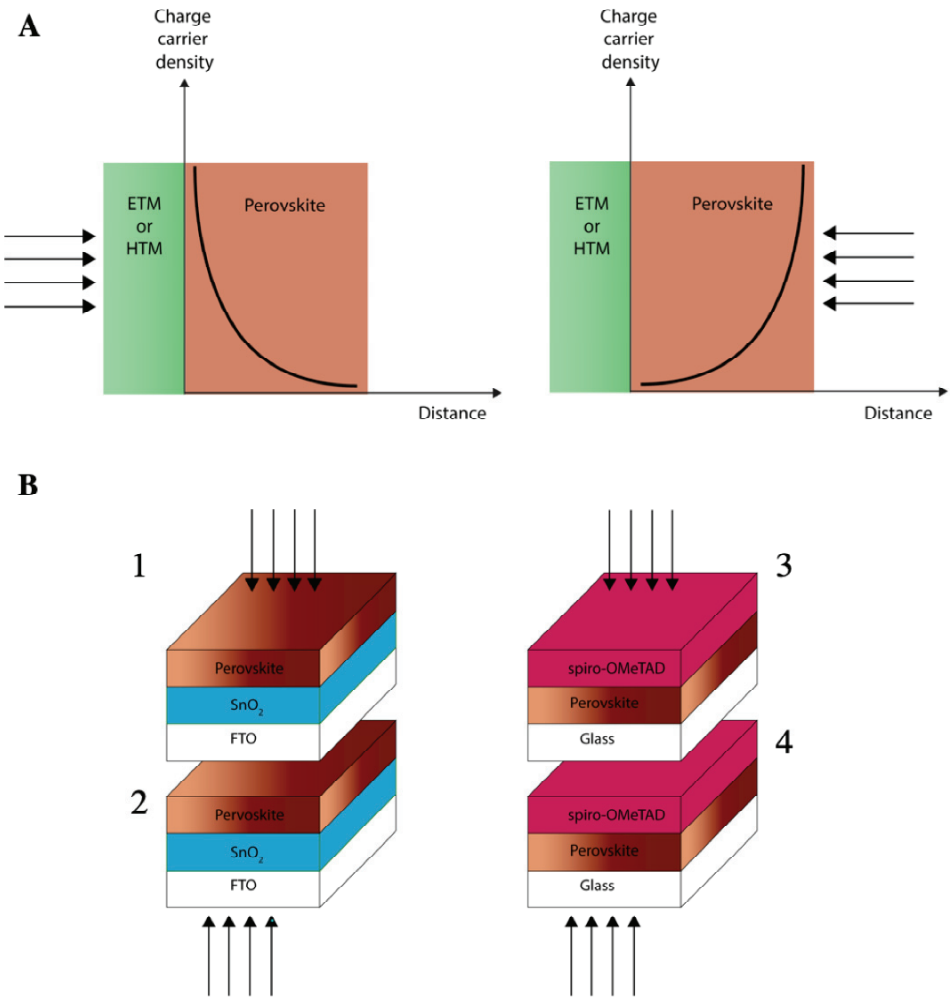

Figure 4-1 A. Illumination-face dependence of the charge carrier distribution. Left: photocarriers are generated mostly at the interface with the ETM or HTM. Right: photocarriers are created in the bulk of the perovskite. **B.** The four samples under study: (1) Front-face illumination within H-SnO_2. (2) Back-face illumination within H-SnO_2. (3) Front-face illumination within H-Spiro. (4) Back-face illumination within H-Spiro.

4.3.1 Illumination-face dependent TA data

Figure 4-2 displays the TA spectra of $MA_yFA_{1-y}PbI_{3-x}Br_x$. at 5 ps, recorded at $\lambda_{ex} = 475$ nm for all four samples of interest (1-4, see Figure 4-1). All samples exhibit a similar signal: A large GSB + SE feature in the red (peaking at 745 nm), and a broad ESA in the 500-630 nm region, still lacking a definitive assignment.[19-21] More interestingly, a series of oscillations spanning the same wavelength region is observable for the four samples, although with different amplitudes and central wavelengths. As discussed in chapter 3 (sect. 3.3), this type of oscillation is assigned to a photoinduced electroabsorption (PEA).[14,22,23]

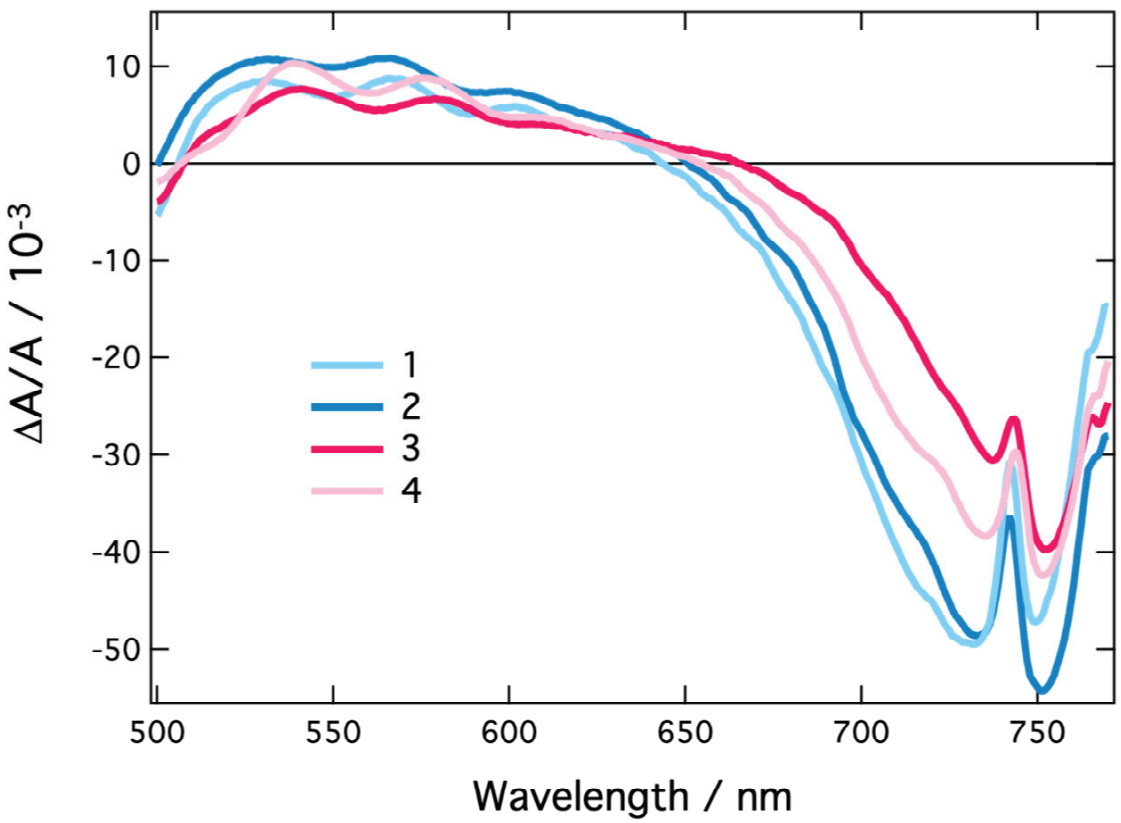

Figure 4-2 TA spectra at a time delay of 5 ps. Data recorded at λ_{ex} = 475 nm and at a fluence of 200 μJ cm^{-2}. The amplitude of each spectrum has been normalized with respect to its absorptance at the excitation wavelength.

Electroabsorption signals, if properly analyzed, provide a clear picture of the degree of correlation and the type of the photocarriers in the sample under consideration, as described in chapter 2 (sect. 2.2). Although the weak carrier correlation in pure $MAPbI_3$ perovskites classify them as continuum-type systems (low field FKA effect), the presence of bromide in their mixed counterpart changes the picture, as already extensively discussed in chapter 3 (sect.3.3).[24] For instance, an increase of the bimolecular and Auger recombination rates with increasing bromide/iodide ratio was reported.[25] Similarly, systematic blue shifts of both the band gap and the photoluminescence maximum of mixed cation, mixed halide perovskites was shown to occur with increasing bromide proportion at the X site.[26] These observations confirm the stronger excitonic character of mixed cation, mixed halide perovskites, allowing us to consider that their PEA signal involves a large contribution from the Stark effect which can be modelled accordingly.

We fitted the oscillations reported in Figure 4-2 with a function describing the linear combination of the first and second derivatives of the absorption spectra of the various samples of interest (see chapter 2, sect. 2.2.4). The resulting fits, together with the corresponding derivatives, are displayed in Figure 4-3. The overlap of the fits and the experimental TA spectra are shown in the insets.

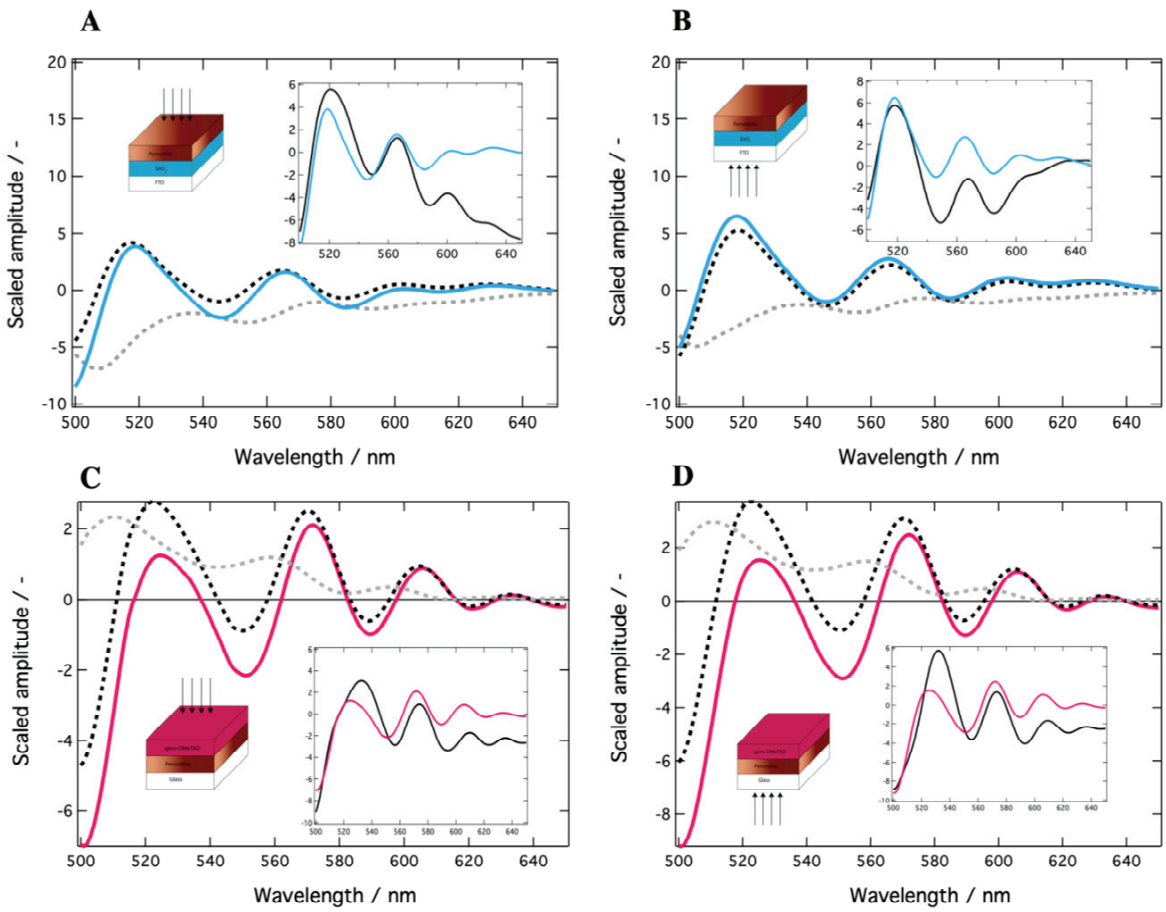

Figure 4-3 Evaluation of the dominant contribution towards the photoinduced electroabsorption signal within the Stark model**.** The best fits (blue or pink lines) are represented with their corresponding absorbance spectrum first- (grey dotted lines) and second (black dotted lines) derivatives. Insets feature the best fits with the corresponding experimental data. **A.** Front-face illumination of H-SnO_2 (sample (1); carriers are generated in the bulk). **B.** Back-face illumination of H-SnO_2 (sample (2); carriers are generated at the interface). **C.** Front-face illumination of H-Spiro (sample (3); carriers at the interface). **D.** Back-face illumination of H-Spiro (sample (4); carriers in the bulk).

For a facilitated understanding of Figure 4-3, we define $B = b_2/b_1$ the ratio between the resulting amplitudes of the second (b_2) and first derivative (b_1), summarized in Table 4-1. We present two close-lying fluences (120 versus 200 μJ cm^{-2}), which correspond to an optimized signal for H-SnO_2 and H-Spiro respectively.

Sample	B ratios [120 μJ cm^{-2}]	B ratios [200 μJ cm^{-2}]
1	60 ± 13	55 ±14
2	113 ± 52	116 ± 68
3	44 ± 9	30 ± 6
4	65 ± 23	51 ±15

Table 4-1 Ratios of the amplitude of the first (b_1) and second (b_2) derivatives of the linear absorbance spectrum for the fitted PEA signal ($B=b_2/b_1$).

For all samples, B > 1, which indicates a predominant second derivative contribution to the PEA signal. As stated in chapters 2 and 3, the PEA of isotropic samples exhibits significant second-derivative amplitudes if, and only if, a large population of charge-transfer (CT) excitons

is involved. The four samples under considerations thus harbor CT excitons when photoexcited. More interestingly, the B ratios converge around the same values of 50-60, with two exceptions: Lower for sample 3 (front-face illumination within H-Spiro), and twice as large in the case of sample 1 (back-face illumination of H-SnO_2).
From those observations, it emerges that the distribution of charge carriers has the strongest impact on the lineshape of the PEA signal. When most charges are generated away from the interface, B is virtually the same, independent of the nature of the interface (SnO_2/perovskite or perovskite/Spiro-OMeTAD). In this case, B describes the presence of CT excitons in the bulk of the system, at the interfaces between domains with different bromide content, as expected (see chapter 3). Alternatively, when the majority of carriers are generated close to an interface, B is significantly drawn away from the bulk values: lower within the H-Spiro half-cell, and larger within H-SnO_2. CT excitons, or absence thereof, hence play a significant role in the device interface physics.

4.3.2 Perovskite/SnO_2 interface

The spontaneous formation of CT excitons when photocarriers reach the SnO_2/perovskite interface is likely to impact the rate and yield of electron injection towards the ETL. Indeed, if transferred electrons are free from any interaction with an interfacial hole, they are expected to quickly diffuse away from the interface, provided that the mobility of the considered ETL is large enough, as is the case for SnO_2.[17] Alternatively, when the transfer is majorly mediated by the formation of CT excitons, the injection rate is slowed down: First, the number of interfacial states being able to accommodate CT excitons is limited; second, for the electron to diffuse away, it has to escape the Coulombic trap retaining it at the interface.

To determine whether the formation of CT excitons is the main limiting factor in the charge transfer process (and not the charge mobility within the ETL), we use the dependence of the interfacial built-in field on the density of electrons and holes lying at or close to the interface: We expect it to be large if, after escaping the coulomb interaction to their holes, the electrons remain in close proximity (charge accumulation); alternatively, it should be weak if electrons quickly move away upon dissociation of the interfacial CT exciton. We moreover propose that, in a reasonably close vicinity of the interface of interest, both the bulk CT excitons, previously demonstrated, and the free carriers embody a good probe of the amplitude of the interfacial built-in field. In the case of significant internal electric fields, we indeed expect the perovskite layer to be polarized in the area directly adjacent to the interface, with preferential formation of dipoles oriented in the field, and preferential electron and hole localization. This would cause a strong optical anisotropy within the sample, visible via photoselection by a controlled (perpendicular or parallel) polarization of the pump beam with respect to the probe (anisotropic transient absorbance). The dynamics resulting from this experimental scheme are displayed in Figure 4-4, together with the calculated anisotropy signal (see chapter 2, sect. 2.1.2). Note that we present dynamic traces predominantly corresponding to the PEA (520 nm; Figure 4-4A) and GSB signals (750 nm; Figure 4-4B), to ensure that our findings are homogeneously reflected by the various species present in our system. The data have been recorded at $\lambda_{ex} = 475$ nm and at a fluence of 120 $\mu J\ cm^{-2}$.

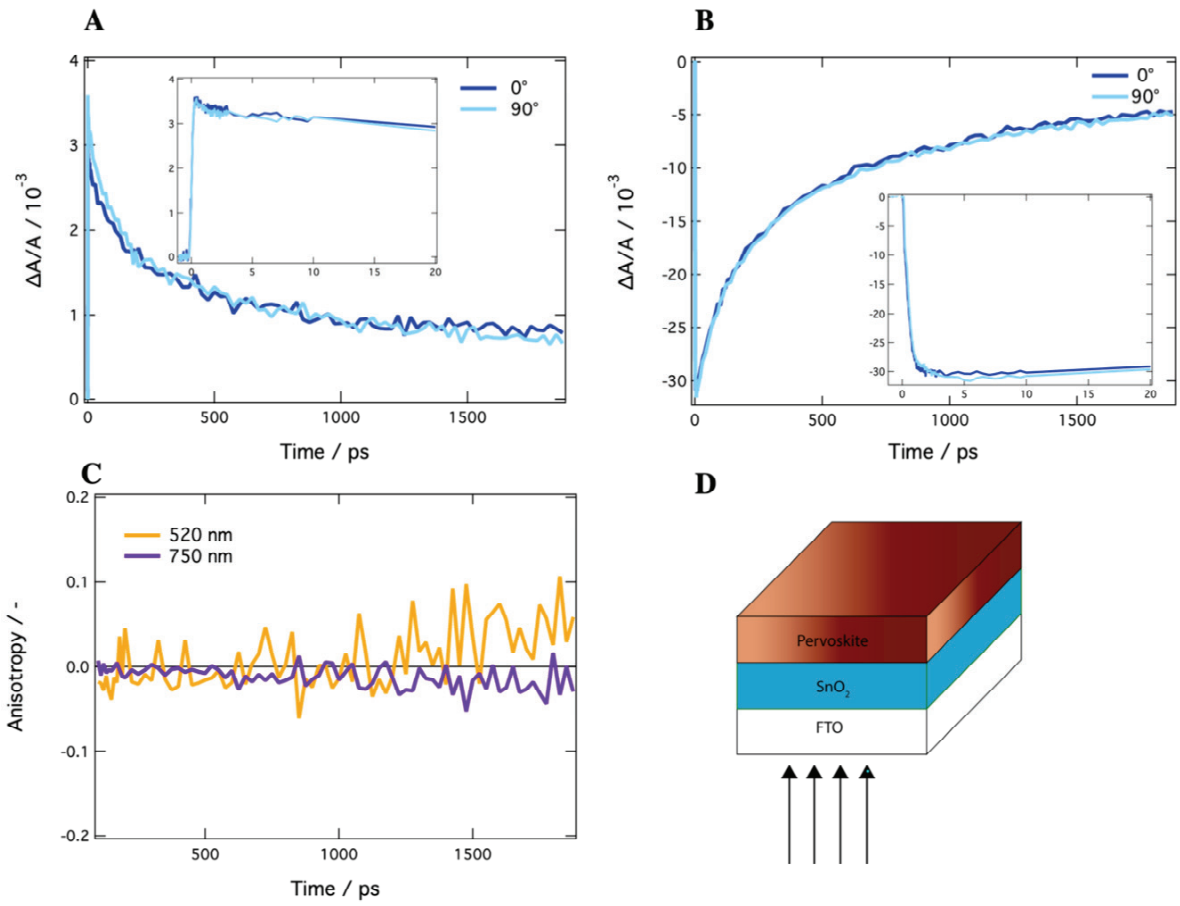

Figure 4-4 Anisotropic transient absorbance for H-SnO_2, recorded at λ_{ex} = 475 nm and at a fluence of 120 μJ cm^{-2}. **A.** PEA signal (520 nm). **B.** GSB signal (750 nm). **C.** Anisotropy at 520 and 750 nm, calculated as described in chapter 2. **D.** Sample under study.

Clearly, both early- and long-time transient absorbance signals are virtually the same for a given illumination side, irrespective of the relative pump-probe polarization angle. This is faithfully reflected in Figure 4-4C, where the anisotropy remains null throughout the time-window of the measurement. This suggests that the perovskite is not subjected to a sensible, macroscopic electric field yielding a preferential carrier localization and dipole orientation. Due to this absence of charge accumulation, we deduce that (i) the number of available states for CT excitons is likely small and (ii) that the formation of CT excitons is indeed the limiting factor towards charge injection. In the context of solar cells, such a slowed-down injection is detrimental, as it increases the recombination probability, decreasing both the V_{OC} and fill factor (FF). We however tie this particular interfacial physics with the fabrication method of our samples: In the present case, SnO_2 has been deposited by atomic layer deposition (ALD), which generates mostly amorphous layers.[14,26-28] The resulting defects generate supplementary energy levels capable of trapping the injected electrons near the heterojunction. These electrons then interact with the holes within the perovskite that are close to the interface, forming the CT excitons. This assumption is confirmed by addressing the performance of ETLs fabricated with methods yielding crystalline SnO_2: First, several studies indeed report better solar cell efficiencies in the presence of a crystalline SnO_2 extraction layer.[15,16] Second, works describing the properties of doped (Nb^+, Li^+) versus intrinsic SnO_2 also claim to obtain better photovoltaic

performance, assigned to an enhanced electron extraction arising from a decreased trap density within the ETM layer.[27-29]

4.3.3 Perovskite/spiro-OMeTAD interface

The injection at the perovskite/spiro-OMeTAD interface has been shown to occur on an ultrafast timescale, with no sign of charge accumulation.[30,31] Our work further confirms this tendency.

As stated earlier, when the majority of carriers are created close to the interface, B is weaker than in the opposite case (see Table 4-1). Following the same reasoning as above, this translates into a smaller second-derivative contribution to the PEA signal, and into a smaller number of CT excitons for interfacial compared to bulk excitation (samples 3 and 4 in Figure 4-1). It follows that charges generated close to the interface are quickly injected into the spiro-OMeTAD layer, preventing the formation of CT excitons.

To complete the picture and address the fate of holes after injection, we probe their propensity to accumulate close to the interface by again resorting to the anisotropic transient absorbance spectroscopy measurements. Figure 4-5A and B present the individual polarization-dependent spectra for interfacial excitation of the H-Spiro sample (sample 3 in Figure 4-1), extracted at 520 nm (dominated by the PEA signal) and at 750 nm (GSB of the perovskite). In contrast to the case of H-SnO_2, the dynamics, although evolving over similar timescales, display different amplitudes from early times onwards (see insets). This is further confirmed by the time-dependent anisotropy reconstructed for both wavelengths and featured in Figure 4-5C: The resulting traces show an almost constant, small, positive amplitude.

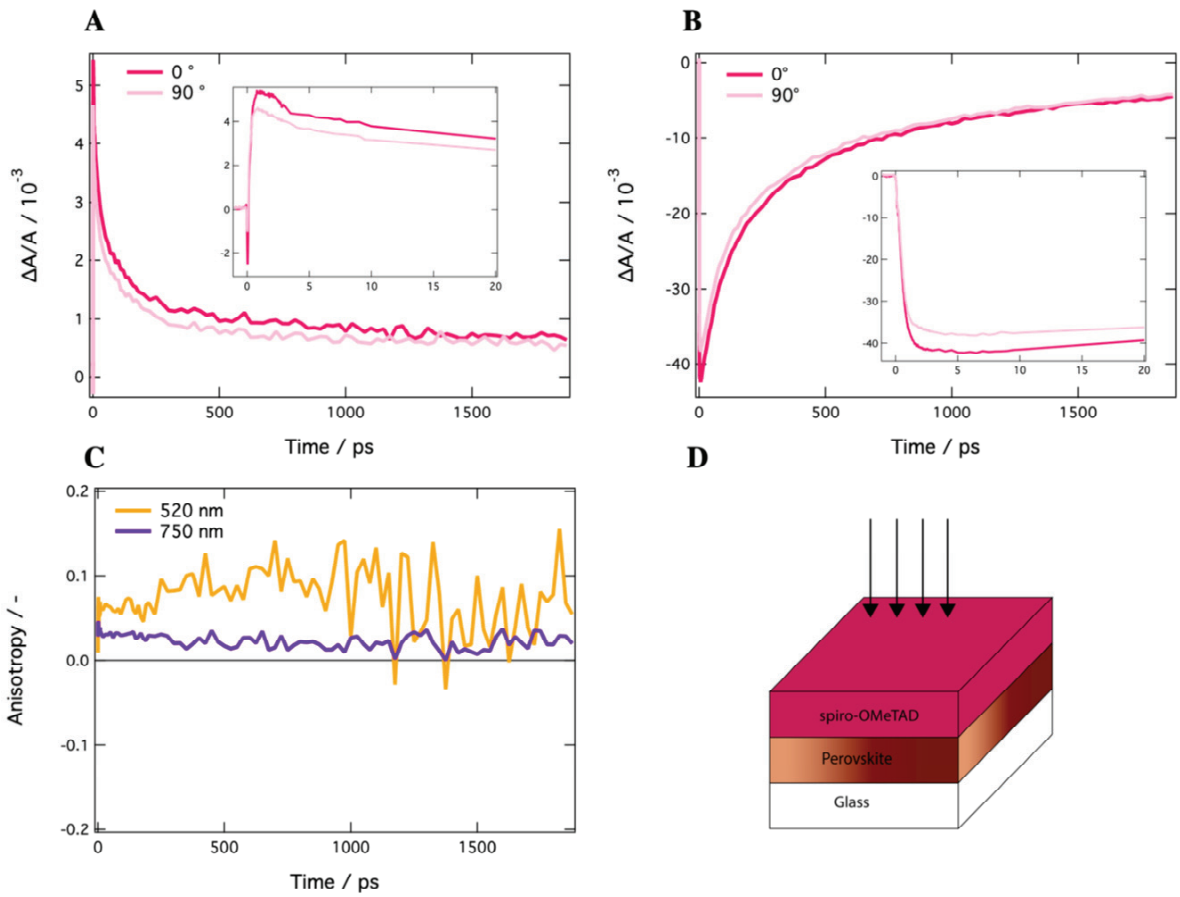

Figure 4-5 Anisotropic transient absorbance for H-Spiro, recorded at λ_{ex} = 475 nm and at a fluence of 200 μJ cm^{-2}. **A.** PEA signal (520 nm). **B.** GSB signal (750 nm). **C.** Anisotropy at 520 and 750 nm, calculated as described in chapter 2. **D.** Sample under study.

The photogenerated carriers in the sample thus exhibit a preferential orientation/localization: A sensible built-in electric field is present close to the interface, attesting that charges accumulate. In addition, because the optical anisotropy appears instantaneously, charge injection is further confirmed to occur on a sub-ps timescale. From these observations, we state that the mobility of the holes within the spiro-OMeTAD layer is the main limiting factor towards an optimized functioning of perovskite devices.[32] This is of course already known, as modifying spiro-OMeTAD with additives quickly emerged as an efficient way to boost solar cell effiencies, from dye-sensitized to perovskite solar cells.[35-37] The best recipe to date, in the context of PSCs, is a mixture of LiTFSI, tBP and CoTFSI: These have been shown to synergically induce a larger charge carrier mobility in spiro-OMeTAD, and prevent interfacial recombination (to some extent).[36,38]

4.3.4 Hypothesis confirmation: charge accumulation in doped vs undoped spiro-OMeTAD HTM

As a consequence, we now focus on a last set of samples, to prove the relevance of our experimental scheme in unravelling interfacial properties within PSCs. These consisted of a perovskite layer interfaced with spiro-OMeTAD (H-Spiro), with and without the abovementioned additives. When the perovskite is interfaced with a bare spiro-OMeTAD layer,

we expect to see charge accumulation, and thus, a nonzero anisotropy. The doping of the acceptor is, on the other hand, expected to prevent charge accumulation, bringing the polarization dependence of the signal to zero.

Figure 4-6 presents the calculated anisotropies, from TA data recorded at λ_{ex} = 475 nm and at a fluence of 100 μJ cm^{-2}. Again, two different wavelengths are presented that correspond to the PEA (520 nm, Figure 4-6A), and the GSB signals (750 nm, Figure 4-6B). The corresponding spectra are presented in the appendix (Figure B-1).

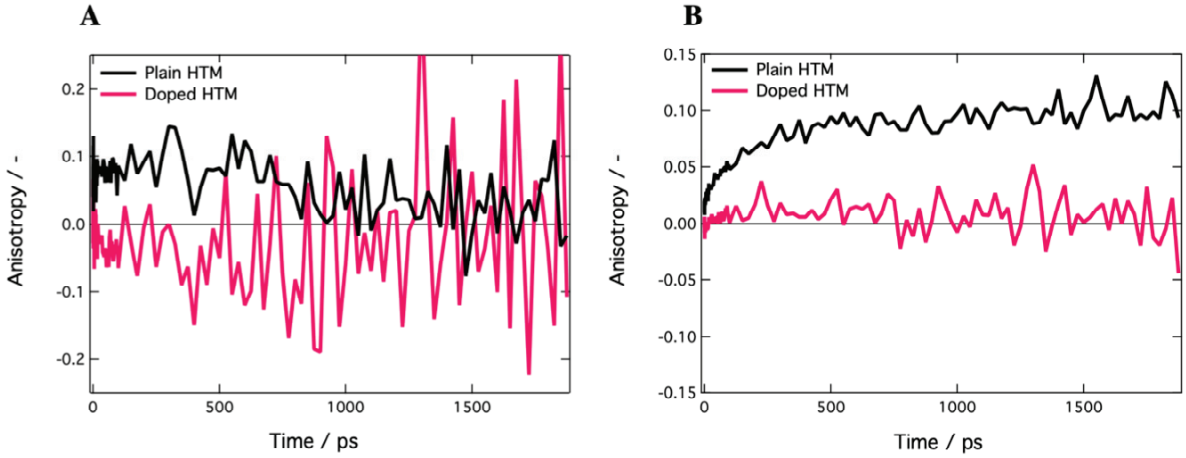

Figure 4-6 Transient absorbance anisotropies close to the perovskite/spiro-OMeTAD interface, recorded at λ_{ex} = 475 nm and at a fluence of 100 μJ cm^{-2}. **A.** 520 nm (PEA signal). **B.** 750 nm (GSB signal).

Figure 4-6A and Figure 4-6B display similar results: The anisotropy is close to zero when the spiro-OMeTAD is doped, while it rises to larger values for the undoped layer. As charges are known to accumulate more in the latter case, this is in complete accordance with our main assumption: the interfacial built-in field, which is a direct probe for charge accumulation, can be observed via the optical anisotropy of a suitably designed sample, via a spatially controlled photogeneration of carriers.

4.4 Conclusion

In this work, we presented a novel way to elucidate the interface physics within mixed perovskite-based solar cells. Focusing on so-called "half-cells", namely, samples consisting of a state-of-the-art perovskite layer interfaced with an ETL (SnO_2) or an HTL (spiro-OMeTAD), the presented experimental scheme consisted of two steps:

1. Characterization of the photoinduced species at the interface via illumination-face dependent transient absorbance measurements (selective generation of charges close to or away from the studied interface).
2. Elucidation of the limiting factor for charge collection (injection towards the ETL/HTL or charge mobility within the ETL/HTL): Assessment of the occurrence of charge accumulation. This is achieved by probing the existence of a significant built-in electric field impacting the local order of the perovskite layer by means of anisotropic transient absorbance.

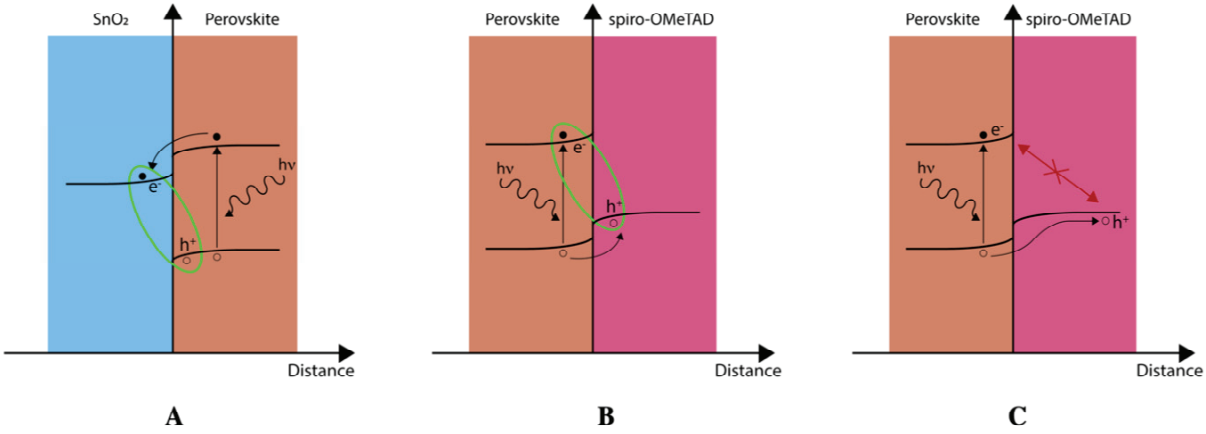

Figure 4-7 SnO_2/perovskite (**A**), perovskite/doped spiro-OMeTAD (**B**) and perovskite/plain spiro-OMeTAD (**C**) interfacial processes as unraveled by our novel experimental scheme. Electron transfer towards SnO_2 is mediated by the formation of CT excitons between trapped electrons and holes in the perovskite (interaction zone depicted in green). Once dissociated, electrons are free to move away from the interface. Hole transfer towards spiro-OMeTAD occurs on a sub-ps timescale. Charges, however, tend to accumulate at or close to the interface, due to the low mobility of the molecular acceptor. The addition of a set of additives to the spiro-OMeTAD layer is an efficient workaround.

The outcomes of our study are summarized in Figure 4-7: Due to its amorphous nature, ALD-deposited SnO_2 is comprised of a large density of interfacial electron traps. Trapped electrons interact with holes across the interface, forming CT excitons that mediate the electron transfer. Upon dissociation of the CT excitons, charges however do not accumulate around the interface (no optical anisotropy): the limiting process for charge collection at the back contact of the SnO_2-based interface is thus their injection, and not their subsequent dynamics within the ETL. This is supported by the better photovoltaic performance of devices based on a crystalline SnO_2 layer (larger V_{OC} and FF).

Alternatively, the injection towards spiro-OMeTAD occurs on a sub-ps timescale, as attested by the lower density of bulk CT excitons. However, the positive anisotropy signal suggests that charges accumulate at or close to the interface: The main factor limiting charge collection at the metal contact of PSCs is thus their transport within the HTL. This is further supported by comparing the anisotropy signals of perovskite/ doped spiro-OMeTAD and perovskite/ undoped spiro-OMeTAD interfaces: charges accumulate less in the former, as attested by an almost zero anisotropy.

The presented experimental scheme thus provides accurate insights into subtle physical processes. Furthermore, it is an example of simple execution and analysis, and appears as a precious tool to work towards optimized perovskite-based optoelectronic devices.

References

(1) Stranks, S. D.; Eperon, G. E.; Grancini, G.; Menelaou, C.; Alcocer, M. J. P.; Leijtens, T.; Herz, L. M.; Petrozza, A.; Snaith, H. J. Electron-Hole Diffusion Lengths Exceeding 1 Micrometer in an Organometal Trihalide Perovskite Absorber. *Science* **2013**, *342*, 341–344.

(2) Wehrenfennig, C.; Eperon, G. E.; Johnston, M. B.; Snaith, H. J.; Herz, L. M. High Charge Carrier Mobilities and Lifetimes in Organolead Trihalide Perovskites. *Adv. Mater.* **2013**, *26* (10), 1584–1589.

(3) Schulz, P. Interface Design for Metal Halide Perovskite Solar Cells. *ACS Energy Lett.* **2018**, *3* (6), 1287–1293.

(4) Yadav, P.; Turren-Cruz, S.-H.; Prochowicz, D.; Tavakoli, M. M.; Pandey, K.; Zakeeruddin, S. M.; Grätzel, M.; Hagfeldt, A.; Saliba, M. Elucidation of Charge Recombination and Accumulation Mechanism in Mixed Perovskite Solar Cells. *J. Phys. Chem. C* **2018**, *122* (27), 15149–15154.

(5) Yadav, P.; Alotaibi, M. H.; Arora, N.; Dar, M. I.; Zakeeruddin, S. M.; Grätzel, M. Influence of the Nature of a Cation on Dynamics of Charge Transfer Processes in Perovskite Solar Cells. *Adv. Funct. Mater.* **2017**, *28* (8), 1706073–1706077.

(6) Tress, W.; Yavari, M.; Domanski, K.; Yadav, P.; Niesen, B.; Correa-Baena, J.-P.; Hagfeldt, A.; Graetzel, M. Interpretation and Evolution of Open-Circuit Voltage, Recombination, Ideality Factor and Subgap Defect States During Reversible Light-Soaking and Irreversible Degradation of Perovskite Solar Cells. *Energy Environ. Sci.* **2018**, *11* (1), 151–165.

(7) Wu, B.; Fu, K.; Yantara, N.; Xing, G.; Sun, S.; Sum, T. C.; Mathews, N. Charge Accumulation and Hysteresis in Perovskite-Based Solar Cells: an Electro-Optical Analysis. *Adv. Energy Mater.* **2015**, *5* (19), 1500829–8.

(8) Zarazua, I.; Bisquert, J.; Garcia-Belmonte, G. Light-Induced Space-Charge Accumulation Zone as Photovoltaic Mechanism in Perovskite Solar Cells. *J. Phys. Chem. Lett.* **2016**, 525–528.

(9) Ulfa, M.; Wang, P.; Zhang, J.; Liu, J.; de Marcillac, W. D.; Coolen, L.; Peralta, S.; Pauporté, T. Charge Injection and Electrical Response in Low-Temperature SnO2-Based Efficient Perovskite Solar Cells. *ACS Appl. Mater. Interfaces* **2018**, *10* (41), 35118–35128.

(10) Paraecattil, A. A.; De Jonghe-Risse, J.; Pranculis, V.; Teuscher, J.; Moser, J. E. Dynamics of Photocarrier Separation in MAPbI 3Perovskite Multigrain Films Under a Quasistatic Electric Field. *J. Phys. Chem. C* **2016**, *120* (35), 19595–19602.

(11) *Impedance Spectroscopy: Theory, Experiment, and Applications*; Macdonald, J. R., Barsoukov, E., Eds.; John Wiley & Sons, 2018.

(12) Macdonald, J. R. Impedance Spectroscopy. *Ann. Biomed. Eng.* **1992**, *20* (3), 289–305.

(13) Boukamp, B. A. Impedance Spectroscopy, Strength and Limitations. *Technishes Messen* **2004**, *71* (9), 454–459.

(14) Bouduban, M. E. F.; Giordano, F.; Rosspeintner, A.; Teuscher, J.; Vauthey, E.; Graetzel, M.; Moser, J. E. *Inter-Domain Charge Transfer as a Rationale for Superior Photovoltaic Performances of Mixed Halide Lead Perovskites*; 2018; pp 1–10.

(15) Kavan, L. Conduction Band Engineering in Semiconducting Oxides (TiO2, SnO2)_ Applications in Perovskite Photovoltaics and Beyond. *Catalysis Today* **2019**, *328*, 50–56.

(16) Li, J.; Bu, T.; Liu, Y.; Zhou, J.; Shi, J.; Ku, Z.; Peng, Y.; Zhong, J.; Cheng, Y.-B.; Huang, F. Enhanced Crystallinity of Low-Temperature Solution-Processed SnO 2for

Highly Reproducible Planar Perovskite Solar Cells. *ChemSusChem* **2018**, *11* (17), 2898–2903.

(17) Baena, J. P. C.; Steier, L.; Tress, W.; Saliba, M.; Neutzner, S.; Matsui, T.; Giordano, F.; Jacobsson, T. J.; Kandada, A. R. S.; Zakeeruddin, S. M.; et al. Highly Efficient Planar Perovskite Solar Cells Through Band Alignment Engineering. *Energy Environ. Sci.* **2015**, *8* (10), 2928–2934.

(18) Giordano, F.; Abate, A.; Baena, J. P. C.; Saliba, M.; Matsui, T.; Im, S. H.; Zakeeruddin, S. M.; Nazeeruddin, M. K.; Hagfeldt, A.; Graetzel, M. Enhanced Electronic Properties in Mesoporous TiO2 via Lithium Doping for High-Efficiency Perovskite Solar Cells. *Nat. Commun.* **1AD**, *7*, 1–6.

(19) Price, M. B.; Butkus, J.; Jellicoe, T. C.; Sadhanala, A.; Briane, A.; Halpert, J. E.; Broch, K.; Hodgkiss, J. M.; Friend, R. H.; Deschler, F. Hot-Carrier Cooling and Photoinduced Refractive Index Changes in Organic&Ndash;Inorganic Lead Halide Perovskites. *Nat. Commun.* **2015**, *6*, 1–8.

(20) Piatkowski, P.; Cohen, B.; Ramos, F. J.; Di Nunzio, M.; Nazeeruddin, M. K.; Grätzel, M.; Ahmad, S.; Douhal, A. Direct Monitoring of Ultrafast Electron and Hole Dynamics in Perovskite Solar Cells. *Physical Chemistry Chemical Physics* **2015**, *17* (22), 14674–14684.

(21) Xing, G.; Mathews, N.; Sun, S.; Lim, S. S.; Lam, Y. M.; Yeng; Grätzel, M.; Mhaisalkar, S.; Sum, T. C. Long-Range Balanced Electron- and Hole-Transport Lengths in Organic-Inorganic $CH_3Nh_3PbI_3$. *Science* **2013**, *342*, 344–347.

(22) Trinh, M. T.; Wu, X.; Niesner, D.; Zhu, X. Y. Many-Body Interactions in Photo-Excited Lead Iodide Perovskite. *J. Mater. Chem. A* **2015**, *3* (17), 9285–9290.

(23) Roiati, V.; Mosconi, E.; Listorti, A.; Colella, S.; Gigli, G.; De Angelis, F. Stark Effect in Perovskite/TiO 2Solar Cells: Evidence of Local Interfacial Order. *Nano Lett.* **2014**, *14* (4), 2168–2174.

(24) Ziffer, M. E.; Mohammed, J. C.; Ginger, D. S. Electroabsorption Spectroscopy Measurements of the Exciton Binding Energy, Electron–Hole Reduced Effective Mass, and Band Gap in the Perovskite CH 3NH 3PbI 3. *ACS Photonics* **2016**, *3* (6), 1060–1068.

(25) Rehman, W.; Milot, R. L.; Eperon, G. E.; Wehrenfennig, C.; Boland, J. L.; Snaith, H. J.; Johnston, M. B.; Herz, L. M. Charge-Carrier Dynamics and Mobilities in Formamidinium Lead Mixed-Halide Perovskites. *Adv. Mater.* **2015**, *27* (48), 7938–7944.

(26) Jacobsson, T. J.; Correa-Baena, J.-P.; Pazoki, M.; Saliba, M.; Schenk, K.; Grätzel, M.; Hagfeldt, A. Exploration of the Compositional Space for Mixed Lead Halogen Perovskites for High Efficiency Solar Cells. *Energy Environ. Sci.* **2016**, *9* (5), 1706–1724.

(27) Ren, X.; Yang, D.; Yang, Z.; Feng, J.; Zhu, X.; Niu, J.; Liu, Y.; Zhao, W.; Liu, S. F. Solution-Processed Nb:SnO 2Electron Transport Layer for Efficient Planar Perovskite Solar Cells. *ACS Appl. Mater. Interfaces* **2017**, *9* (3), 2421–2429.

(28) Halvani Anaraki, E.; Kermanpur, A.; Mayer, M. T.; Steier, L.; Ahmed, T.; Turren-Cruz, S.-H.; Seo, J.; Luo, J.; Zakeeruddin, S. M.; Tress, W. R.; et al. Low-Temperature Nb-Doped SnO 2Electron-Selective Contact Yields Over 20% Efficiency in Planar Perovskite Solar Cells. *ACS Energy Lett.* **2018**, *3* (4), 773–778.

(29) Park, M.; Kim, J.-Y.; Son, H. J.; Lee, C.-H.; Jang, S. S.; Ko, M. J. Low-Temperature Solution-Processed Li-Doped SnO2 as an Effective Electron Transporting Layer for High-Performance Flexible and Wearable Perovskite Solar Cells. *Nano Energy* **2016**, *26* (C), 208–215.

(30) Grancini, G.; Viola, D.; Lee, Y.; Saliba, M.; Paek, S.; Cho, K. T.; Orlandi, S.; Cavazzini, M.; Fungo, F.; Hossain, M. I.; et al. Femtosecond Charge-Injection Dynamics at Hybrid Perovskite Interfaces. *ChemPhysChem* **2017**, *18* (17), 2381–2389.

(31) Ponseca, C. S., Jr.; Hutter, E. M.; Piatkowski, P.; Cohen, B.; Pascher, T.; Douhal, A.; Yartsev, A.; Sundström, V.; Savenije, T. J. Mechanism of Charge Transfer and Recombination Dynamics in Organo Metal Halide Perovskites and Organic Electrodes, PCBM, and Spiro-OMeTAD: Role of Dark Carriers. *J. Am. Chem. Soc.* **2015**, *137* (51), 16043–16048.

(32) Poplavskyy, D.; Nelson, J. Nondispersive Hole Transport in Amorphous Films of Methoxy-Spirofluorene-Arylamine Organic Compound. *Journal of Applied Physics* **2003**, *93* (1), 341–346.

5 Energy and Charge Transfer Cascade in Methylammonium Lead Bromide Perovskite Nanoparticle Aggregates

5.1 Introduction

Organolead halide perovskites have emerged as a thrilling novel material for photovoltaic technology. Since their first demonstration a few years ago, perovskite solar cells (PSCs) have already reached power conversion efficiencies of 22 %.[1] While nanostructured perovskites were originally deposited within mesoscopic metal oxide scaffolds,[2-4] architectures of efficient PSCs have now evolved towards the use of homogeneous thin films in planar multilayer configurations. Perovskite films and large single crystals have so far been the focus of experiments aimed at gaining a fundamental knowledge of the material bulk properties. Alternatively, methylammonium or cesium perovskite nanocrystals and colloidal nanoparticles dispersed in a solvent have been shown to be highly promising in the context of LEDs and lasing applications.[5-11] The observation by photoluminescence nano-imaging and transient absorption microscopy of the surface of multigrain thin films in perovskite solar cells suggested that their efficiency is influenced by the nanoscopic structure of the active semiconducting layer.[12-14] Recently, energy transfer between crystal grains and photon recycling effects were shown to contribute, to a large extent, to the long path lengths of photocarriers.[15] Controlled nanoparticle aggregates, thus, constitute ideal model systems for the characterization of interfacial non-radiative energy and charge transfer processes at grain boundaries, which appear to be key to the exceptional photovoltaic performances of perovskite devices.

The study of perovskite nanoparticles provides also an opportunity to focus on a different paradigm for the photogenerated species. As it happens, it has been shown that above-bandgap photoexcitation of methylammonium lead trihalide perovskite thin-films mostly yields free carriers at room temperature, although an increasing proportion of excitons is observed as one moves up in the halogens group from iodine to chlorine.[16-20] As a consequence, excitonic features in perovskites can hardly be studied for thin-film architectures. Synthesizing and characterizing their nanostructured counterpart that present much larger exciton binding energies,[21] however, allows for direct observation of excitonic behavior.

A first synthesis of $CH_3NH_3PbBr_3$ perovskite nanoparticles was proposed by Schmidt *et al.*,[22] where the stability of the suspension in aprotic, moderately polar solvents is ensured by the presence of an organic capping layer, typically consisting of alkylammonium long-chain cations. Ulterior studies endeavored to characterize those colloidal suspensions and highlighted the presence of a broad distribution of nanostructures. On top of 3D perovskite nanoparticles, perovskite nanoplatelets of various thicknesses exhibiting 2D quantum confinement were identified.[21,23] Further synthesis attempts, aiming at getting improved $CH_3NH_3PbX_3$ (X=Br, I) suspensions in terms of stability, emission properties and monodispersity, were later reported, although with mitigated results.[24,25]

The presence of nanoplatelets in colloidal suspension was exploited in quantum confinement studies. It was shown in particular that the proportion and thickness of the quasi-2D nanoplatelets can be tuned by varying (i) the ratio between the long-chain alkylammonium

capping ligand and the methylammonium halide precursor and (ii) the length of the capping alkyl chain with use of butylammonium and octadecylammonium instead of octylammonium, for example.[21,26,27] Investigations on those species later demonstrated the presence of a strong quantum confinement, yielding a blue-shift of the emission and absorption as the thickness of the platelets decreases.[26,28]

Only few studies focused on the photophysical properties of methylammonium lead-bromide perovskite nanoparticles. Remarkably high values of the photoluminescence quantum yield of 17-20 % were reported,[28-30] which were generally attributed to an enhanced exciton binding energy compared to bulk perovskites, sustained by reported values of around 320 meV.[21]

In this work, we focus on colloidal suspensions of methylammonium lead-bromide perovskite nanoparticles in chlorobenzene. Excitation wavelength-dependent ultrafast transient absorbance measurements were performed to characterize their optical properties. Two different reductive quenchers were then added to the solution, providing insights into charge-transfer dynamics and related interfacial phenomena that were probed with a combination of techniques, namely ultrafast transient absorbance spectroscopy, nanosecond flash photolysis and time-correlated single-photon counting.

5.2 Methods

5.2.1 Samples

Colloidal $CH_3NH_3PbBr_3$ nanoparticles were prepared following the method described by Schmidt *et al.*,[20] yielding octylammonium-capped nanoparticles. Dried nanoparticles were stored in the dark and under dry air at all times.

Thorough solvent tests were performed to maximize the stability of the colloidal suspensions. In this context, it appeared that colloidal suspensions in chlorobenzene exhibited desirable features, such as a high stability, in particular for highly concentrated solutions, and favorable solvation interactions, limiting the adsorption of the nanoparticles onto the walls of the vial/cuvette.

A stable stock colloidal suspension was prepared every month, and various dilutions were made and used for the different experiments. Transient-absorbance and steady-state absorbance data have been recorded at a nanoparticle density of 100 µg/ML, while TCSPC and steady-state fluorescence measurements have been recorded with 10 µg/mL samples. The stability of the stock solution was routinely checked through absorbance spectra measurements. In addition, every sample was carefully degassed by bubbling with argon for 30 minutes before optical measurements.

5.2.2 Optical methods

Ultrafast transient absorbance (TA) spectra of methylammonium lead bromide perovskite nanoparticles were acquired using femtosecond pump-probe spectroscopy at two different excitation wavelengths. The pump beam at λ_{ex} = 480 nm or 390 nm was obtained either by pumping a two-stage non-colinear optical parametric amplifier (NOPA, see sect. 4.2.2) with

the output of the CPA laser described in sect. 3.2.3 or by frequency doubling in a BBO crystal, respectively (sect. 3.2.3). In the first case, pulses were compressed to ~43 fs FWHM duration by a pair of SF10 prisms. The generation and characteristics of the probe beam are the same as explained previously. The time resolution of the experiment depended on the excitation wavelength and was 200 fs for λ_{ex} = 390 nm (second harmonic) and 90 fs for λ_{ex} = 480 nm.

Similarly, long-time behavior of the sample was characterized using nanosecond flash photolysis. The pump beam (λ_{ex} = 480 nm) was generated by a frequency-tripled Q-switched Nd:YAG laser (Ekspla NT-342, 355 nm, 20 Hz repetition rate) pumping an optical parametric oscillator (OPO), yielding pulses of *ca*. 5 ns duration (FWHM). The probe beam was obtained from a cw halogen lamp and was passed through a monochromator to select the detection wavelength and avoid undesired illumination before being focused onto the sample. The transmitted probe light was then passed through a second monochromator and detected either by a fast photomultiplier tube (R9910, Hamamatsu) in the visible or by an InGaAs photodiode (SM05PD5A, Thorlabs) for near-infrared measurements. The resulting signals were recorded and digitalized with a broad bandwidth digital oscilloscope (Tektronix, DPO 7254), with a typical averaging over 2000 shots.

In turn, the long-time time-dependence of the nanoparticles emission was unraveled via time-correlated single-photon counting (TCSPC) measurements. TCSPC dynamics were recorded by a Horiba Fluorolog-3 spectrofluorometer, using a 405 nm NanoLed laser diode as an excitation source (< 200 ps pulse duration, 11 pJ/pulse). In order to avoid pile-up phenomena, the portion of photons reaching the detector per cycle was kept under 2 % by adjusting the width of various slits within the setup.

Finally, steady-state characterization of the nanoparticles was performed. UV-vis absorbance spectra were recorded on a PerkinElmer Lambda 950 UV/vis/NIR spectrophotometer equipped with an integrating sphere to account for light-scattering by the sample. Steady-state photoluminescence spectra were measured using a PerkinElmer LS 50B spectrofluorometer.

5.3 Results and discussions

5.3.1 Evidence for cascade transfer: steady-state properties, excitation-dependent transient absorbance measurements and luminescence lifetimes

We prepared suspensions of $CH_3NH_3PbBr_3$ nanoparticles in chlorobenzene. As presented in Figure 5-1A, these suspensions exhibit several optical features, which were already reported and demonstrated to arise from a broad distribution of nanostructures:[23] Specifically, bulk-like tri-dimensional perovskite nanoparticles and various-sized nanoplatelets with formula $(C_6H_{13}NH_3)_2(CH_3NH_3)_{m-1}Pb_mBr_{3m+1}$.[21,23,25,27,28] These are denominated "quasi-2D" (q-2D) perovskites, as they exhibit an almost two-dimensional structure comprising *m* layers of perovskite unit cells, surrounded by the octylammonium cations of the capping layer.

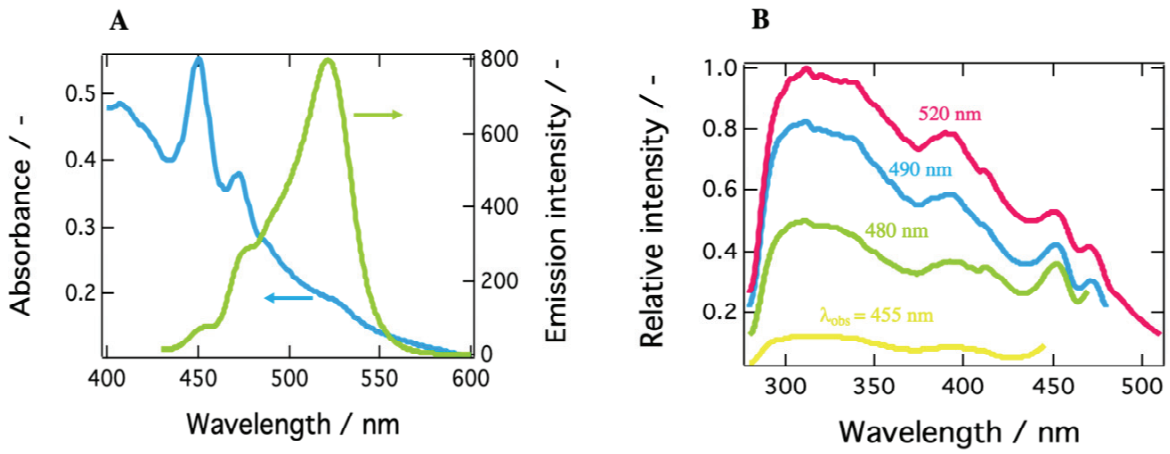

Figure 5-1 Steady-state optical properties of a suspension of $CH_3NH_3PbBr_3$ nanoparticles in chlorobenzene. **A.** Absorption (blue) and photoluminescence (green) spectra. The emission spectrum was obtained with an excitation wavelength λ_{ex} = 390 nm. **B.** Photoluminescence excitation spectra measured for four emission wavelengths corresponding to 3D and q-2D perovskite nanoparticles, with m = 5, 4 and 3, respectively. Red: λ_{obs} = 520 nm, blue: λ_{obs} = 490 nm, green: λ_{obs} = 480 nm, and yellow: λ_{obs} = 455 nm.

We observe an absorption spectrum similar to the one reported by Tyagi et al. From the abovementioned papers, the various absorption peaks in Figure 5-1A were assigned as follows: The peak with λ_{max} = 409 nm corresponds to 2D or q-2D perovskite with m=1. The absorbance maxima at λ_{max} = 453 nm, λ_{max} = 472 nm and λ_{max} = 489 nm are attributed to q-2D perovskite with m = 3, q-2D perovskite with m = 4 and q-2D perovskite with m = 5, respectively. Finally, bulk 3D perovskite nanoparticles absorb at λ_{max} = 520 nm, as expected for pristine $CH_3NH_3PbBr_3$.[21]

Similarly, we observed that the five different perovskite nanostructures could also be distinguished in the emission spectrum, which displays peaks displaced by a Stokes shift of about 8 nm compared to the absorbance features. Interestingly, the relative intensities between the absorbance peaks and their corresponding emission features do not follow the same trend. In particular, the maximum of the emission spectrum at λ_{obs} = 530 nm corresponds to the lower edge of the absorbance spectrum and therefore to the 3D perovskite, with an absorbance maximum at 520 nm. Such a discrepancy can be rationalized in two ways: Either a cascade of energy and/or charge transfer processes occurs between different nanostructures, with preferential radiative recombination from the 3D sites, or those nanostructures simply exhibit very different emission quantum yields. The latter is a reasonable postulate, as one expects the emission quantum yield in a semiconductor to increase with the exciton binding energy and decrease as the surface area increases, because of the higher density of trap states yielding non-radiative decay pathways. In this context, it was shown that the exciton binding energy diminishes as the thickness of the platelets increases, yielding a minimum for the bulk perovskite material.[31] Thus, a trade-off emerges: the thinner platelets exhibit, at the same time, a larger binding energy and more trap states and one, hence, expects an optimum quantum yield for the type of platelets exhibiting the best compromise between those two parameters. As a matter of fact, quantum yields for various-sized nanoplatelets up to m = 5, as well as for bulk bromide perovskite, were recently measured and this effect is perfectly illustrated. The quantum

yield is indeed maximized for platelets with $m = 4$ and $m = 5$ (20 - 30 %), and then decreases to reach 2 % for single-layer platelets and 4 % for bulk perovskite.[26] In this light, the hypothesis of cascade energy and/or charge transfer within our suspensions appears very probable. As evidence of the occurrence of cascade energy transfer, Figure 5-1B displays a series of excitation spectra corresponding to four different nanostructures (3D and q-2D perovskites with $m = 3$, 4 and 5). It emerges that the shape of the excitation spectra is completely independent of the excitation wavelength, which indeed reflects excitation energy transfer between the different domains present.

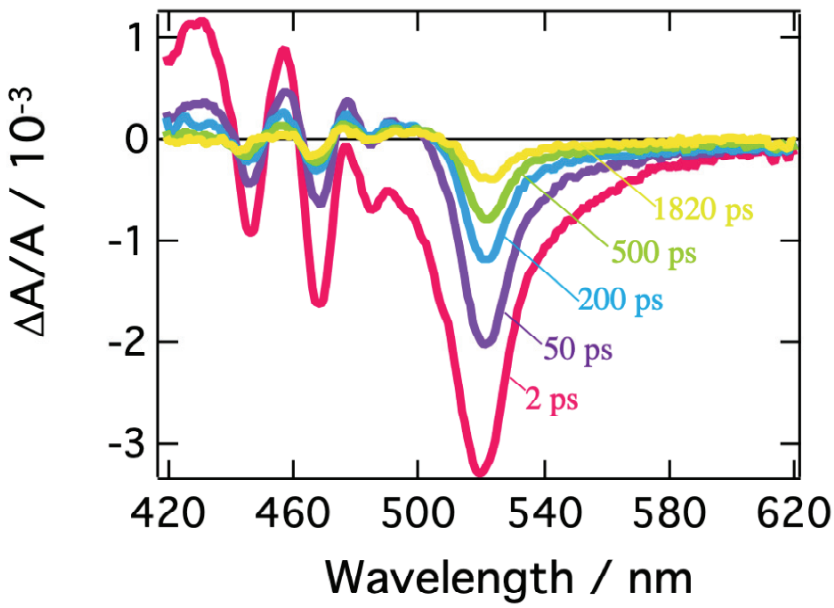

Figure 5-2 Transient absorption spectra of a suspension of $CH_3NH_3PbBr_3$ nanoparticles in chlorobenzene at different time delays following $\lambda_{ex} = 390$ nm pulsed excitation. Red: $t = 2$ ps, purple: $t = 50$ ps, blue: $t = 200$ ps, green: $t = 500$ ps, and yellow: $t = 1820$ ps.

Figure 5-2 displays the transient absorbance change following $\lambda = 390$ nm pulsed excitation. We observe a strong bleaching feature peaking at 525 nm and strong oscillations on the blue side of the spectrum. Data for $\lambda_{ex} = 480$ nm excitation are provided in the appendix (Figure C-1). These two excitation wavelengths have been chosen to selectively excite a given subset of the nanostructures present. While all nanostructures are excited at 390 nm, only three of them are activated upon $\lambda = 480$ nm excitation: 3D perovskite, and q-2D perovskites with $m = 4$ and $m = 5$. To further support the occurence of a cascade of energy and possibly charge transfer among nanostructures, a global fitting procedure of the time-resolved spectral data to a kinetic equation was performed. With such a process, we can express a time-series of transient absorbance spectra as a linear combination of the spectra of the various populations constituting the system, with their own dynamics (decay associated spectra, DAS). Population kinetics, as well as their individual spectra, are obtained this way, allowing us to shed light on interacting populations, and the possibility of charge and/or energy transfer processes. Details of the multiexponential fitting procedure are provided in chapter 2 (sect. 2.1.1) along with sample

results. In addition, Figure assesses the fitting quality by displaying it on top of experimental points.

A biexponential decay for excitation at 480 nm and a triexponential decay for excitation at 390 nm were extracted from the fitted dynamical data. These were obtained in conditions where the excitation energy fluence was kept sufficiently low as to remain below the non-geminate recombination regime. The corresponding decay associated spectra are reported in Figure 5-3A and B, along with the dynamics recorded at 520 nm (Figure 5-3C and D). Those dynamics are attributed to a combination of ground-state bleaching and stimulated emission (GSB+SE).

In Figure 5-3A (λ_{ex} = 480 nm), one distinguishes two decay associated spectra with time constants of 54 ps and 489 ps respectively. The former contribution covers the spectral region of the q-2D perovskites with m=5 and exhibits a negative peak centered at 515 nm. The second contribution, in turn, mostly features a negative amplitude centered at 520 nm aside a weaker positive signal extending into the blue region. This second contribution faithfully reflects the long-time TA spectra reported in Figure C-1, and represents the decay kinetics of the bulk nanoparticle population. Alternatively, the first contribution is assigned to the transfer of population from q-2D perovskites with m=5 towards the 3D sites. These two decay associated spectra confirm that at least two nanostructures contribute to the dynamics of the 520 nm peak (GSB+SE). To further support the fact that those two contributions indeed arise from interacting nanostructures and do not reflect an excessively high carrier density, we refer to Figure 5-3C that displays fluence-dependent dynamics at 520 nm. At short times, and as excitation energy fluence increases, it clearly appears that one moves from a monomolecular process (exponential decay) to a higher-molecularity kinetics attributed to non-geminate carrier recombination (fluence > 21 μJ cm^{-2}). We can then safely assume that the DAS obtained from global fitting our data with λ_{ex} = 480 nm (Figure 5-3A, recorded at an energy fluence of 10.5 μJ cm^{-2}) describes the interaction of two nanostructures and is not due to an excitation density artifact.

Alternatively, following λ_{ex} =390 nm excitation, one obtains three decay associated spectra with time constants of 1.3 ps, 50 ps and 377 ps, displayed on Figure 5-3B. The first contribution mainly consists of strong oscillations between 420 nm and 490 nm and represents the rise of the oscillatory signal already described in Figure 5-2. The two other contributions feature diminishing oscillations and a growing and sharpening negative amplitude centered at 520 nm. This is assigned, again, to population transfer from the blue side of the spectrum to the 3D sites. Figure 5-3D (fluence-dependent dynamics at 520 nm following λ_{ex} =390 nm excitation) unambiguously demonstrates that the decay rate is triphasic at all fluences. This confirms that the three decay associated spectra described above result from the excitation of all the nanostructures present and their ensuing interactions, and, again, are not an excitation density artifact.

As additional supporting evidence of cascade transfer processes, we characterized the photoemission of the nanoparticle suspension, as it is particularly sensitive to those phenomena. In this respect, we resorted to the TCSPC technique to consider the long-time behavior, at the microsecond time-scale, of emission at λ_{obs} = 455, 475, and 523 nm, following λ_{ex} = 405 nm excitation. The signals measured at these three wavelengths are dominated by the emission of the m = 3 and m = 4 platelets, as well as of the 3D bulk-like nanoparticles.

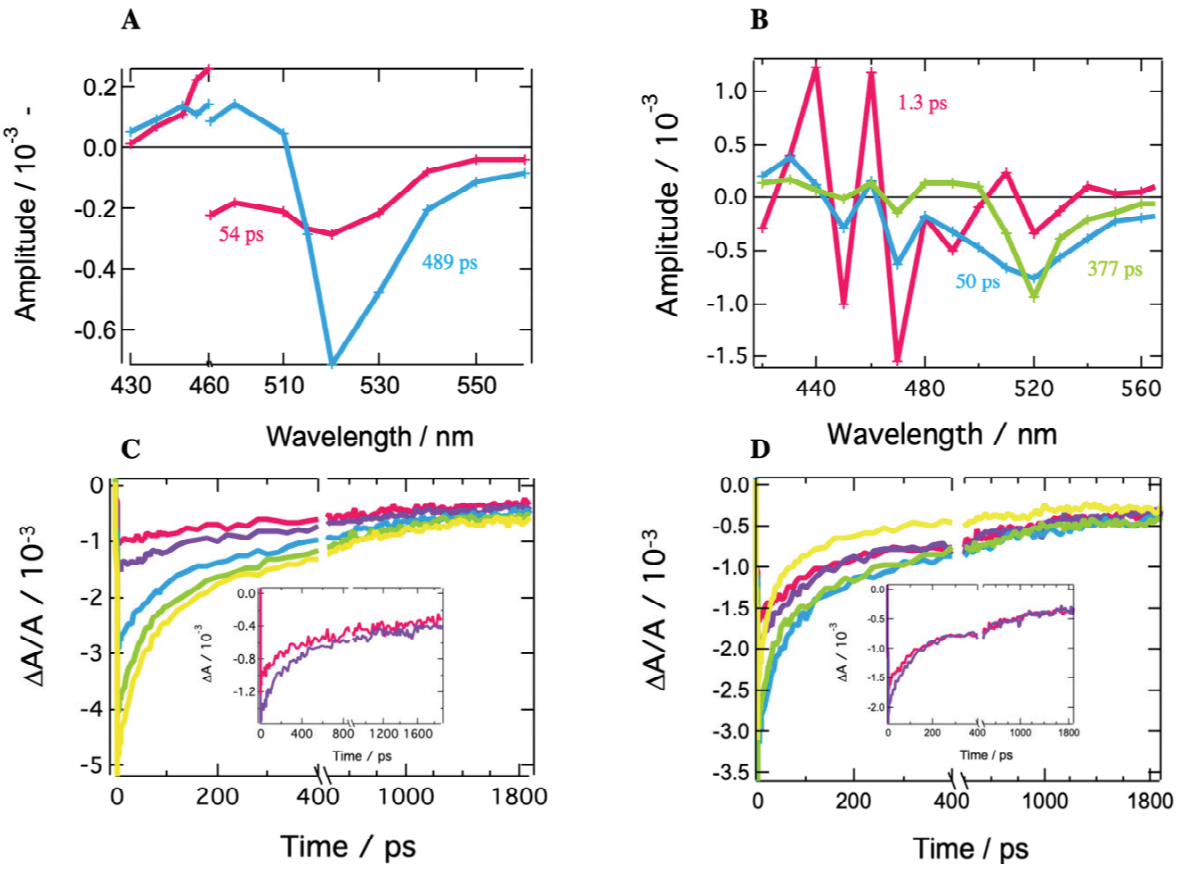

Figure 5-3 A. Result of a global fitting procedure of transient absorbance data obtained for a suspension of $CH_3NH_3PbBr_3$ nanoparticles in chlorobenzene for the excitation wavelength λ_{ex} = 390 nm at an energy fluence of 10.5 μJ cm^{-2}. Red: τ = 54 ps, blue: τ = 489 ps. **B.** Result of the global fitting procedure of transient absorbance data obtained in the same conditions for λ_{ex} = 390 nm and an energy fluence of 14 μJ cm^{-2}. Red: τ = 1.3 ps, blue: τ = 50 ps, and green: τ = 377 ps. **C.** Combination of ground-state bleaching (GSB) and stimulated emission (SE) peak (520 nm), intensity-dependent dynamics for λ_{ex} = 480 nm. Red: 7 μJ cm^{-2}, purple: 10.5 μJ cm^{-2}, blue: 21 μJ cm^{-2} green: 35 μJ cm^{-2} and yellow: 52 μJ cm^{-2}. Inset: zoom on the two transient signals obtained at lower fluences. The appearance of a third exponential emerges clearly with fluences ≥ 21 μJ cm^{-2}. **D.** GSB+SE peak intensity-dependent dynamics for λ_{ex} = 390 nm. Three exponentials are needed at all fluences. In this case, red: 9 μJ cm^{-2}, purple: 14 μJ cm^{-2}, blue: 27 μJ cm^{-2}, green: 45.5 μJ cm^{-2}, and yellow: 68 μJ cm^{-2}. Inset: Zoom on the two transient signals obtained at lower fluences.

Similarly, we addressed the short-time luminescence behavior with transient absorbance (TA) following 390 nm excitation and extracting the dynamics at wavelengths involving a pure or a major fraction of emission: λ_{obs} = 476, 491, and 555 nm. The small discrepancy between the TCSPC and TA selected wavelengths arises from the high complexity of the TA spectrum, demanding a selection outside of the expected emission maxima**.**

Each of the traces on Figure A and B can be fitted with a triexponential model, the latter moreover involving a convolution with the Gaussian response function of the instrument. We present the resulting time constants in Table . Note that the shortest TA time constant reflects the rise of the signal, while the two others correspond to its decay. On the contrary, TCSPC dynamics effectively feature a triexponential decay. In both cases, we attribute these

multiexponential decays to the entanglement of various nanostructures, as already discussed above.

At all wavelengths under study, the photoluminescence appears to decay over two very different timescales (ps *vs* µs) and the photoluminescence lifetime increases significantly as one moves to longer wavelengths for both timescales. In addition, we stress the notably slower rise time for 3D nanoparticles. We attribute the first of those features to the presence of different types of excitons with different lifetimes (*vide infra*). The second and third feature arise from interacting nanostructures and can be considered symptomatic of a cascade transfer process from the larger bandgap nanoplatelets all the way to the bulk 3D nanoparticles.

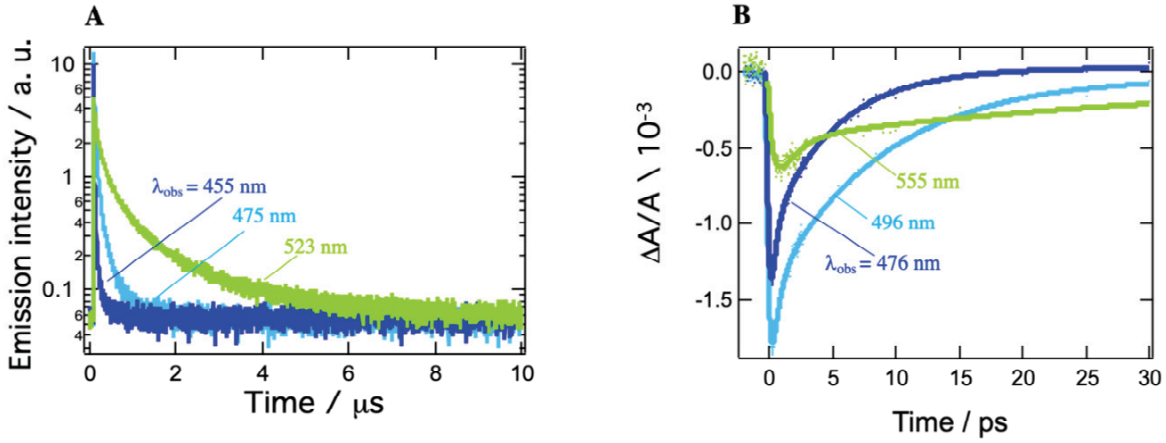

Figure 5-4 Dynamics of the emission of a suspension of $CH_3NH_3PbBr_3$ nanoparticles in chlorobenzene on two different timescales. **A.** Microsecond timescale from TCSPC following 405 nm excitation. Dark blue: λ_{obs} = 455 nm, light blue: 475 nm and green: 523 nm**. B.** Picosecond timescale, extracted from the λ_{ex} = 390 nm TA spectrum in regions where emission could be isolated. Dark blue λ_{obs} = 476 nm, light blue: 496 nm and green: 555 nm. Note that we chose to display here dynamics recorded at a higher fluence (52 µJ cm^{-2}), to further highlight the considered trends. Excitation energy fluences as low as 10 µJ cm^{-2} have been applied, yielding identical behaviors.

A

λ_{obs}	τ_1(ns)	τ_2(ns)	τ_3(ns)
455 nm	2.05 ± 0.02	21 ± 1	145 ±10
475 nm	6.82 ± 0.16	51 ± 1	262 ± 3
523 nm	29 ± 1	203 ± 5	1200 ± 25

B

λ_{obs}	τ_1(ps)	τ_2(ps)	τ_3(ps)
476 nm	0.153 ± 0.04	0.381 ± 0.09	5.14 ± 0.25
496 nm	0.186 ± 0.03	0.507 ± 0.09	8.67 ± 0.36
555 nm	0.61 ± 0.4	1.2 ± 0.8	32 ± 5

Table 5-1 Fitted photoemission lifetime for three nanostructures (m = 3 and m = 4 platelets, and 3D bulk-like nanoparticles). Table A presents the time constants obtained with TCSPC (λ_{ex} = 405 nm), while Table B presents the time constants (λ_{ex} = 390 nm) extracted from transient absorption measurements.

5.3.2 Evidence for CT excitons: Analysis of the transient absorption spectra and of the different emission lifetimes

Looking back at the transient absorption data in Figure 5-2, one observes strong oscillations on the blue side of the spectrum. This feature looks very much like the first or second derivative of the absorption spectrum of q-2D nanoplatelets within the 400-480 nm wavelength region. To shed light on the underlying process, the transient absorption spectrum at a time-delay of 2 ps is shown in Figure 5-4, along with a simulated differential electroabsorption spectrum (see Figure C-3 for details). The correspondence between the measured and simulated differential spectra allows us to assign a significant part of the transient optical features observed below 500 nm to a photoinduced electroabsorption.

The term "electroabsorption" designates the change in the absorption spectrum of a system subjected to an electric field, be it applied externally or originating from photogenerated carriers. For molecular and excitonic systems, the electroabsorption generally results from a quadratic Stark effect.[32] Based on a perturbative approach, such electroabsorption signals can be shown to correspond to a linear combination of the first and second derivatives of the linear absorption spectrum (see chapter 2). For anisotropic samples such as nanoparticle suspensions, the related amplitudes of these two components are then respectively given by the change in polarizability of the material and by the change in dipole moment upon the electronic transition of interest.

Figure 5-4 shows that the observed differential electroabsorption signal appears to be dominated by the second derivative of the absorption spectrum (see sect. C.3 for details), whose amplitude is given by the change of a permanent dipole moment. Because Frenkel and Wannier-Mott bulk excitons do not display a permanent dipole moment, they are not likely to generate any significant electric field that could induce the observed electroabsorption.[33] On the contrary, interfacial charge transfer (CT) states, where the electron and the hole occupy adjacent domains, exhibit a permanent dipole. These CT excitons are known to occur primarily in ionic solid materials,[34] such as the lead halide perovskites, and are believed to be responsible for the observed photoinduced electroabsorption.

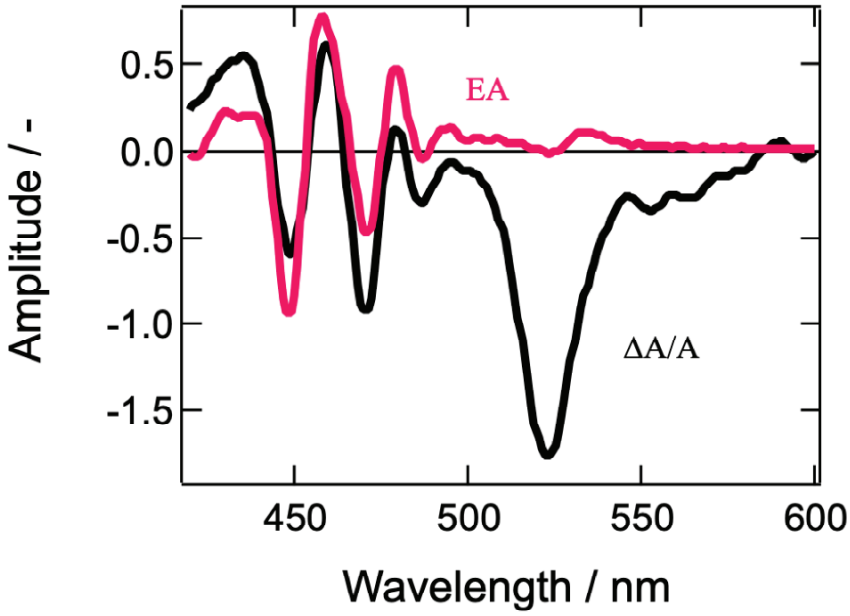

Figure 5-4 Modeled electroabsorption signal of a suspension of $CH_3NH_3PbBr_3$ nanoparticles in chlorobenzene. The blue part of the observed transient absorption spectrum measured at a time delay of 2 ps (black line) fits well with a simulated electroabsorption spectrum (red) dominated by the second derivative component of the ground state absorption spectrum (see appendix for details).

Aside from the photoinduced electroabsorption signal, the presence of CT excitons fits well with the observation, outlined above, of two different emission timescales (ps *vs* µs). We indeed assigned this phenomenon to the recombination of two different exciton populations. From the long lifetime of the photoinduced electroabsorption signal (longer than 2 ns), we deduce that the CT states are long-lived. As a consequence, those two exciton populations would correspond to localized excitons (within one nanostructure), that recombine on the ps timescale, and CT excitons.

Furthermore, the presence of CT excitons is of high interest as it provides evidence for the occurrence of interstructure charge transfer in addition to the previously discussed energy transfer processes.

5.3.3 Interaction between nanostructures and global photophysical perspective

In the above sections, we gathered evidence towards cascade energy and CT exciton-mediated charge transfer, from the larger bandgap to the lower bandgap nanostructures. The cascade transfer is supported by steady-state optical measurements, global analysis of transient absorption data at two different wavelengths and emission lifetime characterization. Excitation energy transfer was evidenced by the wavelength independence of the excitation spectra (Figure 5-1B). Similarly, the occurrence of charge transfer is sustained by the presence of interfacial charge transfer states, whose involvement is deduced from the observation of a second derivative-dominated photoinduced electro-absorption signal in TA experiments and by the presence of two very different emission timescales (ps vs µs), assigned to different exciton populations.

We hence come up with a photophysical model where our colloidal suspensions involve two distinct exciton populations generated upon photoexcitation: Localized excitons whose localized character increases as we move to thinner platelets and CT excitons, yielding the processes illustrated in Figure 5-5.

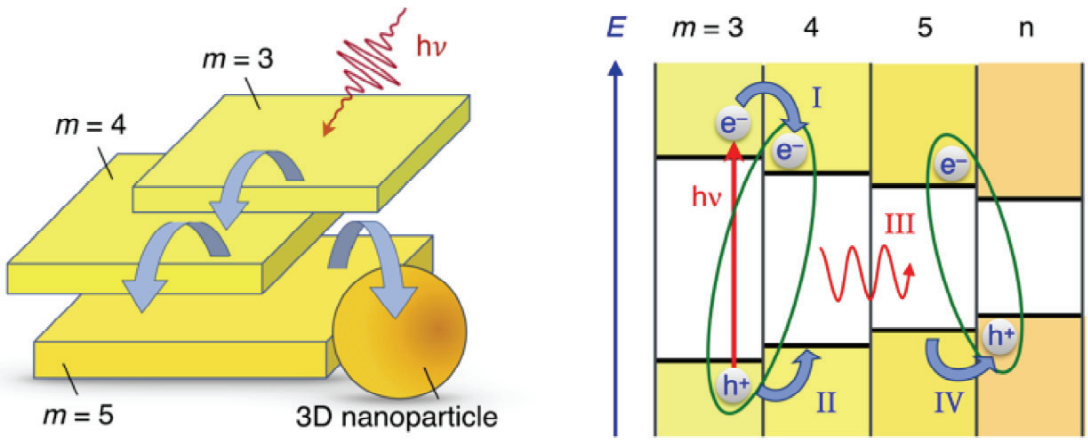

Figure 5-5 Cartoon illustrating the energy and charge transfer processes occurring between the various nanostructures constituting the $CH_3NH_3PbBr_3$ perovskite colloid. Left: Energy and/or charge transfer cascade (curved blue arrows) between q-2D nanoplatelets of increasing thicknesses and eventually a 3D bulk-like nanoparticle. Right: Energetic scheme of some examples of photophysical processes taking place in a nanoparticle aggregate: Upon photoexcitation of a thin q-2D ($m = 3$) nanoplatelet, interfacial electron transfer can take place to the adjacent particle (process I). Electrostatic interaction of the electron with a hole remaining on the other side of the interface yields a CT exciton (green ellipse). Subsequent hole transfer (process II) leads to the excitation of the $m = 4$ q-2D nanoplatelet. Energy transfer to a neighbouring nanostructure characterized by a narrower bandgap is then possible (process III). Interfacial hole transfer (process IV) finally enables the formation of a new interfacial CT excitonic species.

First, the photoexcitation of two or more nanostructures forms localized excitons yielding a bleaching of the excitonic transition in the transient absorbance measurements. Then, localized exciton emission for all excited nanostructures, with a picosecond lifetime, competes with the formation of CT excitons with neighboring, smaller band-gap nanostructures. Finally, dissociation of the CT excitons on the nanosecond timescale allows for the radiative recombination of relocalized electron-hole pairs and results in the observed long-lived emission.

The cascade charge transfer processes reported here have been recently highlighted in solution-processed, highly efficient, LEDs devices.[9] They are thus likely to occur in the same way between different perovskite domains that could coexist within a thin-film photovoltaic device and, therefore, take place within the charge transport process following light absorption. Hence, this picture could occur in parallel and, similarly to the recently highlighted photon recycling (long distance radiative energy transfer), play a crucial role in the remarkable efficiency of PSCs.[13]

5.3.4 Interaction with donors and acceptors: Dynamics of charge transfer at the solution interface

Charge-transfer processes occurring at the particle/ solution interface were scrutinized to provide a comprehensive characterization of the nanoparticle interfacial properties. Two organic electron donor molecules, *N*,*N*,*N*,*N*-tetrakis(4-methoxyphenyl)benzidine (MeO-TPD) and 1,4-bis(diphenyl-amino)benzene (BDB) (molecular structures provided in the appendix, insets of Figure), were selected based on three different criteria. The first criterion concerns the thermodynamics: The energetics of the quencher must match that of the nanoparticles for an electron transfer to occur. The second emerges as a discrimination criterion, as the absorption of the quencher must not overlap with that of the nanoparticles to allow optical observation of the reaction. The third and last criterion also aims at optimizing the monitoring of the reaction: The oxidized quencher must exhibit an optical signature in an accessible spectral range, typically in the vis-NIR domains, and the transient species should ideally not exhibit any overlap with the optical features of the nanoparticles.

Figure 5-6 shows that MeO-TPD and BDB absorption spectra, and that of the corresponding oxidized species, fulfil the abovementioned criteria.[35-37] Besides their favorable thermodynamics, both molecules show an absorbance cut-off below 400 nm, fulfilling the discrimination criterion. In addition, their oxidized species have intense bands in the IR with maxima at 1400 and 900 nm, respectively, which do not overlap with the bare nanoparticle absorption spectrum.

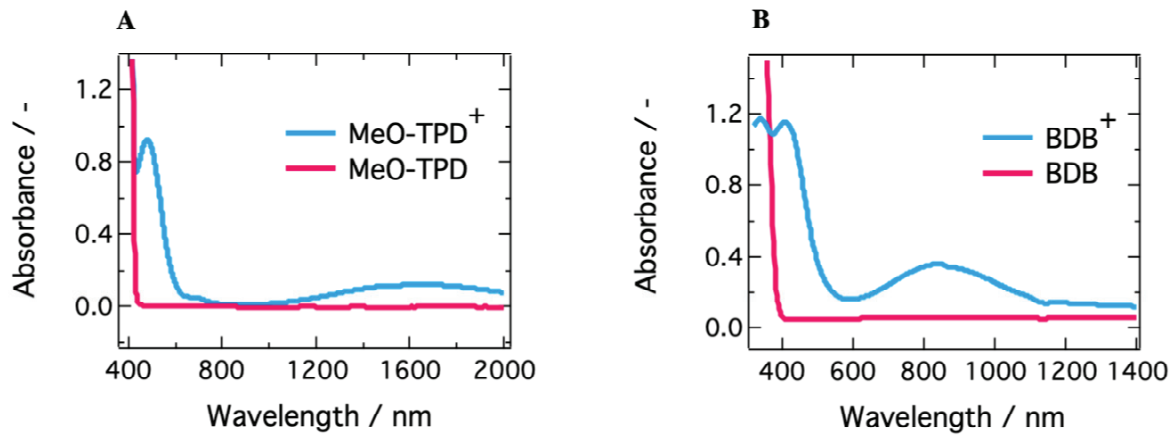

Figure 5-6 Absorption spectra of both quenchers in the neutral (red) and oxidized (blue) form. **A.** MeO-TPD and **B.** 1,4-bis(diphenylamino)benzene (BDB). The spectra of the oxidized species have been recorded after quantitative reaction of the neutral compounds with the one-electron oxidizer $NOBF_4$.

Thorough Stern-Volmer analyses have demonstrated that the two selected electron donors efficiently quench the emission of a nanoparticle mixture as reported in Figure C-3. The dynamics of those charge-transfer processes have been studied on two different timescales and with two different techniques, namely ultrafast transient absorbance (TA) to monitor the forward electron transfer and nanosecond flash photolysis to resolve the charge recombination reaction.

In the framework of time-resolved spectroscopy, a charge transfer should result in sizeable changes in the dynamics of bleaching or stimulated emission signals and the concomitant appearance of an optical signature corresponding to an oxidized quencher species. No such features could be resolved with ultrafast transient absorbance on a timescale up to 2 ns. Hence, we were not able to resolve the electron transfer dynamics from the quencher to the nanoparticles.

Figure 5-7 shows flash photolysis transient dynamics of oxidized quenchers, following λ_{ex} = 480 nm excitation of the nanoparticle solution under inert Ar atmosphere, up to 5 ms. The prompt appearance of transient absorption signals corresponding to the the oxidized state of MeO-TPD at λ_{obs} = 1500 nm and of BDB at 950 nm was observed. The rise of the signal lies within the laser pulse, and we can then assume that photoinduced interfacial charge separation occurs with a time constant of between 5 ns (TA timescale) and 1 µs (flash photolysis time resolution in the near infrared). The analysis of Stern-Volmer plots (see Figure C-3) shows that electron transfer to the valence band of perovskite involves donor molecules associated within the organic capping layer. Time constants for forward electron transfer of τ = 170 ns and 60 ns were estimated for MeO-TPD and BDB, respectively.

The recombination of conduction band electrons with the oxidized MeO-TPD$^+$ and BDB$^+$ was followed by monitoring the time evolution of the transient absorption of the latter species (Figure 5-7). The decay of the transient absorption of MeO-TPD$^+$ at λ_{obs} = 1500 nm was fitted with a biexponential rate law, yielding time constants τ_1 = 1.6 ms and τ_2 = 22 ms. In turn, the decay of the oxidized BDB appeared mainly monoexponential with τ_1 = 26 ms. Although great care was taken to minimize the excitation energy fluence to the actual limits of the instrument detection (hence the large noise marring the kinetic traces reported in Figure 5-7), it was not possible to ensure that at most one conduction band electron-oxidized donor cation pair was produced per particle and per laser pulse. Therefore, it is not expected that the recombination dynamics can be fitted by a single exponential and the initial fast component of the kinetics is likely due to a bimolecular process.

A complex kinetics for forward electron transfer and recombination could also result from a distribution of the distances separating the perovskite surface from the donor molecules that could penetrate, to some degree, the organic capping layer of the particle or rest at its external boundary. Due to the large difference in timescale, the photophysical processes intrinsic to the nanoparticles are not affected by the addition of quencher molecules. When electron transfer occurs, most of the inter-nanostructure cascade processes must, therefore, already be over, implying that the interfacial electron transfer predominantly takes place from the 3D bulk-like nanostructures. Depending on the morphology of the nanoparticle aggregates, the latter 3D structures might be more or less exposed to the solution and the donor molecules, constituting an additional source of dispersion for the kinetics of interfacial charge transfer.

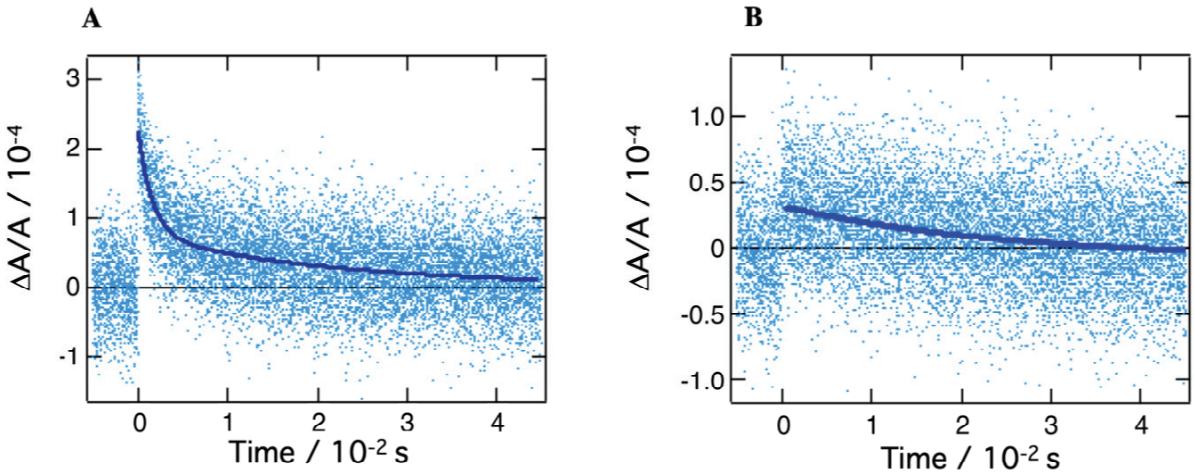

Figure 5-7 Nanosecond flash photolysis dynamics (λ_{ex}=480 nm, Ar atmosphere) for a mixture of $CH_3NH_3PbBr_3$ nanoparticles with two electron donors: MeO-TPD **(A)** and 1,4-Bis(diphenylamino)benzene **(B)** A different detection wavelength was selected for each quencher, in order to match their respective absorption maxima: λ_{obs} = 1500 nm (MeO-TPD) and 950 nm (1,4-bis(diphenylamino)benzene). Dark blue lines represent biexponetial fits of the experimental points.

5.4 Conclusion

We synthesized $CH_3NH_3PbBr_3$ perovskite nanoparticles and studied their suspension in chlorobenzene. Such suspensions contain various nanostructures: quasi-2D nanoplatelets of variable thickness and 3D bulk-like nanoparticles. These structures exhibit several optical signatures that were previously reported and assigned. The nanoplatelets are blue-shifted compared to the bulk perovskite, due to a significant confinement regime. Using a combination of steady-state, excitation-dependent ultrafast transient absorbance and TCSPC measurements, we unraveled the presence of significant inter-structure interactions in the form of a cascade of energy and charge transfer, the latter being mediated by the formation of interparticle charge transfer states. Upon photoexcitation, localized excitons are formed within one nanostructure. They either rapidly recombine, yielding a short-lived emission on the picosecond timescale, or turn into CT states following injection of one type of carrier into a narrower band-gap neighboring nanostructure. These CT excitons possess a permanent dipole and submit the material at close proximity to an electric field, which produces a significant photoinduced electroabsorption contribution to the transient absorption spectra. Carrier pairs contained in CT excitons eventually recombine, resulting in the long-lived, microsecond emission observed with TCSPC. Similar cascade charge transfer processes in highly efficient LEDs and photovoltaic devices are likely to occur in materials characterized by a multigrain morphology. As much as long-distance radiative energy transfer within the active film of a perovskite solar cell (photon recycling), non-radiative energy transfer and inter-domain charge transfer mediated by interfacial CT states could play an important role in slowing down the recombination of photocarriers and increasing their diffusion length.

The dynamics of interfacial charge transfer from donor molecules in solution to the $CH_3NH_3PbBr_3$ nanoparticles was studied. Efficient electron transfer from *N*,*N*,*N*',*N*'-tetrakis(4-methoxy-phenyl)benzidine (MeO-TPD) and 1,4-bis(diphenylamino) benzene (BDB) resulted

in an efficient quenching by up to 90% and 96%, respectively, of the photoemission of the semiconductor. The time constants of forward electron transfer were estimated at $\tau = 170$ ns and 60 ns, while a remarkably long photoinduced charge separation could be sustained for more than 20 ms in the presence of both donors.

References

(1) Saliba, M.; Matsui, T.; Seo, J.-Y.; Domanski, K.; Correa-Baena, J.-P.; Nazeeruddin, M. K.; Zakeeruddin, S. M.; Tress, W.; Abate, A.; Hagfeldt, A.; et al. Cesium-Containing Triple Cation Perovskite Solar Cells: Improved Stability, Reproducibility and High Efficiency. *Energy Environ. Sci.* **2016**, *9* (6), 1989–1997.

(2) Lee, M. M.; Teuscher, J.; Miyasaka, T.; Murakami, T. N.; Snaith, H. J. Efficient Hybrid Solar Cells Based on Meso-Superstructured Organometal Halide Perovskites. *Science* **2012**, *338* (6107), 643–647.

(3) Kim, H.-S.; Lee, C.-R.; Im, J.-H.; Lee, K.-B.; Moehl, T.; Marchioro, A.; Moon, S.-J.; Humphry-Baker, R.; Yum, J.-H.; Moser, J. E.; et al. Lead Iodide Perovskite Sensitized All-Solid-State Submicron Thin Film Mesoscopic Solar Cell with Efficiency Exceeding 9%. *Sci. Rep.* **2012**, *2*, 1–7.

(4) Im, J.-H.; Lee, C.-R.; Lee, J.-W.; Park, S.-W.; Park, N.-G. 6.5% Efficient Perovskite Quantum-Dot-Sensitized Solar Cell. *Nanoscale* **2011**, *3* (10), 4088–6.

(5) Xing, J.; Yan, F.; Zhao, Y.; Chen, S.; Yu, H.; Zhang, Q.; Zeng, R.; Demir, H. V.; Sun, X.; Huan, A.; et al. High-Efficiency Light-Emitting Diodes of Organometal Halide Perovskite Amorphous Nanoparticles. *ACS Nano* **2016**, *10* (7), 6623–6630.

(6) Bai, S.; Yuan, Z.; Gao, F. Colloidal Metal Halide Perovskite Nanocrystals: Synthesis, Characterization, and Applications. *J. Mater. Chem. C* **2016**, *4* (18), 3898–3904.

(7) Liu, S.; Sun, W.; Li, J.; Gu, Z.; Wang, K.; Xiao, S.; Song, Q. Random Lasing Actions in Self-Assembled Perovskite Nanoparticles. *Opt. Eng* **2016**, *55* (5), 057102–057110.

(8) Veldhuis, S. A.; Boix, P. P.; Yantara, N.; Li, M.; Sum, T. C.; Mathews, N.; Mhaisalkar, S. G. Perovskite Materials for Light-Emitting Diodes and Lasers. *Adv. Mater.* **2016**, *28* (32), 6804–6834.

(9) Wang, N.; Cheng, L.; Ge, R.; Zhang, S.; Miao, Y.; Zou, W. Perovskite Light-Emitting Diodes Based on Solution-Processed Self-Organized Multiple Quantum Wells. *Nat. Photon.* **2016**, *10* (11), 699–704.

(10) Protesescu, L.; Yakunin, S.; Bodnarchuk, M. I.; Krieg, F.; Caputo, R.; Hendon, C. H.; Yang, R. X.; Walsh, A.; Kovalenko, M. V. Nanocrystals of Cesium Lead Halide Perovskites (CsPbX 3, X = Cl, Br, and I): Novel Optoelectronic Materials Showing Bright Emission with Wide Color Gamut. *Nano Lett.* **2015**, *15* (6), 3692–3696.

(11) Nedelcu, G.; Protesescu, L.; Yakunin, S.; Bodnarchuk, M. I.; Grotevent, M. J.; Kovalenko, M. V. Fast Anion-Exchange in Highly Luminescent Nanocrystals of Cesium Lead Halide Perovskites (CsPbX 3, X = Cl, Br, I). *Nano Lett.* **2015**, *15* (8), 5635–5640.

(12) deQuilettes, D. W.; Vorpahl, S. M.; Stranks, S. D.; Nagaoka, H.; Eperon, G. E.; Ziffer, M. E.; Snaith, H. J.; Ginger, D. S. Impact of Microstructure on Local Carrier Lifetime in Perovskite Solar Cells. *Science* **2015**, *348* (6235), 683–686.

(13) Srimath Kandada, A. R.; Petrozza, A. Photophysics of Hybrid Lead Halide Perovskites: the Role of Microstructure. *Acc. Chem. Res.* **2016**, *49* (3), 536–544.

(14) Leblebici, S. Y.; Leppert, L.; Li, Y.; Reyes-Lillo, S. E.; Wickenburg, S.; Wong, E.; Lee, J.; Melli, M.; Ziegler, D.; Angell, D. K.; et al. Facet-Dependent Photovoltaic Efficiency Variations in Single Grains of Hybrid Halide Perovskite. *Nat. Energy* **2016**, *1* (8), 16093–16097.

(15) Pazos-Outòn, L. M.; Szumilo, M.; Lamboll, R.; Richter, J. M.; Crespo-Quesada, M.; Abdi-Jalebi, M.; Beeson, H. J.; Vrućinić, M.; Alsari, M.; Snaith, H. J.; et al. Photon Recycling in Lead Iodide Perovskite Solar Cells. *Science* **2016**, *351* (6280), 1430–1433.

(16) Manser, J. S.; Kamat, P. V. Band Filling with Free Charge Carriers in Organometal Halide Perovskites. *Nat. Photon.* **2014**, *8* (9), 737–743.
(17) Wehrenfennig, C.; Eperon, G. E.; Johnston, M. B.; Snaith, H. J.; Herz, L. M. High Charge Carrier Mobilities and Lifetimes in Organolead Trihalide Perovskites. *Adv. Mater.* **2013**, *26* (10), 1584–1589.
(18) Valverde-Chàvez, D. A.; Ponseca, C. S.; Stoumpos, C. C.; Yartsev, A.; Kanatzidis, M. G.; Cooke, D. G.; Sundström, V. Intrinsic Femtosecond Charge Generation Dynamics in Single Crystal CH3NH3PbI3. *Energy Environ. Sci.* **2015**, *8* (12), 3700–3707.
(19) Miyata, A.; Mitioglu, A.; Plochocka, P.; Portugall, O.; Wang, J. T.-W.; Stranks, S. D.; Snaith, H. J.; Nicholas, R. J. Direct Measurement of the Exciton Binding Energy and Effective Masses for Charge Carriers in Organic–Inorganic Tri-Halide Perovskites. *Nat. Phys.* **2015**, *11* (7), 582–587.
(20) Innocenzo, V. D. R.; Grancini, G.; Alcocer, M. J. P.; Kandada, A. R. S.; Stranks, S. D.; Lee, M. M.; Lanzani, G.; Snaith, H. J.; Petrozza, A. Excitons Versus Free Charges in Organo-Lead Tri-Halide Perovskites. *Nat. Commun.* **1AD**, *5*, 1–6.
(21) Zheng, K.; Zhu, Q.; Abdellah, M.; Messing, M. E.; Zhang, W.; Generalov, A.; Niu, Y.; Ribaud, L.; Canton, S. E.; Pullerits, T. Exciton Binding Energy and the Nature of Emissive States in Organometal Halide Perovskites. *J. Phys. Chem. Lett.* **2015**, *6* (15), 2969–2975.
(22) Schmidt, L. C.; Pertegás, A.; Gonzalez-Carrero, S.; Malinkiewicz, O.; Agouram, S.; Mínguez Espallargas, G.; Bolink, H. J.; Galian, R. E.; Pérez-Prieto, J. Nontemplate Synthesis of CH3Nh3PbBr3 Perovskite Nanoparticles. *J. Am. Chem. Soc.* **2014**, *136* (3), 850–853.
(23) Tyagi, P.; Arveson, S. M.; Tisdale, W. A. Colloidal Organohalide Perovskite Nanoplatelets Exhibiting Quantum Confinement. *J. Phys. Chem. Lett.* **2015**, *6* (10), 1911–1916.
(24) Gonzalez-Carrero, S.; Galian, R. E.; Pérez-Prieto, J. Maximizing the Emissive Properties of CH3NH3PbBr3 Perovskite Nanoparticles. *J. Mater. Chem. A* **2015**, *3* (17), 9187–9193.
(25) Vybornyi, O.; Yakunin, S.; Kovalenko, M. V. Polar-Solvent-Free Colloidal Synthesis of Highly Luminescent Alkylammonium Lead Halide Perovskite Nanocrystals. *Nanoscale* **2016**, *8* (12), 6578–6583.
(26) Sichert, J. A.; Tong, Y.; Mutz, N.; Vollmer, M.; Fischer, S.; Milowska, K. Z.; García Cortadella, R.; Nickel, B.; Cardenas-Daw, C.; Stolarczyk, J. K.; et al. Quantum Size Effect in Organometal Halide Perovskite Nanoplatelets. *Nano Lett.* **2015**, *15* (10), 6521–6527.
(27) Hassan, Y.; Song, Y.; Pensack, R. D.; Abdelrahman, A. I.; Kobayashi, Y.; Winnik, M. A.; Scholes, G. D. Structure-Tuned Lead Halide Perovskite Nanocrystals. *Adv. Mater.* **2015**, *28* (3), 566–573.
(28) Luo, B.; Pu, Y.-C.; Yang, Y.; Lindley, S. A.; Abdelmageed, G.; Ashry, H.; Li, Y.; Li, X.; Zhang, J. Z. Synthesis, Optical Properties, and Exciton Dynamics of Organolead Bromide Perovskite Nanocrystals. *J. Phys. Chem. C* **2015**, *119* (47), 26672–26682.
(29) Zheng, K.; Zhu, Q.; Abdellah, M.; Messing, M. E.; Zhang, W.; Generalov, A.; Niu, Y.; Ribaud, L.; Canton, S. E.; Pullerits, T. Exciton Binding Energy and the Nature of Emissive States in Organometal Halide Perovskites. *J. Phys. Chem. Lett.* **2015**, *6* (15), 2969–2975.
(30) Zhang, F.; Zhong, H.; Chen, C.; Wu, X.-G.; Hu, X.; Huang, H.; Han, J.; Zou, B.; Dong, Y. Brightly Luminescent and Color-Tunable Colloidal CH3Nh3PbX3(X = Br,

I, Cl) Quantum Dots: Potential Alternatives for Display Technology. *ACS Nano* **2015**, *9* (4), 4533–4542.
(31) Sapori, D.; Kepenekian, M.; Pedesseau, L.; Katan, C.; Even, J. Quantum Confinement and Dielectric Profiles of Colloidal Nanoplatelets of Halide Inorganic and Hybrid Organic–Inorganic Perovskites. *Nanoscale* **2016**, *8*, 6369–6378.
(32) Lanzani, G. The Photophysics Behind Photovoltaics and Photonics. **2012**, 1–4.
(33) Trinh, M. T.; Wu, X.; Niesner, D.; Zhu, X. Y. Many-Body Interactions in Photo-Excited Lead Iodide Perovskite. *J. Mater. Chem. A* **2015**, *3*, 9285–9290.
(34) Cudazzo, P.; Sottile, F.; Rubio, A.; Gatti, M. Exciton Dispersion in Molecular Solids. *J. Phys.: Condens. Matter* **2015**, *27* (11), 113204–113222.
(35) Gao, W. Z.; Li, X. G.; Wang, S. R. Synthesis of Hole-Transporting Materials Containing Triarylamine and Its Properties. *AMM* **2012**, *161*, 121–127.
(36) Cheng, H.-C.; Chiu, K. Y.; Lu, S. H.; Chen, C.-C.; Lee, Y. W.; Yang, T.-F.; Kuo, M. Y.; Chen, P. P.-Y.; Su, Y. O. Linear Oligoarylamines: Electrochemical, EPR, and Computational Studies of Their Oxidative States. *J. Phys. Chem. A* **2015**, *119* (10), 1933–1942.
(37) Zhao, H. D.; Tanjutco, C.; Thayumanavan, S. Design and Synthesis of Stable Triarylamines for Hole-Transport Applications. *Tetrahedron Lett.* **2001**, *42* (27), 4421–4424.

6 Crystal Orientation drives the Interface Physics at 3/2-Dimensional Hybrid Perovskites

6.1 Introduction

Before getting into the heart of the matter, note that this work results from the unified efforts of a large team of people. In particular, the idea for this project comes from Dr. Giulia Grancini, and the core of the story was built equally by her, her student Valentin Queloz and myself.

The intrinsic hybrid organic-inorganic nature of 3D HOIPs enables great versatility in their structural properties, providing an interesting playground for the design of structures with desirable physical and optoelectronic parameters.[1,2] As mentioned in chapter 1 (sect. 1.3.2.1), cutting the 3D framework along specific crystal planes results in layered systems where the [PbI_6] inorganic slabs are spaced by large organic cations. Among them, *Ruddlesden-Popper* or quasi-2D perovskites, with the formula $R_2A_{n-1}Pb_nI_{3n+1}$, where R is the organic spacer and n the number of inorganic slabs held together by the small A cation, have recently attracted attention for their key role in addressing the stability issue of perovskite PVs.[3-8] Within this family, if n=1 they form a R_2PbX_4 structure, called hereafter 2D perovskite. These exhibit potential for PVs with a power conversion efficiency (PCE) of around 15%.[9] This limit is dictated by the reduced charge transport with respect to the 3D parent, which is intimately linked to the poor control of the crystal growth kinetics. To surpass this limit, 3D/2D mixed systems have been proposed as efficient and stable solutions.[10-16] These can take the form of a 3D/2D blend, where the 2D acts as a dopant, or a 3D/2D interface, where the 2D functionalizes the perovskite/electron (or hole) transporting layers (ETL/HTL); such mixed systems have propelled PSC performances. However, such an empirical evolution of device processing prevents a clear control of the interface properties and structure, leading to a poor "trial and error" device optimization. A solid rationalization of the relation between interface structure and physics is thus urgent. For example, how to manipulate crystal growth by material design to drive proper crystallization of the 2D on top of the 3D, or how this impacts upon the interface charge carrier dynamics in terms of surface trapping, recombination, and device physics are paramount issues to address.

Here, we consider a stratified nanometer-thick 3D/2D interface based on $Cs_{0.1}FA_{0.74}MA_{0.13}PbI_{2.48}Br_{0.39}$/PEA-based 2D perovskites, which, when embedded in the device stack (i.e. between the mesoporous oxide ETM and the organic HTM on top) outperforms the standard 3D solar cells by increasing device open-circuit voltage (V_{oc}). We reveal that the beneficial effect of the 2D on the device performance is strictly related to the orientation of the crystal planes when growing on top of the 3D, as determined by grazing-incidence wide-angle X-ray scattering (GIWAXS). Importantly, this is dictated by specific fluorination of the cation, resulting in fluorophenethylammonium (FPEA). This cation indeed modifies the in-situ growth of the 2D, changing the ordering of the plane growth from parallel (with respect to the 3D substrate) to a disordered configuration. In turn, this impacts the interface energetics and

subsequent dynamics, which we monitored by combining time-resolved optical spectroscopy from picosecond to microsecond timescales, together with time-resolved photo-conductivity experiments.
Our results demonstrate that by modulating the cation, either planar or out-of-phase crystal orientation can be achieved, which results in a different interface physics and a more efficient electron barrier and passivation effect for the ordered planar PEAI-based 2D. Embedded in the device, the PEAI-2D functions as a physical spacer between the 3D and the HTL, and is able to retard charge recombination, ultimately explaining the enhanced V_{OC}. Importantly, the functional interface does not inhibit the current extraction, yielding solar cells with PCEs of more than 20%. Our results highlight the importance of properly choosing the 2D organic cation, providing valuable insights towards the exact control and understanding of the 3D/2D structure-function relation, paramount for the proper design of efficient multi-dimensional perovskite interfaces.

6.2 Methods

6.2.1 Device Fabrication and Testing

Fluorine doped tin oxide (FTO) glass substrates (Nippon sheet glass) were sequentially cleaned with the detergent solution, deionized water, acetone, and ethanol. A compact TiO_2 layer was coated onto the cleaned FTO substrate, heated at 450 °C, by spray pyrolysis deposition. A precursor solution was prepared by diluting titanium diisopropoxide (Sigma-Aldrich) with isopropanol (0.6 mL; 10 mL). Thereafter, we prepared a bilayer electron transport layer with mesoporous TiO_2 and SnO_2. Mesoporous TiO_2 films were prepared using a diluted TiO_2 paste (Dyesol 30 NR-D) solution. Films were prepared by spin-coating and were sintered on a hot plate at 500 °C for 30 min. The SnO_2 layer was prepared by spin-coating a precursor solution of $SnCl_4$ (Acros) dissolved in water. 0.1 M of $SnCl_4$ aqueous solution was spin-coated and sintered on a hot plate at 180 °C for 1 h. The lead excess $(FAPbI_3)_{0.85}(MAPbBr_3)_{0.15}$ precursor solution was prepared by mixing FAI (1.1 M), PbI_2 (1.15 M), MABr (0.2 M), and $PbBr_2$ (0.2 M) in a mixed solvent of DMF:DMSO = 4:1 (volume ratio). Another solution of $CsPbI_3$ was also prepared as 1.15 M solution in DMF:DMSO (same volume ratio). For the triple cation mixed perovskite solution, $(FAPbI_3)_{0.85}$, $(MAPbBr_3)_{0.15}$ and $CsPbI_3$ solutions were mixed with a 10:1 vol% ratio. The perovskite precursor solution was spin coated at 2000 rpm for 10 s, followed by 5000 rpm for 30 s. Trifluorotoluene (110 µL) was dropped onto the spinning substrate a 10 s into the second step. The films were annealed at 100 °C for 60 min in the glove box. For forming an additional 2D perovskite film on top of this perovskite film, substrates were treated with a PEAI (or FPEAI) isopropanol solution. 100 ml of PEAI (or FPEAI) solution (10 mg/ml) were spin-coated on the 3D perovskite films at 5000 rpm, which is similar to the anti-solvent dropping method. The films were annealed once more at 100 °C for 10 min to make a 2D perovskite layer on the 3D perovskite film. Spiro-OMeTAD was spin-coated at 4000 rpm for 20 s. A 70 mM spiro-OMeTAD solution was prepared by dissolving in chlorobenzene with 4-tert-butylpyridine, Li-TFSI in acetonitrile, and $Co[t\text{-}BuPyPz]_3[TFSI]_3$ (FK209) in acetonitrile

at a molar ratio of spiro:TBP:Li-TFSI:FK209 of 1:3.3:0.5:0.03 Finally, 70 nm of Au was deposited by thermal evaporation as the back electrode.
The solar cell measurement was done using commercial solar simulators (Oriel, 450 W, Xenon, AAA class). The light intensity was calibrated with a Si reference cell equipped with an IR-cutoff filter (KG3, Newport) and it was recorded before each measurement. Current–voltage characteristics of the cells were obtained by applying an external voltage bias while measuring the current response with a digital source meter (Keithley 2400/2604). The voltage scan rate was 50 $mV \cdot s^{-1}$ and no device preconditioning, such as light soaking or forward voltage bias, was applied before starting the measurement. The cells were masked with the active area of 0.16 cm^2 to fix the active area and reduce the influence of the scattered light.

6.2.2 Optical measurements

Ultrafast transient absorbance (TA) spectra were acquired in the same ways as described in chapter 3 (sect. 3.2.3) and 4 (sect. 4.2.2), with two different excitation wavelengths: λ_{ex} = 390 nm and λ_{ex}=600 nm.

Steady-state absorption spectra were acquired with a Perkin Elmer Lambda 950s UV/vis/NIR spectrophotometer using an integrating sphere to account for optical losses outside of the active layer.

Steady-state and time-resolved photoluminescence measurements were carried out using a Horiba Fluorolog-3, with a PMT as the detector. The excitation source for the TCSPC was a Horiba nanoLED-370 with an excitation wavelength of 369 nm, a pulse duration of 1.3 ns and a repetition rate of 1 MHz.

6.2.3 TRMC measurements

For TRMC measurements the samples have been loaded into air-tight resonant cavity (low intensity measurements) and open cell (high intensities) holders in a N_2 filled glovebox. The traces have been measured upon pulsed (10 Hz, 3 ns FWHM) photoexcitation at 650 nm from a Q-switched Nd:YAG laser ("Infinity 15-30", Coherent).[10] Excitation intensities were varied in the range 10^9-10^{12} photons/cm^2.

6.2.4 GIWAXS measurements

GIWAXS measurements were carried out in reflection geometry at beamline 7.3.3 of the Advanced Light Source, Lawrence Berkeley National Laboratory. Samples were measured at a detector distance of 0.249 m using an X-ray wavelength of 1.240 Å, at 0.18° angle of incidence with respect to the substrate plane. Calibration was performed with a silver behenate standard. Scattering intensity was detected by a PILATUS 2M detector.[1] Nika software package was used to sector average the 2D GIWAXS images.[2] Data plotting was done in Igor Pro (Wavemetrics, Inc., Lake Oswego, OR, USA).

6.2.5 Solar cell characterization

The photovoltaic device performance was analyzed in air under AM 1.5G (100W cm^{-2}) simulated sunlight using a potentiostat (Keithley). The light intensity was calibrated with an NREL certified KG5 filtered Si reference diode. The solar cells were masked with a metal aperture of 0.16 cm^2 to define the active area. The density current-voltage curves were recorded scanning at 10 mV s^{-1}.

6.3 Results and discussion

6.3.1 Sample architecture and device characterization

Figure A represents a sketch of the 3D/2D perovskite solar cell architecture, highlighting the chemical structures of the PEAI and fluorinated analogue, F-PEAI, obtained by the para-substitution of one fluorine atom on the phenyl moiety cations. Recently, similar compounds have been used in quasi-2D based solar cells, showing that the fluorinated version imparts a better alignment of the perovskite sheet stacking, responsible for the better PCE (around 14%). In our work, we develop a stratified 3D/2D interface where the 2D is dynamically grown on top of the 3D. This results in a few tens of nanometers thick 2D crust (20-60 nm, see scanning electron microscopy images in Figure D-1).[11,12] Device current-voltage characteristics and parameters are presented in **Figure** B and Table , while **Figure** C shows the V_{OC} statistics (see Figure D-2 for full device statistics). Solar cells involving a 3D/2D interface outperform their 3D reference, with a clear improvement in the device V_{OC}, without causing a detrimental loss of current. Notably, the boost in the V_{OC} appears higher for the PEAI-based 2D with respect to the F-PEAI-based 2D, overall leading to a 20.62% PCE for the champion device. Such improvement asks for a deeper understanding on the optoelectronic processes governing the device operation, which is of key importance for device development, often disregarded. We herein investigate the processes at the 3D/2D interface as well as at the 3D/2D/HTM interfaces, using a combined series of light-induced spectroscopic tools to shed light on the interface energetics and carrier dynamics, from the picosecond to the microsecond timescale.

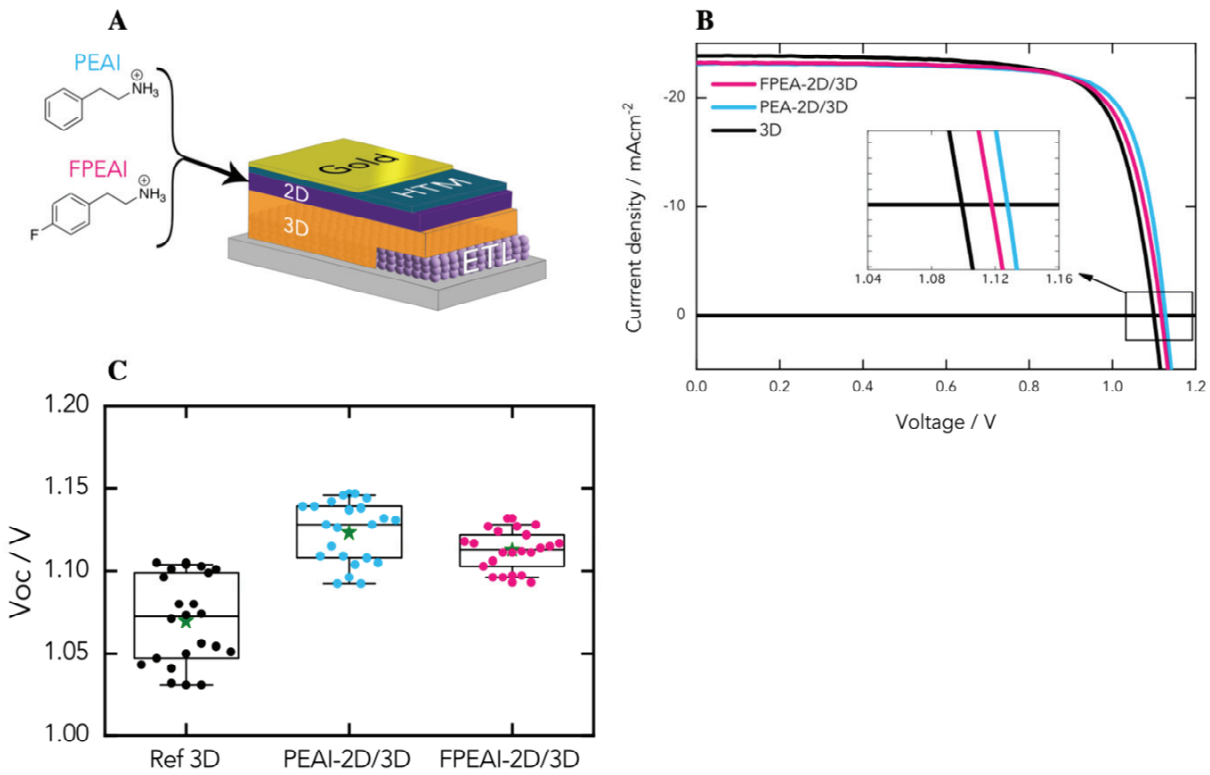

Figure 6-1 A. Scheme of the solar cell with the chemical structure of the two PEAI cations used for the 2D layer. **B.** J-V characteristics of the 3D solar cell compared to the 2D-PEAI/3D and 2D-FPEAI/3D devices. Inset: close-up of the JV curve close to V_{OC}. **C.** V_{OC} statistics for the two bilayers and the reference cell.

	PCE (%)	V_{oc} (V)	J_{sc} (mAcm^{-2})	FF
FPEAI-2D/3D	20.53	1.127	23.21	0.784
PEAI-2D/3D	20.62	1.138	23.43	0.774
Ref 3D	19.48	1.104	23.25	0.759

Table 6-1 Solar cell parameters corresponding to the curves in Figure A.

6.3.2 Energetic picture within PEAI-2D/3D and FPEAI-2D/3D bilayers

Given the complexity of the 3D/2D system and the paramount importance of the 3D/2D interface energy level alignment, we have combined X-ray photoelectron spectroscopy (XPS) with broadband transient absorbance (TA). In TA, the selective excitation of the components will enable us to monitor the photoinduced processes from the 3D to the 2D inversely, allowing us to retrieve the energy level alignment.

Figure 6-2A and B display the TA spectra and dynamics for 3D perovskite and 3D/2D systems upon excitation at λ_{ex}=600 nm (selectively exciting the 3D), while Figure 6-2C and D are obtained upon pumping at λ_{ex}=390 nm (exciting both 2D and 3D). When exciting only the 3D (Figure 6-2A), the signal is dominated by a large negative feature peaking at 750 nm, which forms with a time constant of 300 fs and persists throughout the investigated time window (1.5 ns). This feature relates to ground state bleaching (GSB) upon state filling at the 3D perovskite band edge.[13] The TA spectra of the 3D/2D systems are identical, with no difference in the

evolution of the GSB (Figure 6-2B). Given that the GSB is proportional to the photoexcited carrier density, its evolution reflects the charge dynamics. This indicates that no energy or charge transfer occurs (from the 3D to the 2D) when only the 3D is excited.

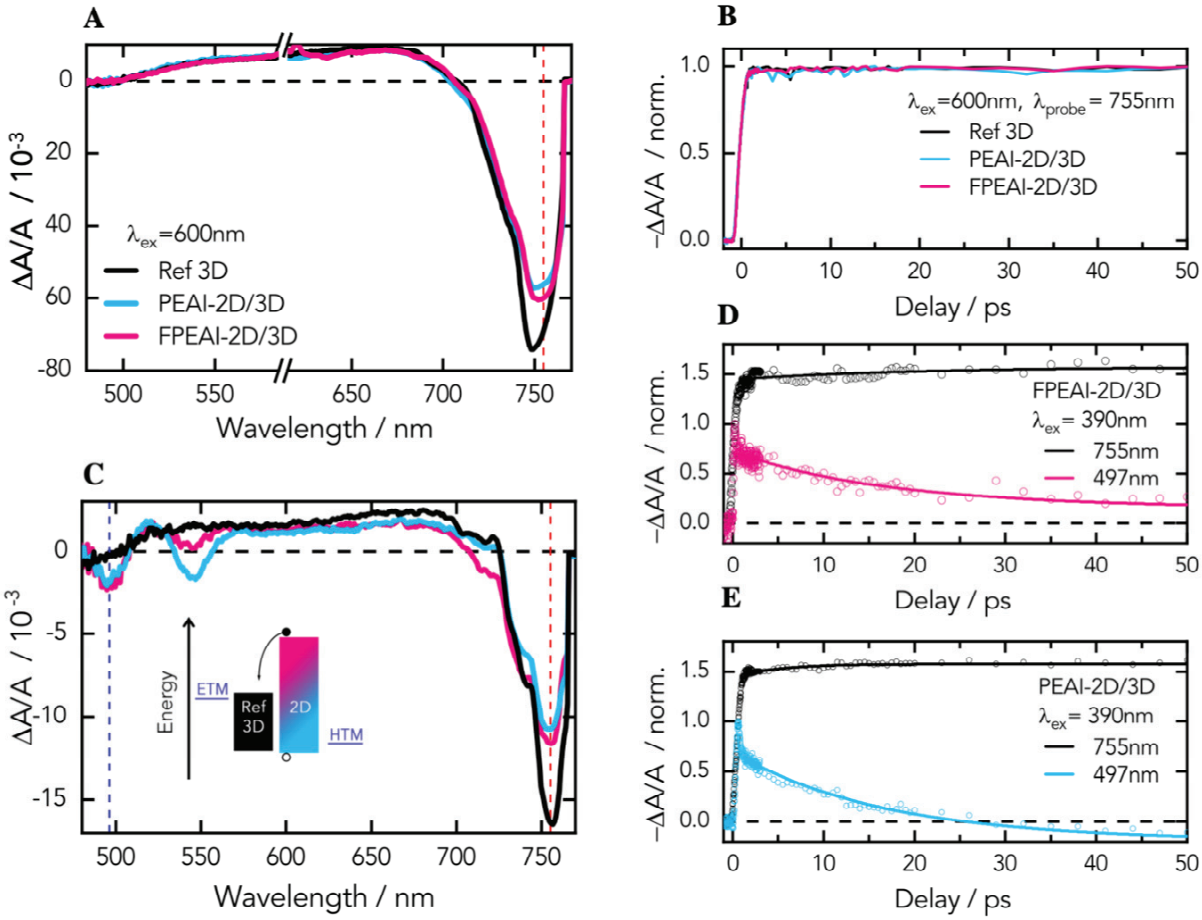

Figure 6-2 A. Transient absorption (TA) spectra of 3D perovskite, PEAI-2D/3D and FPEAI-2D/3D bilayers (excitation wavelength λ_{ex}= 600 nm, carrier density of 10^{18} cm^{-3}) at 1 ps delay (spectra up to 1 ns in Figure D-3) **B.** TA dynamics at 755 nm comparing 3D perovskite with PEAI-2D/3D and FPEAI-2D/3D bilayers (excitation wavelength λ_{ex}= 600 nm, carrier density of 10^{18} cm^{-3}). **C.** TA spectra of 3D perovskite, PEAI-2D/3D and FPEAI-2D/3D bilayers (excitation wavelength λ_{ex}= 390 nm, carrier density of 10^{18} cm^{-3}) at 1 ps delay (spectra up to 1 ns in Figure D-4). In inset: illustration of band diagram and of the charge transfer from the 2D to the 3D perovskite. **D, E.** TA dynamics of FPEAI-2D/3D and PEAI-2D/3D respectively, at 497 nm and 755 nm upon excitation at 390 nm (carrier density of 10^{18} cm^{-3}).

Alternatively, when exciting at λ_{ex}=390 nm, the TA spectra (Figure 6-2C) for the 3D/2D differ from the sole 3D. Two additional bumps appear in the blue region (500-575 nm). They arise from the excitation of the 2D layer, and relate to the GSB of the 2D perovskite. The corresponding dynamics for both FPEAI-2D/3D and PEAI-2D/3D are presented in Figure 6-2D and E, and are compared to the GSB dynamics of the 3D at 750 nm. A clear trend is observed: the GSB at 750 nm rises (with a time constant of a few ps, see Table D-1) while the GSB at 500 nm decays with a similar time constant. This can be rationalized as charge or energy transfer from the 2D to the 3D. However, we can safely exclude the latter through photoluminescence (PL) and PL-excitation (PLE) analysis (Figure D-5, D-6), indicating no

energy transfer at the interface. Combining this information with the dynamical picture retrieved from the TA analysis, we can thus conclude that charge transfer occurs from the 2D to the 3D. From this picture, together with XPS (Figure D-7) measurements, we extracted the energy level alignment in our systems as illustrated in the inset of Figure 6-2C. The valence band maximum (VBM) of the 2D perovskite is just slightly down shifted by 0.1 eV with respect to the VBM of the 3D perovskite. Given the band gap of 2D perovskites, of around 3 eV, their conduction band minimum (CBM) lies well above the CBM of the 3D perovskite. We thus propose that 2D perovskites act as a barrier for electrons.

6.3.3 Free carrier dynamics at the PEAI-2D/3D and FPEAI-2D/3D interfaces

To gain insight into the free carrier dynamics at the interfaces, the main goal of our work, we employed time resolved photoluminescence (TRPL) and time-resolved microwave-conductivity (TRMC) targeting the 3D/2D interfaces (Figure 6-3A, B) as well as the 3D/2D/HTM system (Figure 6-3C, D).

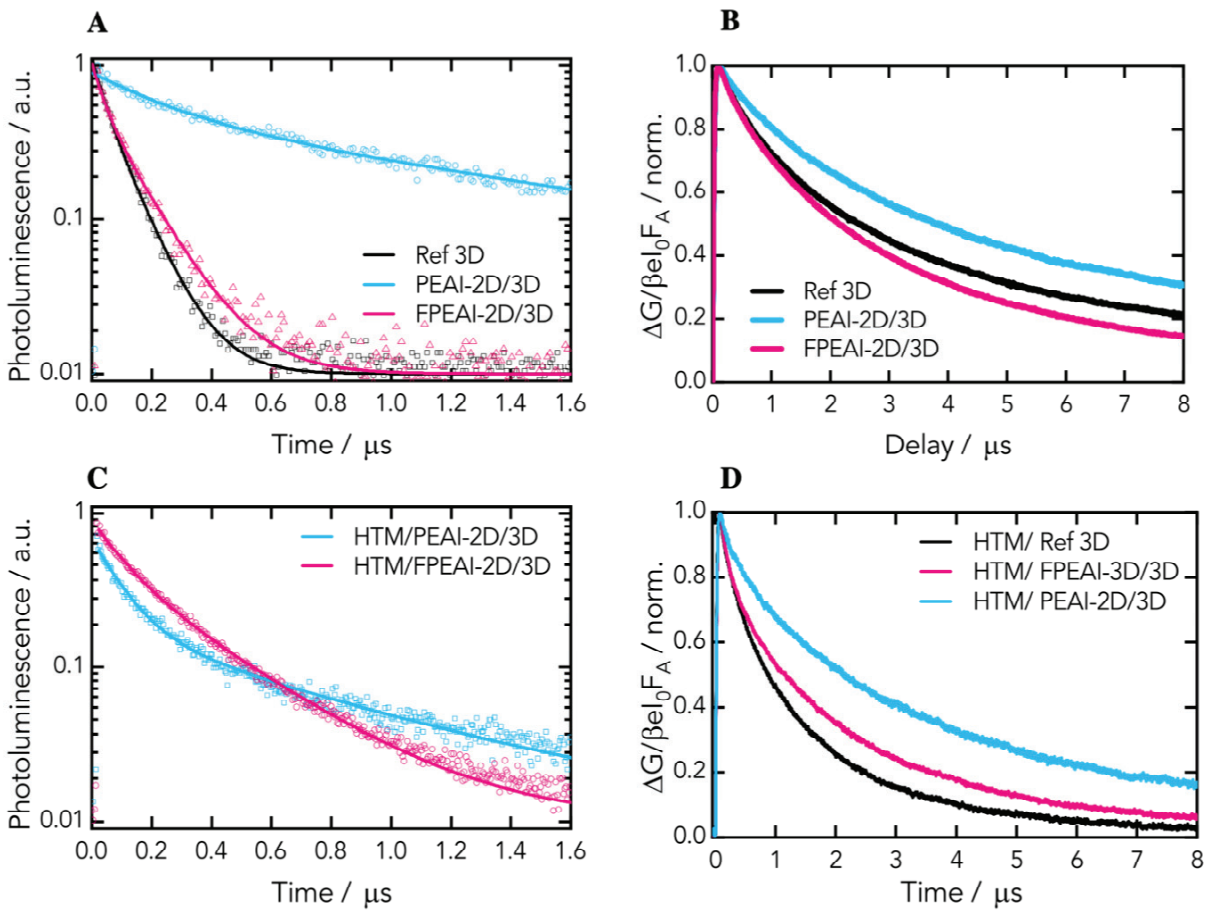

Figure 6-3 A. Normalized Photoluminescence (PL) decay of PEAI-2D/3D, FPEAI-2D/3D and Ref 3D sample (excitation wavelength λ_{ex}= 635 nm, carrier density of 10^{14} cm^{-3}) **B.** Normalized time resolved microwave conductivity (TRMC) of the same samples (λ_{ex}= 650 nm, carrier density of 10^{14} cm^{-3}). **C.** Normalized PL decay of HTM/PEAI-2D/3D, HTM/FPEAI-2D/3D sample (λ_{ex}= 635 nm, carrier density of 10^{14} cm^{-3}). **D.** Normalized

TRMC of bilayers of HTM/PEAI-2D/3D, HTM/FPEAI-2D/3D and HTM/3D (λ_{ex}= 650 nm, carrier density of 10^{14} cm^{-3}).

Figure 6-3A shows the TRPL decays at 780 nm, monitoring the 3D emission with or without the 2D layer. Note that in both cases we selectively excite the 3D with an excitation density of 10^{14} carriers/cm^3. Decays of 3D and FPEAI-2D/3D perovskite show a similar behavior (slightly slower for the FPEAI-2D/3D), while the PEAI-2D exhibits a much slower PL decay (Table D-3 for time constants). Figure 6-3B shows the TRMC signal, which monitors the free charges generated within the 3D slab and their dynamical evolution (see Figure D-8 for carrier density dependent dynamics). Notably, the initial amplitude of the TRMC signal is proportional to both the yield of free charges generated upon photoexcitation and their mobility, while the decay mirrors the charge immobilization or recombination.[14] No sizeable differences are observed between the initial TRMC amplitudes of the 3D and the 2D/3D-modified surfaces (see Figure D-9). However, their dynamics are different, as PEAI-2D shows a slower decay with respect to the bare 3D, while the decay of FPEAI-2D is similar to that of the bare 3D.
The combined TRPL and TRMC findings can be rationalized as follows: i) the initial TRMC amplitudes indicate that no significant 3D to 2D hole transfer is taking place, as this would have lowered the amplitude of the signal at time zero (for instance, as is the case at the HTM/3D interface, see Figure D-9), confirming the TA results; ii) the slower decay in both PL and TRMC results for PEAI-2D/3D indicates a delayed electron-hole recombination, possibly related to surface passivation (see Table D-3); iii) this does not extend to the FPEAI-2D/3D system, which exhibits similar behavior with respect to the bare 3D. To determine the kinetic parameters from the TRMC measurements, we have applied the kinetic model described in the paper by Hutter *et al*. (see the relevant parameters summarized in Table D-4, together with a description of the model and experimental fits in Figure D-10).[15] Interestingly, the bimolecular recombination rate constant, k_2, is halved upon addition of PEAI- or FPEAI-2D layers on the 3D perovskite. As previously reported, k_2 represents the sum of all bimolecular recombination processes.[16] The bimolecular recombination process occurring at the 3D surface is therefore considerably retarded by introducing the 2D perovskite. The enhanced lifetimes in the case of the PEAI-2D/3D samples are related to the significantly reduced number of background charges in the material, which slows down the bimolecular recombination. In light of this, and in agreement with the energy level alignment previously discussed, we conclude that the PEAI-2D/3D interface can retard the electron-hole recombination and passivate the 3D surface much more efficiently compared to the FPEAI-based system.

Figures 6-3C and D show the TRPL and TRMC signals for 3D/2D/HTM systems. From Figure 6-3C, the PL of both samples show similar decays, with a slower tail component for the PEAI-2D/3D system (see Table D-4 for the time constants). In turn, the TRMC measurements in Figure 6-3D (see also Figure D-9) indicate that the initial amplitudes drop, and the dynamics become faster when an HTM is added to the system. This is indicative of a reduction of the charge density due to hole transfer and of a faster decay due to interfacial recombination. Comparing the TRMC signals of the 3D/HTM and 3D/2D/HTM samples, we observe that the addition of a 2D layer does not hinder the charge transfer to the HTM (initial amplitude reduction, see Figure D-9), but recombination is slowed down, more visibly for the PEAI-based

system. As a consequence, the 2D layer can act as a physical spacer, especially in the case of PEAI-2D, where back electron-hole recombination is retarded.

Overall, our results point to a beneficial effect of the 2D layer that reduces surface recombination, which can explain the improvement in the device V_{OC}. As an important remark, we observe that this statement does not hold a general validity but strongly depends upon the chemical nature of the organic cation in the 2D. In particular, despite the close energetics and similar electronic structure of their corresponding 2D, PEAI-2D/3D and FPEAI-2D/3D behave differently.

6.3.4 Structural insights

To address the reason behind such different behaviors, we investigated the structural properties of the interfaces and the crystal orientation by GIWAXS. This technique is extremely surface-sensitive at incident angles below the critical angle, allowing us to directly probe the 2D perovskite layer. GIWAXS maps and corresponding sector averages are shown in Figure 6-4.

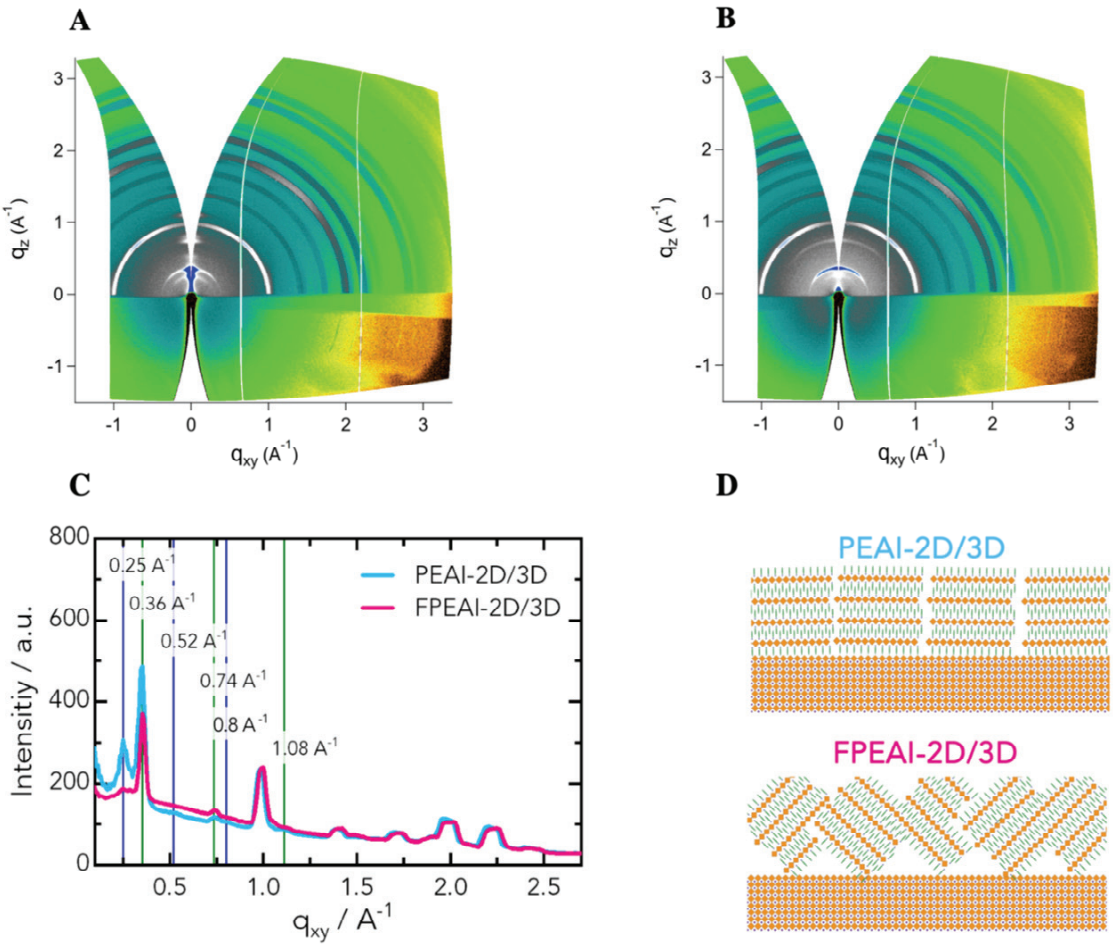

Figure 6-4 Orientation analysis from GIWAXS. **A.** 2D layers of PEAI-2D/3D are found to be strongly oriented parallel to the underlying 3D phase, as schematized in **B.** On the other hand, the 2D layers in FPEAI-2D/3D has a considerably more random orientation. **C.** 2D GIWAXS sector average for PEAI-2D and FPEAI-2D layers atop 3D bulk. Note the oriented rings in low-q region below the 3D bulk perovskite peak of qz = qxy = 1.0 Å^{-1}. PEAI-

2D layer clearly shows relatively more intermixing of lower dimensionalities compared to the FPEAI-2D. This is highlighted in **D**.

Diffraction peaks associated with the lamella structure of the 2D phase are clearly visible for q_{xy} <1.0 Å^{-1} and correspond to the (0k0) planes. Both the PEAI-2D and FPEAI-2D layers show a major diffraction peak for the pure 2D phase (n=1), with first order at 0.36 Å^{-1} and higher orders at 0.74 Å^{-1} and 1.08 Å^{-1}. We also report a minor intermixing phase reflecting in a weak n=2 diffraction peak (first order at 0.25 Å^{-1}, higher orders at 0.52 Å^{-1} and 0.80 Å^{-1}). Interestingly, the PEAI-2D layer exhibits a larger extent of n=2 phase compared to FPEAI-2D with a stronger first-order 0.25 Å^{-1} peak. This assignment is also supported by the PL and TA spectra. PL spectra (Figure D-5, D-6) show a weak shoulder at 550 nm assigned to n=2 quasi-2D perovskite emission; and TA spectra (λ_{ex}=390 nm, Figure 6-2A) exhibit a second peak at 540 nm associated to the GSB of the n=2 Quasi-2D perovskite, as previously discussed. The first-order peak 0.36 Å^{-1} belonging to the n=1 lattice was integrated with respect to the azimuthal angle (χ) to glean information regarding the orientation of the 2D perovskite planes. Results are reported in Figure comparing the FPEAI-2D- and the PEAI-2D-based interfaces. From Figure 6-4A, it is clear that the peak integral is almost entirely in a range of χ = 0°-5°, suggesting that the PEAI-2D layers assume a parallel orientation with respect to the underlying 3D phase and the substrate (as observed in other 2D-based systems).[17] On the contrary, the formation of FPEAI-3D layers is more random: a majority of these layers have a 40°-45° orientation with respect to the 3D phase and the substrate (see Figure 6-4D).
We suggest that the different crystallite orientation of PEAI-2D and FPEAI-2D is the reason behind the different interfacial physics observed. The parallel orientation of PEAI-2D delays charge recombination, with a direct positive impact on the charge carrier lifetime and thus on the device V_{OC}. On the contrary, the random orientation of FPEAI-2D compromises the beneficial effect of the 2D interlayer in terms of enhanced charge carrier lifetime. In addition, this would allow partial interpenetration of the HTM, resulting in a similar behavior for the FPEAI-2D compared to the pure 3D system. Our findings put forward a different picture with respect to common knowledge: while much effort has been put to orient the 2D planes perpendicular to the substrate in a way to maximize charge transport and extraction[18-20], here we reveal that, contrarily, planar orientation is needed for the case of 3D/2D interfaces, to optimize interface processes and device performances. A similar finding has only been revealed for Sn-based 3D/2D interfaces where planar growth of the 2D is essential for device operation.[17] Further analysis, beyond the scope of the presented work, will be needed to clarify the transport mechanism through the organic barrier.

6.3.5 Conclusion

To conclude, we elucidate the opto-electronic properties and carrier dynamics at 3D/2D interfaces leading to highly efficient solar cells. Our results provide compelling evidence of the crucial role of the crystal alignment of the 2D perovskite on top of 3D perovskite. If the 2D perovskite is oriented “flat” with respect to the substrate, it can effectively passivate the surface while retarding charge recombination. This results in an enhanced V_{OC} of the solar cells and overall improved performances. On the other hand, a more disordered 2D perovskite alignment

limits such beneficial effect. We demonstrate that such alignment can be controlled by fine tuning the chemical composition of the 2D cation, i.e. by simple atomic substitution, providing a new guideline for material and interface design. Our findings provide a deeper understanding of the main parameters governing the 3D/2D interface physics with important reverberation on interface development for solar cells, and opto-electronics devices.

References

(1) Grancini, G.; Nazeeruddin, M. K. Dimensional Tailoring of Hybrid Perovskites for Photovoltaics. *Nat Rev Mater* **2018**, 1–19.

(2) Brenner, T. M.; Egger, D. A.; Kronik, L.; Hodes, G.; Cahen, D. Hybrid Organic—Inorganic Perovskites: Low-Cost Semiconductors with Intriguing Charge-Transport Properties. *Nat Rev Mater* **2016**, *1* (1), 1443–17.

(3) Milot, R. L.; Sutton, R. J.; Eperon, G. E.; Haghighirad, A. A.; Martinez Hardigree, J.; Miranda, L.; Snaith, H. J.; Johnston, M. B.; Herz, L. M. Charge-Carrier Dynamics in 2D Hybrid Metal–Halide Perovskites. *Nano Lett.* **2016**, *16* (11), 7001–7007.

(4) Becker, M. A.; Vaxenburg, R.; Nedelcu, G.; Sercel, P. C.; Shabaev, A.; Mehl, M. J.; Michopoulos, J. G.; Lambrakos, S. G.; Bernstein, N.; Lyons, J. L.; et al. Bright Triplet Excitons in Caesium Lead Halide Perovskites. *Nature* **2018**, *553* (7687), 189–193.

(5) Protesescu, L.; Yakunin, S.; Bodnarchuk, M. I.; Krieg, F.; Caputo, R.; Hendon, C. H.; Yang, R. X.; Walsh, A.; Kovalenko, M. V. Nanocrystals of Cesium Lead Halide Perovskites (CsPbX 3, X = Cl, Br, and I): Novel Optoelectronic Materials Showing Bright Emission with Wide Color Gamut. *Nano Lett.* **2015**, *15* (6), 3692–3696.

(6) Even, J.; Pedesseau, L.; Katan, C. Understanding Quantum Confinement of Charge Carriers in Layered 2D Hybrid Perovskites. *ChemPhysChem* **2014**, *15* (17), 3733–3741.

(7) Chen, Y.; Sun, Y.; Peng, J.; Tang, J.; Zheng, K.; Liang, Z. 2D Ruddlesden-Popper Perovskites for Optoelectronics. *Adv. Mater.* **2017**, *30* (2), 1703487–15.

(8) Achtstein, A. W.; Prudnikau, A. V.; Ermolenko, M. V.; Gurinovich, L. I.; Gaponenko, S. V.; Woggon, U.; Baranov, A. V.; Leonov, M. Y.; Rukhlenko, I. D.; Fedorov, A. V.; et al. Electroabsorption by 0D, 1D, and 2D Nanocrystals: a Comparative Study of CdSe Colloidal Quantum Dots, Nanorods, and Nanoplatelets. *ACS Nano* **2014**, *8* (8), 7678–7686.

(9) Askerka, M.; Li, Z.; Lempen, M.; Liu, Y.; Johnston, A.; Saidaminov, M. I.; Zajacz, Z.; Sargent, E. H. Learning-in-Templates Enables Accelerated Discovery and Synthesis of New Stable Double Perovskites. *J. Am. Chem. Soc.* **2019**, *141* (8), 3682–3690.

(10) Kroeze, J. E.; Savenije, T. J.; Vermeulen, M. J. W.; Warman, J. M. Contactless Determination of the Photoconductivity Action Spectrum, Exciton Diffusion Length, and Charge Separation Efficiency in Polythiophene-Sensitized TiO 2Bilayers. *J. Phys. Chem. B* **2003**, *107* (31), 7696–7705.

(11) Cho, K. T.; Grancini, G.; Lee, Y.; Oveisi, E.; Ryu, J.; Almora, O.; Tschumi, M.; Schouwink, P. A.; Seo, G.; Heo, S.; et al. Selective Growth of Layered Perovskites for Stable and Efficient Photovoltaics. *Energy Environ. Sci.* **2018**, *11* (4), 952–959.

(12) Cho, K. T.; Zhang, Y.; Orlandi, S.; Cavazzini, M.; Zimmermann, I.; Lesch, A.; Tabet, N.; Pozzi, G.; Grancini, G.; Nazeeruddin, M. K. Water-Repellent Low-Dimensional Fluorous Perovskite as Interfacial Coating for 20% Efficient Solar Cells. *Nano Lett.* **2018**, *18* (9), 5467–5474.

(13) Grancini, G.; Kandada, A. R. S.; Frost, J. M.; Barker, A. J.; De Bastiani, M.; Gandini, M.; Marras, S.; Lanzani, G.; Walsh, A.; Petrozza, A. Role of Microstructure in the Electron-Hole Interaction of Hybrid Lead Halide Perovskites. *Nat. Photon.* **2015**, *9* (10), 695–701.

(14) Hutter, E. M.; Hofman, J.-J.; Petrus, M. L.; Moes, M.; Abellón, R. D.; Docampo, P.; Savenije, T. J. Charge Transfer From Methylammonium Lead Iodide Perovskite to

Organic Transport Materials: Efficiencies, Transfer Rates, and Interfacial Recombination. *Adv. Energy Mater.* **2017**, *7* (13), 1602349–8.
(15) Hutter, E. M.; Eperon, G. E.; Stranks, S. D.; Savenije, T. J. Charge Carriers in Planar and Meso-Structured Organic–Inorganic Perovskites: Mobilities, Lifetimes, and Concentrations of Trap States. *J. Phys. Chem. Lett.* **2015**, *6* (15), 3082–3090.
(16) Brenes, R.; Guo, D.; Osherov, A.; Noel, N. K.; Eames, C.; Hutter, E. M.; Pathak, S. K.; Niroui, F.; Friend, R. H.; Islam, M. S.; et al. Metal Halide Perovskite Polycrystalline Films Exhibiting Properties of Single Crystals. *Joule* **2017**, *1* (1), 155–167.
(17) Shao, S.; Liu, J.; Portale, G.; Fang, H.-H.; Blake, G. R.; Brink, ten, G. H.; Koster, L. J. A.; Loi, M. A. Highly Reproducible Sn-Based Hybrid Perovskite Solar Cells with 9% Efficiency. *Adv. Energy Mater.* **2017**, *8* (4), 1702019–10.
(18) Arai, R.; Yoshizawa-Fujita, M.; Takeoka, Y.; Rikukawa, M. Orientation Control of Two-Dimensional Perovskites by Incorporating Carboxylic Acid Moieties. *ACS Omega* **2017**, *2* (5), 2333–2336.
(19) Zhang, X.; Wu, G.; Yang, S.; Fu, W.; Zhang, Z.; Chen, C.; Liu, W.; Yan, J.; Yang, W.; Chen, H. Vertically Oriented 2D Layered Perovskite Solar Cells with Enhanced Efficiency and Good Stability. *Small* **2017**, *13* (33), 1700611–1700618.
(20) Chen, A. Z.; Shiu, M.; Ma, J. H.; Alpert, M. R.; Zhang, D.; Foley, B. J.; Smilgies, D.-M.; Lee, S.-H.; Choi, J. J. Origin of Vertical Orientation in Two-Dimensional Metal Halide Perovskites and Its Effect on Photovoltaic Performance. *Nat. Commun.* **2018**, 1–7.

7 A speculative study of the polaronic character of excitons in 2D perovskites

7.1 Introduction

The enhanced charge carrier correlation of 2D HOIPs, due to quantum and dielectric confinement, is prone to generate higher-order interactions (biexcitons, trions).[1] Similarly, because of the polar nature of the inorganic lattice, charge carriers are likely to self-trap, forming polarons, as already demonstrated for 3D perovskites.[2-5] The combination of these effects, along with the current effort to link specific cation properties to specific photophysical behavior, reflects the complex nature of 2D perovskites.

In the following discussion, we will focus on two different 2D HOIPS based on the following cations: Butylammonium (BUA) and fluorophenetylammonium (FPEA), whose structures are presented in Figure 7-1. Those perovskites are herein labeled BUAI-2D and FPEAI-2D, respectively. We perform fluence-dependent transient absorbance (TA) measurements on the two systems and report complex spectral features. By analyzing the dependence of the carrier density on both the amplitude of the features of interest and their dynamics, we propose that the photophysics of our systems results from the interplay of various polaronic interactions. We further extend our study by measuring the steady-state and long-time electroabsorption signals of BUAI-2D and another perovskite based on a highly disordered cation (A43I-2D, see Figure 7-4). From this, we speculate on the electron/hole-phonon coupling strength in four different perovskites, and formulate the following principle: the photophysics of 2D HOIPs is dominated by polarons, whose size can be directly related to a given macroscopic property of the cation: its disorder!

7.2 Experimental

7.2.1 Sample preparation

The $(FPEA)_2PbI_4$ and $(BUA)_2PbI_4$ thin-films were made from solutions prepared by dissolving 1.2M of PbI_2 and 2.4M of the BUA (FPEA) cation in DMSO. The solutions were then deposited onto the substrates via a consecutive two-step spin-coating process at 1000 rpm for 10 s and 5000 rpm for 30 s. During the second step, 100 µL of chlorobenzene was deposited. The resulting films were then annealed at 100 °C for 15 minutes.
The $(A43)_2PbI_4$ thin films used in the EA and ns-TA measurement were fabricated by preparing a precursor solution with a 2:1 molar ratio of the corresponding cation (A43) and PbI2 in DMSO. We used a one-step deposition method using chlorobenzene as antisolvent. The thin film was annealed at 100 ºC for 15 minutes.
Samples intended for transient absorbance measurements (ns and fs) were simply deposited on glass substrates. In turn, samples subjected to EA experiments were deposited on FTO (back

contact), while the top electrode was obtained by gold evaporation. For a more complete description, see ref [6].

7.2.2 Optical measurements

Steady-state absorption spectra were acquired with a Perkin-Elmer Lambda 950s UV/vis/NIR spectrophotometer using an integrating sphere to account for optical losses outside of the active layer.

Nanosecond transient absorbance (ns-TA) measurements were performed with a LP980 laser flash spectrometer (Edinburgh Instruments). The system is based on a standard transient absorbance setup where the sample is excited by a ns laser pulse and the time evolution of the differential absorption changes induced by the pump is monitored by a CW light source probe. The pump pulses are provided by a nanosecond tunable Ekspla NT340 laser (5 Hz repetition rate). The probe light is provided by a pulsed Xenon arc lamp. The sample was kept at a 45° angle to the excitation beam. The beams are focused onto the sample ensuring spatial overlap. The transmitted probe is spectrally filtered by a monochromator and detected with a photomultiplier enabling one to collect the single-wavelength kinetics with high sensitivity. The signal is finally recorded by an oscilloscope. The system has a sensitivity of $\sim 5 \cdot 10^{-4}$ and a temporal resolution of ~ 8 ns. The data were smoothed by a fit with biexponential functions of the form $A_1\exp(-t/\tau_1) + A_2\exp(-t/\tau_2)$, where A_1 and A_2 are prefactors and τ_1 and τ_2 are time constants. In turn, femtosecond transient absorbance measurements were carried out in the exact same way as described in chapter 6 (λ_{ex}=390 nm).

Finally, electromodulated differential absorbance (EDA) measurements consisted of detecting a probe light beam after its interaction with a sample subjected to an externally applied electric field. In the present case, these measurements were performed on a common Ti:Sapphire amplified femtosecond laser system by Clark-MXR (CPA-2001), yielding 780-nm pulses at a repetition rate of 1 kHz. The probe beam was obtained by passing the 780-nm laser output through a sapphire plate yielding a white light continuum detected over the 400-850 nm region. After being transmitted through the sample (transmittance mode, semi-transparent gold electrode) or being reflected off of its gold electrode (reflectance mode), the probe beam was dispersed in a grating spectrograph (SpectraPro 2500i, Princeton Instruments or SR163, Andor Technology) and finally detected shot by shot at a 1 kHz rate with a 512 × 58 pixel back-thinned CCD detector (S07030- 0906, Hamamatsu). Part of the probe beam was split, before the sample, into a reference beam reaching a second detector, which allowed for corrections for shot-to-shot fluctuations. The externally applied voltage was controlled by a function generator (AFG 2021, Tektronix), yielding square voltage pulses (100-µs pulse duration). The voltage pulses were modulated at 500 Hz, allowing to get the desired differential signal $\Delta A = A_{field} - A_{nofield}$. Multiple samples were measured under the same conditions, yielding consistent results.

7.2.3 Quantum mechanical simulations

The lead-iodine and iodine-iodine radial distribution function (RDF) in Figure 7-4 have been obtained via frozen glass simulations based on Density Functional Theory. A short Born-Oppenheimer molecular dynamics simulation was performed at high temperature (600 K, in the present case), so as to allow the system to explore the configurational space extensively. Subsequently, snapshots from the trajectory were extracted and their atomic positions re-optimized at zero Kelvin temperature. In this way, the system is initially in a conformation that can be very far from the global minimum of the potential energy surface and the subsequent optimization will relax the system towards the closest local minimum energy configuration. As a result, this kind of simulation provides information about the possible presence of (potentially several) local minima, as in the case of amorphous materials.
Both molecular dynamics simulations and subsequent zero Kelvin structural relaxations were performed using Density Functional Theory (DFT), in the planewave-pseudopotential formalism, as implemented in the Quantum-Espresso Suite program.[7] We adopted Ultrasoft pseudopotentials along with 25Ry/200Ry cutoff for the wave-function/electron density, respectively. Structural models consisted of a 2x2x1 supercell of the investigated layered perovskites (consisting of ~18 Å of lattice for the inorganic sheet). Consistently, only the G point of the first Brillouin zone has been considered. This computational set up provided structural information (radial distribution functions) for 3D perovskites in nice agreement with the experimental data available.[8] Molecular dynamics simulations were performed with a time step of 0.96975 fs. To speed up the molecular dynamics simulations, we defined fictitious masses of 10 amu for the Pb and I atoms, 5 amu for C, N, O, F and 2 amu for H. This trick allows to considerably accelerate the sampling of structural configurations without loss of accuracy. The only drawback is that the timescale of the simulation is not completely arbitrary, hence affecting the prediction of time-dependent quantities (which is not the case here). Structural optimizations have been performed over 40 structures regularly sampled, using the same computational approach.

7.3 Results and discussion

7.3.1 A complex photophysics (1): Transient absorbance measurements on FPEAI-2D and BUAI-2D.

Figure 7-1A-B presents TA spectral data spanning a time window of 2 ns (λ_{ex} = 390 nm, $3 \cdot 10^{18}$ carriers/cm^3) for BUAI-2D and FPEAI-2D with the corresponding structures of the cations presented as insets of Figure A and B, respectively. Note that, due to the high excitation energy, an initial hot carrier population is generated, which thermalizes over the course of a few picoseconds.[9,10]

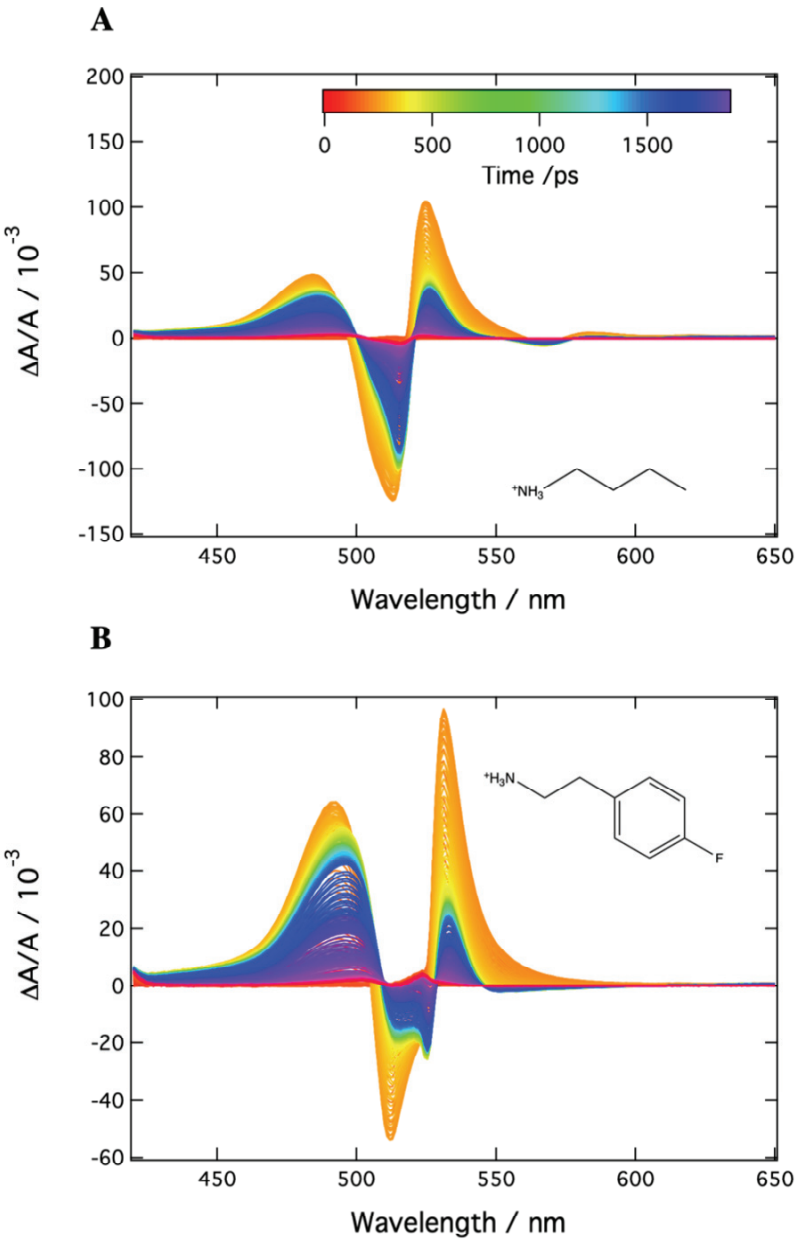
A
200
150
100
50
0
-50
-100
-150
0
500
1000
1500
Time /ps
ΔA/A / 10^-3
+NH3
450
500
550
600
650
Wavelength / nm
B
100
80
60
40
20
0
-20
-40
-60
+H3N
F
ΔA/A / 10^-3
450
500
550
600
650
Wavelength / nm

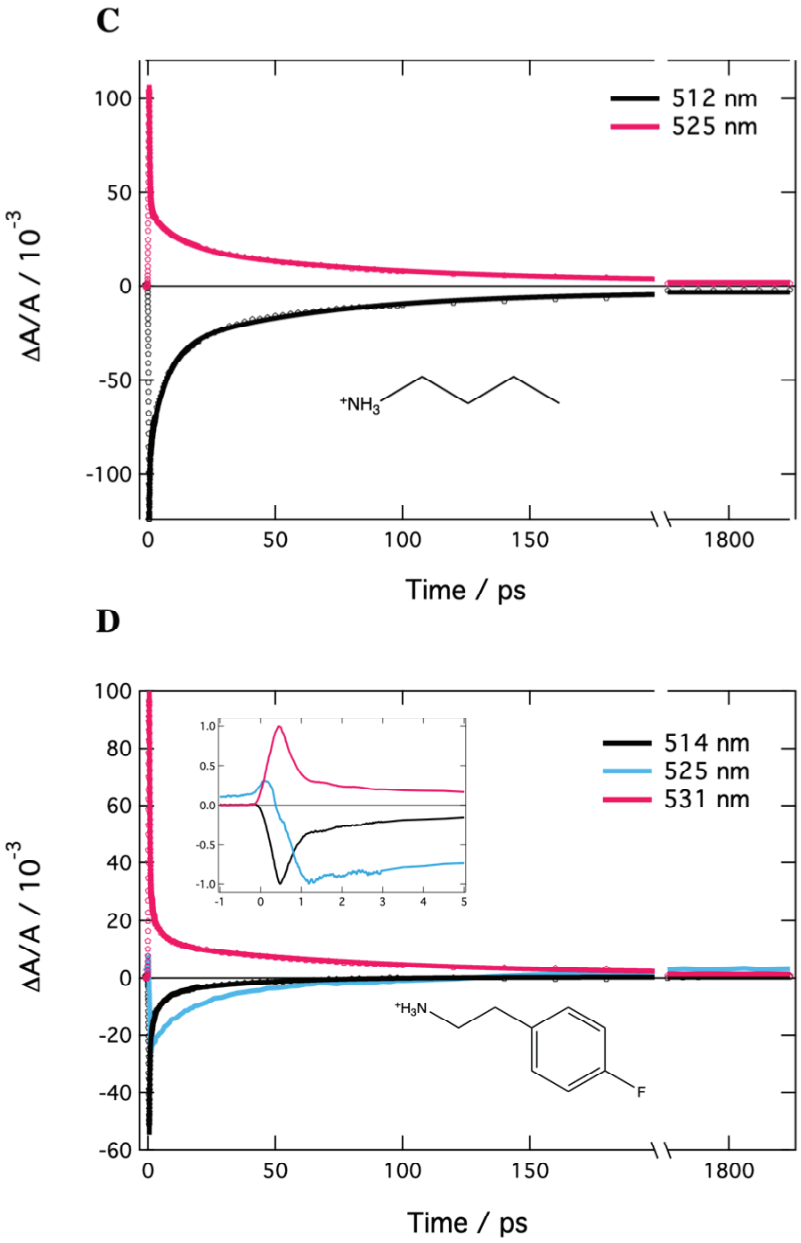

Figure 7-1 TA spectral data at λ_{ex}=390 and at an excitation regime of $3{\cdot}10^{18}$ carriers/cm^3. **A.** BUAI-2D. **B.** FPEAI-2D. The structures of the corresponding cations are presented in the insets. **C.** Selected dynamics at two peaks of interest for BUAI-2D **D.** Selected dynamics at three peaks of interest for FPEAI-2D. Inset**:** Oscillatory behavior of the dynamics in FPEAI-2D.

The TA spectra for BUAI-2D (Figure 7-1A) exhibits the same features as what is commonly observed for layered HOIPs: a large negative feature, here peaking at 512 nm, and designated to a mixture of GSB and SE, surrounded by two positive peaks. Such a derivative-like spectral shape is usually associated to a combination of exciton broadening due to many-body interactions, and spectral shifts, arising from the presence of internal electric dipoles.[9,11] The small positive and negative bands visible between 560 and 620 nm are assigned to the photoinduced electroabsorption originating from the population of trap states.[11] In contrast, the TA spectra of FPEAI-2D HOIPs (Figure 7-1B) differ from the derivative-like picture: An

additional sharp negative feature peaking at 525 nm appears; furthermore, the positive peaks are proportionally bigger than the GSB + SE feature, compared to BUAI-2D.

Dynamically speaking, all the features underlying the TA spectrum of BUAI-2D evolve over a similar timescale, as is visible from the 2 ns-long spectral stack in Figure 7-1A, as well as from the extracted dynamics presented in Figure 7-1C (for the sake of readability, only two representative dynamics have been extracted, peaking at 512 and 525 nm respectively). In the case of FPEAI-2D (Figure 7-1D), a similar time-dependent behavior is observable for the same two peaks. On the contrary, the second, sharp, negative feature at 525 nm decays on a slower timescale. FPEAI-2D also harbors another intriguing dynamical feature: As illustrated in the inset of Figure 7-1D, dynamics representative of the whole spectrum show clear, regular oscillations between 1 and 3 ps. These oscillations are present throughout the whole fluence range, and exhibit an average periodicity of about 0.8 ps.

7.3.2 A complex photophysics (2): Tentative carrier density dependence study on BUAI-2D and FPEAI-2D

The various observations above suggest that the energetic landscape within BUAI-2D and FPEAI-2D differ significantly, and a proper assignment of the various TA features is necessary to determine in what way. In this respect, many reports of structured absorption spectra at low temperature can be found in literature for 2D perovskite based on the phenethylammonium (PEA) cation, which is structurally very similar to FPEAI-2D. Originally assigned to the absorption of bound versus free excitons[12,13], phononic side bands[14,15], and/or vibronic progression[16,17], more recent works suggest that the various absorption peaks of FPEAI-2D arise from degeneracy lifting due to coupling to the lattice (polaronic effects).[2,9,18] In an attempt to extract new pieces of evidence towards one of the other of these hypotheses, we focus on the individual carrier density dependence of three TA peaks of interest, both in terms of their amplitude and time constants: Peak 1 (~512 nm, GSB +SE, both cations), peak 2 (525 nm, only present in FPEAI-2D) and peak 3 (~530 nm, undetermined ESA, in both cations).

We carry out multiexponential fits of the decay dynamics of those TA peaks, for excitation regimes between $3{\cdot}10^{17}$ and $6{\cdot}10^{18}$ carriers/cm^3. The resulting time constants are summarized in the appendices (Table E-1). For both cations, the fitting of peaks 1 and 3 necessitate a triexponential function, yielding similar time constants per cation and per fluence: The fast component decays with τ_1~0.3 ps, the intermediate component exhibits τ_2 between 3 and 15 ps, and the slow component τ_3 spans the 50-250 ps range. In contrast, peak 2 is accurately described by a biexponential function, with τ_2 between 10 and 30 ps, and τ_3 covering values between 70 and 350 ps.
We assign τ_1 to a combination of the abovementioned thermalization, exciton broadening and spectral shifts known to govern the early-time dynamics within HOIPs. Alternatively, τ_2 and τ_3 can be understood together as a stretched charge carrier lifetime, arising from mixed bimolecular and Auger recombination (due to the high excitation regimes employed), on top of possible transfer processes between neighboring states. We thus propose that the dependence

of τ_2 and τ_3 on the carrier density, for each of the peaks 1-3, constitutes a direct insight into the nature of the species underpinning them. The evolution of each of these lifetimes with the carrier density is hence plotted in Figure 7-2. Note that, when excluding any transfer contribution, such curves are typically flat at low densities, and exhibit a steep decay further along the abscissa, which results from the convolution between the Shockley-Read-Hall (SHR), bimolecular and Auger recombination processes.[19-21]

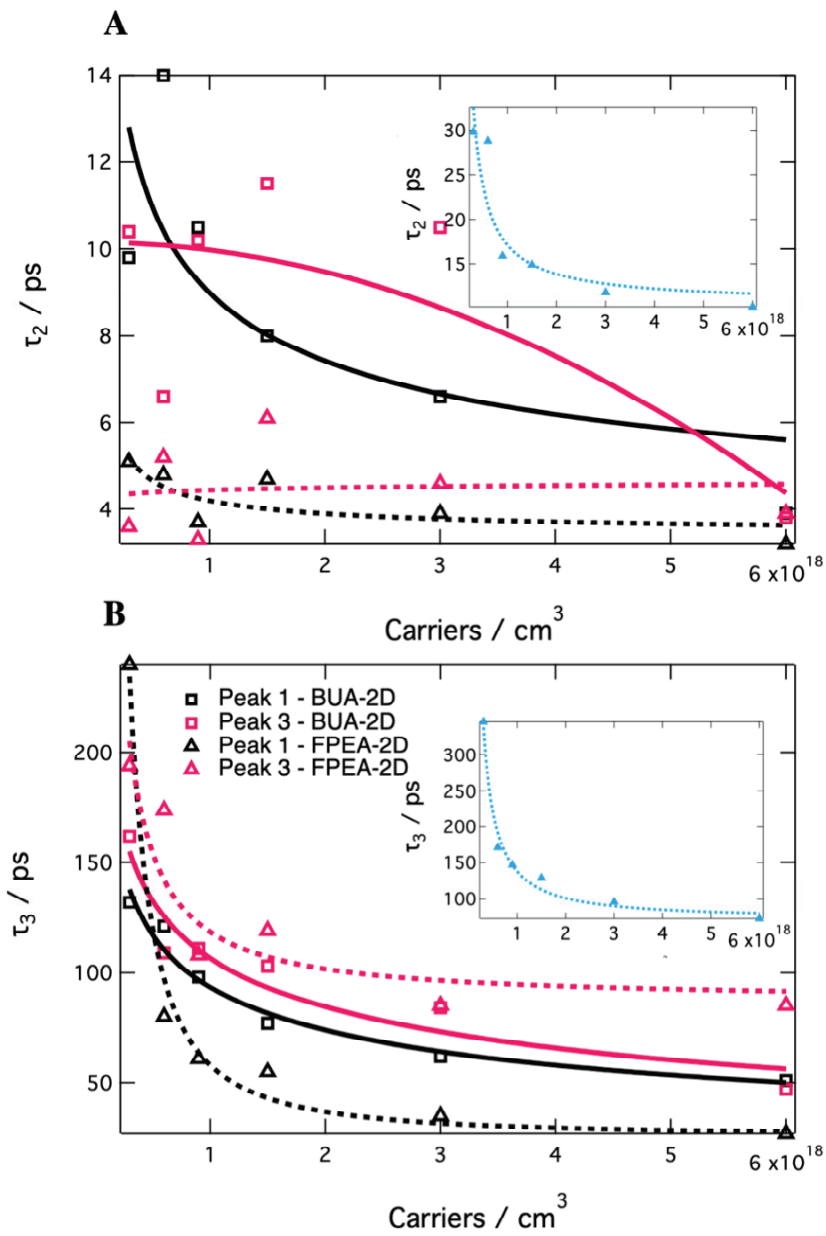

Figure 7-2 Dependence of the time constants from a multiexponential fit on carrier density (λ_{ex}=390 nm, $3\cdot10^{17}$, $6\cdot10^{17}$, $9\cdot10^{17}$, $1.5\cdot10^{18}$, $3\cdot10^{18}$, and $6\cdot10^{18}$ carriers/cm^3). **A.** τ_2 **B.** τ_3. Pink symbols denote the evolution of peak 3, while black symbols describe peak 1. BUAI-2D is represented with squares, and FPEAI-2D with triangles. Eye-guiding lines are plotted on top of the experimental points, full for BUAI-2D and dotted in the case of FPEAI-2D. Insets describe the evolution of peak 2 (FPEAI-2D).

We observe that, except for the second decay constant of peak 3 (τ_2, Figure 7-2A, pink lines) the shape of the curves in Figure 7-2, strongly deviates from this description: for peak 1 and 2,

τ_2 (Figure 7-2A, black lines; and inset) and τ_3 (Figure 7-2B, black lines; and inset) first show a fast decay with increasing carrier density, and then flatten out. The third time constant of peak 3 (Figure 7-2B, pink lines) shows the same behavior. This is true for the lifetimes of both BUAI-2D (squares) and FPEAI-2D (triangles), which solely differ by their amplitude and the slope of their decay with increasing carrier density.

We now focus on the dependence of the amplitude of peaks 1-3 on the carrier density. The process of light absorption, although independent from the radiation field, depends on the number of available states to accommodate photocarriers. We thus propose that peaks exhibiting a sublinear dependence on the carrier density involve a contribution from trapped carriers or excitons. Figure 7-3A (BUAI-2D) and B (FPEAI-2D) present the resulting curves, which have been fitted with a power law ($y = A \cdot x^{power}$). The corresponding parameters are summarized in Table 7-1.

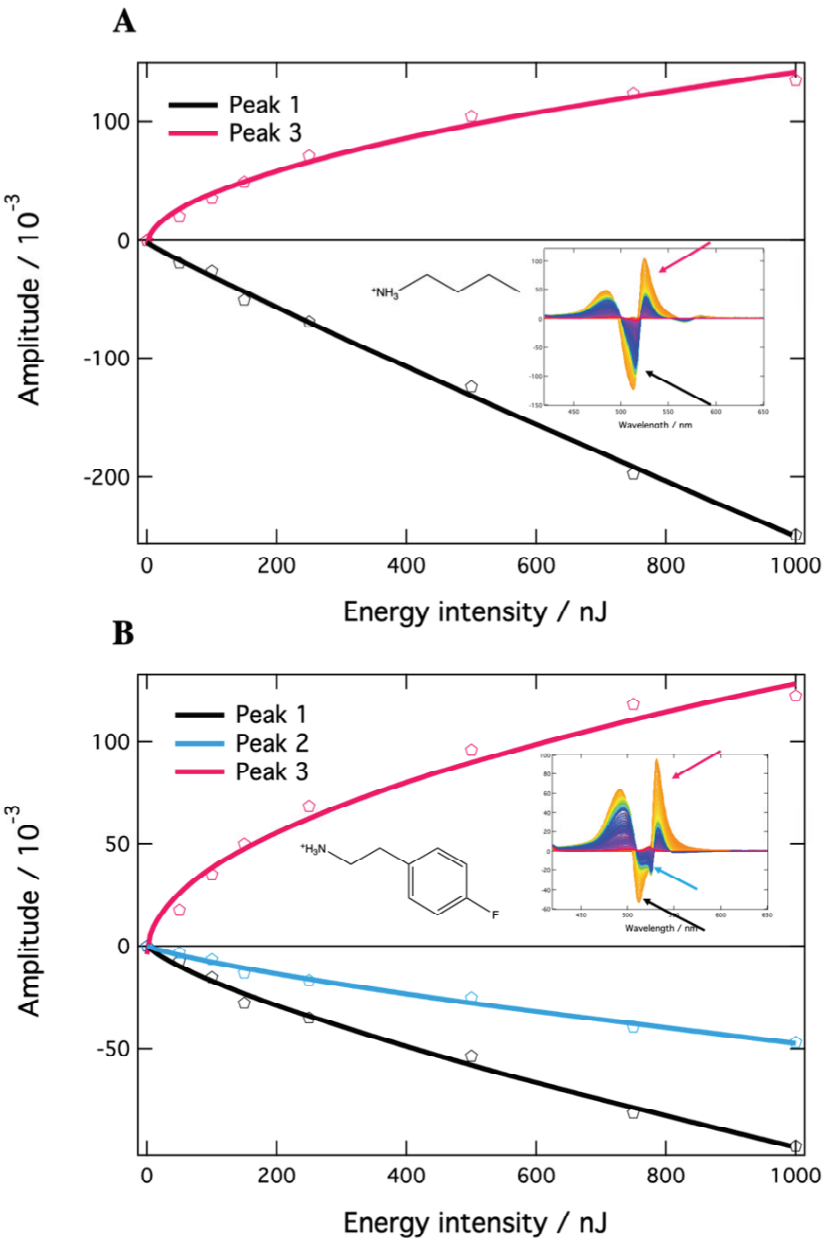

Figure 7-3 Amplitude of TA peaks 1-3 as a function of the excitation energy (λ_{ex}=390 nm). The associated carrier densities are $3{\cdot}10^{17}$, $6{\cdot}10^{17}$, $9{\cdot}10^{17}$, $1.5{\cdot}10^{18}$, $3{\cdot}10^{18}$, and $6{\cdot}10^{18}$ carriers/cm^3 respectively. **A.** BUAI-2D. **B.** FPEAI-2D. Black lines denote peak 3, blue lines peak 2 and pink lines peak 3.

BUAI-2D	Power
Peak 1	0.9 ± 0.1
Peak 3	0.5 ± 0.1

FPEAI-2D	Power
Peak 1	0.8 ± 0.1
Peak 2	0.8 ± 0.1
Peak 3	0.5 ± 0.1

Table 7-1 Extracted parameters from power law fitting.

It emerges that, in all cases, the fluence dependence of peak 3 is clearly sublinear. In contrast, the situation is significantly less clear for peaks 1 and 2: in the case of BUAI-2D, the fluence dependence of peak 1 is linear, while that of peaks 1 and 2 in FPEAI-2D deviates from linearity. We deduce that peak 3 is dominated by the absorption of trapped charges. In turn, peaks 1 and 2 likely involve a superposition of different processes, including trap absorption.

7.3.3 A complex photophysics (3): Traps and polarons

Gathering the various insights obtained from the above analyses, a clearer picture starts to form: from the different time-evolution of peak 2 compared to peaks 1 and 3 in FPEAI-2D (Figure 7-1), we know that peak 2 originates from a different species or process. From the carrier density dependence of the time constants (Figure 7-2), we know that peak 3 reflects at least two different species: one that decays within about 10 ps, and another one with lifetimes up to 350 ps. Finally, the peak's amplitude dependence on the carrier density (Figure 7-3 and Table 7-1) tells us that one of the two species underlying peak 3 are trapped carriers or excitons. We furthermore assign τ_2 of peak 3 to the decay of those trapped species, as its dependence on the carrier density (i) is closer to the typical model arising from the convolution of SHR-Bimolecular-Auger processes and (ii) exhibit a relatively weak variation, as is expected for SHR-type recombination.

As for the remaining species in our systems, we go back to the behavior represented in Figure 7-2, where the decay of most of the time constants flatten out at high carrier densities. As this depicts a saturation of the recombination at high fluences, this behavior points to polaronic species. Indeed, when the distance between large polarons of opposite charges is large, they tend to be attracted to one another. However, at high enough charge carrier densities, the polaronic clouds start to overlap, which results in a net repulsion between oppositely charged polarons, with a correspondingly slower recombination.[22,23] Note that the behavior of polaronic species of the same charge is opposite.[24] In 3D lead halide perovskites, it is known that the polarons start to overlap for carrier densities $\geq 10^{18}$.[25] Because the ionicities of the 3D and the 2D lattice are similar, we can reasonably assume that this number is also valid in the present case. This is coherent with our experimental results, and further strengthens our assignment.

As a second evidence, we discuss the oscillations observed in the TA dynamics of FPEAI-2D (Figure 7-1D), which is an easy task in light of the recent work by Thouin *et al*. They indeed report oscillations with a similar period in the low temperature differential transmission spectrum of a 2D perovskite based on the phenethylammonium cation (PEAI-2D), structurally very similar to FPEAI-2D. By assigning them to phonon coherences generated via resonant impulsive Raman scattering (RISRS), they were able to unravel the vibrational modes involved in the coupling of electrons and holes to the lattice, revealing the importance of polaronic interactions in PEAI-2D. Similar experiments on BUAI-2D, in spite of the lack of observations of coherent oscillations, yielded the same conclusions, although with the dominance of hole polarons.[9]

The assignment of the complex spectral features of FPEAI-2D in Figure 7-1B follows straightforwardly from the above arguments. Peaks 1 and 2 correspond to the bleaching of two excitonic transitions involving the coupling to different lattice vibrational modes, while peak 3 is an overlap of polaronic contributions and of the absorption of trapped charge carriers. Although the TA spectrum of BUAI-2D does not exhibit the same combination of peaks, the ubiquity of polaronic species in this system is also valid, as demonstrated by the carrier density dependence of the time constants and by ref.[9].

7.3.4 Cation influence on the polaron formation: Role of disorder?

Polaronic interactions dominate the photophysics of BUAI-2D, FPEAI-2D and PEAI-2D. It thus begs the question whether this can be generalized to most 2D HOIPs, and, if yes, how it relates to the nature of the organic cation. In this respect, a recent paper by Gong *et al*. reports faster nonradiative decay rates within BUAI-2D compared to PEAI-2D. This is associated to a stronger electron-phonon coupling in the former, originating in its larger conformational freedom.[18] This observation suggests that the disorder of the organic cation constitutes a macroscopic property usable in the prediction of the strength of charge-phonon coupling. In this context, we define the disorder as the number of stable configurations a given cation can adopt.

To explore this hypothesis, we now focus on an additional cation (A43) exhibiting a complex structure, represented in Figure 7-4A (top).[26] A43 is an interesting candidate in the present context due to its high disorder, as demonstrated by the larger number of stable configurations adopted by A43I-2D compared to BUAI-2D (see Figure 7-4A bottom, featuring radial distribution functions for both Pb-I and I-I atom pairs).[27]
Due to the high inhomogeneity of thin-films made out of A43I-2D, we cannot accurately perform the same analyses as for BUAI-2D and FPEAI-2D. As an alternative, we measure the EDA spectra of BUAI-2D and A43I-2D, as direct insights into the nature of the dominant photoinduced species in a given system can be obtained via lineshape analysis of its EA spectrum. Assuming that the EA of the two perovskites under study is accurately modeled by the Stark effect, we compare the resulting signals with the first- and second-derivatives of their respective absorption (see chapter 2).

A

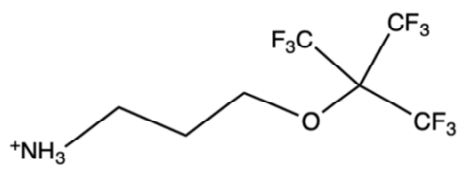
F3C
CF3
O
CF3
+NH3

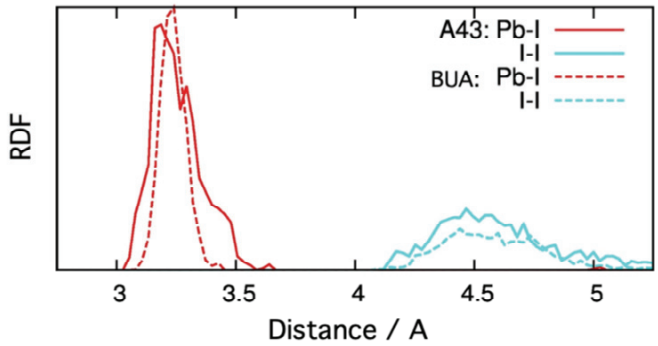
A43: Pb-I
I-I
BUA: Pb-I
I-I
RDF
3
3.5
4
4.5
5
Distance / A

B

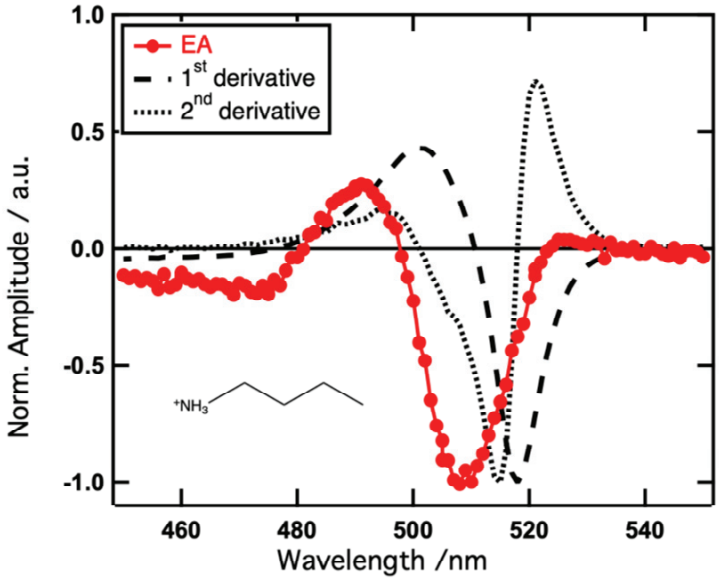
EA
1st derivative
2nd derivative
1.0
0.5
0.0
-0.5
-1.0
Norm. Amplitude / a.u.
+NH3
460
480
500
520
540
Wavelength /nm

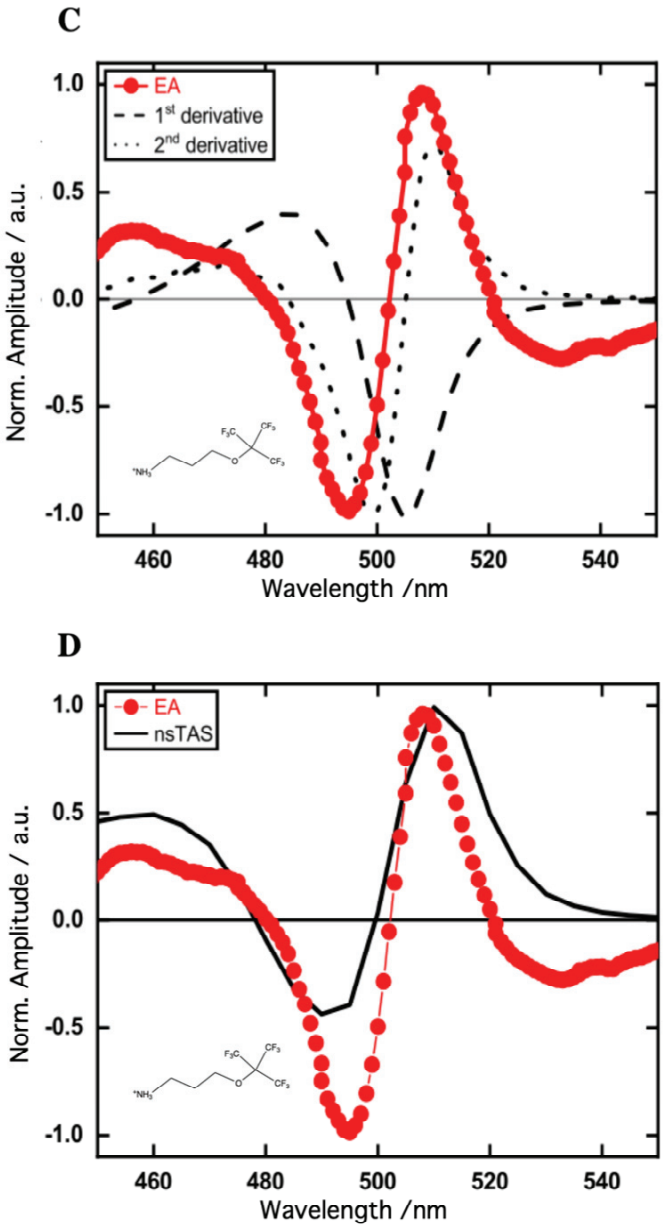

Figure 7-4 Comparison of BUAI-2D vs A43I-2D. **A.** Structure (top) and radial distribution function (bottom) of A43. **B.** Electroabsorption spectrum of A43I-2D (red symbols), recorded at an applied voltage of 10 V (approximately 1000 V/cm), together with the first and second derivative of its absorption spectrum (black dash and dot). **C.** Electroabsorption spectrum (red symbols) overlapped with the time-resolved spectrum of A43I-2D at 300 ns (black line) upon excitation at 420 nm using a carrier density of 10^{19} carriers/cm^{-3}. **D.** Electroabsorption spectrum of BUAI-2D (red symbols), recorded at an applied voltage of 10V, together with the first and second derivative of its absorption spectrum (black dash and dot).

It appears that the EA of A43I-2D (Figure 7-4C) matches well with the second-derivative of its absorption spectrum, while BUAI-2D (Figure 7-4D) resembles a first derivative. Furthermore, Figure 7-4B shows the ns-TA spectrum of A43I-2D at 300 nanoseconds: we observe a strong photoinduced electroabsorption signal, mimicking the steady-state EA. This demonstrates the particularly long lifetime of the species generating the second-derivative-like EA of A43I-2D. As explained in detail in chapter 2, and assuming both samples to be reasonably isotropic, the EA lineshapes presented above state that A43I-2D harbors a species featuring a strong

permanent dipole, on the contrary to BUAI-2D. As also described in chapter 2, second-derivative-like EA signals are typically assigned to the presence of charge-transfer (CT) excitons, as they are deemed to be the only type of photogenerated carriers carrying a permanent dipole. However, because of the strength of the polaronic interactions in 2D perovskite systems, (large polarons), we can argue that this could also be valid for an electron-polaron and a hole-polaron interacting across their vibration clouds. In such a situation, the electron and the hole would indeed experience very different dielectric environments, mimicking an interaction across an interface. In addition, the long lifetime of the photoinduced electroabsorption signal supports the notion that the dipole carrying species is protected against recombination, which further supports hole- and electron- polarons to be at the origin of the EA signal of A43I-2D.
If this assignment is correct, it follows that the electrons and/or hole polarons in A43I-2D are larger than in BUAI-2D, with a correspondingly larger electron/hole-phonon coupling strength in the former case.[28]

This discussion, together with the works of Thouin *et al*. and Gong *et al*. seems to draw the following trend as for the strength of the charge-phonon coupling: PEAI/FPEAI-2D < BUAI-2D < A43-2D, which follows perfectly the trend of increasing disorder.

7.4 Conclusion

In this chapter, we first work out the assignment of the TA features of BUAI-2D and FPEAI-2D by means of fluence-dependence analyses combined with a thorough literature review. We show that, aside from trapped carriers, the photophysics of those perovskites is largely dominated by electron and hole polarons. This lifts the degeneracy between different excitonic transitions, sometimes yielding structured absorption and transient absorption spectra, as is the case for PEAI-2D and FPEAI-2D, for example.

In addition, we attempt to discuss a reliable macroscopic property of the organic cation that could be used as a predictive tool for the strength of polaronic interactions within 2D HOIPs. We suggest that the degree of disorder of the cation can be a good candidate, and try to support this hypothesis by comparing the size of the polarons in the very disordered A43I-2D with those in BUAI-2D by electroabsorption and ns-TA spectroscopy. We show that A43I-2D harbors a long-lived species carrying a permanent dipole moment, contrary to BUAI-2D. We propose that those species are polarons with a particularly large coupling to the lattice. Combining this result with relevant literature data, we observe that the electron/hole-phonon coupling strength in 2D HOIPs indeed seems to increase with increasing disorder of their organic cation.

References

(1) Thouin, F.; Neutzner, S.; Cortecchia, D.; Dragomir, V. A.; Soci, C.; Salim, T.; Lam, Y. M.; Leonelli, R.; Petrozza, A.; Kandada, A. R. S.; et al. Stable Biexcitons in Two-Dimensional Metal-Halide Perovskites with Strong Dynamic Lattice Disorder. *Phys. Rev. Mat* **2018**, *2* (034001), 1–10.

(2) Neutzner, S.; Thouin, F.; Cortecchia, D.; Petrozza, A.; Silva, C.; Kandada, A. R. S. Exciton-Polaron Spectral Structures in Two-Dimensional Hybrid Lead-Halide Perovskites. **2018**, 1–10.

(3) Yin, J.; Li, H.; Cortecchia, D.; Soci, C.; Brédas, J.-L. Excitonic and Polaronic Properties of 2D Hybrid Organic–Inorganic Perovskites. *ACS Energy Lett.* **2017**, *2* (2), 417–423.

(4) Zheng, F.; Wang, L.-W. Large Polaron Formation and Its Effect on Electron Transport in Hybrid Perovskites. *Energy Environ. Sci.* **2019**, *12* (4), 1219–1230.

(5) Miyata, K.; Meggiolaro, D.; Trinh, M. T.; Joshi, P. P.; Mosconi, E.; Jones, K. C.; De Angelis, F.; Zhu, X. Y. Large Polarons in Lead Halide Perovskites. *Sci. Adv.* **2017**, *3*, 1–10.

(6) Paraecattil, A. A.; De Jonghe-Risse, J.; Pranculis, V.; Teuscher, J.; Moser, J. E. Dynamics of Photocarrier Separation in MAPbI 3Perovskite Multigrain Films Under a Quasistatic Electric Field. *J. Phys. Chem. C* **2016**, *120* (35), 19595–19602.

(7) Giannozzi, P.; Baroni, S.; Bonini, N.; Calandra, M.; Car, R.; Cavazonni, C.; Ceresoli, D.; Chiarotti, G. L.; Coccioni, M.; Dabo, I.; et al. QUANTUM ESPRESSO: a Modular and Open-Source Software Project for Quantum Simulations of Materials. *J. Phys.: Condens. Matter* **2009**, *21*, 395502.

(8) Quarti, C.; Mosconi, E.; De Angelis, F. Structural and Electronic Properties of Organohalide Hybrid Perovskites From Ab Initio Molecular Dynamics. *Phys. Chem. Chem. Phys.* **2015**, *17*, 9394.

(9) Thouin, F.; Valverde-Chàvez, D. A.; Quarti, C.; Cortecchia, D.; Bargigia, I.; Beljonne, D.; Petrozza, A.; Silva, C.; Kandada, A. R. S. Phonon Coherences Reveal the Polaronic Character of Excitons in Two-Dimensional Lead Halide Perovskites. *Nature Materials* **2019**, 1–9.

(10) Guo, Z.; Wu, X.; Zhu, T.; Zhu, X.; Huang, L. Electron–Phonon Scattering in Atomically Thin 2D Perovskites. *ACS Nano* **2016**, *10* (11), 9992–9998.

(11) Wu, X.; Trinh, M. T.; Zhu, X. Y. Excitonic Many-Body Interactions in Two-Dimensional Lead Iodide Perovskite Quantum Wells. *J. Phys. Chem. C* **2015**, *119* (26), 14714–14721.

(12) Ishihara, T.; Takahashi, J.; Goto, T. Optical Properties Due to Electronic Transitions in Two-Dimensional Semiconductors $(C_nH_{2n+1}NH_3)_2PbI_4$. *Phys. Rev. B* **1990**, *42* (17), 11099–11107.

(13) Fujisawa, J.-I.; Ishihara, T. Excitons and Biexcitons Bound to a Positive Ion in a Bismuth-Doped Inorganic-Organic Layered Lead Iodide Semiconductor. *Phys. Rev. B* **2004**, *70* (20), 11 099–6.

(14) Tanaka, K.; Sano, F.; Takahashi, T.; Kondo, T.; Ito, R.; Ema, K. Two-Dimensional Wannier Excitons in a Layered-Perovskite-Type Crystal $(C_6H_{13}Nh_3)_2PbI_4$. *Solid State Commun.* **2002**, 249–252.

(15) A V Nurmikko, X. H. T. I. Dielectric Confinement Effect on PbI_4-Based Layered Semiconductors. *Phys. Rev. B* **1992**, *45* (12), 6961–6964.

(16) Cortecchia, D.; Yin, J.; Petrozza, A.; Soci, C. White Light Emission in Low-Dimensional Perovskites. *J. Mater. Chem. C* **2019**, *7*, 1700264–14.

(17) Straus, D. B.; Hurtado Parra, S.; Iotov, N.; Gebhardt, J.; Rappe, A. M.; Subotnik, J. E.; Kikkawa, J. M.; Kagan, C. R. Direct Observation of Electron–Phonon Coupling and Slow Vibrational Relaxation in Organic–Inorganic Hybrid Perovskites. *J. Am. Chem. Soc.* **2016**, *138* (42), 13798–13801.

(18) Gong, X.; Voznyy, O.; Jain, A.; Liu, W.; Sabatini, R.; Piontkowski, Z.; Walters, G.; Bappi, G.; Nokhrin, S.; Bushuyev, O.; et al. Electron–Phonon Interaction in Efficient Perovskite Blue Emitters. *Nature Materials* **2018**, 1–10.

(19) Olson, B. V.; Kadlec, E. A.; Kim, J. K.; Klem, J. F.; Hawkins, S. D.; Shaner, E. A.; Flatté, M. E. Intensity- and Temperature-Dependent Carrier Recombination in InAs/InAs1−xSbxType-II Superlattices. *Phys. Rev. Applied* **2015**, *3* (4), 044010–044012.

(20) Arafat, Y.; M Mohammedy, F.; M Shahidul Hassan, M. Optical and Other Measurement Techniques of Carrier Lifetime in Semiconductors. *IJOE* **2012**, *2* (2), 5–11.

(21) Kiermasch, D.; Rieder, P.; Tvingstedt, K.; Baumann, A.; Dyakonov, V. Improved Charge Carrier Lifetime in Planar Perovskite Solar Cells by Bromine Doping. *Sci. Rep.* **2016**, 1–7.

(22) Emin, D. Barrier to Recombination of Oppositely Charged Large Polarons. *Journal of Applied Physics* **2018**, *123* (5), 055105–055105.

(23) Fratini, S.; Quémérais, P. Melting of a Wigner Crystal in an Ionic Dielectric. *Eur. Phys. J. B* **2000**, *14*, 99–113.

(24) Rastelli, G.; Ciuchi, S. Wigner Crystallization in a Polarizable Medium. *Phys. Rev. B* **2005**, *71* (18), 1744–19.

(25) Frost, J. M.; Whalley, L. D.; Walsh, A. Slow Cooling of Hot Polarons in Halide Perovskite Solar Cells. *ACS Energy Lett.* **2017**, *2* (12), 2647–2652.

(26) García-Benito, I.; Quarti, C.; Queloz, V. I. E.; Orlandi, S.; Zimmermann, I.; Cavazzini, M.; Lesch, A.; Marras, S.; Beljonne, D.; Pozzi, G.; et al. Fashioning Fluorous Organic Spacers for Tunable and Stable Layered Hybrid Perovskites. *Chem. Mater.* **2018**, *30* (22), 8211–8220.

(27) Zimm, B. H. The Scattering of Light and the Radial Distribution Function of High Polymer Solutions. *J. Chem. Phys.* **1948**, *16* (12), 1093–1099.

(28) Neukirch, A. J.; Nie, W.; Blancon, J.-C.; Appavoo, K.; Tsai, H.; Sfeir, M. Y.; Katan, C.; Pedesseau, L.; Even, J.; Crochet, J. J.; et al. Polaron Stabilization by Cooperative Lattice Distortion and Cation Rotations in Hybrid Perovskite Materials. *Nano Lett.* **2016**, *16* (6), 3809–3816.

8 Conclusions and outlooks

The work conducted in this thesis aimed at uncovering the nature and dynamics of the photoinduced species within hybrid organic-inorganic lead halide perovskites, exhibiting mixed compositions and dimensionalities.

Chapters 3 and 4 explored the charge carrier dynamics of 3D mixed halide, mixed cation perovskites ($MA_yFA_{1-y}Br_xI_{3-x}$) in their bulk and at their interfaces with SnO_2 (electron-transporting material) and spiro-OMeTAD (hole-transporting material). In Chapter 3, the transient absorbance measurements on $MA_yFA_{1-y}Br_xI_{3-x}$ thin-films highlighted the presence of a strong photoinduced electroabsorption signal dominated by the second derivative of the linear absorbance spectrum. Together with a global analysis performed on the whole spectral window, this unraveled the formation of CT excitons at the boundaries between domains with different iodide/bromide proportion. We proposed this phenomenon to be at the origin of the superior photovoltaic performance of mixed cation, mixed halide perovskites, as it yields efficient charge separation and thus decreases electron-hole recombination.

Chapter 4 presented a description of the charge dynamics at the $SnO_2/MA_yFA_{1-y}Br_xI_{3-x}$ and the $MA_yFA_{1-y}Br_xI_{3-x}$/spiro-OMeTAD interfaces by means of a novel combination of experimental schemes and analyses based on ultrafast transient absorbance spectroscopy. This strategy first made use of the exponential attenuation of light when it interacts with a material. In particular, it exploited the illumination-face dependence of the photoinduced electroabsorption signal in TA spectra to shed light on the injection processes at the interfaces of interest. Charge carrier dynamics following injection was then unraveled with anisotropic transient absorbance measurements, characterizing the amplitude of the interfacial built-in field and thus the propensity of charges to accumulate at, or close to, the interfaces.
Our experimental strategy showed that electron transfer towards ALD-deposited SnO_2 is mediated by CT excitons, which limits the rate of charge transfer and yields interfacial charge accumulation. In turn, we confirmed the ultrafast injection and subsequent diffusion of holes in doped state-of-the-art spiro-OMeTAD in contrast to the plain molecular acceptor.

Chapter 5 addressed the photophysics of nanoparticle aggregates of lead bromide perovskite ($CH_3NH_3PbBr_3$) and constitutes the transition towards the two-dimensional systems lying at the core of the following chapters. Colloidal suspensions of $CH_3NH_3PbBr_3$ nanoparticles comprised of a mixture of quasi-2D (nanoplatelets) and 3D nanoparticles. Using a combination of steady-state, excitation-dependent ultrafast transient absorbance and TCSPC measurements, we unraveled the presence of significant inter-structure interactions in the form of a cascade of energy and charge transfer, the latter being mediated by the formation of interparticle CT excitons. In particular, we proposed a complete photophysical model accounting for the various optical signals observed, in which the recombination of localized excitons (yielding short-lived emission) competes with the formation of the inter-structure CT states (visible from a photoinduced electroabsorption signal), recombining on significantly slower timescales. We furthermore addressed the dynamics of interfacial charge transfer from donor molecules in

solution to the $CH_3NH_3PbBr_3$ nanoparticles. We reported efficient, although slow (tens of ns timescale), electron transfer from *N*,*N*,*N*',*N*'-tetrakis(4-methoxy-phenyl)benzidine (MeO-TPD) and 1,4-bis(diphenylamino) benzene (BDB), with a resulting remarkably long-lived charge separation.

Chapter 6 described the photophysics at the interface between a 3D and a 2D perovskite layer for solar cell applications. We tackled the photophysics of stratified 3D/2D interfaces involving 2D perovskites based on the phenethylammonium (PEA) cation and its fluorinated counterpart, fluorophenethylammonium (FPEA). We demonstrated the important role of the 2D layer, both as a surface passivant and as a protection against back recombination, yielding larger open-circuit voltages (V_{OC}) in the corresponding devices. In addition, we showed that these beneficial effects were directly dependent on the crystal growth and orientation of the 2D layer on top of the 3D, itself determined by the nature of the organic cation of the 2D layer: PEAI-2D orients parallel to the substrate and proved more effective than FPEAI-2D, which exhibits a disordered orientation.

Chapter 7 presented a fundamental, yet partially speculative, study of the nature of the photoinduced species within pure perovskite quantum wells. We started from the complexity of the time-resolved TA spectra of a 2D perovskite based on the FPEA cation (FPEAI-2D) compared to that of a butylammonium-based 2D perovskite (BUAI-2D). We used the carrier density dependences of both the decay constants and amplitudes of the TA features of interest to show that the photophysics of these 2D HOIPs is dominated by polaronic interactions. Because such a statement can already be found in literature, and for different organic cations, we speculated that polaronic interactions be ubiquitous in 2D HOIPs, with the strength of the charge-phonon coupling determined by the degree of disorder of the cation. Arguing that large enough polarons can carry a permanent dipole moment, similar to CT excitons, we then attempted to provide evidence for this hypothesis by comparing the lineshape of the electroabsorption (EA) signal of an additional, highly disordered 2D perovskite (A43I-2D) with that of BUAI-2D.

Although the perovskite adventure in the context of optoelectronics is rather recent, the field has progressed incredibly fast in the past few years, with a broadened focus now including HOIPs with all kinds of dimensionalities and compositions, tailored to suit the needs of an increasingly large field of applications. In this respect, answers are still more sparse than questions, which makes for a thrilling research field.

The first thing that comes to mind after reading the work presented in this thesis is the need for a broader understanding of the occurrence of species carrying a permanent dipole moment in HOIPs. Indeed, whether these are systematically CT excitons, and/or sometimes, very large polarons, their impact on the photophysics of lead halide perovskites is significant and can appear both detrimental and beneficial depending on the targeted application. In particular, the mechanisms of their formation and, more importantly, their dissociation, needs to be understood and controlled, possibly by dielectric tuning of interfaces or grain boundaries.

In turn, the versatility of 2D HOIPs via simple variation of their organic cation appears as another fascinating and seemingly never-ending research topic. Indeed, provided we gain a better and more generalized understanding of the impact of the structure of the cation on their optoelectronic properties, 2D HOIPs could potentially be used in a much broader range of applications than they are now, or, at least, lead to better performing devices. For instance, we could imagine to predictively custom-build 2D perovskites with biexcitons as primary carriers; or to be able to precisely tune the strength of the charge-phonon coupling for a controlled kinetic competition between recombination and other competing processes. Similarly, by controlling the phonon modes and their resulting coupling to excitons, we could imagine the possibility of creating long-lived coherences between defined excitonic states.
However, I strongly believe that, to reach such an understanding, one must develop one of the two following strategies: Either a new way to think in terms of macroscopic observables, such as disorder, the localization or delocalization of the charges (for example due to interactions between the inorganic layer and a delocalized π system in the organic barrier), or the polarization of the whole structure (possibly arising from the presence of electronegative atoms or groups on the cation chains). Alternatively, we can focus on microscopic observables, and develop new methodological schemes to systematically assign these microscopic cation properties to specific photophysical behaviors, aiming at building big data banks. Predictability would then follow from the use of machine learning algorithms. This is of particular importance to me as it fits my (admittedly naive) ideal of globalized and openly shared science unified towards common goals, in contrast to the current climate of competitiveness.

Finally, still in the context of property tuning, I want to discuss an idea that I hold dear, namely the possibility to exploit the versatility of perovskites, in particular in their 0D form, in the context of plasmon-exciton interactions. Indeed, because it is now possible to make perovskite quantum dots of various sizes, and thus, with tunable absorption, it becomes possible to create semiconductor-metal nanoparticle systems with a broad range of metallic partners. This by itself constitutes an interesting possibility to target various applications; but we can go one step further still. Varying the size of the perovskite quantum dot not only modifies its absorption wavelength but also the degree of correlation of the excitons (quantum confinement). As a consequence, by manipulating both the resonance condition (overlap of the absorption of the plasmon and the exciton) and the exciton correlation, it appears possible to build exciton-plasmon interactions extending from the strong to the weak coupling limit. Each of these coupling regimes pertains to different applications, from sensor development in the weak coupling limit to quantum information in the strong coupling limit, for example. Such studies are thrilling from a fundamental standpoint, but also bring up many new and potentially accessible developments for perovskite-based optoelectronic applications.

Hybrid lead halide perovskites started out as an extraordinary system for photovoltaics. Today, they represent a high-potential material in a much broader range of applications. From my own perspective, their greatest appeal lies in the perpetually new questions and ideas that arise from their study. They have been a strong driving force of my scientific curiosity and creative freedom throughout this work.

Acknowledgements - Remerciements

I first want to express my gratitude to my PhD advisor, Prof. Jacques Moser, for having welcomed me in his lab a bit more than four years ago, and for putting up with my strong emotional relationship with my research, for better or worse! You were always supportive in the bad moments, and patient with my occasional stubbornness.

Then, I want to thank my precious labmates, that usually managed to put up a smile on my face, even on the bad days. Thank you, first, to the original dynamic duo, Arun and Andrés, for your great companionship all those years, and your always attentive ears! Thank you, Arun, the chillest and smartest guy on earth, for always being there to pick me up off the ground when I was desperate for one reason or another, and for talking some sense into me in these moments! Thank you, Andrés, for your steady and calm presence, great counterpart to the Marine storm, and for your inspirational patience, meticulousness and out-of-the-box thinking! Thanks also to Heewon, always discrete, but so determined to see her PhD through!

In turn, thank you to our newest and beloved members, the fantastic trio: Etienne, George and Brener. I think all of us older group members became quickly very fond of you three! Thank you for your refreshing enthusiasm and curiosity, thank you for reviving a bit of my passion for research, and for being such attentive and well-thinking students. Etienne, tu es capable d'une telle abnégation dans ta recherche, d'une telle prise d'initiative que c'en est inspirant. Ta gentillesse et ton humour me font chaud au cœur ! George, I'll always be grateful to you for bringing to this group this touch of pinky-raising Britishness and British humour that was lacking. Your perseverance is impressive, as your motivation remains intact despite the research hiccups you already went through…I have to learn from that! Brener, you embody what we call in French "la force tranquille", but ineluctable! The way you keep searching for solutions, workarounds, new ideas, by skimming literature with an unbelievable efficiency is downright impressive and inspirational!

Je tiens aussi à te remercier tout spécialement, Joël. « Office mate" pendant trois ans, et tellement plus que ça. Sans toi, je ne sais pas si je serais émotionnellement arrivée à bout de ce doctorat. Tu m'as toujours encouragée, soutenue, aidée. Avec patience, tu as partagé mes doutes, de même que mes excitations momentanées pour l'une ou l'autre quasiparticule exotique ! C'était bien.

Thanks to my students, Rachele, Andrés, Etienne and Roger! You taught me at least as much as I taught you…and I hold these memories very dear!

And I am not forgetting to thank two very important previous group members, Jelissa and Arianna! They indeed had a lot to do with my writing these words today. I have known them as teaching assistants during my studies, have read their work during my PhD, and have always admired them, as powerful and brilliant women. Later on, I had the opportunity to work with Jelissa for a few weeks, and thinking back at these moments still makes my heart shine!

Another very special thanks goes to Dr. Giulia Grancini. Giulia gave a second wind to my passion for science, when she offered me the opportunity to collaborate. Discussions with her were probably the embodiment of what “emulation” means and I have learnt so much! I also want to thank her student, Valentin, for providing the calmness and serenity that Giulia and I occasionally lacked, our excessive excitation being to blame!

Je veux à présent remercier mes amis, cette famille étendue et en perpétuelle évolution qui m’entoure et me ressource.
Merci aux copines de toujours, mes chères Aline (Tutu), et Alexandra (Persil) ! Une relation d’amitié belle et simple, basée sur la bienveillance, la tolérance et le partage libre de nos états d’âmes.
Merci aussi à la team des morgiennes (bien que nous eussions quelque peu émigré depuis !), Alex, Ailsa, Jessica et Noëllie. Vous êtes toutes les quatre des femmes si fortes et déterminées ! Je suis toujours ressortie de nos rencontres régulières avec une sérénité renouvelée et une confiance dans l’existence. Les évènements heureux qui vous arrivent en ce moment me remplissent particulièrement de joie !

Merci à Flo, mon compagnon d’aventures, de rires, de galère (mais jamais vraiment, parce que la galère avec nous deux c’était toujours plutôt rigolo) et de découvertes. Ton énergie positive, ta perpétuelle bonne humeur, ta confiance indicible dans la vie et ton émerveillement pour le monde qui nous entoure…te côtoyer est un véritable bonheur et m’a longtemps portée ! Je souhaite que cette positivité que tu exhales continue à te revenir en mââsse !

Merci, à vous, Rosanne, Sophie. Je vous ai rencontrées à peu près au début de ma thèse, et vous m’avez accompagnée depuis, avec bienveillance et patience. Merci pour ces longs footings-papote, tellement bienvenus après une longue journée de frustration scientifique; merci pour toutes ces aventures en montagnes, pour notre grand travail sur notre girlitude, pour tous ces rires, ces pleurs et ces émotions partagées. Bref, merci pour tous ces moments de bonheur !

Merci à mes « running vaginas », Coralie, Marion et Delphine, pour ces sessions de courses partagées, ces lunches à cœur ouverts et ces moments de partages autour d’un bout de rocher ou autre objet naturel. Vous m’avez toujours acceptée telle que j’étais, avec mes bizarreries, et je vous en suis tellement reconnaissante !

Merci à mes chimistes, Cyril et Yann pour avoir toujours été là pour moi, m’avoir fait rire et m’avoir écoutée, malgré la difficulté à m’attraper, par moments !

Merci aussi à ma chère Jess. Avec toi, je me sens si libre de parler et de partager mes peurs et mes doutes, car je sais que tu les comprends. Merci aussi pour nos voyages partagés, nos conversations, nos rires et pour ton identité si forte qui souvent m’inspire !

Merci à mon coloc, Nico ! Vivre avec toi a été la première étape d'une transition dans ma vie…et ce fut une transition douce ! La coloc des procrastinateurs aux horaires aléatoires me laissera un souvenir à chérir.

Merci à Hugo, Nadia, Sylwia, Matthieu et Guillaume pour votre support inconditionnel et vos oreilles si attentives !

Merci aux montagnards, Antoine, Greg, Jé, Florian, Jérôme, Yannick, JP, Guillaume pour m'avoir prise sous votre aile et m'avoir fait découvrir ce bonheur incomparable qu'est celui de parcourir la montagne, en liberté et avec admiration.

Merci aux coureurs et aux traileurs, David, Matthieu, Greg, Julien, Tara, Dorian, Charlotte, Aurélien, Silvia, Sara, Carolina, Romain, Blandine, My-Linh et tant d'autres. Vos grands cœurs, et l'atmosphère si chaleureuse de notre groupe de course m'a portée, et m'a véritablement permis de rebondir dans un moment où je ne m'en sentais plus capable.

Merci aux grimpeurs, Matthieu, Sylwia, Noëmie, Fred, Dax, Greg, Jules, Thomas, Daria, Gaëlle, Claire, Angi, Alex. Vous m'avez permis de vivre et de partager ma passion pour la grimpe, dans des conditions exceptionnelles de joie et d'amitié.

Merci à ma famille, Papa, Maman et Eric. Malgré des remous parfois tumultueux, vous avez toujours été mon refuge, mon ancre, et un support incommensurable à l'égard des peurs qui me hantent parfois. J'ai en vous une confiance indéfectible. Et je vous porte un amour inconditionnel.

Enfin, merci à Louis. Nous nous sommes trouvés alors que, tous deux, nous cherchions qui nous étions, et comment demeurer nous-mêmes dans le lien à autrui. Depuis lors, tu m'as permis d'explorer cette question, avec une bienveillance infinie. Tu m'as laissé le temps, et donner l'opportunité de réaliser mes peurs et d'en surmonter certaines. Beaucoup. Je suis tombée profondément amoureuse de toi. Et je t'en suis tellement reconnaissante.

Appendix

A Inter-Domain Charge Transfer as a Rationale for Superior Photovoltaic Performances of Mixed Halide Lead Perovskites

A.1 Global analysis

In the global analysis of chapter 3, the choice between a parallel or sequential model was tricky. We selected the former, as some parts of the TA signal actually arise from a linear combination of individual processes (such as the bleaching dynamics, or the dynamics of the broad positive signal between 600-700 nm). However, we did not go as far as applying an actual kinetic model but focused on extracting the spectral range of individual dynamical processes.

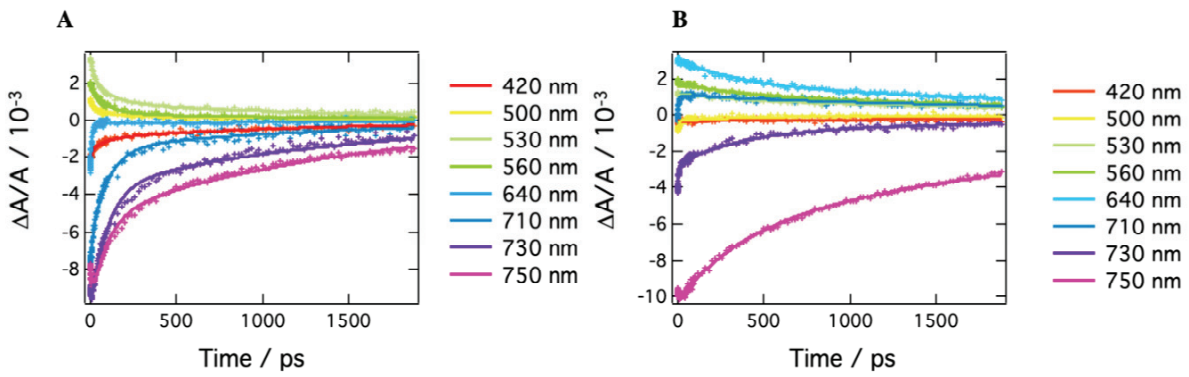

Figure A-1 Sample of triexponential global fit results for transient absorption data recorded at λ_{ex} = 390 nm. **A.** Mixed $MA_yFA_{1-y}Br_xI_{3-x}$ perovskite thin film. **B.** Standard $MAPbI_3$ perovskite thin film.

A.2 Current density-voltage (*J-V*) curves

The data presented in Table 1 of the main text are based on the following *J-V* (Figure A-2) and maximum power point tracking (Figure A-3) measurements, on 5 × 5 mm square solar cells. Note that the *J-V* data have been obtained for both backward and forward directions with a scan rate of 10 mV/s, in air and at ambient temperature.

A xenon lamp equipped with AM1.5 G filter from Newport was used as the light source, together with a silicon reference diode equipped with a KG3 filter. A 4 × 4 mm (0.16 cm^2) black mask was employed throughout the measurements.

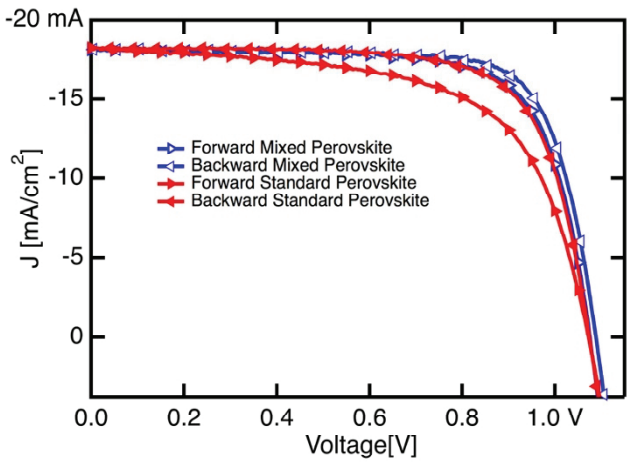

Figure A-2 Backward and forward scanned J-V curve recorded for test solar cell elements (0.16 cm2) made of standard and mixed perovskite films.

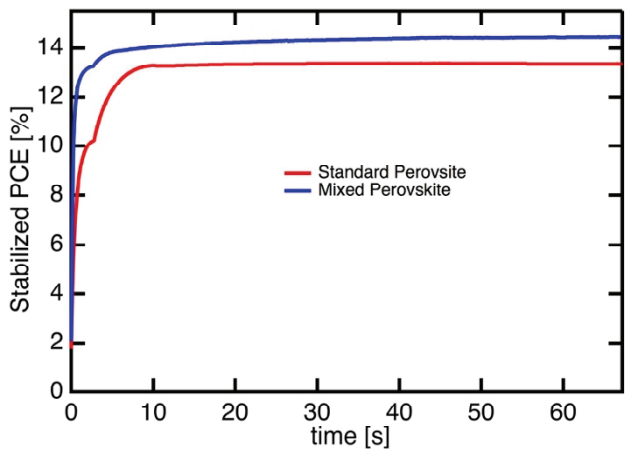

Figure A-3 Maximum power point tracking measured for test solar cell elements made from standard and mixed perovskite films.

It is important to note that PCE values presented in Figure A-2 are relatively low compared to the figures reported for the very best solar cells made of the same materials and fabricated in similar ways. These comparatively low efficiencies are actually due to the use of thin perovskite layers, whose absorbance is not sufficient for harvesting totally the incident light. The thickness of the active layer was limited to match that of the samples used for spectroscopic measurements.

B Unravelling Interfacial processes in mixed anions, mixed cations perovskite solar cells

B.1 Anisotropic TA spectra of perovskite/spiro-OMeTAD samples (complement to Figure)

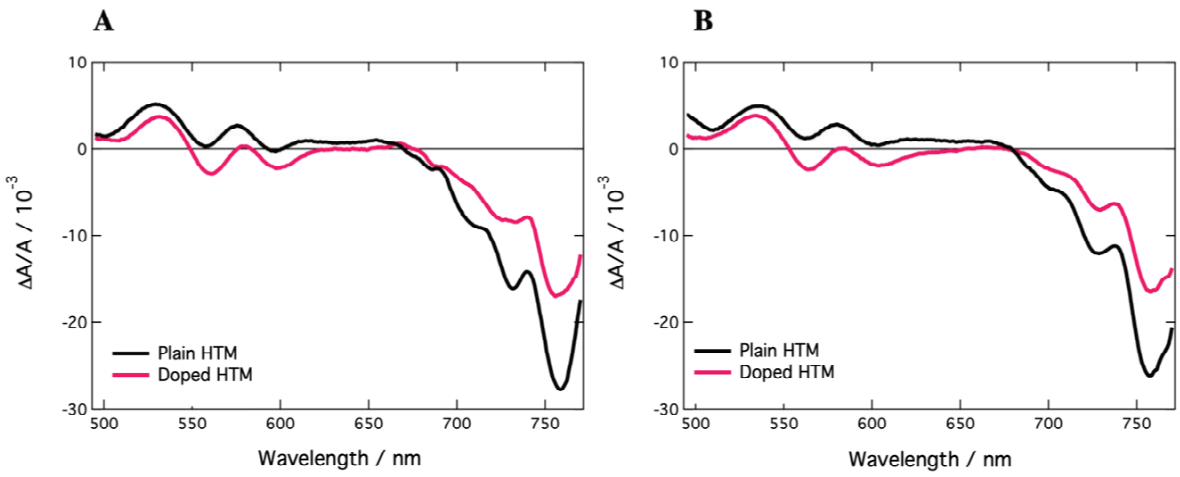

Figure B-1 Anisotropic TA spectra of perovskite/spiro-OMeTAD with the majority of photocarriers created close to the interface**. A.** 0° pump-probe polarization. **B.** 90° pump-probe polarization. Data recorded at λ_{ex}= 390 nm, and at a fluence of 100 mJ cm-2.

C Energy and Charge Transfer Cascade in Methylammonium Lead Bromide Perovskite Nanoparticle Aggregates

C.1 TA spectra for λ_{ex} = 480 nm (complement to Figure 5-2)

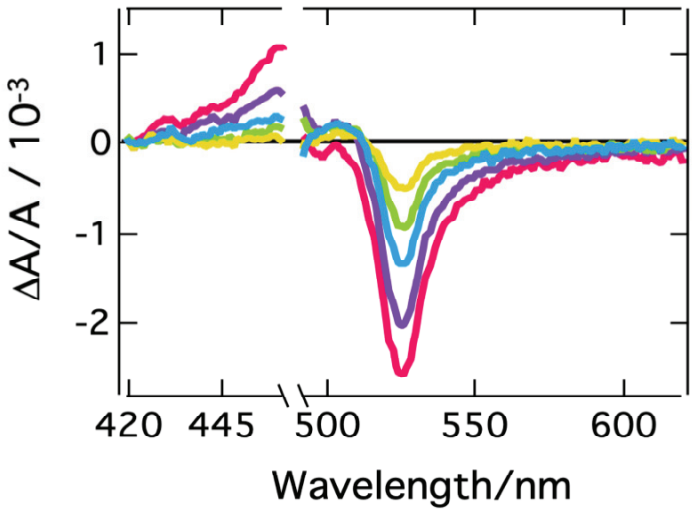

Figure C-1 Transient absorbance spectra for λ_{ex}=480 nm. Red: 2 ps, Purple: 20 ps, Blue: 50 ps, Green: 500 ps and Yellow: 1820 ps.

C.2 Fitting equations (complement to Figure 5-3 and Figure 5-4)

Dynamic traces have been fitted with multiexponential functions, convoluted with a Gaussian IRF when needed.

Datasets in Figure 5-3A and B span a time window between 1 ps and 1880 ps. As a consequence, no convolution with the IRF was needed (gaussian IRF with FWHM= 90 fs for λ_{ex} = 480 nm, FWHM = 200 fs for λ_{ex} = 390 nm).

a. Biexponential function, with equation:

$$\Delta A(\lambda, t) = y_0 + A_1(\lambda) \cdot e^{\left(\frac{-t}{\tau_1}\right)} + A_2(\lambda) \cdot e^{\left(\frac{-t}{\tau_2}\right)} \quad (1)$$

b. Triexponential function, with equation:

$$\Delta A(\lambda, t) = y_0 + A_1(\lambda) \cdot e^{\left(\frac{-t}{\tau_1}\right)} + A_2(\lambda) \cdot e^{\left(\frac{-t}{\tau_2}\right)} + A_3(\lambda) \cdot e^{\left(\frac{-t}{\tau_3}\right)} \quad (2)$$

Ultrafast photoemission data (Figure 5-4B) has been fitted with a triexponential function convoluted with a Gaussian IRF with FWHM = 200 fs (λ_{ex} = 390 nm), with equation: [1]

$$\Delta A(\lambda, t) = \frac{1}{2} \cdot \sum_{i=1}^{3} A_i(\lambda) \cdot e^{\left[\frac{\mu - t}{\tau_i} + \frac{1}{2}\left(\frac{\sigma}{\tau_i}\right)^2\right]} \cdot \left[1 + erf\left(\frac{t - \left(\mu + \frac{\sigma^2}{\tau_i}\right)}{\sqrt{2}\sigma}\right)\right] \tag{3}$$

where μ defines the time-origin of the IRF, with σ its width, with $FWHM = 2\sigma \cdot \sqrt{2ln2}$.

TCSPC dynamics have been fitted with a triexponential function with equation:

$$\Delta A(\lambda, t) = y_0 + A_1(\lambda) \cdot e^{\left(\frac{-t}{\tau_1}\right)} + A_2(\lambda) \cdot e^{\left(\frac{-t}{\tau_2}\right)} + A_3(\lambda) \cdot e^{\left(\frac{-t}{\tau_3}\right)} \tag{4}$$

C.3 Sample fits from the global fitting procedure (complement to Figure 5-3)

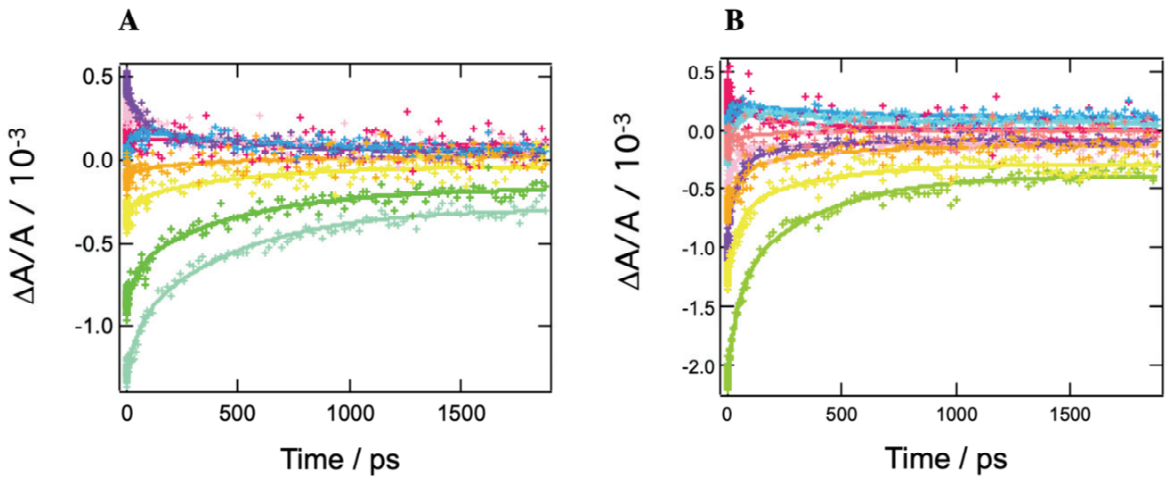

Figure C-2 Sample of global fit results for **A.** λ_{ex} = 480 nm (markers) fitted with a biexponential function (bold lines). Red: 430 nm, pink: 450 nm, purple: 460 nm, blue: 500 nm, turquoise: 520 nm, green: 530 nm, yellow: 540 nm and orange: 560 nm. **B.** λ_{ex} = 390 nm (markers) fitted with a triexponential function (bold lines)**.** Red: 420 nm, pink: 430 nm, purple: 450 nm, blue: 470 nm, turquoise: 480 nm, green: 490 nm, , yellow: 520 nm, orange: 530 nm, dark red: 540 nm, and dark pink: 580 nm.

C.4 EA signal contributions (complement to Figure 5-5)

Figure C-3A shows the linear absorbance spectrum of a suspension of $CH_3NH_3PbBr_3$ nanoparticles, together with its first and second derivatives as well as a linear combination of those (S(λ)) defined by eq. C1 :

$$S(\lambda) = \frac{\partial A(\lambda)}{\partial \lambda} + 10 \cdot \frac{\partial^2 A(\lambda)}{\partial \lambda^2} \qquad (C1)$$

Figure C-3B represents the modelled linear combination S(λ) superimposed with a transient absorbance spectrum (2 ps).

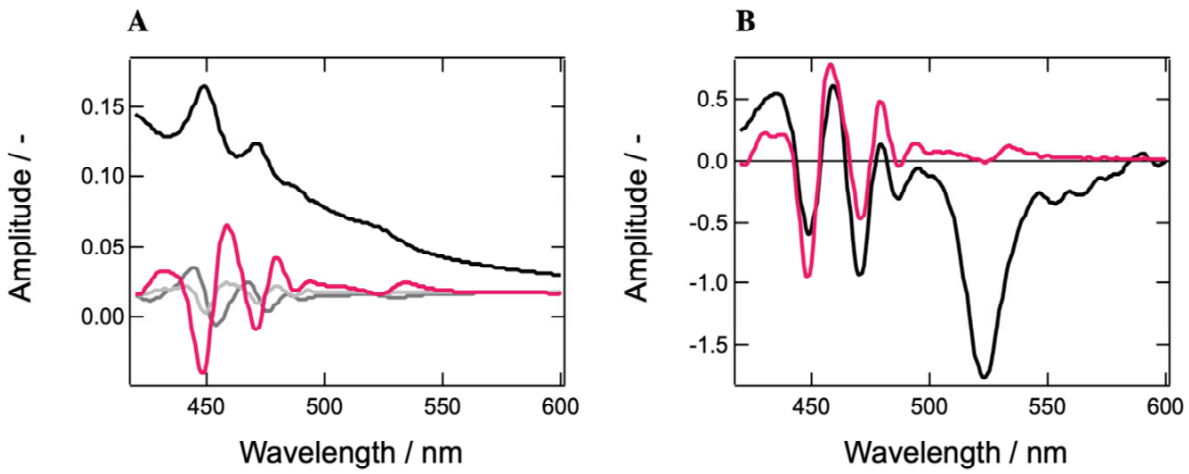

Figure C-3 A. Linear absorbance spectrum of $CH_3NH_3PbBr_3$ nanoparticles (black line) together with its first (dark grey line) and second (light grey line) derivatives. A fitting model (red line) is obtained as a linear combination of first and second derivatives (see equation below). **B.** Obtained fitting model (red line) on top of the 2 ps TA trace (black line, λ_{ex} = 390 nm, Fluence= 9 μJ cm^{-2}).

C.5 Stern-Volmer plots

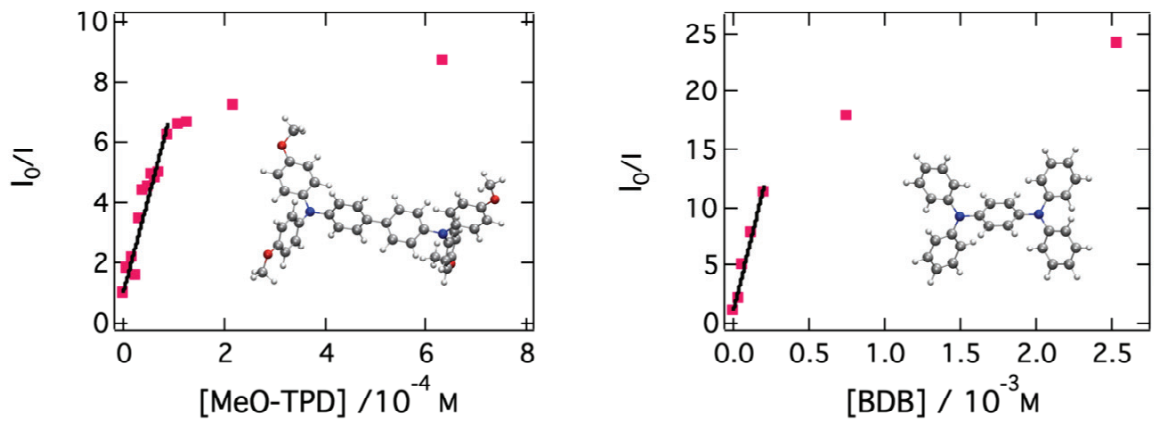

Figure C-4 Stern Volmer plots for chlorobenzene solutions of $CH_3NH_3PbBr_3$ nanoparticles in presence of two different quenchers (λ_{em} = 520 nm): MeO-TPD (**A,** structure in the inset) and BDB (**B,** structure in the inset). The deviation from linearity observed at high quencher concentration translates into a saturation of the quenching process and is not considered in the fitting. Note that an initial nanoparticle concentration of 1 μg/mL was chosen for both plots.

The Stern-Volmer constant K_{SV} is defined as $K_{SV} = k_q\tau_0$, where k_q is the quenching rate constant and τ_0 the fluorescence lifetime without quenchers present in the solution. As such, Stern-Volmer plots provide a direct insight into the value of k_q for a given quenching process. Now, knowing that diffusion-limited processes usually exhibit maximum k_q of the order of 10^{10} $M^{-1}s^{-1}$, we get that these plots allow, to some extent, to discriminate between static or dynamic quenching.

	K_{SV} (M^{-1})
MeO-TPD	$6.3 \cdot 10^4 \pm 3.3 \cdot 10^3$

BDB	$5.3 \cdot 10^4 \pm 3.2 \cdot 10^3$

Table C-1 Extracted Stern-Volmer constants. These values have been obtained from a linear regression on the linear part of the Stern-Volmer plots of Figure C-4.

Considering τ_0 close to 1 μs (from TCSPC measurements), it appears that all of the above Stern-Volmer constants yield k_q well within the range of a diffusion-limited process. We could hence straightforwardly conclude that the quenching processes involving $CH_3NH_3PbBr_3$ nanoparticles are dynamic for the most part. A warning must nonetheless be evoked at this point: this whole model is based upon the fact that the formation of the activated complex, and hence the transfer reaction itself, occurs reasonably fast compared to the diffusion of the partner molecules. However, recall that the nanoparticles are capped with a long aliphatic chain (octylammonium). This likely prevents any intimate contact between the donor and the acceptor, and can result in a slow activated complex formation. As such, even if the partner molecules are in close proximity (no significant diffusion), the static quenching rate can be of the same order of magnitude as a typical dynamic quenching rate.

The obtained rate constants thus can be interpreted in two different manners: either they draw the picture of dynamic quenching, with a fast formation of the donor-acceptor complex; or they simply reflect a loose donor-acceptor contact arising from the octylammonium capping layer. Note that a mixture of both types of interaction is unlikely due to the fact that mixed quenching processes yield quadratic Stern-Volmer plots.

D Crystal Orientation drives the Interface Physics at 3/2-Dimensional Hybrid Perovskites.

D.1 Complements to Figure 6-1

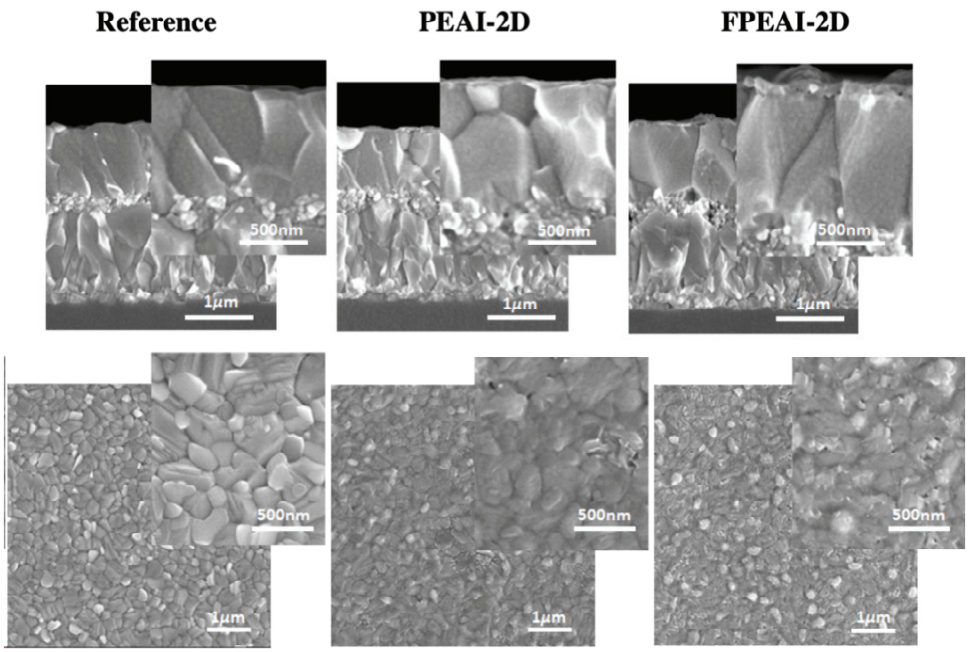

Figure D-1 Top line: cross section SEM for thin film of pure PEAI-2D, FPEAI-2D and Ref 3D. **Bottom line**: top view SEM image for the same samples.

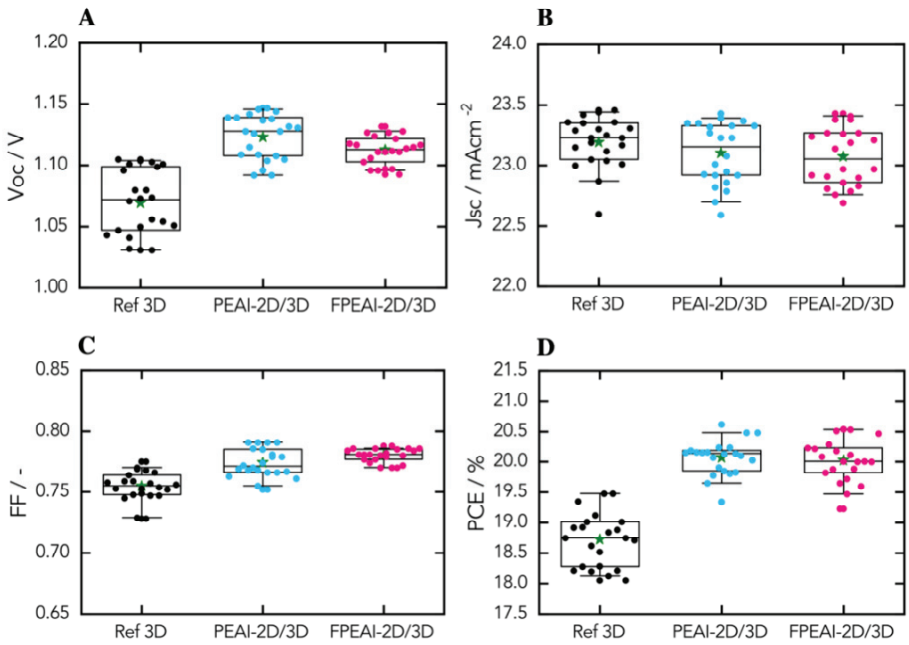

Figure D-2 Device statistics the 3D reference (black), PEAI-2D/3D (blue) and FPEAI-2D/3D (pink).

D.2 Complements to Figure 6-2

D.2.1 TA spectra and relevant fitting parameters

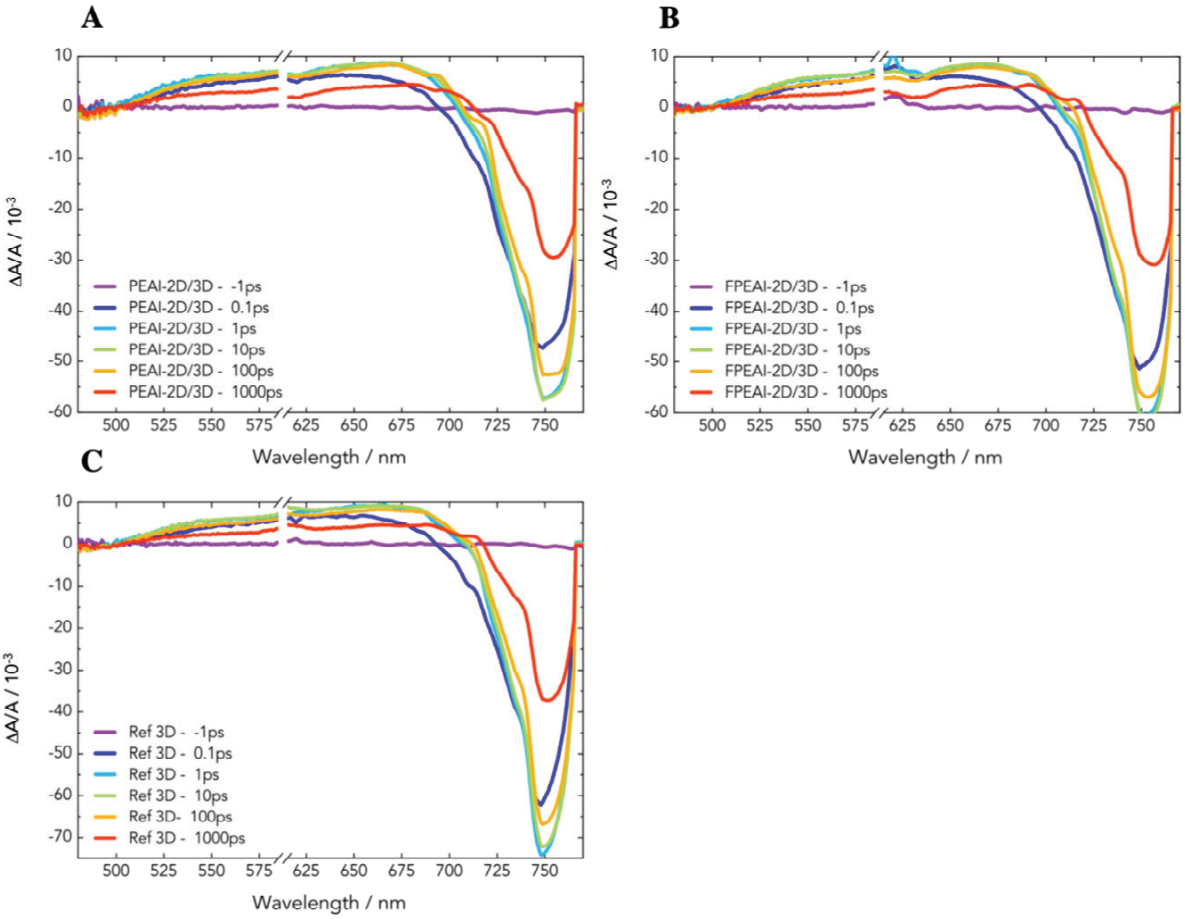

Figure D-3 Femtosecond transient absorption spectra for all three samples of interest with λ_{ex} = 600 nm and at a carrier density of 10^{18} cm^{-3}. **A.** Ref-3D **B.** PEAI-2D/3D **C.**FPEAI-2D/3D.

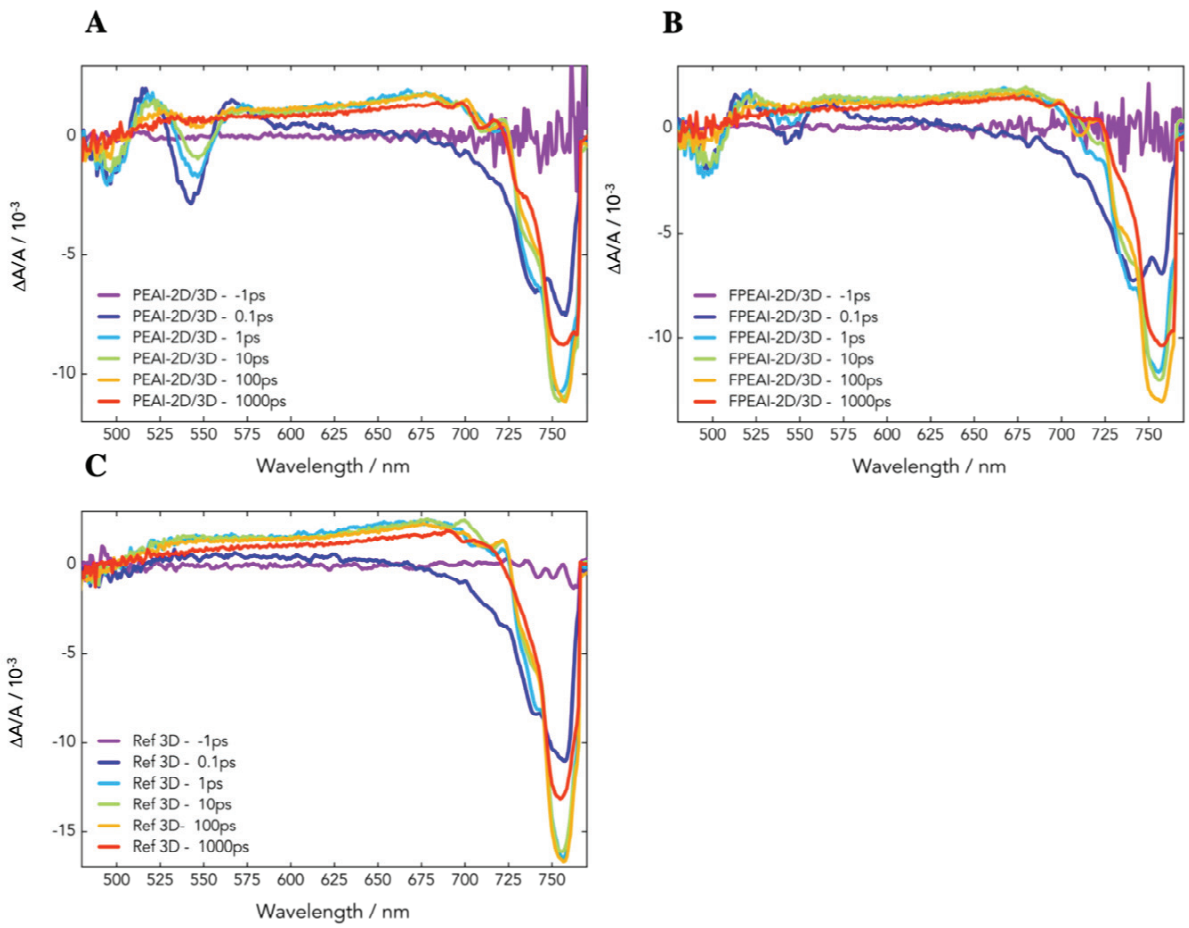

Figure D-4 Femtosecond transient absorption spectra for all three samples of interest with λ_{ex} = 390 nm and at a carrier density of 10^{18} cm^{-3}. **A.** Ref-3D **B.** PEAI-2D/3D **C.** FPEAI-2D/3D.

	PEAI-2D/3D (τ, ps)	**FPEAI-2D/3D (τ, ps)**	**REF 3D (τ, ps)**
497 nm (2D GSB)	16 ± 5	17 ± 4	-
755 nm (3D GSB)	6 ± 1	6± 1	long

Table D-1 Extracted time constants from monoexponential fitting of the traces presented in Figure 6-2C, between 1.5 and 100 ps, at λ_{ex} = 390 nm.

D.2.2 PL and PL map measurements

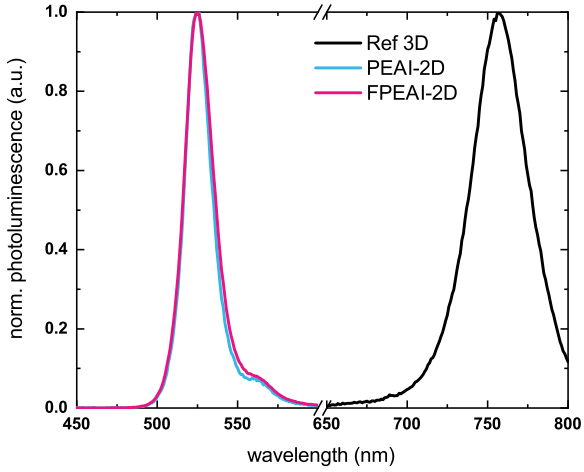

Figure D-5 Photoluminescence spectra for thin film of pure PEAI-2D (blue), FPEAI-2D (pink) and the reference 3D (black).

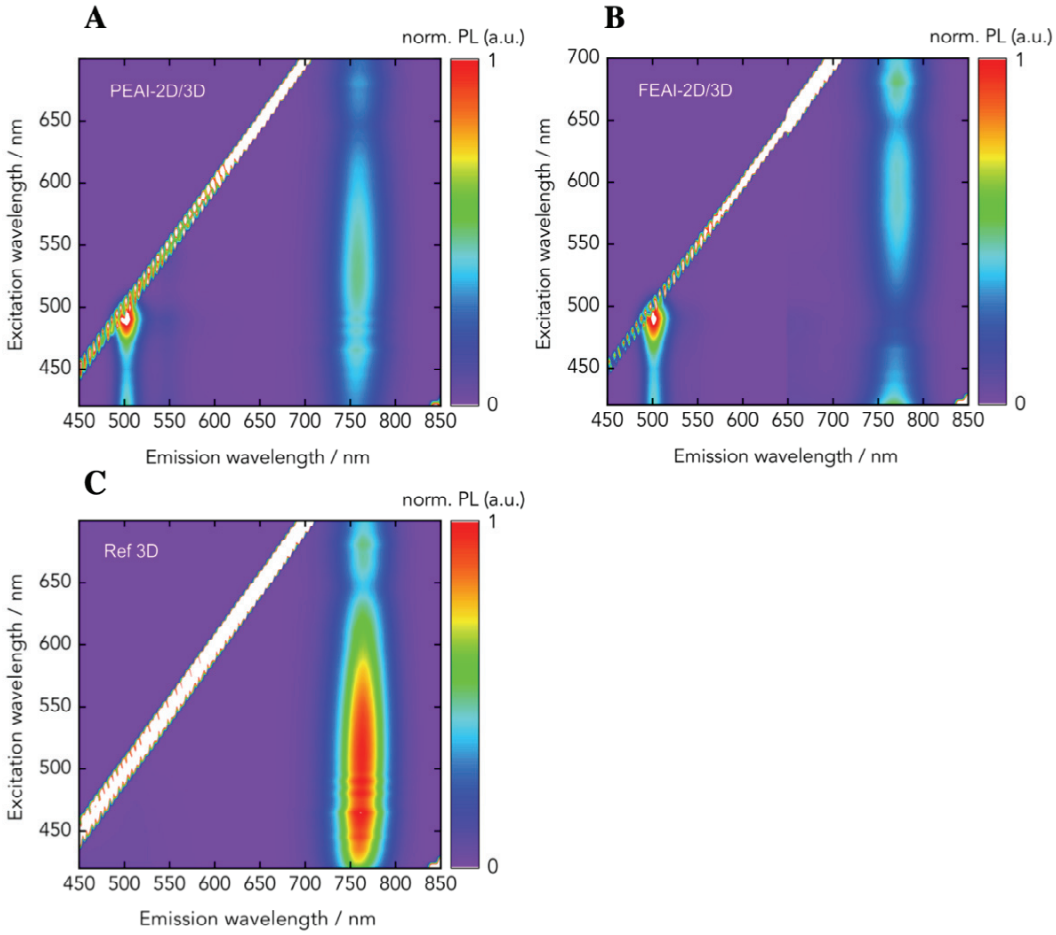

Figure D-6 Photoluminescence excitation map of **A.** PEAI-2D/3D **B.** FPEA-2D/3D **and C.** 3D Reference**.** The samples are excited from the 2D layer. The trace at 500nm correspond to the emission of the 2D layer and the one at 750 nm to the 3D layer underneath.

D.2.3 XPS data

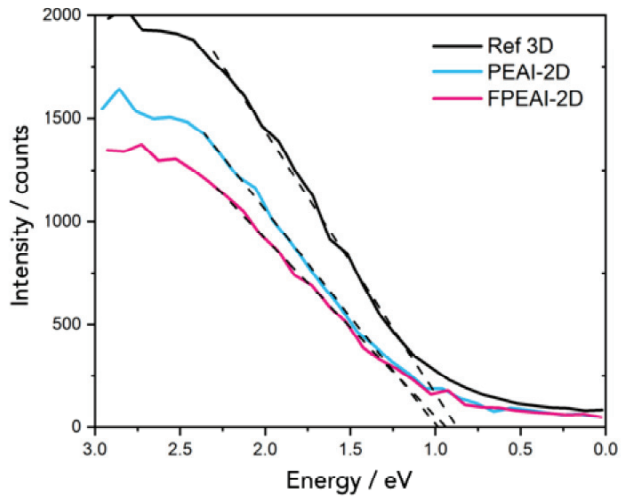

Figure D-1 XPS spectrum zoom around the valence band for thin film of pure PEAI-2D (blue), FPEAI-2D (pink) and the reference 3D (black).

D.3 Complements to Figure 6-3

D.3.1 PL decay parameters

	A_1	τ_1 (ns)	A_2	τ_2 (ns)
PEAI-2D/3D	0.387 ± 0.004	244 ± 4	0.450 ± 0.004	1401 ± 10
FPEAI-2D/3D	0.22 ± 0.01	38 ± 2	0.49 ± 0.01	129 ±1
Ref-3D	0.052 ± 0.02	96 ± 1	0.22 ± 0.02	40 ± 2

Table D-2 Extracted parameters from the biexponential fitting of the PLdecays shown in Figure 6-3A, at λ_{ex} = 635 nm.

	A_1	τ_1 (ns)	A_2	τ_2 (ns)
HTM/PEA-2D/3D	0.50 ± 0.01	97 ± 1	0.20 ± 0.01	675 ± 6
HTM/FPEA-2D/3D	0.40 ± 0.01	97 ± 2	0.47 ± 0.01	321 ± 1

Table D-3 Extracted parameters from the biexponential fitting of the PL decays shown in Figure 6-3C, at λ_{ex} = 635 nm.

D.3.2 TRMC data

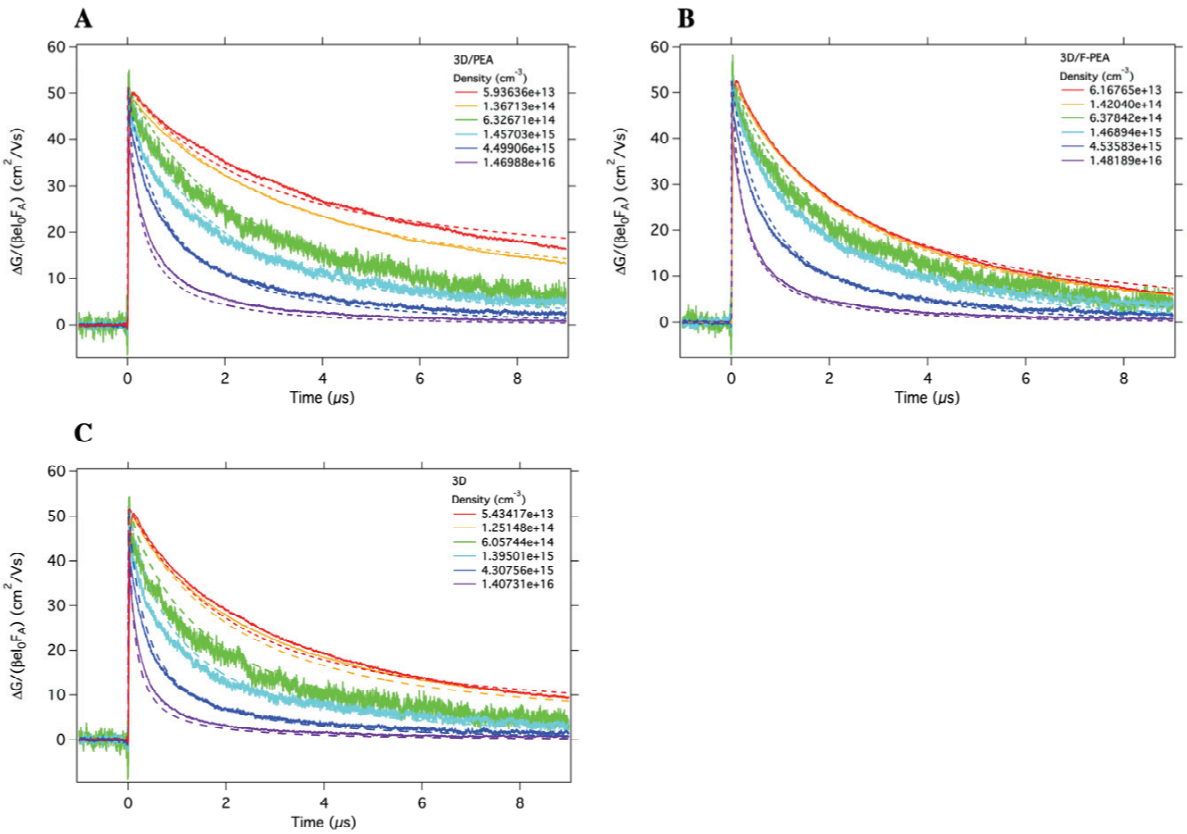

Figure D-2 Intensity dependent TRMC data for **A.** Ref 3D. **B.** PEAI-2D/3D and **C.** FPEAI-2D/3D with corresponding fits.

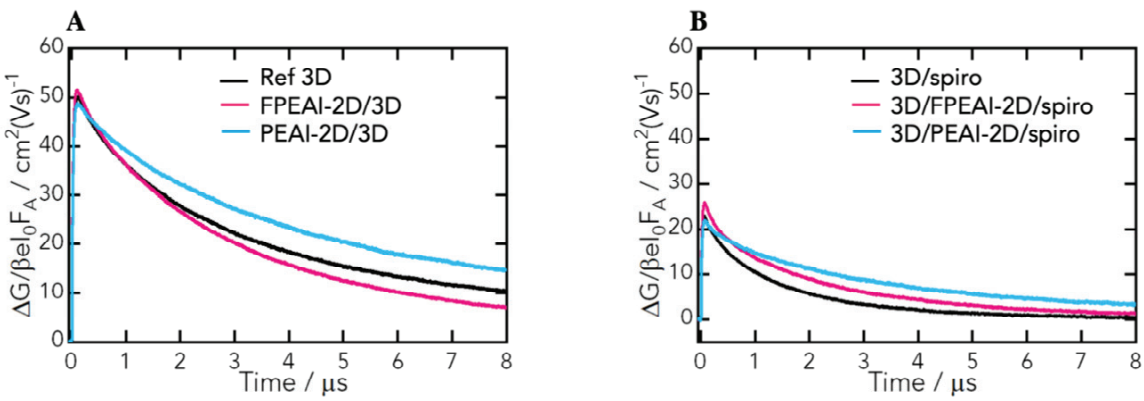

Figure D-3 TRMC data for Ref 3D, PEAI-2D/3D and FPEAI-2D/3D without **(A)** and with **(B)** HTM, as indicated in the legends.

D.3.3 Kinetic model for fitting of the TRMC data

Schematically, the kinetic model used to fit the TRMC data reads as follows:

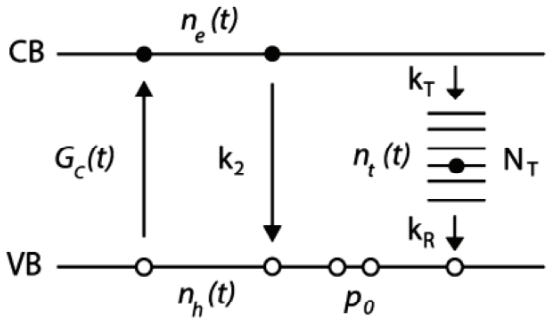

Figure D-4 Schematic representation of the generation (G_c) and recombination processes accounted in the kinetic model mentioned in the main text.

with the corresponding kinetic equations:

$$\frac{dn_{CB}}{dt} = \frac{dn_e}{dt} = G_C - k_2\, n_e(n_h + p_0) - k_T n_e(N_T - n_T) - k_e n_e$$
$$\frac{dn_{VB}}{dt} = -\frac{dn_h}{dt} = -G_C + k_2\, n_e(n_h + p_0) + k_D n_t(n_h + p_0) + k_h n_h$$
$$\frac{dn_t}{dt} = k_T\, n_e(N_T + n_T) - k_D n_t(n_h + p_0),$$

yielding:

Parameters	3D	3D/PEAI	3D/FPEAI
k_T	2e-09	1e-09	2e-09
k_2	6e-10	2.8e-10	3e-10
k_D	5e-10	8e-10	1e-09
N_T	2.5e+14	5e+14	3e+14
p_0	9e+13	5e+12	1e+14

Table D-1 Fitting parameters obtained from the fitting of a kinetic model to the intensity-dependent TRMC data.

D.4 Complements data for Figure 6-4

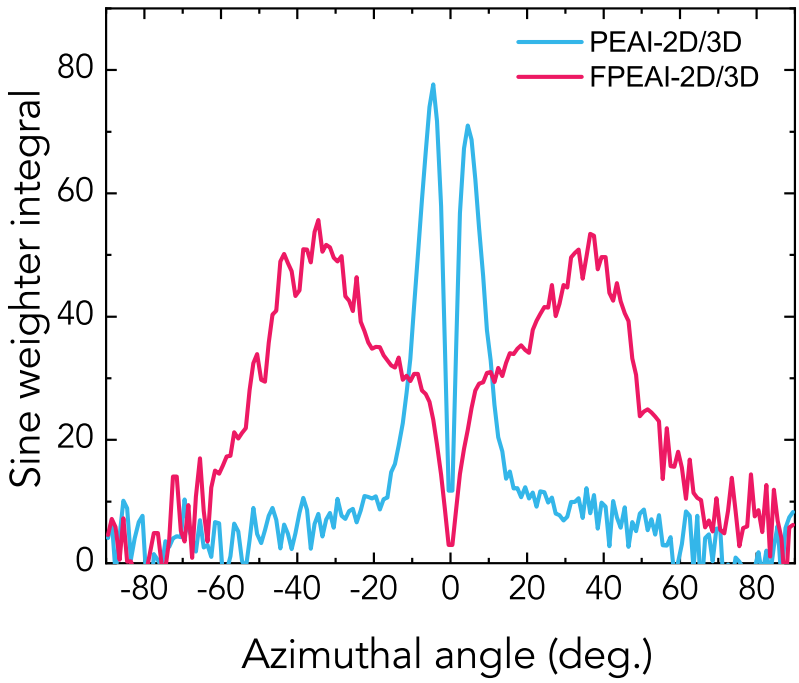

Figure D-11 Sine weighted integral of Figure A, B for PEAI-2D/3D and FPEAI-2D/3D, showing the different preferred orientation.

E A speculative study of the polaronic character of excitons in 2D perovskites

BUA – 512 nm (carriers / cm^3)	τ_1	τ_2	τ_3
$3 \cdot 10^{17}$	0.26 ± 0.01	9.8 ± 0.8	132 ± 6
$6 \cdot 10^{17}$	0.28 ± 0.01	14.0 ± 0.7	121 ± 5
$9 \cdot 10^{17}$	0.32 ± 0.01	10.5 ± 0.5	98 ± 4
$1.5 \cdot 10^{18}$	0.34 ± 0.01	8.0 ± 0.4	77 ± 3
$3 \cdot 10^{18}$	0.31 ± 0.01	6.6 ± 0.2	62 ± 2
$6 \cdot 10^{18}$	0.41 ± 0.02	3.9 ± 0.1	51 ± 469

BUA – 525 nm (carriers / cm^3)	τ_1	τ_2	τ_3
$3 \cdot 10^{17}$	0.31 ± 0.01	10.4 ± 0.9	162 ± 6
$6 \cdot 10^{17}$	0.285 ± 0.03	6.6 ± 0.5	109 ± 3
$9 \cdot 10^{17}$	0.324 ± 0.004	10.2 ± 1	111 ± 6
$1.5 \cdot 10^{18}$	0.315 ± 0.003	11.5 ± 0.8	103 ± 5
$3 \cdot 10^{18}$	0.306 ± 0.003	10.5 ± 0.7	84 ± 4
$6 \cdot 10^{18}$	0.32 ± 0.01	3.8 ± 0.5	47 ± 2

FPEA – 514 nm (carriers / cm^3)	τ_1	τ_2	τ_3
$3 \cdot 10^{17}$	0.35 ± 0.02	5.1 ± 1.1	240 ± 37
$6 \cdot 10^{17}$	0.39 ± 0.01	4.8 ± 1.6	80 ± 12
$9 \cdot 10^{17}$	0.32 ± 0.01	3.7 ± 0.7	61 ± 7
$1.5 \cdot 10^{18}$	0.35 ± 0.01	4.7 ± 0.8	55 ± 8
$3 \cdot 10^{18}$	0.33 ± 0.01	3.9 ± 0.4	35 ± 4
$6 \cdot 10^{18}$	0.38 ± 0.01	3.2 ± 0.2	27 ± 3

FPEA – 525 nm (carriers / cm^3)	τ_2,	τ_3
$3 \cdot 10^{17}$	29.8 ± 5.6	346 ± 48
$6 \cdot 10^{17}$	28.8 ± 3.2	171 ± 16
$9 \cdot 10^{17}$	15.9 ± 0.8	147 ± 8
$1.5 \cdot 10^{18}$	14.9 ± 0.6	129 ± 6
$3 \cdot 10^{18}$	11.8 ± 0.5	96 ± 6
$6 \cdot 10^{18}$	10.2 ± 0.5	72 ± 6

FPEA – 531 nm (carriers / cm^3)	τ_1	τ_2	τ_3

$3 \cdot 10^{17}$	0.40 ± 0.01	3.6 ± 0.3	194 ± 10
$6 \cdot 10^{17}$	0.42 ± 0.01	5.2 ± 0.5	174 ± 12
$9 \cdot 10^{17}$	0.34 ± 0.01	3.3 ± 0.3	108 ± 5
$1.5 \cdot 10^{18}$	0.38 ± 0.01	6.1 ± 0.7	119 ± 13
$3 \cdot 10^{18}$	0.33 ± 0.06	4.6 ± 0.6	85 ± 9
$6 \cdot 10^{18}$	0.31 ± 0.01	3.9 ± 0.6	82 ± 13

Table E-1 Time constants extracted from multiexponential fits of peaks 1-3 of BUAI-2D and FPEAI-2D.

MARINE BOUDUBAN

LAUSANNE, 1006, SUISSE | 0041 79 790 19 76

OBJECTIVES

Apply my thinking to impactful projects
Challenge my comfort zone
Learn new soft and hard skills

DETAILS

Rue du Crêt 10, Lausanne,
1006, Suisse
0041 79 790 19 76
marine.bouduban@gmail.com

SKILLS

Project management

Experiment design

Scientific communication

Out-of-the-box thinking

Spectroscopy

LANGUAGES

French

English (C2)

German (B2)

HOBBIES

Trail running, Climbing, Ski touring

EDUCATION

EPFL, Lausanne

February 2015 – Present

Degree: PhD candidate

Spectroscopist: specialist of semiconducting materials for optoelectronics.

Various conference contributions and prizes.

EPFL and Stanford University, Lausanne / Stanford

September 2012 – April 2014

Degree: Master of Chemistry

Major in physical and theoretical chemistry.

Various research projects in theoretical chemistry: Quantum dynamics and electronic structure methods.

Master thesis carried out in the group of Todd J. Martinez, Stanford University.

Winner of the prize for the best Master of Chemistry.

EPFL, Lausanne

September 2009 – July 2012

Degree: Bachelor of Chemistry

Major in physical and theoretical chemistry.

Gymnase de Morges, Morges

August 2006 – July 2009

Degree: Maturité Gymnasiale

Major in philosophy and psychology, with a particular interest for Idealism and Existentialism.

Strong interest for languages. Successful procurement of a C1 diploma in German.

Winner of the excellence prize for the Maturité Gymnasiale.

EMPLOYMENT HISTORY

PhD Candidate at EPFL, Lausanne

February 2015 – Present

Research focusing on the spectroscopical investigation of the charge carriers interaction and dynamics, within semiconducting materials intended for optoelectronic applications.

Senior Teaching Assistant at EPFL, Lausanne

February 2015 – Present

Project Researcher at Stanford University, Stanford

September 2013 – April 2014

Research project focusing on the development, implementation and testing of the gradient of a multireference electronic structure method.

Project Researcher at Imperial College, London

October 2014 – December 2014

In the context of a collaboration with an experimental physics group, design of a working active- space aiming at describing accurately core-ionization of the glycine molecule.

Higher Education Teacher at Guigoo, Lausanne

August 2010 – August 2012

PUBLICATION LIST

Nonadiabatic Molecular Dynamics Based on Trajectories

Felipe Franco de Carvalho, Marine E.F. Bouduban et al., *Entropy,* 2014, 16, 62-85

Analytic First derivatives of floating occupation molecular orbital-complete active space configuration interaction on graphical processing units

Edward G. Hohenstein, Marine E.F. Bouduban et al., *J. Chem. Phys*, 2015, 143, 014111

Unreacted PbI2 as a Double-Edges Sword for Enhancing the Performance of Perovskite Solar Cells

T. Jesper Jacobsson, […], Marine E.F. Bouduban et al., *J. Am. Chem. Soc,* 2016, 138, 10331-10343

Energy and charge transfer cascade in methylammonium lead bromide perovskite nanoparticle aggregates

Marine E.F. Bouduban, Andrés Burgos-Caminal et al., *Chem.Sci,* 2017, 8, 4371-4380

Unveiling the Nature of Charge Carrier Interactions by Electroabsorption Spectroscopy: An Illustration with Lead-Halides Perovskites

Marine E.F. Bouduban, Andrés Burgos-Caminal et al., *Chem.Sci,* 2017, 8, 4371-4380

Charge migration engineered by localization: electron-nuclear dynamics in polyenes and glycines

Iakov Polyak, […], Marine E.F. Bouduban, et al., *Mol. Phys*, 2018, 19, 2474-2489

Photophysical heavy-atom effect in iodinated metallocorroles: Spin-orbit coupling and density of states

Enrico Pomarico, […], Marine E.F. Bouduban, et al., *J. Phys. Chem. A*, 2018, 122, 7256-7266

Inter-Domain Charge Transfer as a Rationale for Superior Photovoltaic Performances of Mixed Halide Lead Perovskites

Marine E.F. Bouduban, Fabrizio Giordano et al., submitted.

EXTRA-CURRICULAR ACTIVITIES

Yadlo organizer at Yadlo, Préverenges

January 2015 – Present

Organization of Yadlo, a festival around the lake and its atmosphere.

Activities Director.

Ce document a été imprimé au Centre d'impression EPFL,
imprimerie climatiquement neutre, certifiée myClimate.